Compliant Mechanisms in Lunar Surface Exploration: Design and Technology Considerations for Dust Mitigation

Dorota Budzyń

Submitted in fulfillment of the requirements for the
Degree of Doctor of Philosophy

James Watt School of Engineering
College of Science and Engineering
University of Glasgow

March 2024

"I think we're going to the Moon because it's in the nature of the human being to face challenges. It's by the nature of his deep inner soul. We're required to do these things just as salmon swim upstream."

– Neil Armstrong (1930 – 2012)

ABSTRACT

The experience gained from Apollo lunar exploration and multiple robotic lunar missions has underscored the considerable challenges posed by the lunar environment for hardware operations. These challenges encompass a wide range of issues, including thermal extremes during the lunar day and night cycle, vacuum conditions limiting the choice of suitable materials (including lubricants), harsh radiation exposure, micro-meteorite impacts, and the prevalent issue of lunar dust and regolith.

Lunar regolith, the surface material covering the Moon, consists of particles of varying dimensions, ranging from fine lunar dust with grain sizes measured in micrometres to larger pebbles and rock fragments. Lunar dust, in particular, has proven to be an exceptionally formidable obstacle for lunar exploration. The array of challenges it presents includes obstructed vision for both astronauts and cameras, potential inhalation and irritation of the respiratory system, loss of traction, false instrument readings, thermal control complexities, dust coating and contamination, abrasion, seal failures, and the vexing problem of clogged mechanisms.

The primary focus of the work presented here lies in the realm of mechanism design, specifically targeting the pressing issue of mechanism clogging induced by the lunar dust. The solution proposed in this work can be characterised as implicit dust mitigation. It focuses on a deliberate design choice that employs compliant mechanisms to eliminate the most dust-sensitive components within mechanisms, namely, inter-element gaps. Unlike traditional mechanisms that rely on rigid-body joints, such as hinges and sliders, compliant mechanisms leverage elastic deformation to achieve motion. Consequently, they are free of the inter-element gaps susceptible to dust accumulation, which can lead to increased friction and eventual jamming. By replacing traditional tribological contacts with compliant hinges and flexures that facilitate motion through flexible deformation, this approach yields mechanisms that are inherently resistant to dust-induced jamming.

However, the design of compliant mechanisms presents its own set of challenges. In this work, a range of design methodologies were explored, encompass-

ing analytical and topology optimisation-based approaches. Additionally, various polymers suitable for additive manufacturing were examined in the context of their compatibility with the compliant mechanism design. The intricate relationship between material properties and design methodologies is discussed within this work, providing useful insight into the potential problems of various methodology and material choices.

The culmination of these efforts resulted in the design, manufacturing, and testing of multiple compliant grippers. Early prototypes were tested to refine the methodology, test procedures, and ultimately design more sophisticated compliant grippers that aimed to emulate the functionality of the Apollo geological tool known as Tongs. The final design approach proposed here comprises a two-step process involving topology optimisation followed by an analytical re-design step. The latter is tailored towards reducing stress levels in the flexures and enhancing large-scale deformations. These advances were followed by a series of tests enhanced with the use of Digital Image Correlation tools, enabling the visualisation of deformation fields within the grippers. Finally, an additional set of tests was conducted using the lunar regolith simulant EAC-1A to validate the dust-resilient behaviour of the mechanisms and demonstrate their effectiveness in the lunar environment. This research not only contributes to addressing the specific challenges of lunar dust but also advances the broader understanding of compliant mechanisms, their design methodologies, and their applicability in lunar exploration.

PREFACE

This thesis presents work carried out by the author in the James Watt School of Engineering at the University of Glasgow in collaboration with European Space Agency (ESA). The project is co-funded by the ESA through ExPeRT - Exploration Preparation, Research and Technology program under the grant number ESA AO/1-10811/21/NL/MG/idb.

ACKNOWLEDGEMENTS

I would like to thank my supervisor Dr Andrea Cammarano for guiding me through my PhD project and for believing in me every step of the way. He has been an inspiration and a friend and I could not imagine having a better mentor. I would also like to recognise and thank my co-supervisor Dr Hossein Zare-Behtash for always being positive and helping me to find a solution for every problem. I am extremely proud to have worked with such incredible individuals and will always aspire to be more like Dr Cammarano and Dr Zare-Behtash.

I would also like to thank my husband Stephen Ennis for making space in our lives for this adventure. For all the creative discussions, for turning our pantry into a 3D printing laboratory, for listening to my research problems over dinner, and for believing in me when I was not able to. I could not have done this without his support.

I was also lucky to work with Dr Aidan Colwey from the European Space Agency. I would like to express my gratitude for putting the trust in me to conduct this research and I would like to thank ESA for providing financial support for this project.

I would also like to thank Zonta International for awarding me with the Amelia Earhart Fellowship and for the recognition of my achievements. This has been an incredible honour and motivated me to continue my work.

I also want to thank Dr Gordon Wasilewski, Dr Kevin Worrall, and Dr Paul Prentice for all the discussions and suggestions provided during my PhD viva. It has been a pleasure to defend my thesis with you.

And to the numerous researchers, scientists, and engineers who I met during my PhD and who gave me advice, guidance, and who shared their experiences with me: thank you all, please know that I will try to support the next generation of researchers as well.

COVID-19 IMPACT

The research presented in this thesis has been influenced by the unprecedented challenges posed by the COVID-19 pandemic. The impact of the pandemic required some adjustments to the course of this work and the methods by which it was conducted.

Almost the entire initial literature survey was carried out in the teleworking setting without any significant impact on the course of the work. However, further activities had to be adjusted to accommodate this new working environment. In particular, the work presented in Chapter 4 of this thesis, titled "Initial Design and Testing: PLA and TPC Grippers", was significantly affected by the constraints and limitations imposed by the pandemic and the restricted access to university laboratories. During this challenging period, a substantial portion of the work was carried out remotely, utilising private 3D printers and test rigs made at home. However, it was done under the close guidance of the thesis supervisors to ensure adequate quality of research.

AUTHOR'S DECLARATION

I declare that, except where explicit reference is made to the contribution of others, this dissertation is the result of my own work and has not been submitted for any other degree at the University of Glasgow or any other institution.

Printed Name: Dorota Budzyń

Signature: ....

CONTENTS

LIST OF FIGURES

LIST OF TABLES

NOMENCLATURE

Acronyms

ABS   Acrylonitrile Butadiene Styrene

AD   Analytical Design

ALSEP   Apollo Lunar Surface Experiments Package

AM   Additive manufacturing

AMF   Additive Manufacturing Facility

AMS   Aerospace Mechanisms Symposium

BYU   Brigham Young University

CAD   Computer-Aided Design

CNSA   China National Space Administration

CSA   Canadian Space Agency

DIC   Digital Image Correlation

DOC   Degree Of Constraint

DOF   Degree Of Freedom

EAC   European Astronaut Centre

EBM   Electron Beam Melting

EDM   Electric Discharge Machining

EDS   Electrodynamic Dust Shield

ESA   European Space Agency

ESMATS   European Space Mechanisms and Tribology Symposium

ESO   Evolutionary Structural Optimisation

EVA   Extra Vehicular Activity

ExPeRT   Exploration Preparation, Research and Technology (ESA programme)

FACT   Freedom And Constraint Topologies

FDM   Fused Deposition Modelling

FEA   Finite element analysis

FEM   Finite element method

FMD   Flip Mirror Device

GA   Geometric Advantage

GUI   Graphical user interface

HDRM   Hold Down and Realease Mechanism

HIP   Hot Isotropic Pressing

ISS   International Space Station

JSC   Johnson Space Center

LISA   Laser Interferometer Space Antenna

LSM   Level Set Method

MA   Mechanical Advantage

ME   Mechanical Efficiency

MEMS   Micro-electro-mechanical systems

MMC   Moving Morphable Components

MoS_2 Molybdenum disulphate

MPE   Mutual Potential Energy

MTG   Meteosat Third Generation

NASA   National Aeronautics and Space Administration

NEEMO	NASA Extreme Environment Mission Operations
PAAM	Point Ahead Angle Mechanism
PANGAEA	Planetary ANalogue Geological and Astrobiological Exercise for Astronauts
PCB	Printed circuit board
PEEK	Polyetheretherketone
PEKK	Polyetherketoneketone
PLA	Polylactic Acid
PTFE	Polytetrafluoroethylene
RBRM	Rigid Body Replacement Method
ROI	Region of interest
SE	Strain Energy
SIMP	Solid Isotropic Material with Penalisation
SLM	Selective Laser Melting
SLSTR	Sea and Land Surface Temperature Radiometer
TO	Topology Optimisation
TPC	Thermoplastic Co-Polyesters
TPU	Thermoplastic Polyurethane
UV	Ultraviolet
X-ray	High energy electromagnetic radiation
Z-PEEK	Polyetheretherketone from company Zortrax

Symbols

σ_y	Yield strength, MPa
C	Global compliance matrix
d_{in}	Input displacement, mm
d_{out}	Output displacement, mm
E	Young's modulus, MPa or GPa
F	Global force matrix
F_{in}	Input force, N
F_{out}	Output force, N
i	Number of iterations
K	Global stiffness matrix
k_{in}	Input stiffness, N/m or N/mm
k_{out}	Output stiffness, N/m or N/mm
$nelx$	Number of elements in horizontal direction
$nely$	Number of elements in vertical direction
$penal$	Penalty in SIMP topology optimisation
$rmin$	Minimum radius, mm
U	Global displacement matrix
$volfrac$	Volume fraction
x	Density of finite element in SIMP topology optimisation

CHAPTER 1

INTRODUCTION

"I think dust is probably one of our greatest inhibitors to a nominal operation on the Moon. I think we can overcome other physiological or physical or mechanical problems except dust."

- Eugene Cernan, Apollo 17 astronaut [1]

1.1 MOTIVATION

In 2017 the Neutral Buoyancy Facility of the European Space Agency (ESA) started prototyping lunar geological sampling tools and Extra Vehicular Activity (EVA) support equipment [2]. The focus of the project was prototyping of the hardware to be tested in the pool of the Neutral Buoyancy Facility, during PANGAEA (Planetary ANalogue Geological and Astrobiological Exercise for Astronauts) activity on volcanic island of Lanzarote and during the NEEMO (NASA Extreme Environment Mission Operations) underwater mission conducted 19 m below the surface of the sea of the coast of the Florida Keys. The core aim of the project was ergonomics of the astronaut tools and integration of the updated scientific exploration goals into the design of the new tools. The author of this work participated in the mentioned ESA activity, gaining invaluable experience that led to the development of the doctoral project at the University of Glasgow.

During the ESA project mentioned above, replicas of surface tools used in Apollo missions were tested (as visible in Figure 1.1) and investigated to identify areas that need improvement for a new generation of surface equipment. Apollo

Figure 1.1: ESA lunar simulations; pictures courtesy of ESA: (a) Test of geological tools during NEEMO 23 in 2019; (b) Test of geological tools during Pangea-X 2018.

geological tools were used by astronauts to collect rocks and regolith samples during EVAs.

As part of the ESA project discussed, the test results of Apollo tools' replicas were analysed to pinpoint areas that require enhancements for the next generation of surface equipment. Furthermore, a historic Apollo data was carefully studied to find out information on the tools performance on the Moon.

In the course of Apollo operations unexpected problems occurred, including increased friction and clogging of the mechanisms, extensive abrasion, seal failures, dust coating and contamination, thermal control problems, loss of traction, false instrument readings, vision obstruction, dust inhalation in lunar module and irritation of the respiratory system [1]. Numerous issues that arose during the missions were either unforeseen or their consequences were undervalued during the planning phase. This was primarily because prior to the historic Apollo 11 landing in 1969, there was limited knowledge regarding the surface conditions of our natural satellite. A prime example of this was the apprehension among certain scientists that the lander might sink into the fine and loose regolith [3]. Although the landing ultimately proved to be a triumph, other challenges emerged as a result of the unique nature of the lunar environment.

As part of the ESA project, it was discovered that addressing the environmental impact on hardware was a critical technology gap that needed to be bridged to ensure the success of future surface operations of equipment. There are various challenges that impact the design of space hardware, particularly for lunar missions. One distinctive challenge on the Moon is the presence of a fine fraction of regolith on the surface. It has shape, size, hardness, and electrostatic properties that make it extremely disruptive to any hardware operation, which will be further discussed in this work. In order to ensure the success of future missions, it is

crucial to understand the processes that affected the hardware on the Moon. A literature review synthesised in this work presents data on lunar dust and its impact on hardware. As will be demonstrated, some of the problems left Apollo hardware and tools unusable or difficult to operate after just a few EVAs. Improvements in hardware performance and dust mitigation would have a tremendous impact on future lunar operations. As already mentioned, the ESA project focused on prototyping for improved ergonomics. The doctoral work presented here is the natural continuation of that project, accessing the challenges that could not be solved in the scope of activities conducted in the Neutral Buoyancy Facility. Dust contamination and dust-driven hardware degradation was identified as the next challenge. The main focus of this work is to explore the methodology for developing hardware with enhanced resistance to dust, in particular, for the moving elements of the hardware, known as mechanisms.

This project aims to showcase particular design and manufacturing technologies that are proposed as effective approaches to mitigate lunar dust, which differ significantly from existing state-of-the-art methods. To date, no dust mitigation technology has been able to demonstrate efficacy 100% in various scenarios of lunar dust mitigation requirements. The literature suggests that multiple dust mitigation solutions should be employed in a layered engineering defence strategy to address lunar dust challenges [4]. As far as the author knows, the solutions presented here were introduced as implicit dust mitigation technologies for the first time during the course of this project.

It is worth noting that NASA and its international partners, including ESA, are working towards crewed landings on the Moon as part of the Artemis programme. The mission's objectives comprise conducting scientific research and exploration on the lunar surface. To ensure the success of these endeavours, it is crucial to design and develop hardware that can withstand the harsh lunar environment and perform its intended tasks without failure. The author of this work aspires that this project will be one of many contributions to ensure that future hardware designed for the lunar surface can fulfil its full potential.

1.2 PROBLEM STATEMENT

This research work focuses on a specific lunar dust-induced problem - clogging of the rigid-body mechanisms. According to the literature [5], the finest dust particles, measuring less than 2 μm in diameter, posed the greatest challenge during Apollo missions. Lunar dust and regolith particles were generated by micrometeorite impacts that resulted in the creation of particulets with sharp edges. Furthermore, on the Moon, they are not exposed to hydrological and aeolian erosion,

and the sharp, abrasive edges persists. According to Rickman and Street [6], the minerals found in the regolith such as arnorthite, bytownite, labradorite, fayalite, or forsterite have a Mohs hardness score of 6 or higher. Most popular engineering materials used in space (steel, aluminium, titanium) present lower values on the same scale, and therefore they are prone to lunar dust-induced abrasion. Furthermore, avoiding dust contamination is challenging as the lunar environment is exposed to solar wind plasma, free electrons, and solar UV rays that cause photoemission and electrostatic charge accumulation [7, 8].

Small lunar dust particles can enter the clearances and backlashes in the hardware. Moving elements in the hardware - mechanisms - are usually designed as rigid-body mechanisms. This means that they consist of stiff, undeformable elements connected by kinematic pairs (hinges, sliders, etc.). To enable motion in kinematic pairs, gaps between elements are necessary. There are numerous engineering approaches to designing kinematic pairs, but typically these gaps are filled with lubricants to minimise friction. Mechanisms that are exposed to dusty environments may also incorporate seals to protect kinematic pairs from environmental debris. As with other elements, these seals can also be damaged given the abrasive nature of the lunar dust and allow debris to penetrate the mechanism's assembly. Consequently, the accumulation of debris in the inter-element gaps leads to an increase in friction within the kinematic pair. This can be observed as an increase in the force required to operate the mechanism. Continuous exposure to dust worsens the problem and can ultimately lead to jamming of the mechanism. During Apollo exploration missions, such problems occurred quite frequently [1, 5]. The specific examples and the current state of the art of possible solutions to such problems will be presented in Chapter 2.

Another aspect of dust contamination is the changing plasma conditions on the lunar surface. The exact mechanism of this phenomenon will be discussed in Chapter 2, but it is important to note that the dynamics of the lunar environment charge can eject dust particles above the surface and cause a levitation-like phenomenon [9]. Although there is no definitive information on the maximum height of travel induced by this process, it implies that attempting to keep equipment elevated above the lunar surface to avoid contact with dust may be futile. The interaction between dust and hardware is inevitable. Seals commonly employed to safeguard inter-element gaps in mechanisms tend to deteriorate due to the abrasive nature of lunar dust. And, as already discussed, the penetration of gaps with the dust particles is detrimental to the hardware. Various dust mitigation technologies that could help prevent some of the dust-induced problems will be discussed in Chapter 2. This study prioritised re-evaluating the design of moving elements to prevent

their degradation. As previously stated, it is impossible to evade lunar dust, but it is feasible to avoid inter-element gaps in mechanisms. To attain motion without employing numerous rigid components connected by kinematic pairs (with gaps), it is necessary to consider utilising compliant mechanisms.

Compliant mechanisms employ elastic deformation to achieve motion [10]. Owing to their absence of inter-element gaps, they possess intrinsic resistance to dust-induced jamming. Consequently, their usage can be considered as an implicit dust mitigation technology and can complement existing active and passive dust mitigation approaches. Furthermore, compliant mechanisms can be manufactured as monolithic pieces, providing an excellent opportunity to utilise additive manufacturing technologies that are gaining popularity in the space industry. However, designing compliant mechanisms is more challenging than designing rigid-body mechanisms. This study explored various design methods, and compliant designs will be presented in Chapters 4 and 5.

1.3 RESEARCH OBJECTIVES

The objectives of this research project include:

- Investigation on how compliant mechanisms can aid dust resilient hardware development for lunar surface operations. Additionally, advocating for compliant mechanisms to be added to dust mitigation methodologies in the literature.

- Identification of materials that can be used to build compliant mechanisms and survive the lunar environment at the same time. If possible, with a focus on materials enabling rapid prototyping.

- Investigation of design methods that can support the synthesis of compliant mechanisms with a focus on topology optimisation.

- Investigation of manufacturing technologies capable of producing compliant mechanisms with satisfactory performance results. If possible, with a focus on additive manufacturing.

- Development of a test plan and methodology to assess the characteristic and performance of compliant mechanisms.

- Design and demonstration of a compliant mechanism application that could be used in the context of a human spaceflight scenario. If possible, with a focus on geological tools.

1.4 THESIS OUTLINE

This thesis comprises six chapters, each offering a distinct contribution to the research presented. Here, a brief overview of each chapter is provided:

- **Chapter 1: Introduction**

  This chapter serves as the foundational cornerstone of this thesis. It provides information on the background that contributed to the emergence of the research problem that underlies this study. Within its pages, it highlights the motivation and objectives that have driven the research undertaken within this project. In addition, this chapter offers a comprehensive list of publications originating from research conducted during the course of this project.

- **Chapter 2: Literature review**

  The chapter discussed here examines the legacy of the Apollo programme and the unique challenges posed by lunar dust. This chapter navigates the reader through various problematic lunar dust characteristics and dust mitigation strategies and, more importantly, sets the groundwork for the implicit dust mitigation solutions proposed in this thesis, which rely on the use of compliant mechanisms. As such, the literature review meticulously surveys publications that focus on lunar environment, Apollo programme experience, compliant mechanisms design, and compliant applications in space hardware.

- **Chapter 3: Design considerations for the compliant lunar gripper**

  This chapter replicates the Apollo geological tool, Tongs, with a compliant gripper. A discussion of the kinematic behaviour and possible design enhancements is provided. This chapter illuminates the anticipated performance characteristics of the compliant gripper, delving into the intricacies of material selection and the thought processes behind manufacturing choices.

- **Chapter 4: Initial design and testing: PLA and TPC grippers**

  In this chapter, four compliant gripper prototypes developed in line with this work are presented. It details the design methodologies (analytical design and topology optimisation) that produced these prototypes and subsequently unveils the results of displacement and force tests. The gripper prototypes were 3D printed with PLA and TPC, which was a basis for comparison of different design methods with different material combinations. In these pages, numerous observations are made, setting the stage for potential improvements of grippers presented in the next chapter.

- **Chapter 5: Revised design methodology and testing: PLA and PEEK grippers**

  This chapter represents a step forward, showcasing the evolution and refinement of design and test methodologies based on the lessons learned from the tests in the preceding chapter. It presents a comprehensive two-step design methodology, offering valuable insight into the intricate world of compliant mechanisms. It showcases topology optimisation followed by an analytical re-design step aiming at reducing the stress in flexures as well as enhancing the range of displacements. It also introduces 3D-printed PLA and PEEK grippers, some of which were thermally treated to strengthen mechanical properties of the material. The results of these tests showcase a considerable improvement in the kinematic behaviour of grippers, as compared to the previous prototypes. Additionally, this chapter unveils the use of the Digital Image Correlation technique, providing a detailed and insightful view into the deformation of compliant mechanisms.

- **Chapter 6: Conclusions**

  The final chapter takes a reflective stance, offering an overview of the results derived from this study. In these concluding pages, valuable observations are provided, paving the way for recommendations on future research avenues in this research domain.

1.5 PUBLICATIONS

The work described in the thesis presented here has contributed directly to the following publications:

- D. Budzyń, A. Cowley, M. Ossowski, M. Siemaszko, H. Zare-Behtash, A. Cammarano, "Design, manufacturing, and testing of 3d printed compliant mechanisms for lunar equipment," *20th European Space Mechanisms and Tribology Symposium,* 2023. Available Online: `https://www.esmats.eu/esmatspapers/pastpapers/pdfs/2023/budzyn.pdf`

- D. Budzyń, H Zare-Behtash, A Cowley, and A. Cammarano, "Compliant mechanisms for dust mitigation in Lunar hardware development: technology and material considerations," *In IOP Conference Series: Materials Science and Engineering* Vol. 1287, No. 1, p. 012001, 2023 Available Online: `https://iopscience.iop.org/article/10.1088/1757-899X/1287/1/012001`

- D. Budzyń, H Zare-Behtash, A Cowley, and A. Cammarano, "Implicit lunar dust mitigation technology : Compliant mechanisms," *Acta Astronautica* issue 203, p. 146-156, 2023. Available Online: `https://www.sciencedirect.com/science/article/pii/S0094576522006506`

- D. Budzyń, E. Tuohy, N. Garrivier, T. Schild, A. Cowley, R. Cruise, M. Adachi, H. Zare-Behtash, and A. Cammarano, "Lunar Dust: Its Impact on Hardware and Mitigation Technologies," *46th Aerospace Mechanisms Symposium*, p. 287, 2022. Available Online: `https://ntrs.nasa.gov/api/citations/20220006415/downloads/46th_AMS_Proceedings_Final.pdf#page=301`

- D. Budzyń, H. Zare-Behtash, A. Cowley, A. Cammarano, "Topology optimisation of compliant mechanisms as a design method to improve hardware performance in lunar dust environment," *19th European Space Mechanisms and Tribology Symposium*, 2021. Available Online: `https://www.esmats.eu/esmatspapers/pastpapers/pdfs/2021/budzyn.pdf`

CHAPTER 2

LITERATURE REVIEW

2.1 APOLLO LEGACY

The first lunar landing with a crew took place in 1969 during the Apollo 11 mission. Astronauts Neil Armstrong and Edwin Aldrin visited Earth's natural satellite with the primary objective to demonstrate the crewed lunar landing and safe return to Earth. The secondary mission objectives included [11]:

- selenological inspection and sampling (sample collection, surface characteristic etc.)

- obtaining data to assess the capabilities and limitations of astronauts and their surface equipment in the lunar environment (EVA operations, landing effects on hardware, assessment of contamination with lunar materials etc.)

To perform their duties and planned experiments astronauts needed surface equipment including spacesuits, geological tools, and scientific hardware: passive seismic experiment, laser-ranging retroreflector experiment, solar wind experiment, and cosmic ray detection experiment. All of this equipment was developed specifically for the lunar environment, even though, at the time, the knowledge of the surface conditions was limited.

Subsequent Apollo missions had additional objectives that included improving and evaluating landing capabilities, capturing lunar surface images from the spacecraft, collecting surface and subsurface samples, photographing various lunar sites, testing lunar soil mechanics, examining thermal coating degradation and testing the lunar roving vehicle [11]. The list of objectives was extensive, and each subsequent mission became more complex in terms of scientific equipment.

Three experiments that are worth mentioning in line with this work were (i) lunar dust detector used in Apollo 12, 14, 15, (ii) lunar ejecta and micrometeorites experiment used in Apollo 17 and (iii) charged particle lunar environment experiment in Apollo 14. The dust detector was intended to measure dust accumulation and was later upgraded to include particle, radiation, and temperature studies. The aim was to determine the long-term effects of dust accumulation on the performance of solar cells [12]. Lunar ejecta and micrometeorites experiment measured the energy, speed, and direction of lunar dust particles. The measured particles included micrometeorites, their ejecta, and possibly levitated dust grains [11]. The charged particle lunar experiment measured the flux of charged particles originating from the Sun (electrons and ions) in the energy band from 50 to 50 000 eV [5]. Furthermore, almost 382 kg of rock, soil, and core samples were brought back from the Moon to Earth for experiments and analysis [13].

Throughout all Apollo missions, lunar dust caused hardware degradation at a much faster rate than anticipated and tested on Earth [1]. The experiments carried out an analysis of the samples recovered from the Moon provided insights into the characteristics of the dust, which clarified its harmful impact on the hardware.
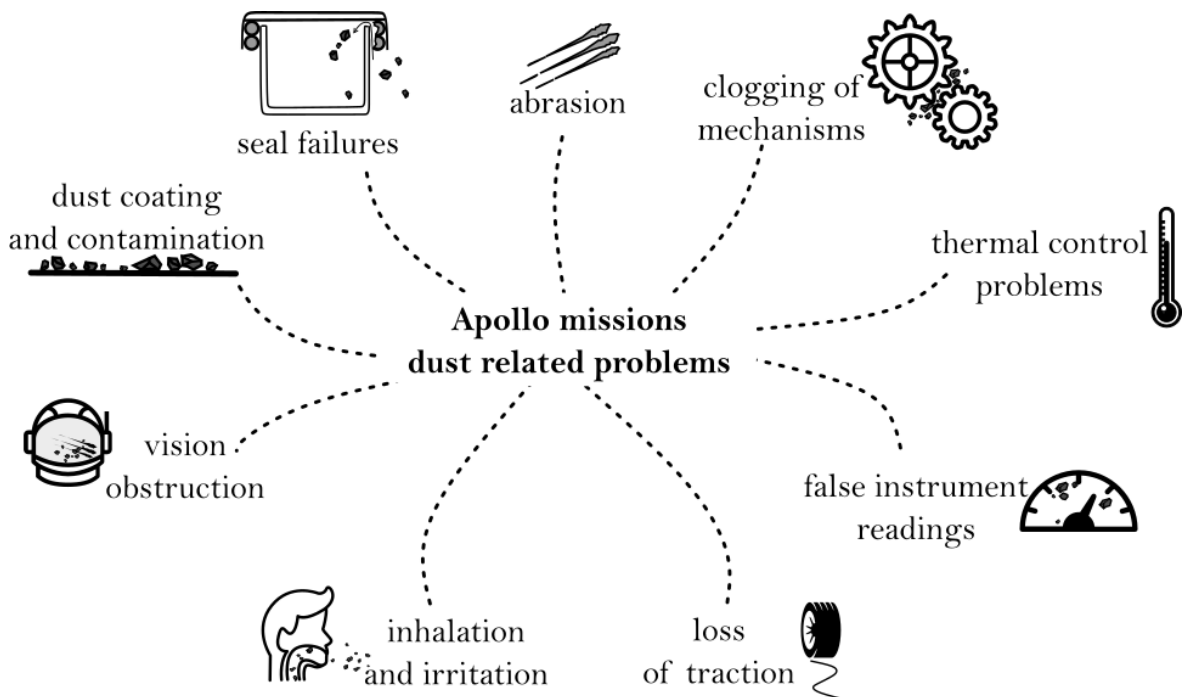
Figure 2.1: Dust related problems; classification done by Gaier [1] based on Apollo reports and crew debriefings.

As previously stated, lunar dust posed challenges during Apollo missions. Gaier collected data on all dust-related problems reported by astronauts [1]. He grouped the recorded problems into nine distinct categories, which are presented in figure 2.1. This classification still serves as the basis to categorise all problems

induced by lunar dust. Examples of the problems (with their categories) include:

- **clogging of the mechanisms**

  problems with operating the sun shade in the visor of spacesuit; problems with geological tool (scoop) angle adjustment mechanism; clogging of zippers, wrist and hose locks, etc.;

- **abrasion**

  wear of external layers of spacesuits and especially the gloves; gauge dials so scratched that it was hard to read from them; sun shades scratched affecting the vision;

- **seal failures**

  suit seals were worn leading to pressure losses; failure of sample and gas sample seals in the containers;

- **dust coating and contamination**

  dust coating led to astronauts tripping over TV cable that got covered by the dust; contrast chart (for pictures) was not suitable for use anymore after being dropped on a surface as it was covered with the dust;

- **thermal control problems**

  dust coating provided an insulation layer on radiators and caused serious thermal control problems; some instruments were also overheating because of the radiators decreased performance;

- **inhalation and irritation**

  the exposure to dust happened inside of the Lunar Module and caused irritation of the eyes and airways;

- **vision obstruction**

  vision obstruction happened at the landing due to the dust-plume interactions;

- **false instrument readings**

  landing velocity trackers gave false readings because of the moving dust and debris during landing; the landing radar outputs were also affected by moving dust and debris;

- **loss of traction**

  slipping on the ladder of the lander; material adhering to the boots causing slipping;

It is clear that dust had a significant impact on various hardware components and the health of astronauts during the Apollo missions. Given the wide range of dust-related problems, it is likely that a variety of mitigation methods will be necessary. As the literature suggests, a 'layered engineering defence' strategy involving multiple technologies may be needed to effectively address these challenges [4, 12]. The classification of dust mitigation technologies will be discussed in Section 2.3. This work addresses a specific problem from the list presented above. It is focusing on the issues of clogged lunar mechanisms. The range of mechanisms problems discussed in the literature [1] is presented in Table 2.1. Examples of the mechanisms listed in the table are also presented in Figure 2.2.

Table 2.1: Apollo mechanisms dust-related problems based on the astronaut debriefings [1, 14].

Mission	Problem
Apollo 12	lock buttons of the equipment conveyor very hard to manipulate because of the dust accumulation in the moving parts
Apollo 15	camera drive mechanisms got jammed with dust and prevented it from working
Apollo 16	battery cover of radiator jammed because of dust accumulation in the mechanism
Apollo 17	some of the moving components of the geopallet got stuck after the second EVA; the angle adjustment of some geological tools (scoop and rake) got fixed in one position which could not be changed anymore; multiple components attached to the rover jammed because of the dust exposure (e.g. bag holders, pallet locks)

It is also important to mention that the severity and frequency of dust-related damages on the Moon were so great that several Apollo astronauts emphasised the importance of developing further solutions. During the Technical Crew Debriefing of Apollo 17 on January 4, 1973, astronaut Gene Cernan said:

"Close to the end of the third EVA, all the mechanical devices on the gate and on the pallet in terms of bag holders and pallet locks and what have you were to the point that they would refuse to function mechanically even though the tolerances on these particular locks were very gross. They didn't work because they were inhabited and infiltrated with this dust. Some could be forced over centre. Others just refused to operate even after dusting,

cleaning, and a slight amount of pounding trying to break the dust loose. I think dust is probably one of our greatest inhibitors to a nominal operation on the Moon. I think we can overcome other physiological or physical or mechanical problems except dust." [1].

(a) (b) (c)
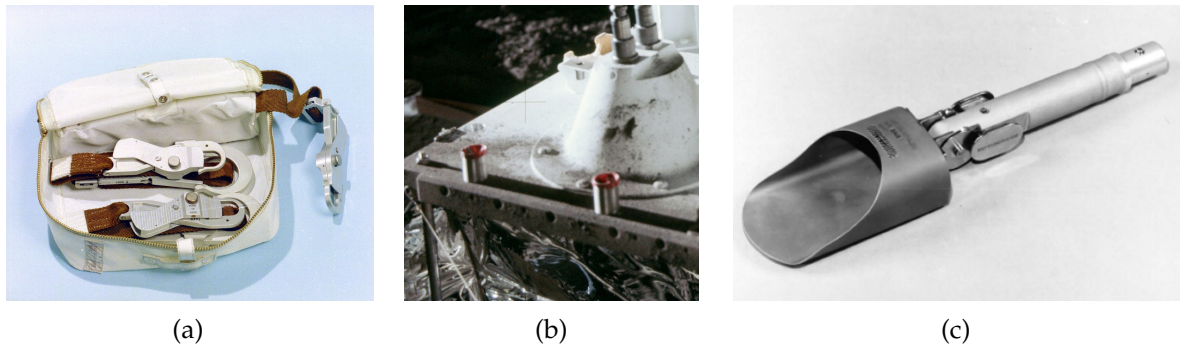
Figure 2.2: Apollo mechanisms impacted by dust related problems. (a) Lunar Equipment Conveyor, (b) Boyd Bolts (red) on the Central Station of Apollo Lunar Surface Experiments Package (ALSEP), (c) scoop with angle adjustment mechanism. Pictures courtesy of NASA.

Gene Cernan gave a compelling account of how dust causes jamming of rigid-body mechanisms. The problem begins with dust accumulating in the clearances of the mechanisms, increasing friction, and making operations more difficult. As dust accumulates further, hand-operated mechanisms require progressively more force to move them. In the case of some mechanisms, the accumulation of dust reaches a critical mass where the additional friction is so great that they become jammed and can no longer be operated. In addition, attempts to clean the dust off the equipment were unsuccessful, which will be further discussed in subsequent sections.

The next crewed missions to the Moon are planned by NASA in collaboration with ESA and other partners as part of the Artemis Programme. Learning from the experience of Apollo astronauts, there is still ample room for improvement in the hardware design for this unique environment. In fact, the "Global Exploration Roadmap Critical Technology Needs" [15] report, prepared by the International Space Exploration Coordination Group, dedicated a full chapter to dust mitigation, highlighting the importance of addressing specific problems such as mechanism clogging caused by dust. To accurately address such issues, it is essential to understand the characteristics of lunar dust, which will be discussed in Section 2.2.

2.2 LUNAR DUST

Surface of the Moon is covered by loose material known as lunar regolith. Individual fragments of the lunar regolith vary in size and shape and include boulders, rocks, pebbles, and fine sand-like material. From a hardware impact point of view,

the smallest grains of lunar material are the most problematic. The fine fraction of lunar regolith is a grey mix of rock fragments, minerals, glass and glass aggregates called agglutinates [16]. The finest fraction of this material is usually called lunar dust. The literature presents a median particle size of lunar soil between 40 μm and 130 μm, while particles of sizes below 20 μm represent 10% to 20% of the sample weight [16]. During Apollo surface missions, particles smaller than 2 μm caused most challenges [1]. Such small particles have the potential of entering gaps between hardware elements. The implications of such intrusions will be discussed in more detail in the next sections. The next problematic characteristic of lunar dust is the mineral composition. Minerals present in lunar soil (such as anorthite, bytownite, labradorite, fayalite, or forsterite) exhibit Mohs hardness values of 6 and above [6]. This means that they are harder than common engineering materials (e.g. aluminium, titanium, and stainless steel alloys). Furthermore, lunar minerals, together with glass (formed by cooling down of regolith molten by the impact of meteoroids), form grains with sharp and serrated edges and are most present in the smallest size fractions [6]. Most of these particles were created in meteorite and micrometeorite impacts. After their formation, they were not exposed to any significant erosive mechanisms (such as hydrological and aeolian processes present on Earth). The morphology of the soil samples collected during Apollo 17 traverses is presented in Figure 2.3. As shown, the individual grains have sharp edges, making lunar dust an extremely abrasive agent.

(a)　　　　　　　　　　　　(b)　　　　　　　　　　　　(c)
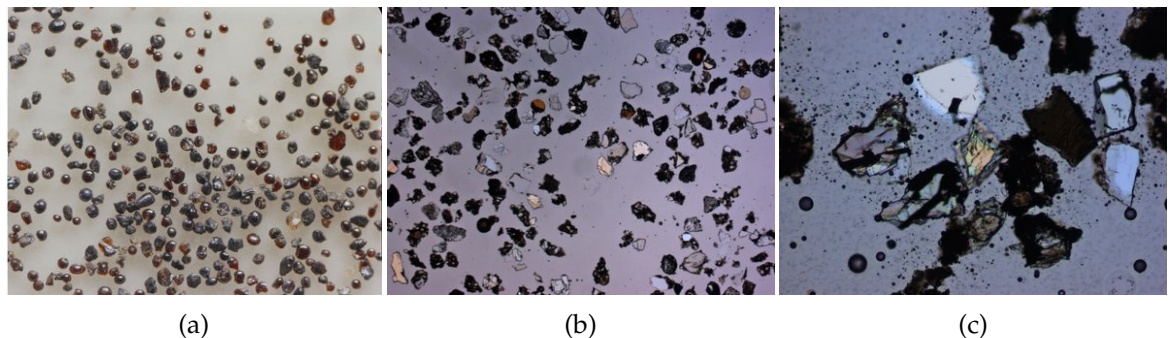
Figure 2.3: Apollo 17 lunar soil samples (a) sample 74220: sieved fraction of soil at 75-90 μm, on the rim of 120 m Shorty crater, (b) sample 72150: plane light microscope image with field of view 2.85 mm, residue sample recovered from sample bag with rock sample 72155, (c) sample 72141: plane light microscope image with field of view 0.7 mm. Pictures courtesy of NASA/JSC and Lunar and Planetary Institute.

The Moon does not have a magnetosphere, and its atmosphere (or rather exosphere) is characterised by the very scant presence of gases surrounding the globe. This leaves the lunar surface exposed to the space environment. Constant solar wind plasma bombing, cosmic ray spallation, solar UV, and X-ray radiation cause electrostatic charge buildup on the surface of the Moon [9, 16, 17]. The Sun-facing

side of the Moon, exposed to the phenomena mentioned above, is dominated by photoemission, which creates a plasma sheath of photoelectrons extending to 1 m above the surface. As such, the day-side of the lunar surface develops a positive potential. In contrast to that, the night-side sheath, extending 1000 m above the surface, is dominated by positive ions (Debye sheath), leading to a negative surface charge. The surface charge ranges between +3 V on the day side and -200 V on the night side [18]. Figure 2.4 illustrates the electrostatic environment of the surface. As visible, the terminator areas (at dawn and dusk, between lunar day and night) undergo changes of the charging environment. Due to this fact, the dust particles present in these areas can float above the lunar surface in a levitation-like manner [12]. It has been determined that gravitational forces still dominate over electrostatic forces, and therefore this levitation-like effect is temporary [9]. Nevertheless, this is a very important characteristic of the lunar environment. Because of this phenomenon, it can be very challenging to keep the equipment away from the dust, as even raising it above the ground might not be enough to avoid contamination. It is also worth mentioning that dust ejected from the surface by any robotic or human activity stays above the surface for longer (as compared to Earth's conditions) because of reduced gravity and it can travel farther because of the lack of atmosphere that could slow down ejected particles.
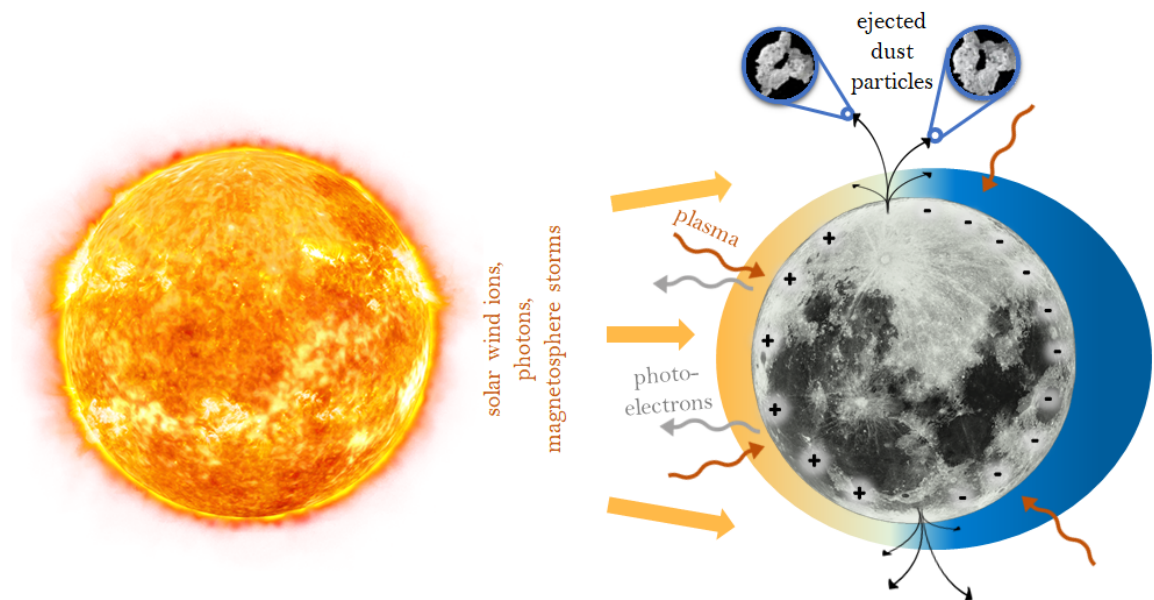
Figure 2.4: Lunar surface charge environment. Sheath colours: yellow – photoelectron sheath, blue - Debye sheath, and terminator areas in between.

All of the surface phenomena mentioned here are influenced by solar activity, and more information can be found in the resources of the Apollo 17 Lunar Ejecta and Meteorites Experiment [7]. In addition, objects moving on the Moon's surface

can accumulate charge due to electrostatic interactions, which can pose a potential threat to the crew if the charge is rapidly discharged. A study focused on rover wheels found that electrostatic discharge could be a danger to Apollo astronauts after long traverses in shadow regions [18]. However, the study suggests that the Lunar Roving Vehicle, which was used as a transport vehicle for astronauts, was safe mainly due to its low speeds that did not allow extensive potential to be built.

Knowing the electrostatic potential of the charge on the surface could be very beneficial for dust mitigation. Unfortunately, the potential of Lunar dust particles is not easy to assess globally, as it depends on the composition of materials present in the regolith (which changes with the location on the globe). The charged potential of materials depends on their work function (the minimum energy needed to remove electrons from a solid's surface). According to the literature, the work function of analysed lunar regolith samples is approximately 5.8 eV [19]. It should be noted that common engineering materials have different work functions compared to the regolith (e.g. aluminium 4.28 eV, stainless steel 4.4 eV). The work function determines the potential to which surfaces charge under given conditions. Because of the work function differences, it is clear that the hardware and lunar regolith particles charge to different potentials, which promotes electrostatic adhesion between them.

Electrostatic forces are not the only driver of dust adhesion on the Moon. Micrometeorite impacts that break the regolith particles into smaller pieces, an ultra-high vacuum environment, and ion and photon bombardment from the Sun create very clean and high surface energy dust particles [20]. When surfaces are newly created in the vacuum of space, they do not react with any gas atmosphere and remain chemically reactive, unlike those on Earth where they develop oxide layers. Additionally, on Earth, these surfaces are contaminated with hydrocarbons and water, creating a thin film. In space, the absence of this film and oxide layers, after surface damage (for example pitting), can lead to cold welding. Cold welding is a process in which two surfaces made of the same (or similar) metal brought into contact in vacuum adhere strongly. As Richard Feyman described it: "The reason for this unexpected behaviour is that when the atoms in contact are all of the same kind, there is no way for the atoms to "know" that they are in different pieces of copper. When there are other atoms, in oxides and greases and more complicated thin surface layers of contaminants in between, the atoms "know" when they are not on the same part" [21]. Clean surfaces stripped of oxides, water molecules, and hydrocarbons beyond causing cold welding also cause the increase of adhesion forces in materials other than metallic. The literature suggests that high vacuum conditions can result in an effective increase in surface energy of up to two orders

of magnitude compared to conditions in the Earth atmosphere [22]. Higher surface energy promotes adhesion based on van der Waals forces; therefore, the electrostatic adhesion discussed earlier is not the only source of adhesion problem on the Moon.

Understanding the lunar environment and dust characteristic can be very beneficial in examining possible solutions. As will be discussed in the next section, understanding the exact mechanism of lunar dust-induced problems can aid in finding an appropriate mitigation solution.

2.3 DUST MITIGATION

In Section 2.1, the challenges of lunar dust during the Apollo era were briefly discussed. As already mentioned, the diverse range of problems requires multiple dust mitigation technologies and there is no single solution that can address all dust-related issues at the same time. The literature suggests a 'layered engineering defence' strategy consisting of multiple mitigation technologies combined into a comprehensive approach [4]. Figure 2.5 provides a simple classification of different dust mitigation methods.
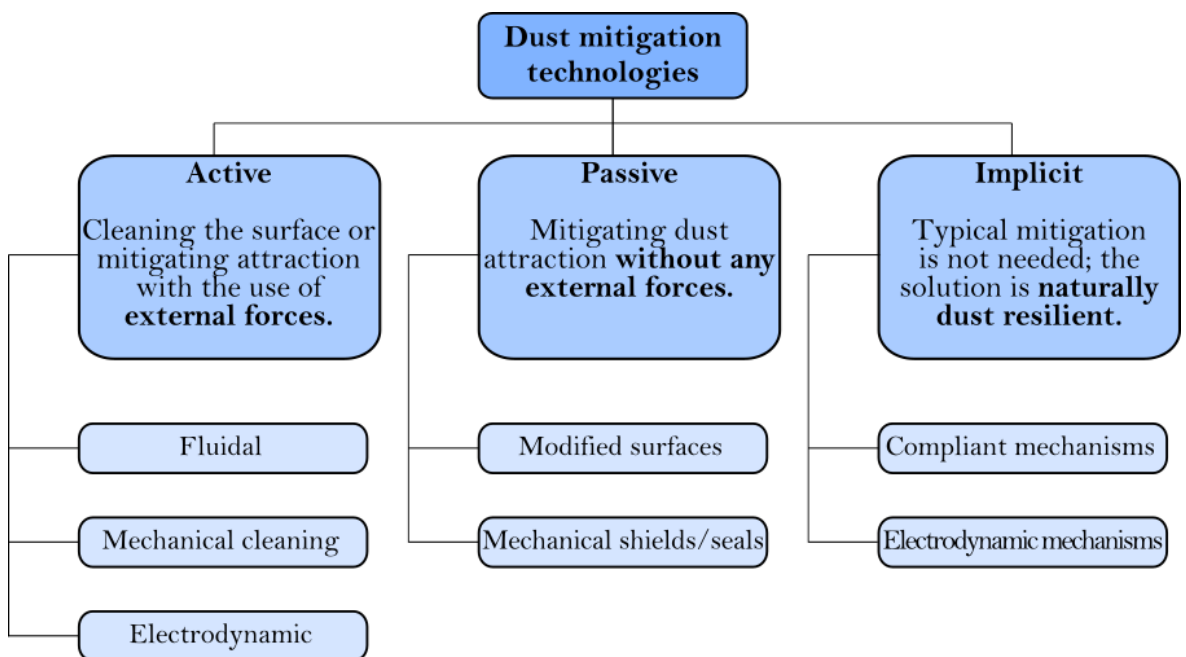
Figure 2.5: Classification of dust mitigation technologies mentioned in this section.

The most popular dust mitigation approaches belong to *active* or *passive* categories. *Active* dust mitigation is characterised by the use of external force to clean (or sometimes protect) the equipment. Fluid methods use fluid to remove dust from equipment. Such an approach is not feasible for use in open space but could still

be a viable option for cleaning off a dust inside of the pressurised lunar outpost or vehicle. Mechanical cleaning involves a cleaning device (often a brush) to remove dust particles from the surfaces being cleaned. It is worth mentioning that mechanical cleaning was the initial approach to cleaning dust in Apollo missions [12]. As mentioned in Section 2.2 the mechanisms of lunar dust adhesion include electrostatic forces and Van der Waals forces. It is hard to estimate the ratio of these forces for all lunar conditions, but the literature suggests that both types have an impact on general adhesion [20]. Moreover, during Apollo missions it was discovered that the adhesive properties of lunar dust decreased in the presence of atmosphere inside the lunar lander [1]. This indicates that mechanical cleaning of the equipment in a pressurised module may be easier, likely because of the presence of gases that aid in discharging. Therefore, cleaning with a brush may have limited effectiveness in a vacuum, since it does not address the electrostatic forces at play. To address them as well, the brush would have to be equipped with discharge mechanisms to equalise the potentials of the particles and the hardware. The combination of brushes with other dust mitigation technologies is also a solution currently evaluated in the literature [23, 24]. However, since additional features were not part of the Apollo brushes, they had limited efficiency and, in addition, caused some abrasion by pulling the sharp particles across the surfaces to be cleaned [4]. The examples of brushes that were designed for the Apollo programme are visible in Figure 2.6.

(a) (b)
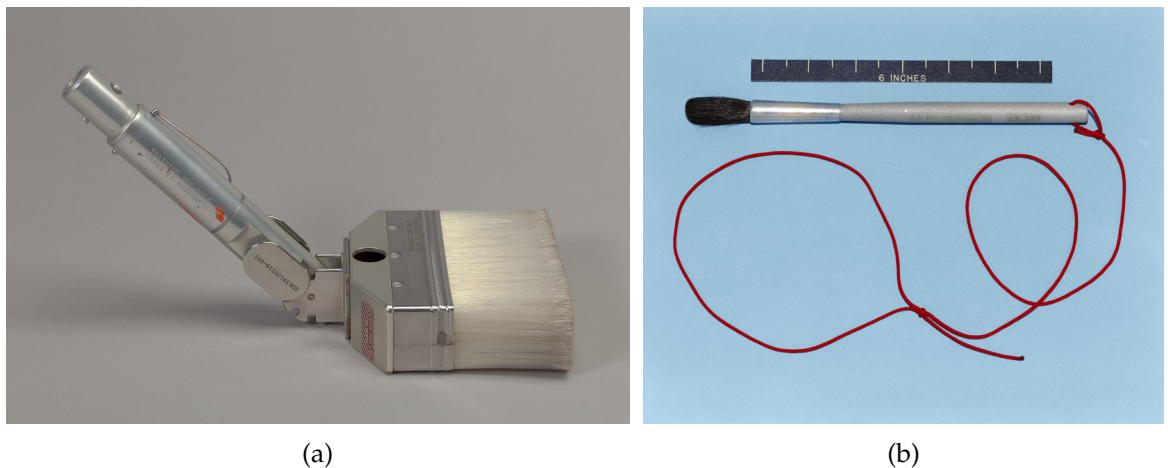
Figure 2.6: Examples of brushes used during Apollo missions (a) brushed developed for cleaning spacesuit before entering the lunar module; picture credit: NASA JSC and National Air and Space Museum, (b) lens brush used as initial cleaning stage for glass lenses; picture credit: NASA Johnson.

The last group of dust mitigation methods in the active category in Figure 2.5 is electrodynamic. Equipment using this methodology consists of electrodes and an electric circuit with high-voltage amplifier. The electrodes are usually embedded in

hardware to be cleaned or protected from dust. Such equipment does not have any mechanical moving elements and the cleaning is carried out by a travelling wave of an electrodynamic field. In such a system, the electrodes are activated alternately to produce a sweeping motion of the mentioned electrodynamic field. There is a significant amount of literature discussing this dust mitigation approach [25–32], and there has been a major development in this field since the first prototype was produced at the University of Tokyo [33]. The most promising systems that use this technology are called Electrodynamic Dust Shields (EDS). Figure 2.7 presents the principles of operations of such systems. As shown, the travelling wave interacts with the charged lunar dust particles, sweeping them off the surface of the system. The literature suggests that such a device can have an efficiency approaching 100% under high vacuum conditions, while having an efficiency of 80-90% in the air atmosphere [28].
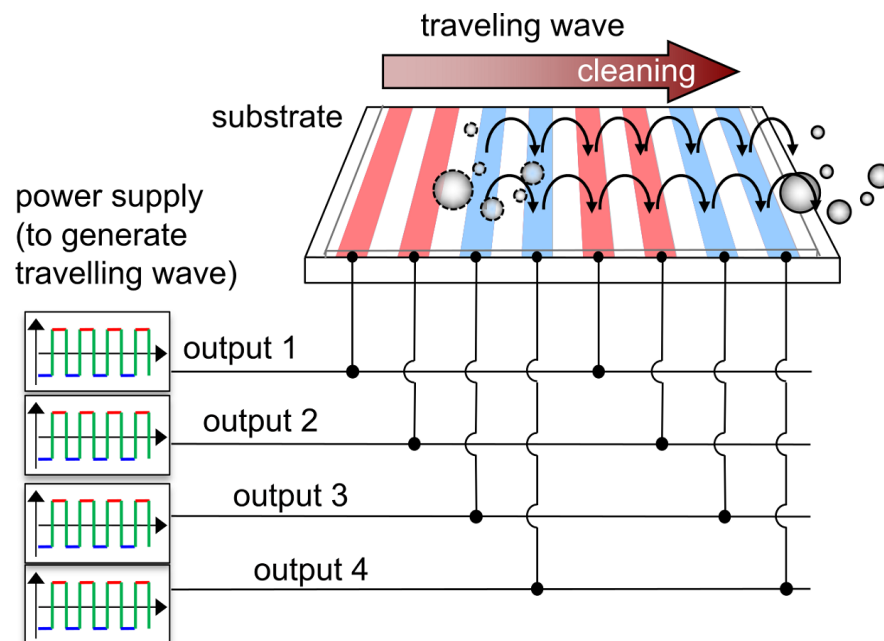
Figure 2.7: Diagram of the general operation of an EDS system. Picture courtesy of Masato Adachi, based on figures from his publication [34].

The results of qualitative experiments carried out by the European Space Agency are presented in Figure 2.8. The upper row shows the removal of polyamide powder from the substrate by an inward-travelling wave, while the two lower rows show the same process with an outward-travelling wave. EDS methodology has the potential to clean rigid materials and could also be applied to clean soft layers of space suits by sewing electrodes into the fabrics [35, 36].

The focus of *passive* dust mitigation is to mitigate the attraction of dust to the hardware without the use of external forces. These methods reduce dust attraction or exposure to dust to eliminate contamination. They focus on prevention rather

(a)

(b)
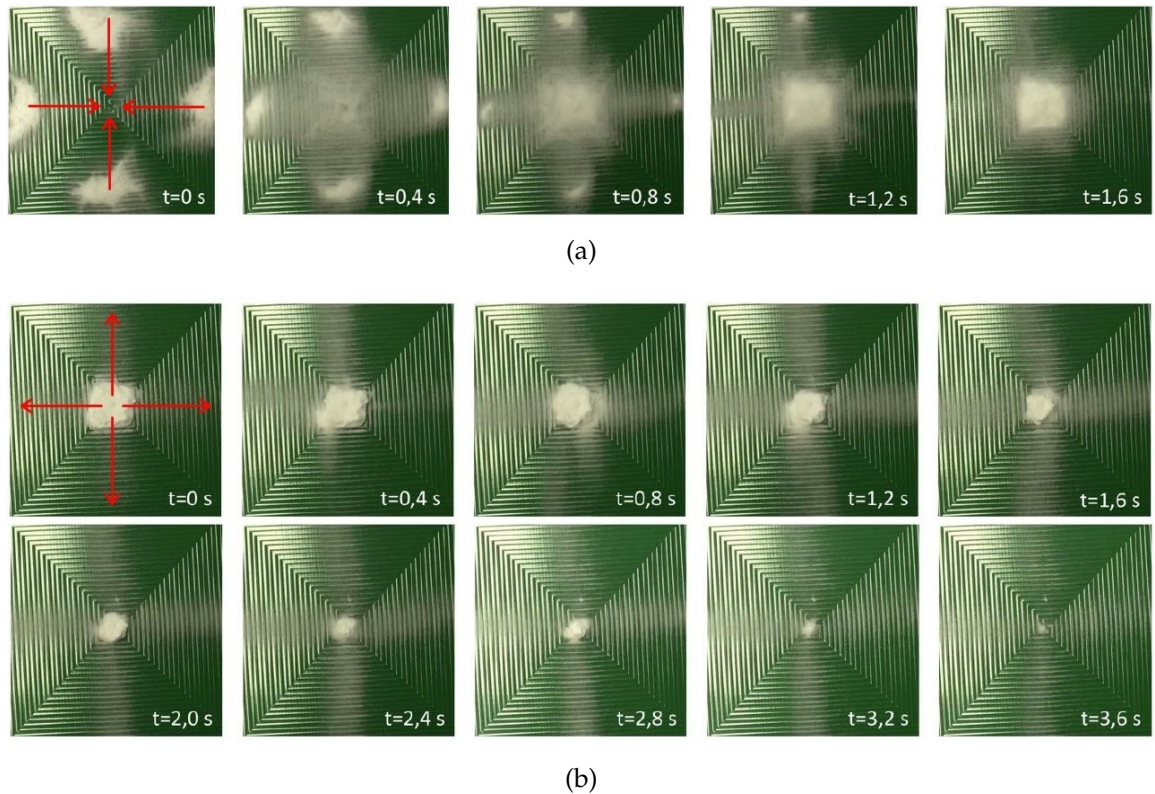
Figure 2.8: EDS system: copper electrodes on PCB substrate, spacing between electrodes = 1 mm, travelling wave frequency = 20 Hz, operating voltage = 2000 V [37]; a) wave travelling inward and b) wave travelling outward.

than cleaning, and they do not require any external energy to be involved. The most popular passive dust mitigation technologies include seals (an example of a ball bearing with a seal visible in Figure 2.9 a), mechanical shields, but also engineered surfaces and coatings. Seals and shields are often popular protection in dirty environments on Earth. An example of a labyrinth seal can be seen in Figure 2.9b.

The efficacy of different solutions depends on their application. In the case of surface treatments, their performance also depends on the adhesion type they target. The development of micro-structured surfaces is helpful in dust mitigation, anti-wetting, and even antimicrobial technologies for Earth applications [39–42]. But this technology, which uses surface topography with microstructures, minimises van der Waals forces. As already discussed in this work, on the Moon the electrostatic adhesion is not to be undermined. Therefore, the methodology relying on micro-structured surface topography might not be effective enough for the lunar dust mitigation, as van der Waals forces are not the only root cause of the adhesion. The literature suggests that passive dust mitigation methodologies for the Moon should focus on minimising electrostatic adhesion [12]. A promising technology that addresses the electrostatic potential difference between lunar dust

(a)   (b)
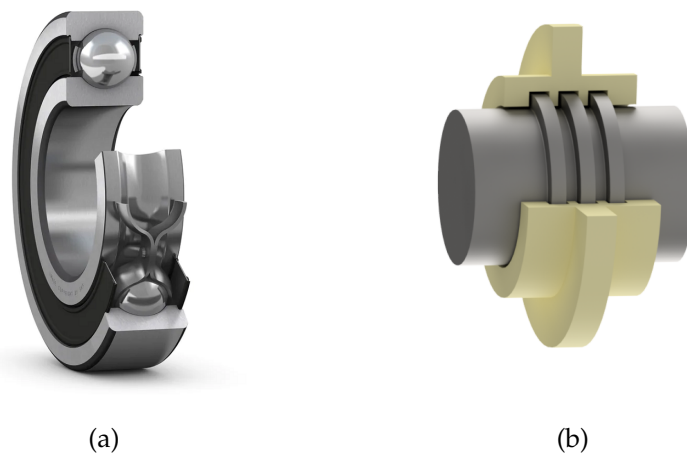
Figure 2.9: Examples of passive seals and shields: (a) ball bearing with rubber seal (black), courtesy of SKF [38], (b) labyrinth seal around the shaft.

and equipment is the use of work function matching coatings. As discussed in Section 2.2, the charge of a material is determined by its work function. Therefore, materials with identical work functions are expected to charge to the same potential, reducing adhesion caused by potential differences [12, 37]. The literature reports that the work function of lunar regolith samples is around 5.8 eV [19]. For comparison, it is worth noting that the work function of aluminium is around 4.28 eV, stainless steel 4.4 eV, platinum 5.7 eV, and polytetrafluoroethylene PTFE 5.75 eV. Selecting materials with closer match of the work function should result in less electrostatic adhesion. But the closest work function similarity to the lunar regolith can be supplied by the regolith itself. The surface coating made of the lunar regolith simulant was accessed by the literature [37, 43]. Gaier et al. [43] tested coating applied via ion beam beam sputter deposition using an argon ion beam source. The work published during the project discussed in this thesis [37] presented the coating achieved using the Marangoni effect of the regolith simulant melted at 1200 °C. Marangoni effect phenomena in molten lunar regolith simulant was first reported by Dominguez and Whitlow [44]. It is migration of the molten material upward, and it is driven by the gradient of the temperature, while relying on surface tension that is strong enough to exceed opposing gravity. The test cubicles coated in this way can be seen in Figure 2.10, where three stages of the coating process are shown. Each cubicle coating process visible was stopped after different time of exposure to 1200 °C (the cubicle on the right in Figure 2.10 was exposed to high temperature for the longest time of the three samples presented; the cubicle on the left was exposed for the shortest time). It is visible that the molten regolith undergoes a process of vertical migration along the walls of the cubicles, thereby forming a regolith simulant coating. Although this technology can be very promis-

ing for some applications, it is important to remember that the simulants used in the research do not necessarily match the work function of an actual lunar regolith. At the same time, the lunar regolith has different work functions (as well as some other properties) depending on the location on the Moon. This means that finding a good coating match might be difficult and only possible for specific missions with known properties of local regolith. Nevertheless, it is a technology that can be helpful for specific missions and, even if not sufficiently effective by itself, the close match work function approach can at least minimise the adhesion as part of layered dust mitigation approach.
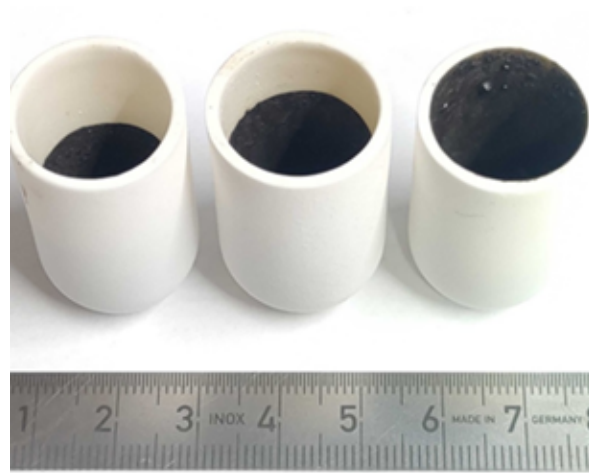
Figure 2.10: Example of work function matching coating (made of lunar regolith simulant JSC-2A) applied bu the use of Marangoni effect [37].

The last group of technologies to be discussed here is *implicit* dust mitigation. The designs presented in this group, while exposed to lunar dust, continue operating nominally and are not affected by dust intrusion. In other words, they are naturally dust resilient in performing their function. One example of implicit dust mitigation technology for sampling of the lunar regolith is an EDS system, similar to EDS used as active dust mitigation, but here used as a sampling tool. In this case, the travelling wave can be used as a transport mechanism for the individual regolith grains. The geometry of the system can also be adapted to sort the grains by their specific size. The literature presents relevant work for the development of such systems [34, 45, 46]. The example of this technology is presented in Figure 2.11, it is visible that regolith particles of a certain size can be transported, while smaller particles can be discarded by utilising a force balance between electrostatic and gravitational forces.

The focus of dust mitigation solutions is to prevent specific dust-related damages. This work primarily proposes solutions to address the issue of dust-induced jamming in mechanisms. Previous literature demonstrated that the problem occurs
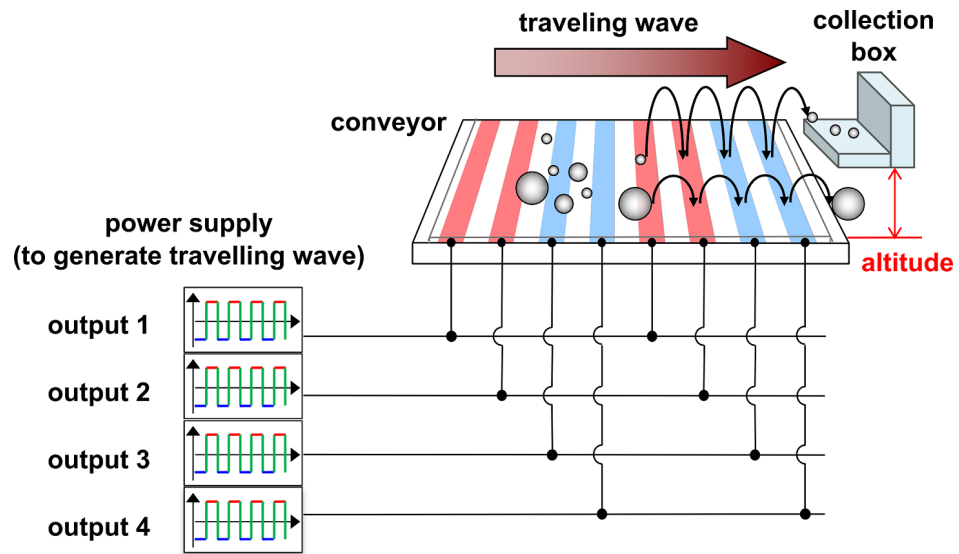
Figure 2.11: Grain size-sorting system using an electrostatic travelling wave [45].

when dust enters the gaps in rigid-body mechanisms, and removing the dust in the vicinity of the hardware is challenging. An alternative approach is to completely eliminate the gaps in the mechanisms. If a gap-free mechanism is constructed, it could generally be resistant to dust-related jamming damage. Compliant mechanisms can provide a viable technology to meet this requirement. They classify as dust-resilient design and as such should be considered an implicit dust mitigation technology. In the following section, compliant mechanisms will be discussed in detail, as they are the primary focus of this work.

2.4 COMPLIANT MECHANISMS

Compliant mechanisms are able to achieve motion by elastically deforming. They are capable of fulfilling kinematic functions just like rigid-body mechanisms, but without the need for multiple components. Additionally, compliant mechanisms can be designed and produced as single integrated pieces, offering advantages from a manufacturing standpoint. In rigid-body mechanisms, motion is accomplished through the relative movement of stiff elements (rigid bodies) connected by hinges, sliders, or other kinematic pairs. It is important to note that such kinematic pairs have backlashes (gaps) needed to ensure motion. These gaps are often filled with lubricant (dry or liquid), and ensuring adequate lubrication for space is not a trivial problem. Liquid lubricants are a very common solution on Earth. They can support high speeds over long periods of mechanisms operations. They also provide lower torque noise and good thermal conductance compared to dry lubricants. Unfortunately, under vacuum conditions, liquid lubricants can evaporate and therefore only lubricants with low vapour pressure can be used.

Vapour pressure also depends on the operational temperature and therefore even space-grade liquid lubricants are limited to use at temperatures below 100°C. On the contrary, dry lubricants such as molybdenum disulphate (MoS_2) or lead can operate in very low and very high temperatures, they can support accelerated testing, minimise the contamination of optical elements (which could be contaminated with vapours from liquid lubricants), and can support electrical contact if needed. This is just a brief summary of some of the considerations for lubrication in space based on the Space Tribology Handbook prepared by the European Space Tribology Laboratory [47]. As demonstrated, selection of appropriate lubrication can be quite challenging.

In contrast, compliant mechanisms do not require multiple elements connected by kinematic pairs with gaps, and therefore they do not require lubrication to support the inter-element movement. Instead, they deflect elastically to provide movement [10, 48]. An example of a rigid-body hinge compared to compliant hinge designs is presented in Figure 2.12. The lack of multiple elements connected by kinematic pairs means that there are no inter-element gaps in the compliant mechanisms. As discussed in Section 2.3, avoiding the gaps that are entry points for lunar dust eliminates the risk of jamming caused by lunar dust particles. This means that from the mechanisms point of view compliant solutions can be classified as implicit dust mitigation technology, as already mentioned in the previous section. However, it is important to remember that components featuring compliant mechanisms can still be subject to surface abrasion and thermal properties change due to dust accumulation. These properties usually do not have a direct impact on the kinematic behaviour of the mechanisms, unless the design of the flexible hinge features gaps that change size with the deformation. In such a case, pebbles could get jammed between the flexures, which could be a potential problem (reducing the range of motion) for the butterfly hinge presented in Figure 2.12b. Careful design of topologies of compliant mechanisms can avoid this specific problem, but for more extensive dust protection requirements (driven by goals beyond dust-induced jamming protection, such as, for example, thermal emissivity), additional methodologies might be added in synergy with the use of complaint mechanisms.

Compliant mechanisms possess the intriguing property of storing some of the input work as elastic energy accumulated in the material of the mechanism. This is also a feature that can be quite useful in space applications as a considerable amount of space mechanisms are spring loaded (sometimes even in the launch phase to reduce possible vibrations). In compliant mechanisms, once the external input force is removed, the mechanism can return to its original (unloaded) shape, as a spring could. Compliant mechanisms with localised compliance, characterised

by thin material areas (flexures), can be modelled as rigid-body hinges with torsion springs applied in each joint to mimic the elastic energy stored in the compliant hinge. This modelling technique is known as the Pseudo-Rigid-Body method [49] and can be used to design compliant mechanisms.

(a)

(b)

(c)
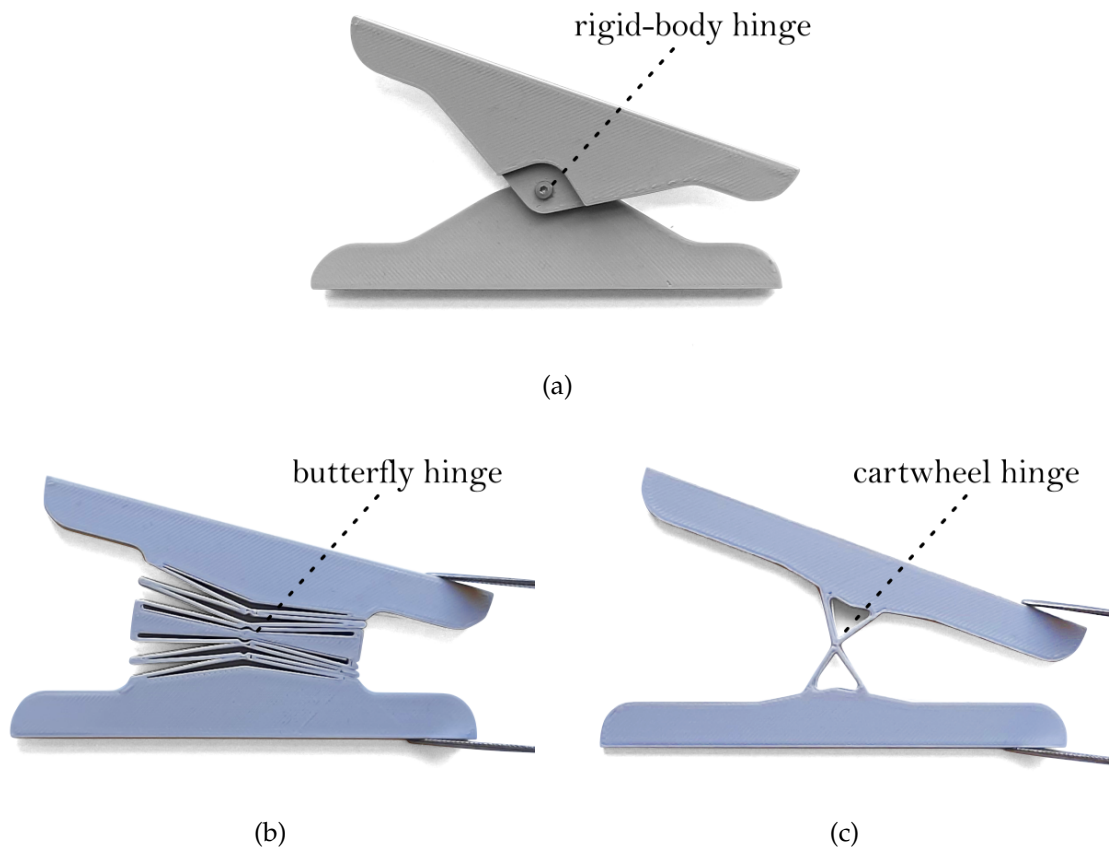
Figure 2.12: Rigid-body hinge (a) and compliant hinges (b) and (c) [14].

There are several advantages and disadvantages to using compliant mechanisms for hardware design [10, 48, 50, 51]. Notable advantages are summarised in Table 2.2 and presented with their associated trade-offs.

Table 2.2 presents a general overview of the characteristics of complaint mechanisms. It is important to note that for space applications, some specific limitations might need to be assessed. For example, environmental conditions in space (vacuum, temperature, etc.) narrow down the material selection. Nonetheless, considering the substances suitable for space use, there are numerous options of compliant mechanism materials. Moreover, choosing complaint mechanisms over rigid-body mechanisms can be valuable in precision applications where the lack of backlashes is a considerable advantage [52–54]. It is beneficial to use compliant mechanisms for applications where avoiding the relative motion between adjacent elements or avoiding friction is needed. By inter-element motion avoidance, com-

Table 2.2: Advantages and associated trade offs of compliant mechanisms.

Advantages	Trade offs
Motion achieved through deflection: Avoids the relative motion of components	Motion range is limited: Full rotation of compliant hinges is not possible
No inter-element friction: No need for lubrication, reduced maintenance	Lower input work efficiency: A portion of input work is stored as elastic energy
No inter-element tribological wear	Bending material segments are more susceptible to fatigue damage
Construction as monolithic pieces: No assembly and reduced costs overheads	More challenging and sometimes less intuitive design processes
Potential for high precision performance due to the lack of backlash between elements	Nonlinear effects must be included in kinematic modelling due to large deflections
Wide selection of potential materials given appropriate design	For stiffer materials the geometry may require extremely thin pieces that are challenging to manufacture
Mechanical energy storage: Compliant hinges can fulfill the job of kinematic pair and attached spring - e.g. a hinge with torsion spring	Under high temperatures stress relaxation may occur if the deflected mechanism is held in a fixed position over extended periods

pliant mechanisms can decrease the number of interface hardware surfaces susceptible to cold welding [51]. This can also help to avoid lubrication, which, as already discussed, is challenging in space. Another good example of an environment where friction-free solutions are desirable is the lunar surface environment [55], which is the focus of this work. On the lunar surface, mechanisms can be degraded by the entry of sharp regolith dust particles into their gaps, causing friction-related wear and damage [12]. The presence of dust-contaminated gaps in the mechanisms, as already mentioned, is the root cause of such problems. Elimination of gaps and sliding friction surfaces also improves wear rates and reduces noise and vibrations [56]. Micro-electro-mechanical systems (MEMS) are also examples of equipment where the size of the mechanism is a limiting factor for manufacturing and assembly of rigid-body mechanisms. Compliant mechanisms, which can be efficiently manufactured in small sizes and do not require assembly, can fulfil the role of spring-loaded mechanisms with more compact designs [57]. Furthermore, normally lubricated mechanisms can be a source of contamination in space payloads. Dry lubricants create solid particle contaminants, and liquid lubricants can evaporate and sublimate on optical components, and the liquid can also creep (migrate)

outside of where it was originally supposed to stay [47]. In applications where these situations must be avoided, compliant mechanisms can be an alternative and safe solution.

It could be argued that bows, which were invented thousands of years ago, are simple compliant mechanisms. However, in most engineering domains, more complex compliant mechanisms are a relatively new development. There are examples of simple compliant mechanisms (or mechanisms with compliant elements) even in consumer products; examples are visible in Figure 2.13. Nevertheless, applications in the space domain are still quite limited. However, it is important to mention that compliant or flexible elements were used in previous space applications. But in this work, compliant mechanisms are understood as systems of more than one flexure, and single flexible components (like springs) are not treated as compliant mechanisms.

(a)   (b)
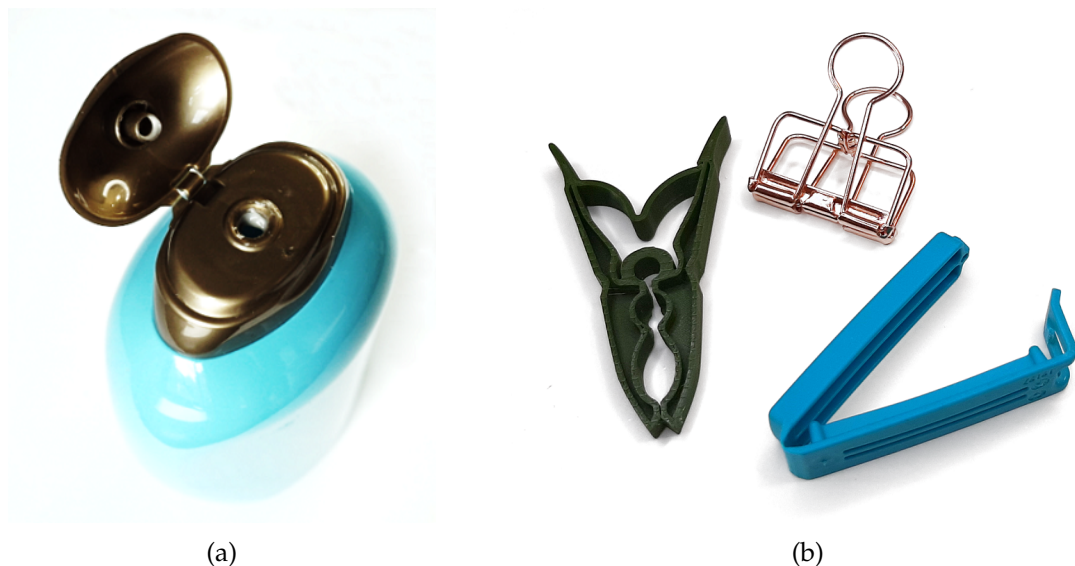
Figure 2.13: Examples of compliant consumer products (a) shampoo bottle with compliant hinge (flexure); (b) various compliant pegs and sealing clips.

In order to understand the state of the art of compliant mechanisms in space applications, it is useful to look into proceedings of two biggest conferences in the field of space mechanisms: European Space Mechanisms and Tribology Symposium - ESMATS and Aerospace Mechanisms Symposium - AMS. Both conferences have published works in the field of compliant mechanisms and they both focus on engineering details and lessons learned. The relevant articles from these conferences will be discussed in this section, along with other literature from relevant journals.

In 2014 during AMS the paper of E. Merriam, J. Jones and L. Howell was published with the title: "Design of 3D-Printed Titanium Compliant Mechanisms" [58].

This paper focuses on the additive manufacturing of compliant mechanisms using titanium powder in an Electron Beam Melting (EBM) 3D printer. The authors present models that were synthesised using analytical design methods. Researchers were faced with some challenges emerging from surface roughness and the fact that the 3D printing method used in the project resulted in the production of elements with considerably porous surfaces. Porosity must be taken into account during the thin flexural design process. The paper clearly indicates that surface finish quality has a direct link to the fatigue-life properties of compliant elements. The authors used hot isostatic pressing for post-processing of the 3D printed elements. However, this process does not fully solve the porosity problem. To improve the results, the authors decided to amend their design process by using a thickness correction factor. For thin elements, it was assumed that due to their porosity, not all of the thickness contributes to the stiffness of the element. In the case of FEM analysis, the thickness factor of 0.83 was applied. The aforementioned method has clearly contributed to obtaining more predictable and durable performance. The further guidance provided by the authors may be intuitive to users of Fused Deposition Modelling (FDM) 3D printers. For instance, they suggested that vertical flexures be printed on the building plate rather than on supports, and flexures at angles different from vertical or horizontal may need to be thicker. The authors also discuss the need to alleviate the possible issues caused by warping. With the technology used by them, they recommend that the thinnest flexures are not thinner than 0.75 mm and with gaps of at least 1 mm. One of the examples shown in the paper is the 2 DOF (degree of freedom) pointing mechanism developed for NASA to demonstrate new technology pointing mechanisms for attitude control thrusters or antennas [59]. The mechanism .stl file was made available by BYU - Brigham Young University, the group responsible for the design. The view of this model is visible in Figure 2.14. The mechanism uses thin flexures with a thickness of 1 mm. Some of the structural tubes also have a small cuts or gaps to allow additional flexibility. The work describes how the final design was obtained using analytical methods beginning with the rigid linkage approach.

The next set of articles comes from researchers of the Swiss company CSEM SA, which, similarly to the BYU team, is interested in applying additive manufacturing technologies to develop compliant mechanisms [60]. CSEM SA focused on the SLM - Selective Laser Melting process and used 316L stainless steel powder as the building material. Observations on porosity and surface roughness were similar to those previously presented by BYU and further discussed in another paper by the same team from CSEM [61], concluding that hot isotropic press (HIP) and annealing have a significant effect on the performance characteristics of compliant mechanisms.
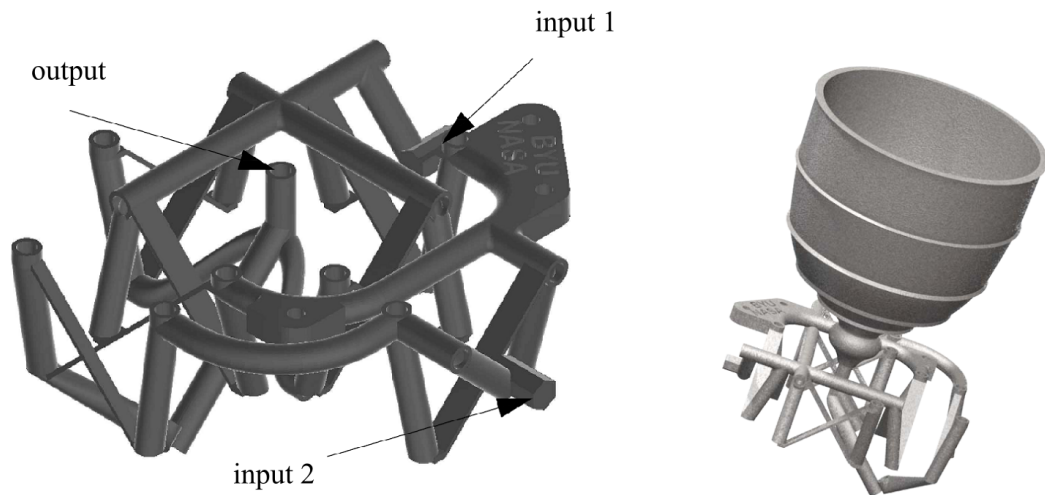
Figure 2.14: Left: view of BYU's 2 DOF pointing compliant mechanism design from the 3D model; right: the pointer mechanism integrated with a small attitude control thruster [59].

The research shows that the developed compliant mechanisms can survive more than 15 mln cycles, potentially making them suitable for certain space applications. The same work also investigates the use of topology optimisation [61]. CSEM team decided to divide their design, which was anyway obtained by analytical methods as the main topology, into complaint/flexible areas and stiff structure-like areas. Topology optimisation was employed only in stiff (structural) areas. This is not an example of topological optimisation of complaint mechanisms, as technically what was obtained is topologically optimised rigid components connected by flexures that were not topology optimised and excluded from the process. The details of topology optimisation versus analytical design methodology for compliant mechanisms will be discussed in further detail in Section 2.5. The important conclusion here is that even leading companies specialising in compliant mechanism design are in the early stages of using topology optimisation to create novel compliant designs. Another project of the same CSEM team used a hybrid design approach that involved the building blocks method and topology optimisation of structural components [62]. The first step of the design was to choose the flexural pivot as a central part of the design, then the rest of the topology was predefined and optimised in structural areas. The reason for such a methodology is well explained in the aforementioned paper [60] and it specifically says: *"As introduced in the previous chapter, the use of a unique optimisation tool to achieve option "a"*(for clarification *"a. optimise structures and flexures simultaneously"* - author's note) *was judged too risky and therefore it was decided to consider it as an ultimate long term objective"*. This is evidence that more research is required in the area to develop the state-of-the-art of topology optimised compliant mechanisms, especially for space.

CSEM also worked on an analytically designed Large Angle Flexure Pivot [63, 64] with ± 90°range of motion. Flexures were manufactured with Marval-X12 steel using wire electrical discharge machining. This mechanism was tested in an engineering model configuration as a scan mirror mechanism. The testing included cryogenic thermal cycling, vibration, and lifetime tests, which are typical tests required for space hardware. One of the objectives of the project was to determine the axis of rotation shift, which was measured at ± 35 μm and ± 70°. This is an outstanding performance as compared to state-of-the-art compliant mechanisms. CSEM seeks to qualify the mechanisms for future scientific space missions [64].

The work carried out by the commercial company Almatech also revolves around the design of the Large Angle Flexible Pivot [65]. The article presented at EMSATS in 2019 discusses the design, material selection, optimisation, manufacturing, and fatigue testing of the compliant pivot. The choice of material was critical, leading to the selection of Titanium Ti6Al4V, which is able to accommodate large deformations while ensuring long fatigue life. The authors also worked on developing an optimisation tool that can adjust the geometry of the flexible pivot for given customer needs. The presented design excels with a ± 70°rotational range and low actuation torque, achieved by careful optimisation of radial and axial stiffness. Furthermore, different manufacturing processes were evaluated, with EDM being the most notable for precision and tolerance adherence. Fatigue testing, a crucial aspect, also demonstrated positive results. EDM-produced samples endured 20 million cycles without failure, one of them achieved 309 million cycles, setting new standards in compliant mechanisms in the space industry. The authors also claim that ongoing efforts aim to qualify these mechanisms for future space missions.

The next notable source is paper "Design and analysis of a novel flexible compliant joint for space mechanisms" [66] from Thales Alenia Space UK and SpaceMech. It presents a compliant element that replaces a slider and pivot assembly that could be used as part of the positioning system. In traditional designs, the slider-pivot combination presented in the paper would have a spherical joint which, in space projects, poses some tribology challenges. Using the complaint mechanism can ease the design in this case. The flexible elements presented consist of thin blades made of Titanium Ti-6Al-4V. Such elements have an additional benefit that they can be pre-loaded for the launch phase of a mission. Although this project was purely conceptual, the authors indicated that they intend to continue developing their experimental setup to assess the fatigue characteristics of the designs presented in their paper.

CSEM wrote another interesting article on compliant focus mechanisms that they developed for the Close-up Imager (CLUPI) on the ExoMars rover [67]. CLUPI,

a high-resolution camera, plays a crucial role in the capture of close-up images of collected samples prior to their chemical analysis. The mechanism is vital for accurate lens positioning, relies on compliant mechanisms to achieve precision, and it is resilient to the harsh Martian environment. Due to the precision needs of this instrument, a flexible structure, comprising of guiding plates, is required. The mechanism is a deformable parallelogram with four flexure blades acting as joints. Three parallelograms were used to ensure stable positioning and a single transnational degree of freedom. The single DOF is a linear movement along the Z-axis (optical axis), whereas other degrees of freedom are blocked. It provides the necessary guiding function for the mechanism while maintaining concentricity and co-alignment at the reference position. During the mechanism tests, some issues emerged, mainly the rupture of vertical blades due to repetitive buckling deformation and fatigue under vibration loads. Design improvements were implemented, including a switch from titanium to Marval X12 stainless steel for guide plates with geometry updates to achieve stiffness similar to that of the previous version. On top of that, anti-buckling pins were added to limit off-axis movement during vibration. In 2019, another work by Verhaeghe et al. [68] suggested the integration of a crossed-blade pivot into the structure of the guiding plate to improve resilience and balance, further refining the design of the focus mechanism.

The next development of compliant mechanisms worth mentioning is the Meteosat Third Generation (MTG) scan mechanism, situated aboard a state-of-the-art Geostationary Earth Orbit Satellite [69]. This satellite, with its three-axis stabilisation, had a stringent set of requirements for this instrument. First, the instrument needed to ensure accurate slope and low jitter in the scanning of the Earth along the east-west and north-south directions. Second, the instrument should have precise knowledge of angular pointing, with a bias requirement of less than 0.5 μrad and jitter less than 0.5 μrad. Lastly, the instrument should achieve an overall position accuracy of 100 μrad or less within the entire scan range. It is clear that the precision requirement had to drive the type of mechanisms selected for this instrument. Within this complex framework, flexural pivots emerged as crucial components in the MTG instrument project, enabling the mentioned precision. Characterised by a three-blade cross-axis flexural pivot design, these flexural pivots demonstrate exceptional load-bearing capabilities. Life tests have also validated the durability of flexures, surpassing an impressive threshold of more than 20 mln cycles. In addition to life tests, meticulous component-level characterisations were performed, assessing stiffness and hysteresis to ensure adherence to the performance standards established by the MTG instrument project.

Another application of a compliant mechanism was flown on Sentinel-3. The

mission of the satellite was to measure sea-surface topography, sea and land surface temperature, and ocean and land surface colour with unparalleled accuracy and dependability. Such stringent performance requirements (10 arcsec pointing stability with averaged 1 arcsec repeatability and life of 3000 million cycles) demand the utilisation of very precise mechanisms with stable performance over their lifetime, precisely the kind of solution provided by flex pivots. By eliminating friction, they played an indispensable role in fulfilling the mission's ambitious goals. The details of the design can be found in the literature [70]. The pivots were part of the Flip Mirror Device (FMD) where they provided rotation capability. Crafted from blades with 50 micrometre thickness, these flexural pivots were meticulously designed to minimise any potential sources of precision disturbance (such as friction). Their primary function was to facilitate the periodic flipping of the mirror, a task of paramount importance for combining the two Sea and Land Surface Temperature Radiometer (SLSTR) views seamlessly. Beyond their mechanical precision, these flexural pivots were engineered to have an infinite operational life, ensuring the longevity and reliability of the FMD.

In the LISA mission, three identical spacecrafts travel 5 mln kilometres apart in a heliocentric triangle formation. The aim of the mission is to observe gravitation waves, and it involves observing proof mass movements and arm length changes in the Point Ahead Angle Mechanism (PAAM) developed by CSEM and RUAG [71]. Due to seasonal shifts in the formation's shape, the precision of the mechanisms is quite challenging to achieve. However, the PAAM compensates for the angle changes. To detect gravitational waves with high precision, LISA relies on flexure structure technology, including flexure pivots that support optical mirrors. These flexure pivots consist of three blades each, have a motion range of ±412 µrad and are designed to provide a rotation free of parasitic shifts. In the actuation path of the pivots, a differential-lever unit is used. This unit consists of two flexible blades and another flexure pivot. These flexure elements are designed to provide high-accuracy guiding without the need for sliding surfaces or rolling bearings. The use of complaint mechanisms in this project definitely enables the precision and enhances the performance of the mechanism.

In 2004 Henein et al. published a peper "Mechanical slit mask mechanism for the James Webb Space Telescope Spectrometer" [72]. That work focused on a complex mechanical slit mask mechanism designed for the James Webb Space Telescope's Near Infrared Spectrograph. This precision instrument needs to operate under cryogenic conditions, forming 24 optical slits within a field of view of 137 x 137 mm² using voice coil actuators. The instrument is equipped with a flexible wheel in the mechanical slit mask mechanism. The wheel is built with flexures and

their aim is to provide a uniform radial stiffness to the wheel while maintaining high stiffness and strength in other directions. It is done by applying a constant preload force to the masking bar to maintain its contact with the rigid wheels in all positions and accommodating the lift of the bar during the launch clamping phase without creating excessive stresses in the blades. Furthermore, the design of the ratchet clutch in the slit mask mechanism enables the translation of each bar with high precision but the utilisation of flexures. It consists of a parallel spring stage with compliant blades used as vertical transnational guides. The clutch is powered on to engage the sapphire tooth in the corresponding teeth of the masking bar, providing precise positioning. As a result, the repeatability of the engagement is better than 1 μm. It is evident that the role of the compliant elements in this mechanism is to provide precision, but also their elastic energy storage was used for preloading. Such task might have been achieved with rigid-body mechanisms and springs, but it is safe to assume the overall mass and assembly costs would be higher.

The papers of Urgoiti et al. [73] and Compostizo et al. [74] discuss the pointing mechanism for GAIA M2 Mirror (M2M). The M2M holds a pivotal role within the GAIA instrument, being responsible for supplying the secondary mirror with five degrees of freedom: three translational and two rotational. Its primary function lies in providing precise adjustment capabilities, characterised by sub-micrometer accuracy. Central to the success of the mechanism is the flexible symmetric structure described in one of the mentioned papers [73]. This structure layout consists of two levers, two flexural joints or pivots, an output interface with a reduction ratio, and an interface for attachment to the trays. Optimisation of this structure stands as a crucial achievement, with a primary focus on achieving stringent tolerances and minimising the length of the flexible blades to avoid potential buckling issues. Furthermore, a noteworthy aspect of the mechanism's design lies in its adjustment, ensuring a minimum tension on the flexural plates along the operational range. This type of calibration guarantees consistent preloading of the spindle nut contact, effectively avoiding the emergence of undesirable backlash. This ensures accuracy and repeatability, vital for its intended mission.

Deployable booms made of flattened tubes (consisting of thin tapes) rolled on a reel represent another category of space mechanisms with compliance. Some cross section shapes of the booms are presented in Figure 2.15 based on the available literature [75–79]. Such booms can be considered a type of compliant mechanism, although the way they work is more similar to spring elements (which, in a way, are always compliant). The boom is usually elastically deformed to make it flat, and then it is coiled around a cylindrical element, a reel. This winding mechanism

is quite similar to the carpenter's tape that usually has a cross section in the shape of letter 'c' and after uncoiling becomes stiff enough to measure distances. In case of the space booms, they are usually used to reduce volume (as compared to rigid segment booms) and after deployment they need to provide sufficient stiffness to support elements that they deploy (e.g. probing devices, antennas, etc.).

(a)   (b)
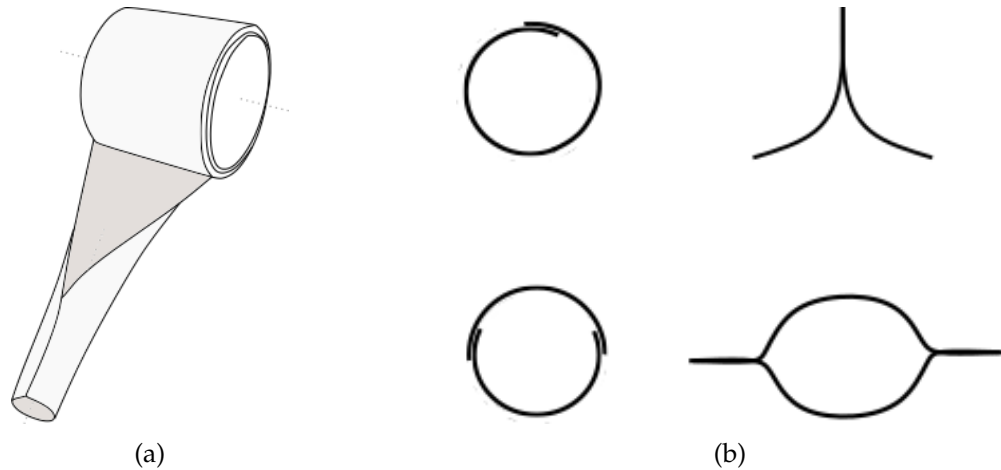
Figure 2.15: Deployable booms drawings (a) flattened tube rolled onto the reel; (b) various shapes (cross sections) of the possible tubes.

The final group of compliant elements presented here are hinges composed of flexible tapes, often referred to as tape spring hinges. Similar to boom technology, this solution utilises thin tapes that can deform elastically to achieve motion. When larger deflections are required, buckling may occur to a significant degree. This technology can generally be used as a substitute for more conventional knuckle joints (spring-loaded hinges). The literature presents multiple examples of usage that cover deployable structures and solar panel deployment mechanisms [75, 80, 81]. A notable example of the use of such flexure in conjunction with shape memory alloy for solar panel deployment mechanisms was presented by Testoni et al. [82]. In their work, the authors presented an active compliant hinge using strain energy from the compliant hinge and force produced by memory shape alloy springs to achieve multiple stable solar panel configurations.

As can be seen in examples of compliant mechanisms in development for space, the range of applications, design methodologies, and materials is quite wide. Section 2.5 focuses on the design methodology, presenting tools available in the literature and commercial software. It is important to mention that the selection of design tools and materials usually have an impact on each other. As demonstrated in literature published in line with this project [83] and discussed in Chapter 4 topology optimisation tends to yield more successful result with materials characterised by low Young's modulus (more flexible). At the same time, using typical analytical tools for compliant mechanisms requires materials that can provide more

stiffness in the selected direction of a flexure. To date, most of the compliant mechanisms and compliant elements developed for space and presented in this literature rview use metals as their base material. Metals make excellent choices for precision mechanisms and can withstand a harsh space environment with ease. On the other hand, most polymers tend to outgas in space, and their properties exhibit significant changes in response to temperature fluctuations, unlike metals. Additionally, polymers are susceptible to stress relaxation and creep. Nonetheless, the new developments in the polymers domain show that more materials can be considered for space use. The notable and promising materials are PEEK (polyether ether ketone) and PEKK (polyetherketoneketone) which are polymers that can be 3D printed and can be used in space due to their low outgassing rates [84, 85].

2.5 DESIGN OF COMPLIANT MECHANISMS

From the perspective of topology synthesis, the design of compliant mechanisms may be more complex than the design of rigid-body mechanisms or structures. This is especially true when designing intricate, compliant mechanisms. To simplify the task, numerous analytical methods were developed. Another approach is using topology optimisation, which will also be discussed in this work. An overview of the relevant design methods available can be found in Figure 2.16.

Howell et al. [10] and Hopkins and Culpepper [86] have extensively discussed the capabilities and limitations of various approaches to design compliant mechanisms. Analytical methods are quite intuitive for those familiar with designing traditional (rigid-body) mechanisms. The right-hand side of Figure 2.16 outlines the division of analytical design methods. The first subgroup, Rigid Body Replacement Method (RBRM)[49] - works by replacing hinges and other rigid-body mechanism kinematic pairs with compliant kinematic pairs. Such solutions rely on existing rigid-body designs. The final topology is usually very similar to the original design and potentially excludes some of the more interesting solutions. Two additional analytical techniques, namely Freedom and Constraint Topology (FACT) [86] and Building Blocks Approach [87], use collections of compliant elements or sub-mechanisms. These two methods are based on the kinematic behaviour of each sub-mechanism. The design process consists of identifying sub-mechanisms needed to fulfil the kinematic function and combining them into a larger compliant mechanism. They can be very effective design tools, and the design process is similar to designing rigid-body mechanisms. It is evident that the current analytical design methods can be advantageous for various applications and aid in creating solutions efficiently and quickly, while also allowing for some flexibility and designer control in the design process. The left side of the Figure 2.16 presents
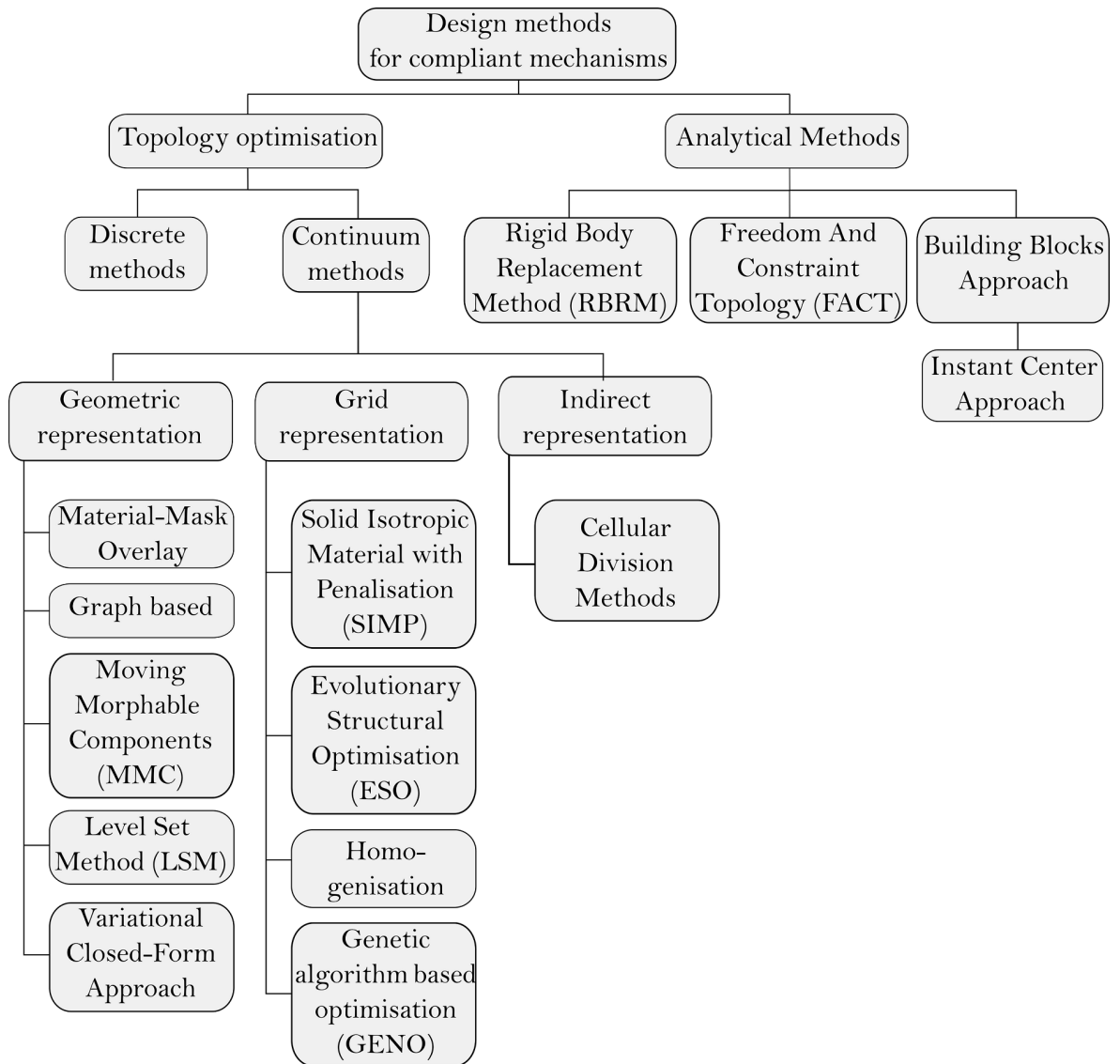
Figure 2.16: Design methods used to synthesise compliant mechanisms.

topology optimisation solutions where a software tool searches for the optimal material distribution of a given problem. As demonstrated, the available design tools are quite diverse.

The selected design methods will be discussed in more detail in Subsections 2.5.1 and 2.5.2. Nonetheless, regardless of the design approach used, it is important to understand that there are multiple methods to adjust the stiffness (and therefore the compliance) of the flexible element. Howell et. al. [10] list three ways to adjust flexibility (or stiffness) by influencing: (i) material properties, (ii) geometry (in their book they mention shape and size), and (iii) loading and boundary conditions. It is safe to assume that for many space mechanisms, loading and boundary conditions are selected in advance at the system level of the design (or at least their range is given). Therefore, it is expected that, for a given problem, those values are
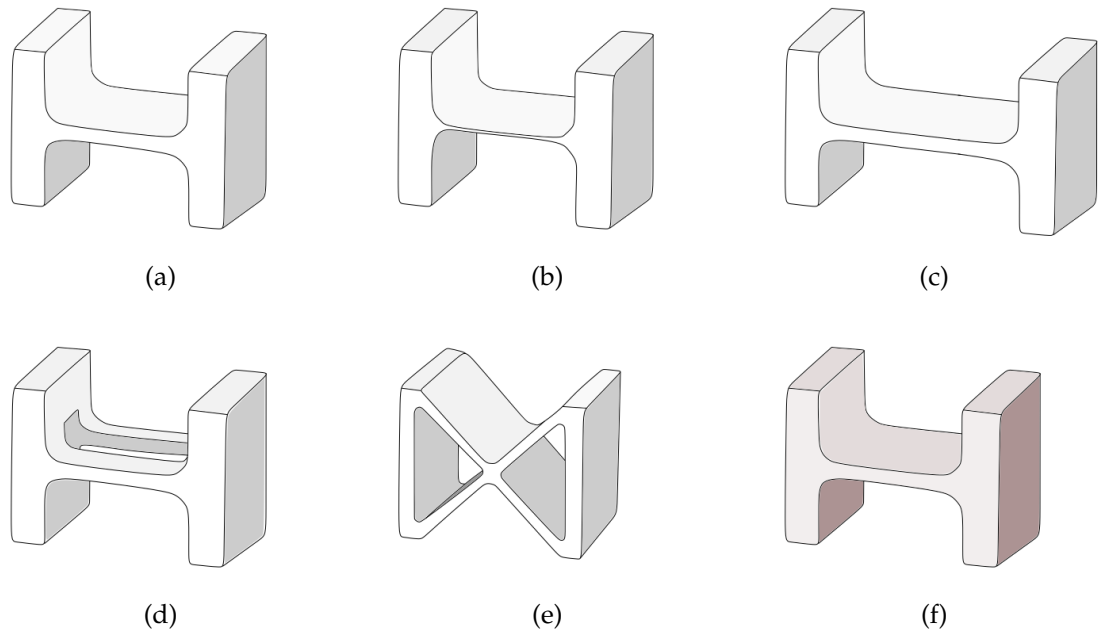
Figure 2.17: Stiffness adjustment of a compliant hinge (a) original flexure; (b) geometry change (reduced flexure thickness); (c) geometry change (flexure length extended); (d) topology change (one flexure substituted with two narrower flexures); (e) topology change (blade flexure substituted with cartwheel hinge); (f) material change (same topology and geometry, different Young's modulus).

fixed. The geometry change from the list of Howell et. al. [10] can also be split into actual geometry (dimensions of flexible element) and topology (shape of the elements, their distribution, type, etc.). This division is particularly useful for single compliant kinematic pair optimisation. It is fair to conclude for the needs of this work that the flexibility of most compliant elements can be altered by changing (i) geometry (length, thickness, etc.), (ii) topology (number, type of flexures etc.), and (iii) material (higher Young's modulus corresponds to higher material stiffness). These three adjustment methods are demonstrated in Figure 2.17 and will also be explored for the specific mechanisms in the Chapters 4 and 5.

2.5.1 ANALYTICAL DESIGN METHODS

In this Section, the primary analytical design techniques will be discussed.

RIGID BODY REPLACEMENT METHOD OR PSEUDO-RIGID BODY MODEL

This approach is based on the kinematics correspondence between the rigid-body mechanisms and the elastic members [10, 88]. This design methodology starts with identifying the rigid-body mechanism capable of performing the desired

movement [56]. Then the existing mechanism is converted into a compliant mechanism following some basic rules (such as selecting flexures with the appropriate degrees of freedom). This method is usually used to achieve lumped compliance designs, which are compliant mechanisms with localised compliance visible as thin flexures and connecting stiffer (rigid) elements. The difference between lumped and distributed compliance is presented in Figure 2.18. In lumped compliance mechanisms, most of the deformation occurs in the localised flexures and therefore such joint can be approximated as rigid-body hinge with torsion spring localised at its axis. For a more specific analysis of compliant designs achieved using this approach, the literature presents equations that help to approximate different types of flexures (compliant beams) in the system [10]. As such, the Pseudo-Rigid Body Model can be useful tool for the design of a compliant system based on rigid-body mechanisms but also as an analytical tool helping to assess the displacements in compliant mechanism.
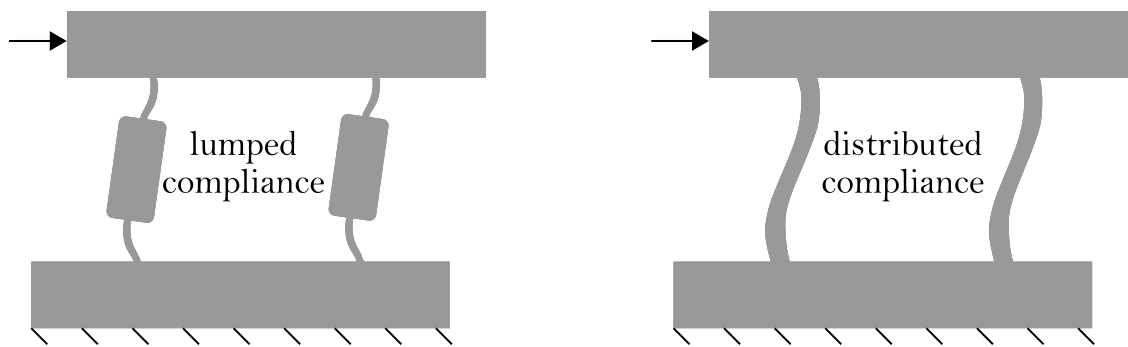
Figure 2.18: Comparison between lumped and distributed compliance in compliance parallelogram example.

Figure 2.19 presents an example of the parallelogram mechanism that can be designed as a rigid-body mechanism, and with the addition of torsion springs in the joints. It can be a base for a compliant mechanism presented in Figure2.19b. Torsional springs demonstrate the strain energy that is normally stored in compliant mechanisms in the same way that springs store strain energy.

FREEDOM AND CONSTRAINT TOPOLOGY (FACT)

This methodology was developed and presented to the scientific community by Jonathan Hopkins [89, 90]. This methodology can be used to synthesise multi-degree of freedom compliant systems. The FACT methodology uses the freedom and constraint lines that are situated in specific flexure shapes. Such an approach helps to graphically visualise degrees of freedom (DOF) and degrees of constraint (DOC). To aid in the search for flexure shapes that match the requirements of
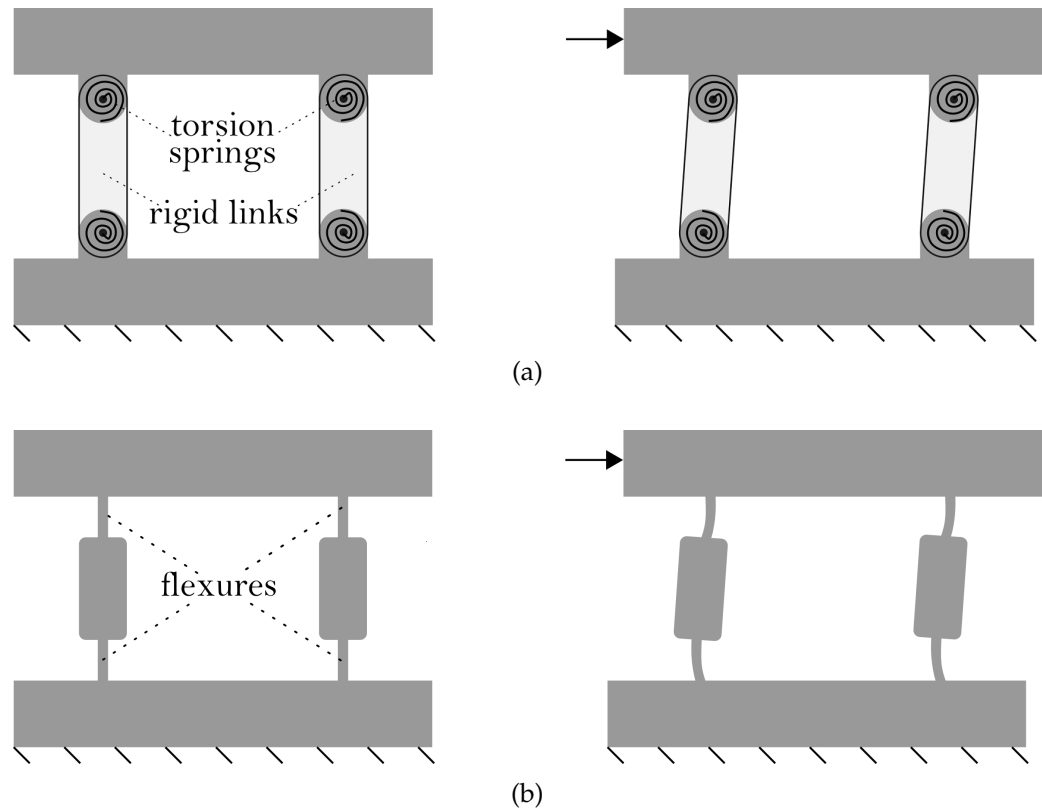
Figure 2.19: Demonstration of link between rigid-body mechanism and compliant mechanism used in Pseudo-Rigid Body Model, (a) rigid-body parallelogram mechanism with torsion springs attached to the joint before (left) and after (right) displacement of top platform, (b) compliant parallelogram mechanism before (left) and after (right) displacement of top platform.

given DOFs, a FACT chart was developed that presents different topologies capable of achieving given DOFs. The complete chart can be found in the literature [91] while the simplified version is also presented in Figure 2.20. The user of the FACT methodology must identify the DOFs that the system is required to satisfy. The DOFs can be found to the left of each subgroup in Figure 2.20. Specific combinations of DOFs (for example: one rotation and one translation like in group 2 in column 2DOF) correspond to the specific constraints space presented on the right of the DOF combination (in Figure 2.20).

By using combination of wire flexures that provide one DOC and blade flexures that provide three DOCs user can synthesise the system matching given constraint lines from the chart. This methodology provides a very precise tool to foresee the motion of compliant elements in a small displacement range. The literature covering this methodology ranges from application to serial flexure design [91, 93], hybrid flexure systems [94] and improvement of existing flexure solutions [95].
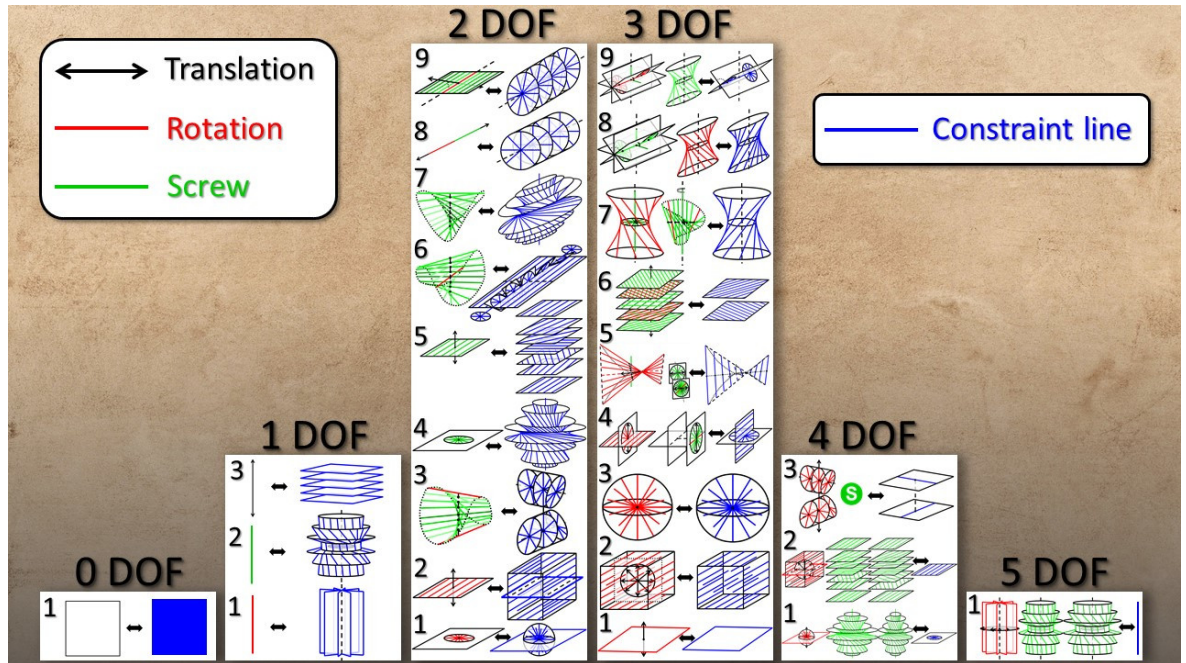
Figure 2.20: Freedom and constraint topologies (FACT) library of freedom and constraint spaces used to design parallel flexure systems, created by Jonathan Hopkins [92].

INSTANT CENTRE APPROACH

In 2006, Kim et al. [96] presented variation of building block approach - Instant Centre Approach. This is a fast analytical method that can aid in the design of compliant mechanisms. It is a graphic method that builds on the concepts from kinematics - instant centre of rotation of rigid bodies. In rigid-body motion, any planar displacement of a rigid-body can be considered as a rotation about a point which is called instant centre of rotation [97]. All velocity vectors of the other points located on that rigid-body generate a circular field around this point. The rigid body movement can be described as a single rotation around the instant centre point. This methodology can be used for the identification of specific points (centres of rotations) in the design of compliant mechanisms consisting of rigid bodies connected by flexures. It helps to identify the direction and positions of the flexures to satisfy the desired motion. An illustration of the steps necessary to adhere to this approach, with an example of a particular mechanism, is provided in Figure 2.21.

The design steps presented in Figure 2.21 are as follows: (a) identification of the design domain with input and output (marked with arrows); (b) drawing lines perpendicular to the input and output (grey dashed lines), selection of the intermediate point (marked with blue dot) and its expected displacement direction (blue arrow); (c) drawing line perpendicular to the intermediate point displacement direction and crossing the intermediate point (blue) - intersections of that line with
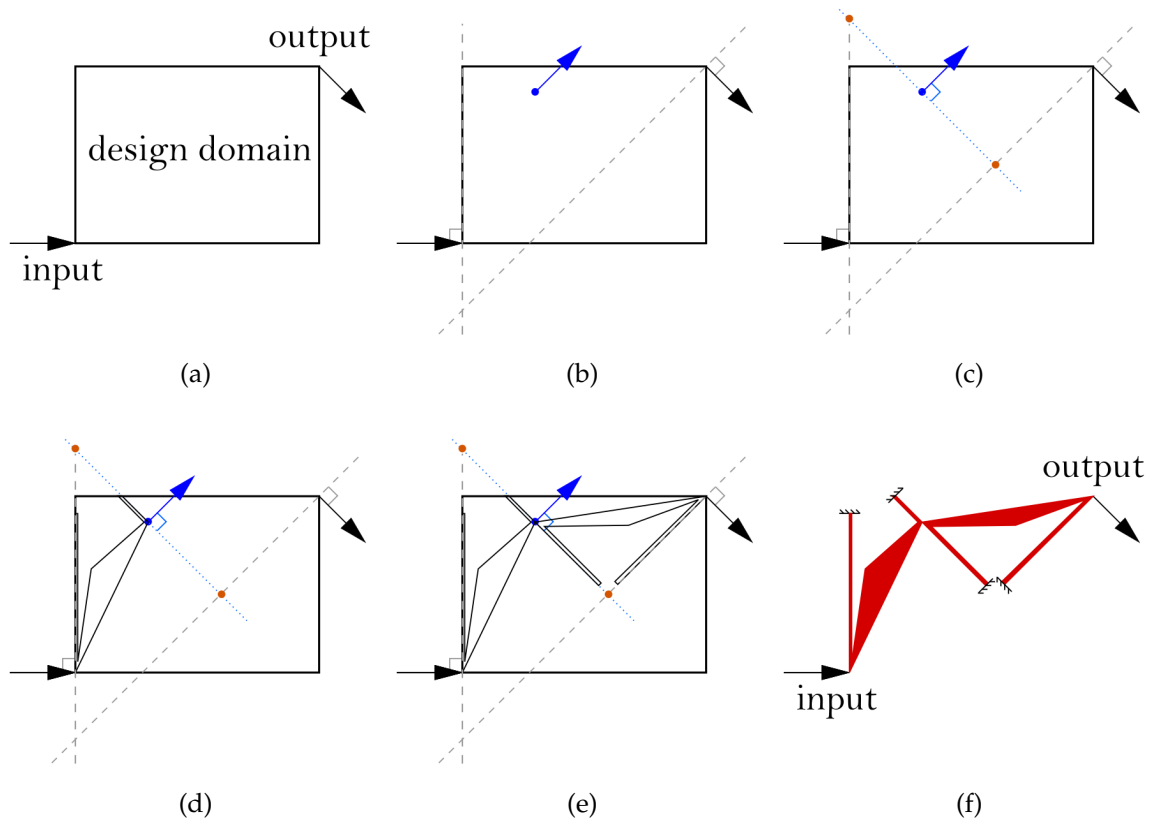
Figure 2.21: Instant Centre Approach demonstrated with an example of one input - one output compliant mechanism. Design steps (a) - (f) are discussed in the text.

the grey dashed lines form two centres of rotation marked in orange; (d) the first stage of the compliant mechanism can be drawn - flexures going towards the first point of rotation and rigid stage connecting input with intermediate (blue) point; (e) second stage drawn analogically to the first one; (f) full compliant design drawn in red with fixed points at the base of the flexures. This methodology can be recreated for a variety of compliant mechanisms that need specific orientations of the input and output displacement directions.

This design methodology also allows for quite straightforward analysis of Geometric Advantage (GA: displacement of the output node in the desired direction divided by the input displacement), which makes this method quite useful for applications where achieving a specific GA is a design requirement. Knowledge of the position of rotation points allows for geometric evaluation of the displacements ratio. An example of such analysis is presented in Figure 2.22 where the final GA can be calculated using Equation 2.1.

$$GA = \frac{d_{out}}{d_{in}} = \frac{X_4}{X_1} * \frac{X_2}{X_3} \tag{2.1}$$

Where d_{out} stands for output displacement and d_{in} for input displacement.
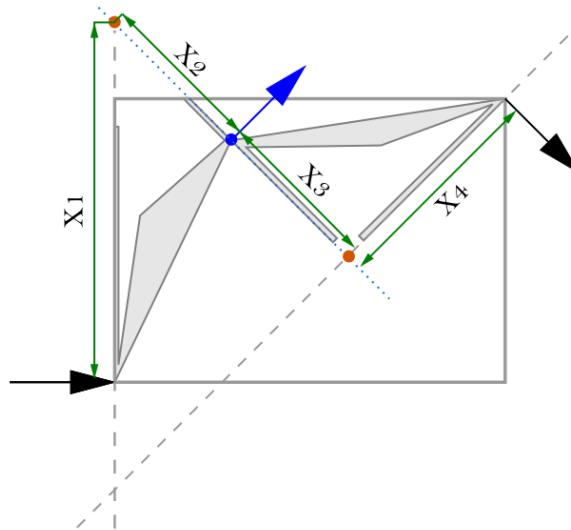
Figure 2.22: Compliant mechanisms designed in Figure 2.21 with distances marked to calculate the Geometric Advantage.

2.5.2 TOPOLOGY OPTIMISATION

To achieve capabilities beyond these of the analytical methods, several works suggest the use of topology optimisation. Topology optimisation is a methodology that identifies the optimal material distribution for given boundary conditions [98]. The problem is described by an objective function and physical constraints. Typical objective functions for structures tend to minimise either displacement or compliance (which maximises the stiffness). In the case of a problem with prescribed loads (forces), a rigid structure is the result. Common design constraints in the field of optimising structures include the volume fraction, the mass fraction, or the total mass. The topology optimisation capabilities for structures are easily accessible in commercial CAD software packages. However, topology optimisation for compliant mechanisms is still in its early stages in current CAD software. Hence, methodologies from the research community, which will be discussed here, are very relevant in the field.

In topology optimisation for compliant mechanisms, there are two main schemes of material distribution in the design domain: discrete topology optimisation and continuum topology optimisation. Figure 2.23 presents the difference between the two methodologies. In discrete methods the design domain is initialised by truss, beam or frame elements that populate the design domain (see Figure 2.23 top right hand side panel) and form a ground structure [99, 100]. In these methods there are void areas in between the ground structure elements. These voids are not considered during the topology optimisation process - they cannot be occupied by the material. Material can only be placed where the elements of the ground structure

are present. The topology optimisation process chooses which elements must be present in the final design and which should be removed. Furthermore, some formulations, for example in the work of Ananthasuresh [99] - allow the topology optimisation solver to vary the thickness of the beams. In contrast, the continuum approach (Figure 2.23 on the left) does not have areas that would be immediately excluded, and the entire design domain is discredited by mesh [101]. As with discrete topology optimisation, continuum topology optimisation also chooses the elements (from the mesh) that will be present in the final design. At present, especially in the context of commercial CAD software, much greater attention is being paid to continuum methods. Those methods also provide more flexibility in terms of possible solutions, and therefore they will be discussed here.
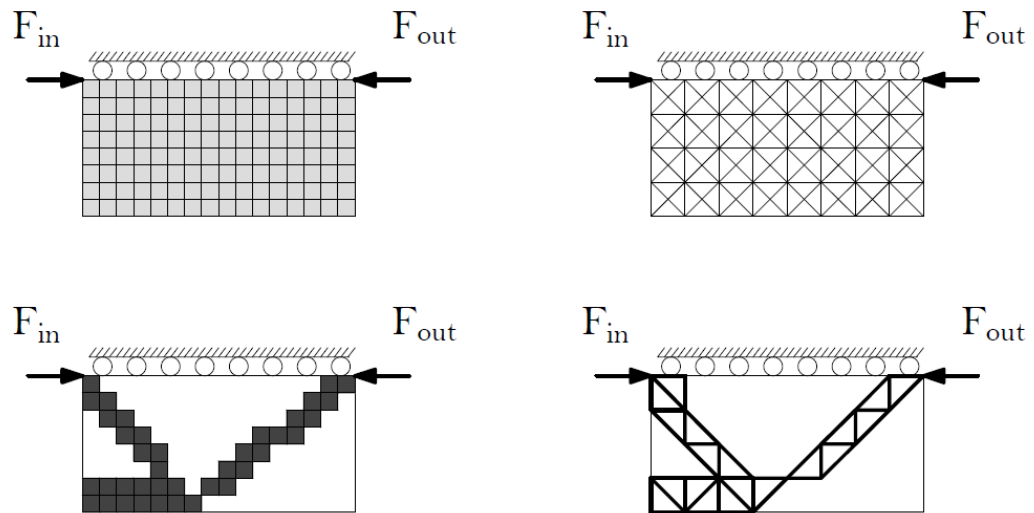
Figure 2.23: Design domains (top) and example topologies (bottom) of a force inverter from discrete topology optimisation (on the left) and continuum topology optimisation (on the right).

Continuum topology optimisation (see Figure 2.16 on the left) can be further split based on the topology representation in the design domain. The design domain is divided into finite elements which are used for Finite Element Analysis and are referred to as physical level representation [101] or phenotype [102]. There is also a mathematical representation [101] or genotype [102] that stores information regarding the state of the sub-regions of the design as function of the design variable. The differences between various methods lie in their mathematical representation of the design (genotype). According to Aulig and Olhofer [102] the mathematical representations can be split into three categories: (i) grid, (ii) geometrical, and (iii) indirect. A brief visualisation of the differences is presented in Table 2.3. In the grid approach, the mathematical level representation (mesh) is linked with the physical level representation (function of design variable x) mean-

ing that there are a number of finite elements in the design domain that can take a binary value of either 0 or 1 (in some methods intermediate values are also used) - Table 2.3 on the left. In contrast, in the geometric representation, the designs can form different shapes and stretch over the initial mesh (the mathematical level representation stretches over the physical level representation) - Table 2.3 in the middle. This implies that there is a mathematical description of the design edges regardless of the mesh edges of the physical-level representation. These geometric methods have elements called movable shape primitives that can change shape, size, and orientation in the search for the optimum topology. The final method is known as the indirect approach, on the right-hand side of the Table 2.3. Here, the best example is the Cellular Division Method, where the evolution can be seen as a growth of the structure with cells that were initialised in the design domain and continued to evolve and divide [103]. The ability of the cells to divide is the key difference between this method and some methods falling into the geometric representation category. In the geometric methods, elements (shape primitives) can change their shape and size, but they do not divide to produce new primitives.

Table 2.3: Mathematical level representations of the design domain marked in black. Grey mesh represents physical level representation.
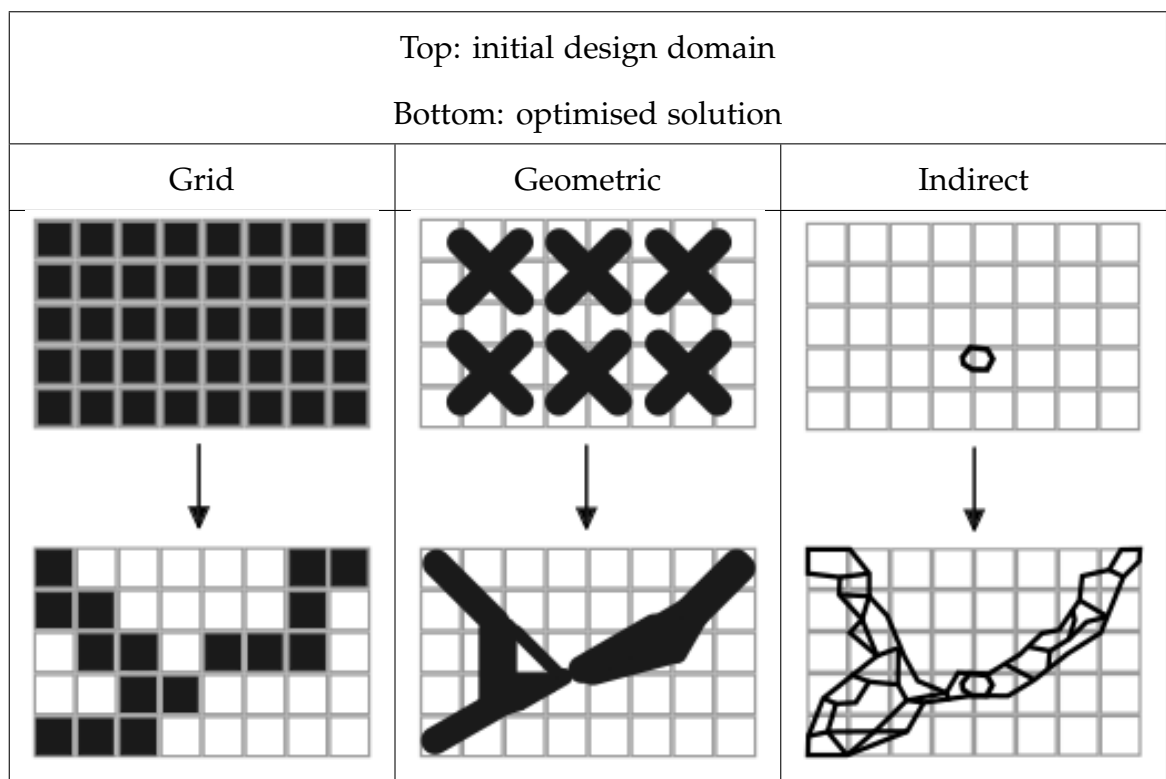
In the bottom half of Figure 2.16 multiple specific methods of continuum topology optimisation are mentioned. They are also listed below and briefly discussed.

- **Material-Mask Overlay method**

  This method uses a number of masks to map the topology by assigning solid and void masks. The shapes of the masks are independent of the physical-level mesh in the design domain. The masks stretch over the finite elements and evolve during the topology optimisation process. The states of finite elements (void or material) are determined by the position of their centres relative to the masks of the representation of the void or material [101, 104]. For example, an element which is covered by more than one mask will inherit a state of the mask stretching over its geometric centre.

- **Graph Based approach**

  In this method, the edges of the topologies are represented as spline curves connected to nodes. The shape of the topology is controlled at the control points of the curves, and their locations are updated by using a genetic algorithm [101].

- **The Moving Morphable Components**

  The MMC method is an approach in which a set of morphable components is defined at the beginning of the process. The morphable components change their parameters (size, shape, position, orientation, etc.) and move inside of the design domain during the optimisation process. These components are used as building blocks of the design and the topologies are found by optimising their positions, shapes, lengths, thicknesses, orientations, and connection with other components [105].

- **Level Set Method**

  LSM uses a scalar level set function [106]. It represents the boundary as an iso-surface of a level set function, allowing for easy tracking and modification of the design's shape. The final topology is obtained by solving a Hamilton-Jacobi partial differential equation [101, 107].

- **Solid Isotropic Material with Penalisation**

  SIMP uses black, white, and grey elements to achieve the final design. The black elements represent the full density of the material, the white is the density of a void (which, for computational reasons, is always a small number, but never 0), and the grey represents intermediate densities [108]. In the final topology, grey areas present challenges for manufacturing; however, their interpretation can be manageable for composite materials [107]. The

optimisation process involves minimising or maximising the objective function subject to additional constraints (e.g. volume) by attractively adjusting the densities of elements in the design domain. A penalisation parameter is introduced to make the optimisation problem mathematically tractable. As optimisation progresses, regions with material densities close to zero tend to become void. This methodology is implemented in most commercial software topology optimisation packages.

- **Evolutionary Structural Optimisation**

  ESO method gives binary outcomes consisting of only black (1) and white (0) regions. These methods can be further divided into hard-kill and soft-kill methods [101, 109, 110]. Hard-kill methods work in one direction, i.e. in a non-reversible manner. The optimisation process starts with a full-domain algorithm from which it can only remove elements. Once an element is removed, it must remain void until the end of the optimisation process. Soft-kill, also referred to as BESO - Bidirectional Evolutionary Structural Optimisation, works in both directions. An element can change its state from full to empty during the optimisation process multiple times. This allows greater flexibility in the topology that might be explored during the optimisation process.

- **Homogenisation method**

  It assumes that the material in the design domain can be porous, which means that there are small cavities within each finite element [111]. The representation of the outcome topology will then consist of typically black elements representing fully filled design regions, white for void regions, and shades of grey representing elements with varying levels of porosity. This poses challenges in the manufacturing process similar to the grey areas in the SIMP methods.

- **Genetic algorithm-based topology optimisation**

  This approach has the advantage of looking for the global optimum. Unfortunately, their convergence is slow compared to other methods [112], requires considerable computational power [101], and therefore other methods are currently more popular.

- **Cellular Division Methods**

  The approaches in this group are biologically inspired methods of topology optimisation. In this methodology, regions with boundaries (inspired by cells

and their walls) can be divided multiple times. This process is inspired by cellular division in living organisms and the idea of survival of the fittest [103, 112]. These methods can also use genetic algorithms, but they are presented as a separate category in Figure 2.16 due to the different mathematical representation of the design domain (see Table 2.3).

As mentioned, topology optimisation commonly aims at maximising the stiffness of the structures. This can also be achieved by minimising displacement or minimising compliance for given input forces. The intuitive approach for designing a compliant element would be to maximise compliance to increase flexible displacements. This is a flawed approach. If maximum compliance is an objective, it can lead to a design that primarily contains void space. The reason is that, in the methodologies listed above, void spaces have a non-zero Young's modulus, set at very low values for numerical stability (for example: 1e-9). Therefore, design domains that are completely empty (consisting of only void) have extremely low stiffness, and solvers may still present such solutions as potential topology outcomes. Additionally, attempting to maximise compliance can result in disconnected regions where certain areas consisting of material (not void) are separated from each other by voids. This means that they are actually connected by regions of low Young's modulus (voids). Finally, by solely focusing on compliance, critical design requirements can be overlooked. For example, when designing a compliant gripper, it is essential that the gripper is sufficiently flexible to respond to the operator's input while also being rigid enough to grip and secure the target object [100]. The balance between stiffness and compliance adds complexity to the development of the objective function for compliant mechanisms. In their work, Saxena and Ananthasuresh [100] investigate various formulations of the objective function for compliant mechanisms. They divided the available formulations into two groups for which the simplified equations can be written as:

$$-f(MPE) + g(SE) \tag{2.2}$$

$$\frac{-f(MPE)}{g(SE)} \tag{2.3}$$

where g and f are monotonically increasing functions. MPE is the Mutual Potential Energy and SE is the Strain Energy. The full explanation of these variables can be found in the work of Saxena and Ananthasuresh [100]. For the purpose of this work the formulas that are crucial for understanding in the following sections are based on the problem formulation presented in Figure 2.24.

The equations for MPE and SE can be written as follows:
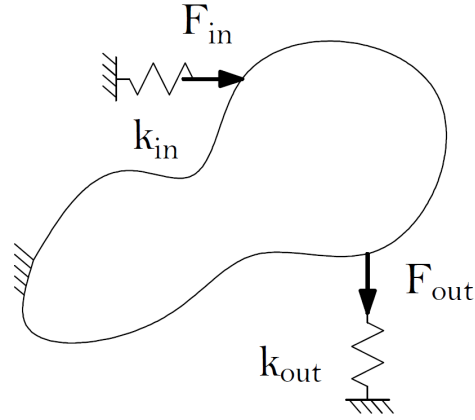
Figure 2.24: Topology optimisation design domain example with input and output forces F_{in} and F_{out}, input and output springs with stiffness constants of k_{in} and k_{out}.

$$MPE = V^T K U \tag{2.4}$$

$$SE = \frac{1}{2} U^T K U \tag{2.5}$$

The explanation of the parameters of Equations 2.4 and 2.5 is based on the schematic in Figure 2.24, which also visualises the vital parameters used in the MATLAB code that will be discussed on the next pages. When only the input force F_{in} is applied, it induces displacements with values stored in the output field U. F_{out} is a dummy unit load (with absolute value equal to 1) that is applied at the output node. The direction of the force is defined by the sign of its amplitude. When only the output dummy load is applied, the induced displacements values are stored in the field V. With the global stiffness matrix K, the relationships mentioned can be written as:

$$\begin{cases} KU = F_{in} \\ KV = F_{out} \end{cases} \tag{2.6}$$

Typically, additional boundary conditions are also applied to the output and\or input nodes of the mechanism: represented as reactive forces from springs with stiffness constants k_{in} and k_{out}. The literature offers two explanations for using an input spring together with input force. First, assume that this approach simulates a linear strain-based actuator as input [107]. The second explanation, proposed by Ansola et al. [113], states that the input spring with input force simulates the work of the actuator. The output spring simulates the resistance of the work piece: the interaction between the output node and the loading object [107, 114]. The goal of the optimisation is to maximise the work performed at the output (on the output spring). Hence, low output spring stiffness should result in a larger output

displacement, while higher spring stiffness should result in a greater force [115]. These springs are shown in Figure 2.24. The spring constants must be included in the global stiffness matrix K by adding them to the corresponding degrees of freedom. For working with models using real material properties (as opposed to Young's modulus equal to 1 set as default in most of the topology optimisation MATLAB codes), it is important to set the spring stiffness constant parameters carefully. The existing literature presents guidelines on how to do so: the recommended stiffness constant of the spring is dependent on the stiffness of the design domain fully filled with material densities equal to 1 [116].

Multiple objective functions exist to achieve the topology optimisation of compliant mechanisms. No standard problem formulation that would be agreed on as best practise exists. However, certain methods that appear to be more robust in terms of working for different case studies have received more attention than others, for example, formulations mentioned in Equations 2.2 (MPE) and 2.3 (SE). A list of existing objective functions is available in the work of Zhu et al. [101]. Alternative formulations from the literature [116] include:

- geometric advantage (GA) - defined as the displacement of the output node in the desired output direction divided by the input displacement,

- mechanical advantage (MA) - the ratio of output force to input force,

- mechanical efficiency (ME) - the result of the multiplication of GA and MA.

As already mentioned, the commercial software (e.g. Comsol, Fusion 360, Hyperworks etc.) uses the **SIMP** method to conduct topology optimisation. To better understand this approach, it is useful to look at MATLAB code that uses the SIMP approach. It was first published by Sigmund [117] as a MATLAB script for topology optimisation of rigid structures. The changes required to adapt the code to topology optimisation for compliant mechanisms are documented in the work of Bendsoe and Sigmund [107]. A shorter version of the script for static structures consists of 88 lines of code and offers greater efficiency in terms of computational resources [108]. Both codes have a similar syntax, therefore the focus here will be on the 99 code version which has been extended to work with compliant mechanisms according to the literature[107]. It shall be noted that the same changes could be applied to the 88 version of the code, extending it to work with compliant mechanism design.

The 99 and 88 lines scripts use the Solid Isotropic Material with Penalisation (SIMP) method. As shown in Figure 2.16, SIMP uses a grid representation approach of continuum topology optimisation. The elements in the design domain are non-binary - meaning the values assigned to them are fractions of the material
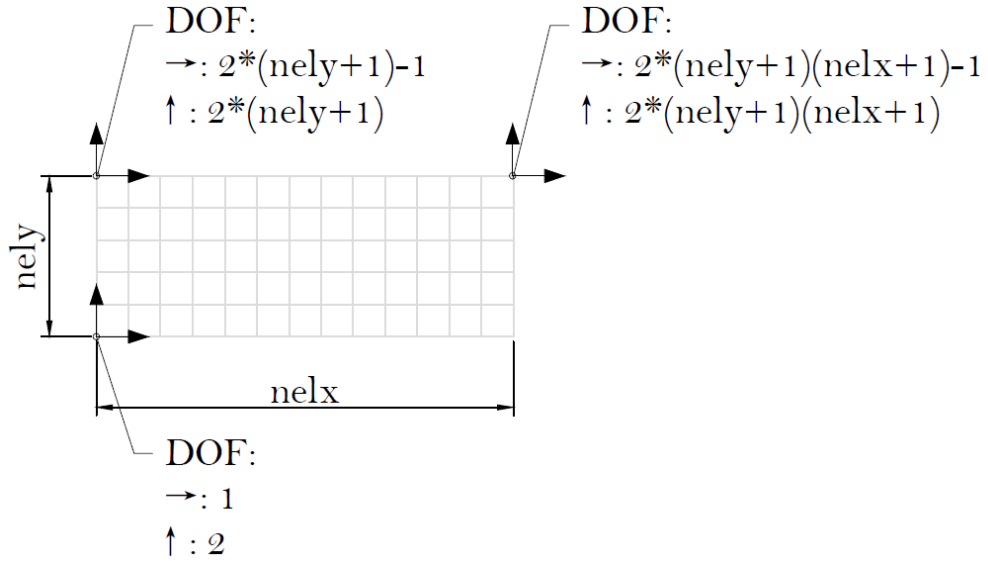
Figure 2.25: Number representation for degrees of freedom of the design domain in 99/88 lines code. *Nelx* is the number of elements in horizontal direction, *nely* is the number of elements in vertical direction.

representation of each element. To initialise the problem, a value between 0 and 1 is chosen for the desired global volume fraction. This volume fraction constrains the volume of the design domain that is to be occupied by material. At the beginning of the script, each element is initialised with the same value (the desired global volume fraction chosen by a user as a number between 0 and 1), which for the sake of an example could be 0.4, with the expected volume fraction being 40% of the volume of the design domain. For each element in the design domain, this value can also be understood as a pseudo-density value. In this work, it will be referred to as *pseudo* because it does not easily translate to an actual physical density. This problem will also be discussed in Chapter 4. In the example mentioned of a volume fraction of 0.4, the design domain would be initialised with some abstract material that has 40% of the density of the (full) material defined in the code. The numerical representation of the material properties is equal to this pseudo-density value (design variable x_e) raised to a power of the penalty multiplied by the material properties of the solid element [117] - see Equation 2.7 for Young's modulus, where *penal* is the penalty. The penalty value is responsible for driving the element densities to one of the extremes: empty (void) or full material representation.

$$E_e(x_e) = E_{min} + x_e^{penal}(E_0 - E_{min}) \qquad (2.7)$$

x_e is the pseudo-density of material in the element e ($x_e \epsilon [0, 1]$), E_0 is the stiffness of the material (with full density), E_{min} is a very low stiffness assigned to void regions [108]. At the end of the optimisation process, some grey elements may still

be present in the design domain. This raises questions about the manufacturing of solutions with varying densities. Binary (black-white) topologies are straight-forward to interpret as material-void designs. The grey areas present in the SIMP method are suggested to be possible to manufacture using composites [107].

The objective value is the displacement of the output in the desired direction, and the sensitivity analysis is written in the code presented in Equation 2.8 (the symbols have been changed compared to some literature to be consistent with previous equations). The objective function is MPE as defined in Equation 2.4. The sensitivity of each finite element (e) in the design domain (dc_e) is a derivative of the objective function with respect to the design variable:

$$dc_e = penal \cdot x_e^{(penal-1)} \cdot U'_e \cdot K_e \cdot V_e \tag{2.8}$$

where U_e is displacement of the eth finite element when input load is applied, K_e is the stiffness of eth element, and V_e is displacement of eth finite element when output unit load is applied.
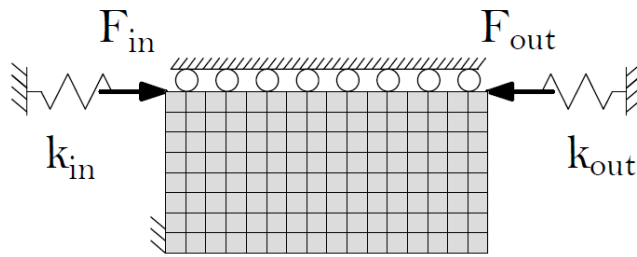
Figure 2.26: Design domain of force inverter with input and output forces and input and output springs.

To change the location of fixed degrees of freedom (DOFs) the numbering scheme visible in Figure 2.25 should be used. Odd numbers represent horizontal DOFs while even numbers represent vertical DOFs. This representation is used to define the position of fixed DOFs, as well as the input and output force and spring application points and their directions. Figure 2.26 illustrates the initial setup of the code with input and output springs, input force, and a dummy output load that has an absolute value equal to 1 and a sign representing the direction of the desired output displacement. Changes to the initial configuration of loads can be made by replacing the original lines of code (78-80) with the ones written for compliant mechanisms. This includes the additional spring constants and the output unit load. The changes to the material definition should be implemented where the Young modulus E and Poisson's ratio nu are defined in lines 88-89. The syntax of the 99 lines function for compliant mechanisms in MATLAB is the following:

topm(nelx,nely,volfrac,penal,rmin)

where *nelx* and *nely* are numbers of finite elements in the horizontal and vertical directions, *volfrac* is the desired final volume fraction, *penal* is the penalty power discussed previously, and *rmin* is the filter size that determines the radius of search to modify sensitivities. The aim of sensitivity filtering is to ensure the design's independence of a mesh size and to avoid a chequerboard pattern that could occur in the design [107]. In this method, the sensitivity of a specific element is based on a weighted average of sensitivities in a neighbourhood - in a circle with a radius of *rmin*. For *rmin* ≤ 1 the material properties are left unfiltered - the filtered properties are the same for a non-filtered design [117].

In Figure 2.27, an example is presented, demonstrating the use of a 99-line code for topology optimisation in compliant mechanisms. This illustration was developed within the context of this study, showing selected intermediate iterations of the topology optimisation process.
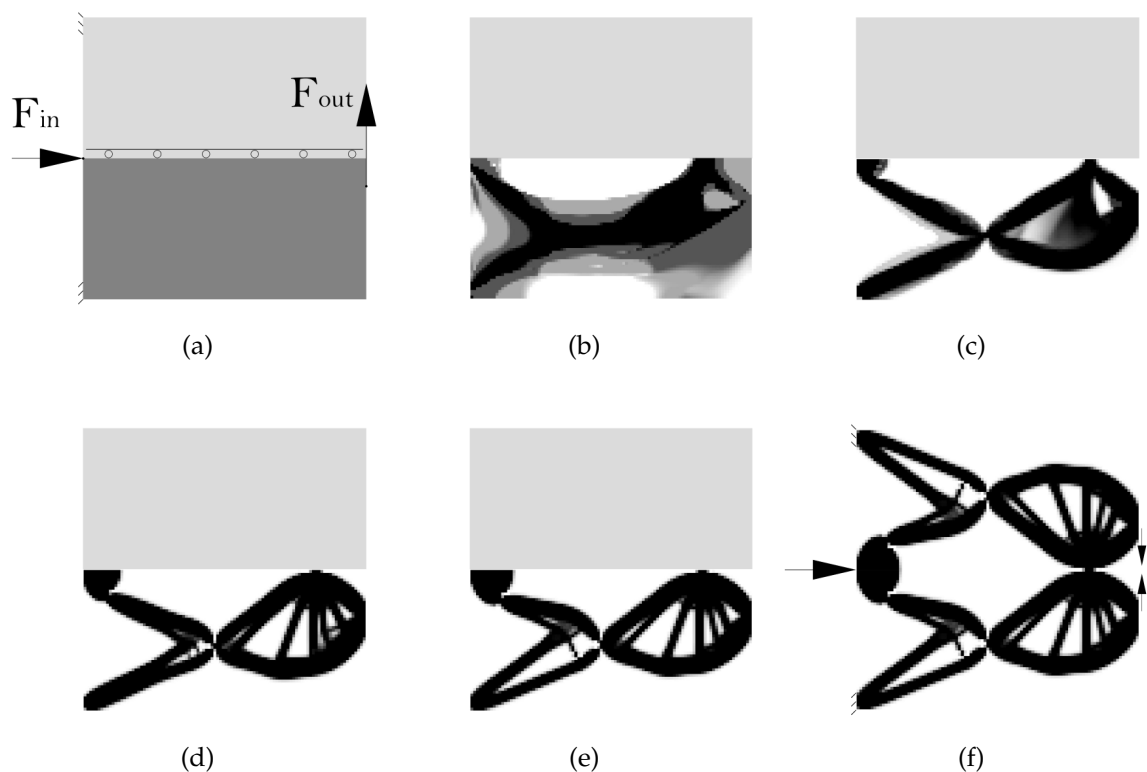
Figure 2.27: Topology optimisation of compliant gripper using 99 lines MATLAB script developed by Sigmund [117]; script adjusted to compliant mechanisms application according to Bendsoe and Sigmund [107] (a) design domain with input force (Fin) output force (Fout) and boundary conditions (fixed left corners), the bottom half is further presented in optimisation steps; (b) iteration no. 3; (c) iteration no. 10; (d) iteration no. 50; (e) iteration no. 200 - final iteration; (f) full compliant gripper design.

Design engineering has undergone significant transformations in all domains over the past century. The advent of AutoCAD in 1982 marked a turning point, as traditional drawing boards became obsolete. The 1980s and 1990s were characterised by the emergence of 3D modelling, which continues to be popular today. The most recent design methods incorporate topology optimisation and generative design. The aim of this work is to make the presented methodology more suitable for a broader commercial audience by utilising commercial software.

Topology optimisation in commercial software does not differ much from the MATLAB solution presented above. It usually also uses the SIMP method, like the code discussed above. The process requires the user to define the boundary conditions and external loads applied to the initial model. The design domain is typically initialised as being fully occupied by material, or occupied by material with pseudo-density matching the expected volume fraction. Software specifies design objectives which are physical values - e.g. deformation to be minimised for the stiffest structure. The objective function can also be a combination of parameters that are more applicable to compliant mechanisms. Typically, additional constraints are applied to volume or mass, for example, to reduce it by 50%. Once the parameters and constraints are defined, the software begins to remove and occasionally add material within the design domain. The algorithm will search for an optimum topology that, depending on the problem definition, minimises or maximises the objective function and will also satisfy the defined constraints.

Generative design is a term that is more commonly used in industrial design and architecture than in mechanical engineering. This term is broader than topology optimisation and frequently refers to optimisation inspired by nature. For example, the process in which ants build their nests in the ground can be referred to as generative design. One could say that topology optimisation is a specific way of using generative design, used in mechanical engineering. In commercial software, generative design is similar to topology optimisation. The user has to define boundary conditions, loads, constraints, and objectives. Typically, user is not required to specify the exact starting design domain. It is possible to mark areas that need to be kept full or empty, but, in general, solutions freely explore the area of applied constraints. Software has more directions to explore compared to typical topology optimisation. In addition, certain algorithms can recognise a variety of distinct solutions to the problem, presenting multiple design options.

Commercially available tools that support topology optimisation or generative design include: Altair's OptiStruct module for Hyperworks; Tosca and ATOM modules for Abaqus; Solidworks; Autodesk Inventor; Audosk Fusion 360; Solidworks; Creo; COMSOL.

This list is not conclusive, and software companies are constantly introducing new topology optimisation tools. Topology-optimisation-like tools are also entering the world of 3D printing slicers. The objective of using a slicer is to convert digital 3D models into printing instructions for 3D printers [118]. In FDM 3D printing, the models are constructed from the bottom up, beginning with the build plate at the bottom of the printer and progressing to the top. Shapes with angles that would be hard or impossible to print without extra structures linking them to the build platform can be found. These additional structures are known as supports and are usually removed mechanically after the print job is complete. Traditionally, the supports had a grid-like structure. However, new tools are emerging that offer the potential to create topology optimised, organic-looking supports. An example of such a design change is shown in Figure 2.28.

<center>(a)   (b)</center>
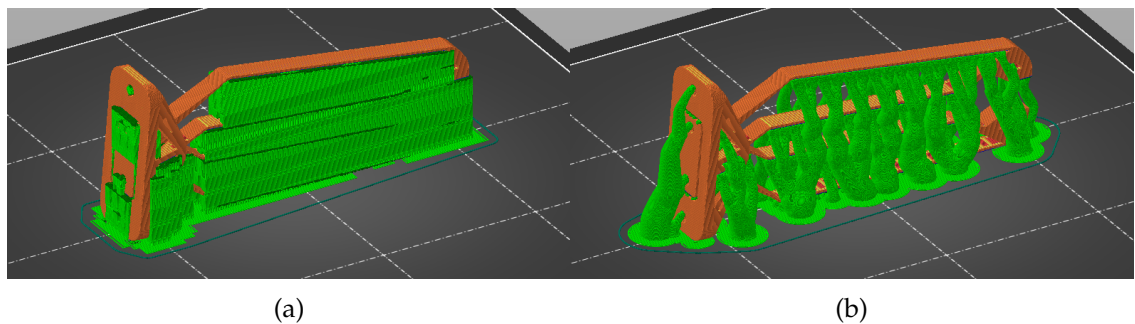
Figure 2.28: Support structures (green) for FDM 3D printing of a gripper (orange) generated in PrusaSlicer (a) typical grid support; (b) novel organic support.

To the best of the author's knowledge, the commercial design tools discussed here do not provide users with an easy way to perform topology optimisation of compliant mechanisms, as is done for static structures. Nonetheless, having a thorough understanding of the connection between stiffness and compliance can be beneficial in the process of designing an effective complaint system.

In 2022 Koppen et. al. [119] presented **a simple and versatile topology optimisation formulation**. This methodology to design compliant mechanisms works by defining two load cases - one of them to maximise stiffness in the direction opposite to desired movement (defining degree of constraint) and another one defining maximum allowable stiffness for a loading case with desirable deflection behaviour (degree of freedom). The load cases in this method are characterised by prescribed displacements rather than forces. Consequently, compliance and stiffness are directly proportional, in contrast to force-driven designs, where compliance is reciprocal (inverse) of stiffness. The mathematical demonstration of the fixed displacement versus fixed force case is presented in Equations 2.10 and 2.9, where C represents compliance, K stiffness, F force, U displacement and T is matrix operator 'transpose'. The equations presented here can also be found in the user manuals of

commercial software for topology optimisation. Example explaining the relationship between compliance and stiffness for prescribed forces and displacements can be found in Altair's user manual [120]. For prescribed force F, the displacement U is inserted into Equation 2.9 based on the Hooks's law (force is equal to stiffness times displacement [121]). In this case the compliance C is inversely proportional to stiffness K (compliance is inverse of stiffness). On the other hand, for prescribed displacement U, the force F (based on the Hooks's law) inserted into compliance equation provides opposite result (as visible in Equation 2.10). In this case the compliance C is proportional to stiffness K. These displacement- and force-driven design differences are further investigated in [122, 123] where both optimisation setups are explored in detail.

$$C = \tfrac{1}{2} \underbrace{U^T}_{U = \frac{F}{K}} F = \tfrac{1}{2} \frac{F^T F}{K^T} = \tfrac{1}{2} \frac{F^2}{K} \tag{2.9}$$

$$C = \tfrac{1}{2} U^T \underbrace{F}_{F = KU} = \tfrac{1}{2} U^T K U = \tfrac{1}{2} U^2 K \tag{2.10}$$

Although the mentioned paper of Koppen et. al. [119] and his displacement-driven methodology for optimisation focuses on the design of compliant hinges, this method can be adapted to design compliant mechanisms such as grippers, force inverters, etc. Here, a simple and versatile topology optimisation formulation will be explained using the example of a force inverter, which is one of the most common examples of compliant mechanisms in the literature. Figure 2.29 presents the design domain of the mechanism in two loading cases. It is important to point out that the mechanism in this simulation is displacement driven and not force driven. As discussed above, it has an impact on the compliance-stiffness relationship; in this case, they are proportional. As presented in Figure 2.29, the first load case includes the input displacement representing the actuation of the mechanism and the output displacement pointed in the direction of the desired output motion (DOF). The second load case consists of the same input displacement, but the output displacement is pointed in opposite directions (DOC) compared to the desired output movement (and load case 1). The absolute values of displacement in this case are equal to one. It is also possible to increase or decrease the numbers to target a specific geometric advantage (GA) - for example, to achieve GA = 2, the output displacement in the first loading case should have double the value of input displacement.

The next step is the definition of the optimisation objectives and constraints. They are presented in Table 2.4. To meet the required design criteria, the mech-

(a) Load case 1   (b) Load case 2
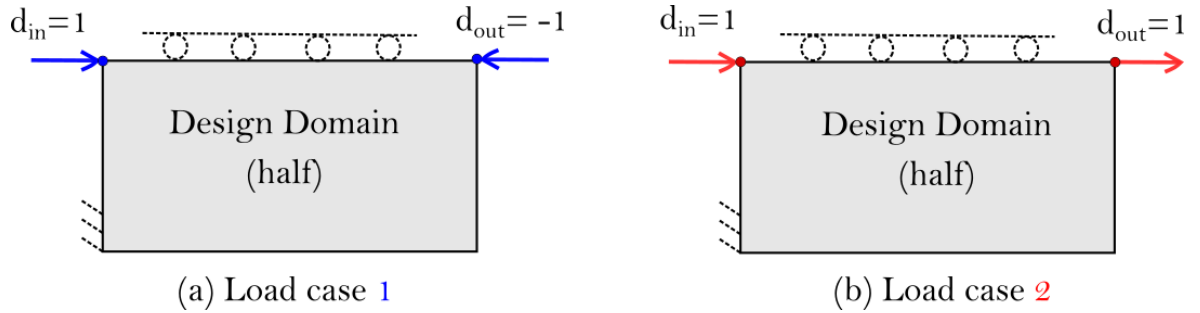
Figure 2.29: Design domain and boundary conditions presented for two load cases of compliant force inverter.

Table 2.4: Summary of objective and constraints applied to the modelled load cases.

	Load case	
	1	2
Objective	-	maximise strain energy
Constraints	strain energy $<=$ upper bound	-
	volume fraction $<=$ upper bound	

anism must possess sufficient compliance to allow the displacement specified in load case 1, while also exhibiting adequate stiffness in other directions (as outlined in load case 2). As such, the objective of the optimisation process is to maximise the stiffness of load case 2. As this is a displacement-driven design, the stiffness is proportional to compliance and strain energy. So in this case, depending on the objectives types available in the software, the user can choose to maximise compliance, stiffness, or strain energy - they all should result in the same outcome. Furthermore, there are two optimisation constraints that need to be defined. The first is based on load case 1. In this case, it is desired to have a design with enough flexibility, and therefore a constraint (upper bound) on the stiffness should be applied. It means that the stiffness of the mechanism for load case 1 shall be lower than the limit defined in this constraint.

The appropriate upper bound for stiffness in the first load case depends on the material, and users should experiment with different values to determine which produces the optimal results. If the value is excessively large, the mechanism may resemble a static structure, incapable of significant deformation. Conversely, if the value is too low, the optimisation may face convergence issues or generate outcomes with highly localised flexure hinges (point hinges) or significant proportion of intermediate densities in the final design. The last constraint presented in table 2.4 is intended to provide the maximum volume fraction of the design. This con-

straint applies to the entire design domain and is not related to any particular load case. Additional constraints are, of course, possible depending on the problem formulation. In Chapter 5 additional stress constraint will also be discussed.

Element Density

| 1.00 | 0.89 | 0.78 | 0.67 | 0.56 | 0.45 | 0.34 | 0.23 | 0.12 | 0.01 |

| i:0 | i:3 | i:6 | i:9 |
| i:12 | i:20 | i:26 | i:42 |
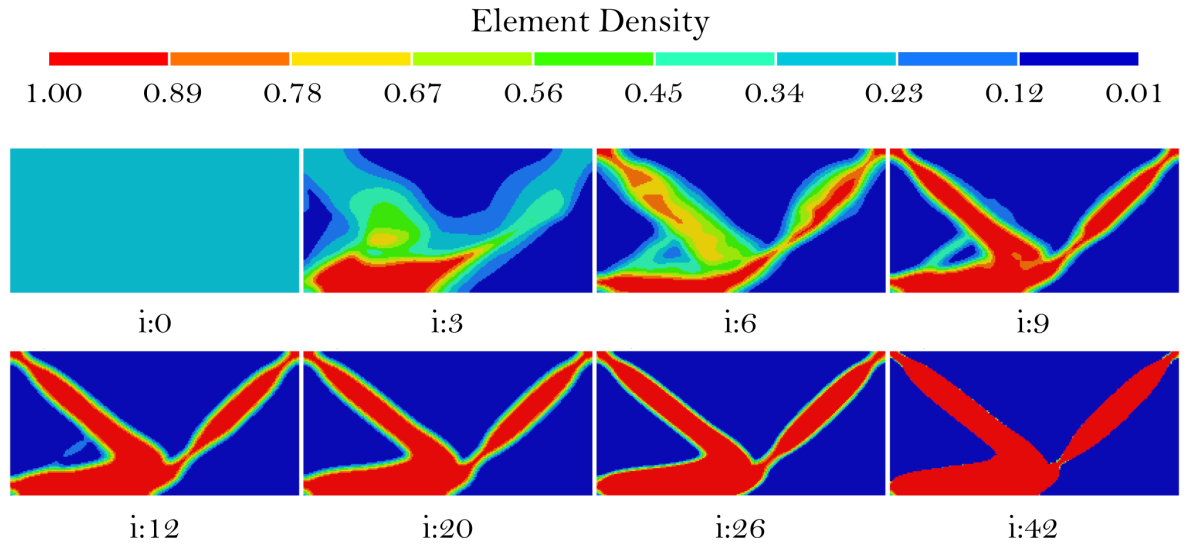
Figure 2.30: Evolution of topology optimisation design process of compliant force inverter; *i* - iteration number.

Figure 2.30 presents the selected iterations of a compliant inverter topology optimisation process with the application of the methodology discussed. It has been obtained using commercial software HyperWorks and using a simple and versatile topology optimisation formulation discussed above. The result is the force inverter mechanism shown in Figure 2.31.
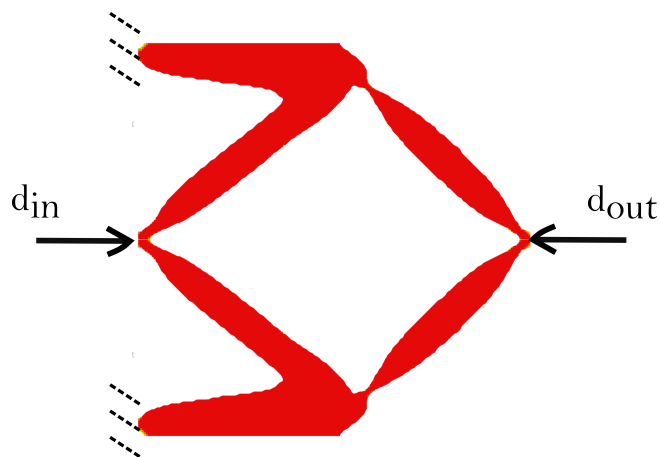
Figure 2.31: Final compliant inverter design; dashed lines represented boundary condition - fixed edges.

CHAPTER 3

DESIGN CONSIDERATIONS FOR LUNAR COMPLIANT GRIPPER

This project aims to showcase compliant mechanisms as an implicit dust mitigation solution to reduce the jamming of the mechanisms induced by lunar dust. There are multiple design and manufacturing considerations to take into account when designing compliant mechanisms. In addition, in this project, there are also considerations concerning space environment and more specifically (and also more restrictive) lunar surface environment. All considerations and requirements were divided into the sections presented below: Kinematic behaviour, Materials, and Manufacturing.

The work presented here focuses on designing, manufacturing and testing a gripper that could be used in Lunar equipment. To narrow down the considerations and focus on a specific mechanism example that could be updated with the usage of compliant mechanisms, the Apollo geological tool, namely Tongs, was selected. Picture 3.1 presents replica of Tongs that was used by the European Space Agency in multiple simulated lunar missions that were mentioned in Chapter 1.

Figure 3.1: The training replica of Apollo Tongs photographed in ESA EAC [14].

Table 3.1 shows all sampling tools used in the Apollo programme and indicates in which surface mission they were used. As visible, Tongs and Hammer were the only geological tools that were used in all of the surface missions, and both

contributed to the collection of interesting lunar samples. Tongs were utilised to grasp rock samples of sizes up to 10 cm [124]. The Apollo spacesuits were quite stiff and did not provide enough dexterity for astronauts to simply kneel down and pick up rocks with their hands. As visible in Figure 3.2 Tongs were used to pick up rocks without the need to kneel down or bend. The drawing showing the movement of the handle and jaws is presented in Figure 3.3. In the next sections, Tongs will be described in more detail to drive design considerations for their compliant mechanism possible successor.

Table 3.1: Geological sampling tools used in Apollo surface missions [124, 125], A tick symbol indicates which tools were employed in each mission.

Tool	Apollo surface mission					
	11	12	14	15	16	17
Contingency sampler	✓	✓	✓	✓		
Tongs	✓	✓	✓	✓	✓	✓
Large scoop	✓	✓				
Adjustable scoop		✓	✓	✓	✓	✓
Adjustable trenching tool		✓	✓	✓	✓	✓
Hammer	✓	✓	✓	✓	✓	✓
2-cm drive tubes	✓	✓	✓			
4-cm drive tubes				✓	✓	✓
Drill				✓	✓	✓
Rake				✓	✓	✓
Surface samplers					✓	

3.1 KINEMATIC BEHAVIOUR

The kinematic behaviour of the grippers developed during this project is intended to resemble that of Apollo Tongs, mentioned in the previous section. The Tongs mechanism is spring-loaded, with the astronaut opening the jaws by pulling a T-bar handle (which expands the spring) and closing them by releasing the same handle (which comes back to the original position with a pull from a spring). In its default position, the jaws remain closed, as depicted in Figure 3.3. The position

(a) (b)
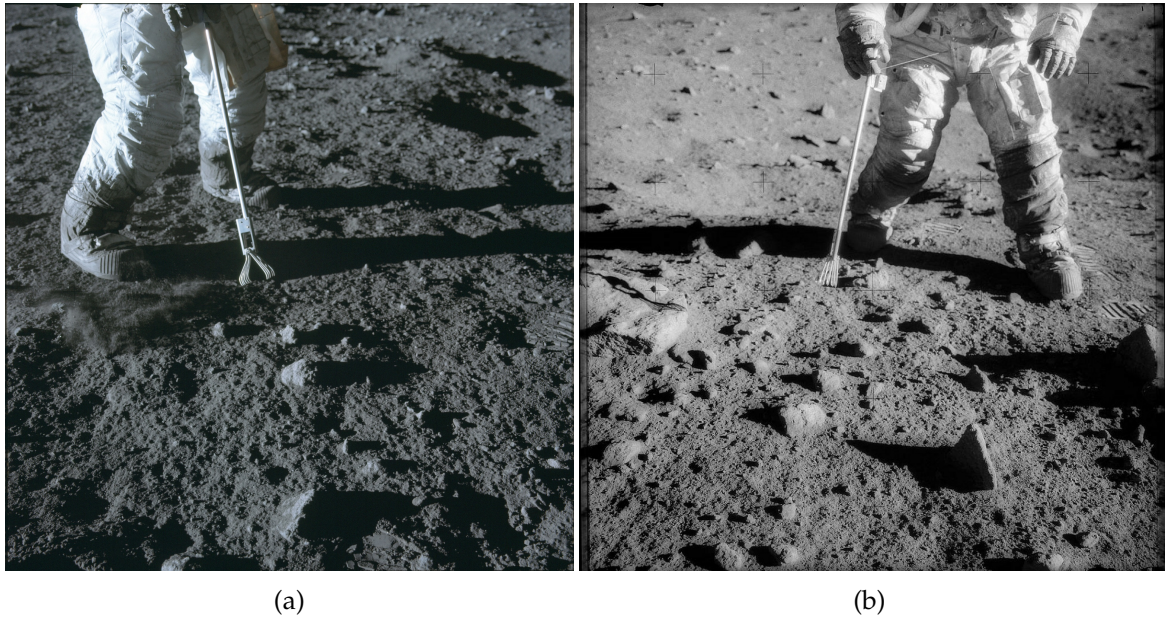
Figure 3.2: Tongs used by astronaut Charles Conrad Jr. during the Apollo 12 mission [126, 127].
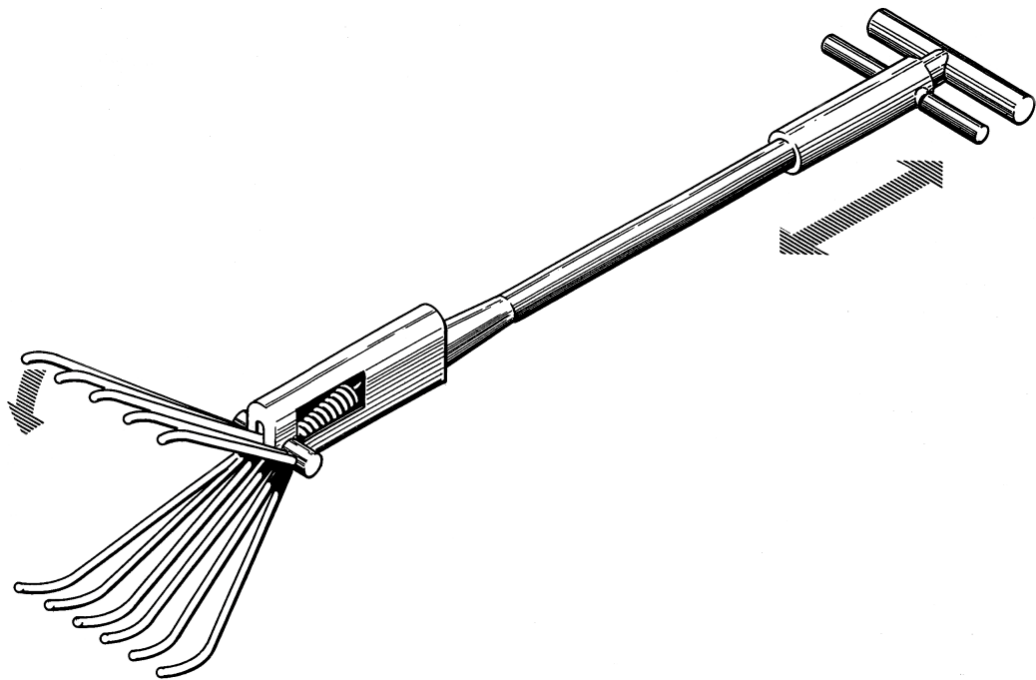
Figure 3.3: Drawing of Apollo Tongs; movement of T-handle and jaws marked with arrows; courtesy of NASA [128].

of the output, that is, the jaws, is directly determined by the position of the input, that is, the handle. As such, this design is a displacement driven mechanism. The new compliant design can have similar functionality while exploring some new design approaches. As compliant mechanisms store elastic energy when deformed,

spring loading is not necessary for their operation, and spring can be avoided in the new design. However, achieving large displacements may be more challenging for compliant mechanisms than for rigid-body mechanisms of comparable size. Nevertheless, in this case, the motion range can be extended using the deformation range working in both directions from the default position. As a result, the default position of the gripper is assumed to be semi-open to extend its range of motion, and in such design, the gripper can close, and it can also open further (beyond the default position). Elastic deformation can be used to support two directions: opening and closing. This principle is demonstrated in Figure 3.4. Figure (a) presents the gripper in its original shape. As visible in (b), the input of the pulling force to the input widens the distance between the gripper jaws, thereby opening it further. Picture (c) shows the behaviour of the gripper with the pushing force supplied to the input, and in this configuration the gripper is closing. As such, the direction of input determines the direction of output (closing versus opening).

As already mentioned, complaint gripper stores elastic energy which matches the function of a spring in the original Tongs design. The linear spring was keeping the Tongs closed and the astronaut could compress it by pulling on a handle (this action is marked with arrows in Figure 3.3). Unfortunately a detailed data concerning the design of Tongs cannot be obtained and as such the stiffness value of the spring is not know, making it impossible to be matched by the stiffness of compliant grippers developed in this work.
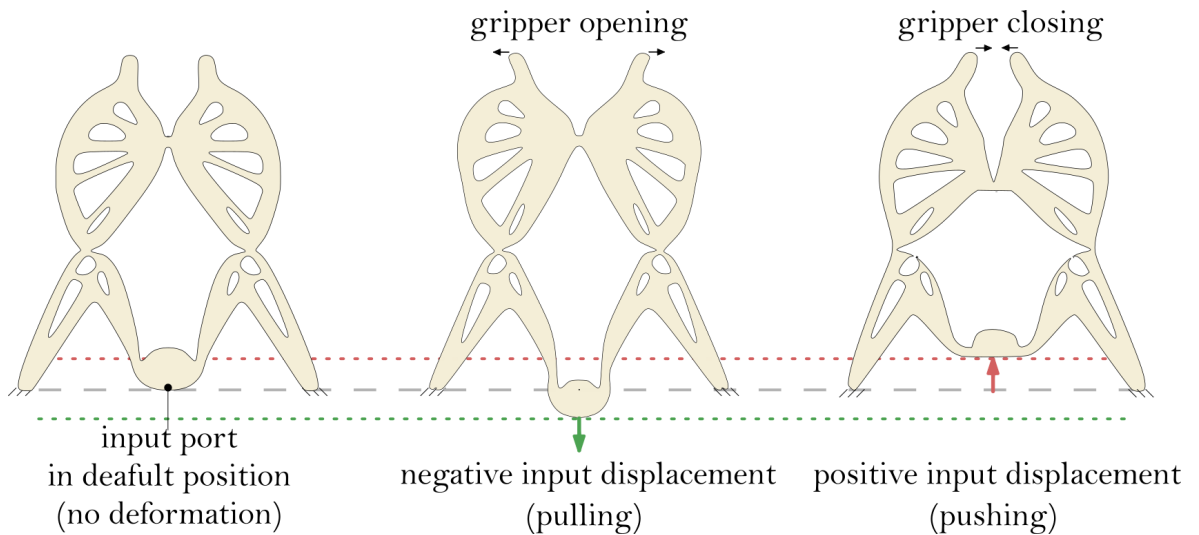
Figure 3.4: Expected kinematic behaviour of complaint gripper. From left to right: default gripper position, pulling on the input port - opening the gripper, pushing on the input port - closing the gripper.

Another aspect to be considered in the design is the vector of output displacement. The opening and closing action should be achieved by means of the horizontal displacement of the jaws in the coordinate system of the Figure 3.4. An

additional vertical movement of the jaws is acceptable, but it should be taken into account that the higher the ratio of vertical movement to horizontal movement, the lower the efficiency of the mechanisms in terms of transferring the input displacement into the desired output displacement.

Compliant mechanisms are easily scalable. To aid the manufacturing and testing processes that will be further discussed in this and the next chapters, it was decided to focus on grippers smaller than Tongs. As mentioned above, the Tongs were able to grasp samples up to 10 cm. In this work, the objective was set to focus on developing grippers capable of grasping elements up to 4 cm. However, it is important to note that the designs presented in Chapter 4 and Chapter 5 can be scaled up or down if necessary.

Another aspect is the thickness of the gripper, which was also not matched with the size of Tongs. Complaint grippers with a thickness of 8 mm (all presented in next sections) were created in this work, creating planar designs. The aim of the study was to find a compliant gripper with kinematic behaviour fulfilling the above mentioned assumptions but it is important to note that for the user experience purposes and sampling performance a further optimisation of gripper jaws and appropriate thickness selection (or stacking of multiple thinner elements) would have to be considered for the compliant gripper to fully replace the Tongs.

3.2 MATERIALS

When designing compliant mechanisms, material selection is crucial and should be considered in conjunction with the design methodology. This will also be demonstrated in the Chapter 4 where different combinations of materials and design methods were tested. As was already discussed in Chapter 2, material change is one of the methods used to adjust the stiffness of a system. As such, material selection has an impact on the kinematic characteristic of a given compliant topology. Compliant mechanisms use elastic deformation to undergo the desired motion. Elastic deformation refers to the reversible deformation of a material under applied stress, where the material returns to its original shape once the stress is removed. At the atomic level, the elastic strain appears as slight variations in the distance between atoms and the expansion of bonds between them, and therefore the modulus of elasticity (Young's modulus) is a measure of resistance to the separation of neighbouring atoms [129]. As different groups of materials (polymers, metals, and ceramics) have different atomic bonds, their Young's modulus values differ as well. On a macro-scale Young's modulus is a measure of a material's stiffness and its ability to resist elastic deformation [129]. It is defined as the ratio of stress to strain in the linear region of the stress-strain curve. Materials with a high

Young's modulus require a larger force to produce a given deformation as compared with materials characterised by low Young's modulus. This is a critical point for compliant mechanisms, which usually require a specific output displacement that will depend on the deformation of the material.

Another crucial parameter from the stress-strain curve is the yield strength. Yield strength is a stress level at which plastic (permanent) deformation can be observed [26]. After that stress is achieved, some of the deformation (plastic deformation) will remain even after the load is removed. When designing compliant mechanisms, the stress values should stay below yield strength and, especially for precision compliant mechanisms, the lower the stress as compared to the yield, the better precision and repeatability are possible. As an example, Flex-16, which is a compliant flexure already mentioned in Chapter 2, was designed not to exceed 40% of the yield strength of the material it was made of. Chapters 4 and 5 of this work will present examples of complaint mechanisms with different maximum stress levels. It will be demonstrated that minimising the stress much below the yield strength is crucial to achieve satisfactory precision.

Howell [50] shared an excellent summary of how the material characteristics mentioned here should be understood in the context of compliant mechanisms. He explains that the amount of deflection that a given loading will produce is related to the structure's stiffness. As discussed earlier, the measure of material stiffness is Young's modulus. Yield strength, on the other hand, is a measure of the maximum stress that a material can withstand before plastic deformation occurs. Plastic deformation is not desirable in compliant mechanisms and can often be considered a failure mode. Therefore, a good material candidate for compliant mechanisms should have a high yield strength to withstand higher stress and a low Young's modulus to provide a wide range of flexible deformation. In another work by Howell [10] he proposes to look at the relationship between yield strength and Young's modulus, with a higher value being more desirable. This characteristic of the material was also described as more desirable for compliant components by Peng and Snyder [130].

However, it is also important to mention that other material parameters such as the melting temperature or fatigue behaviour should be taken into account when designing for a specific environment and application. Maximum service temperature that takes into account creep, decomposition, changes in chemical structure, oxidisation for different group of materials can be found in the literature [131]. This is an indication of maximum temperature materials can withstand to sustain their structural integrity. In the case of complaint mechanisms another challenge is caused by the fact that Young's modulus changes with the temperature [132],

which may result in mechanisms needing different amount of energy to be actuated in different temperature condition. For this reason, it should be recommended to start the design of complaint mechanism for space with a selection of the material suitable for the environment (including the temperature range) and then move to the topology synthesis with the mechanical properties of the selected material.

Metals have predictable material properties (desired for precision mechanisms), can perform in high-temperature environments, have low susceptibility to creep, a reliable fatigue life, and the ability to operate in many harsh environments. On the other hand, they also have lower strength to Young's modulus ratio compared to most polymers, their density is quite high (which can result in higher mass of a system), and their machining is rather costly [50]. They are quite often a preferred choice for the compliant mechanisms in space (as visible in the examples in Section 2.4), mainly due to their predictable properties, which make it possible to use them for very precise space applications lasting over a long time.

Brittle materials, such as ceramics, can also be used in compliant mechanisms, but are less forgiving when over-stressed [50]. Brittle materials experience very little to no plastic deformation before fracture occurs [132]. Flexures made of brittle materials can be flexible, but when stress is excessive, they fail catastrophically [50]. Although, in principle, they can find applications for compliant mechanisms, ceramics are not considered for the big deflection mechanisms discussed in this work.

Polymers have a high strength to Young's modulus ratio, low manufacturing costs, and low density, but their variability in mechanical properties makes them less predictable in some cases. They also have quite low melting temperatures, and can undergo creep and stress relaxation [50]. It is also important to note that many polymers emit gases in space (outgasing), although a large group of novel polymers are capable of surviving exposure to open space [133, 134]. Polymers are often used in consumer products that feature compliant mechanisms, such as lids for food containers, pegs, etc. With the development of new polymers designed for vacuum applications, they are indeed interesting candidates for compliant mechanisms, especially those that do not have strict precision requirements (such as geological tools).

In this work, the focus was placed on the evaluation of polymers that can be used in additive manufacturing. The low cost and ease of manufacturing were considerable factors in prototyping, as well as in the production of a more refined compliant gripper design, which will be presented in Chapters 4 and 5. Three materials were used in line with this project: Thermoplastic Co-Polyesters (TPC), Polylactic Acid (PLA), and Polyetheretherketone (PEEK). Their material properties

are presented in Table 3.2 based on available manufacturer data sheets and the literature [135–143]. The exact values vary between different publications and different filament manufacturers. The Poisson ratio of TPC was approximated based on data from material with similar mechanical properties, namely TPU [144] due to the inaccessibility of the information for TPC. As visible in the Table 3.2 PLA and PEEK are considerably stiffer than TPC, which is an elastomer. The parameters presented here were used in topology optimisation so they ultimately affect the final designs. More details of these selected materials are provided in the next paragraphs.

As previously stated, the ratio of yield strength to Young's modulus is a reliable parameter for assessing a material's fitness to support the function of compliant mechanisms. When this ratio is presented on a material property chart, it can serve as a valuable tool for material selection. Such material property charts were introduced by Ashby and can be found in the literature [131]. Figure 3.5 depicts such a graph, which was created to highlight differences among selected groups of materials, including elastomers, polymers, ceramics, metals, and composites. As previously mentioned, the yield strength to Young's modulus ratio is an indication of the suitability of a material for use in compliant mechanisms (although for some applications other parameters can be of high importance). The higher yield strength to Young's modulus the ratio, the more likely it is that the material can be considerably deformed and remain in its elastic range. The dashed sloping lines in Figure 3.5 present various ratio values, which increase toward the upper left corner of the figure. TPU, PLA, and PEEK were also highlighted in red on the graph with data from Table 3.2. As shown in the figure, polymers and elastomers generally have yield strengths to Young's modulus ratios higher than those of metals (which are often used in compliant mechanisms in space hardware). Therefore, polymers and elastomers are excellent candidates for compliant mechanisms in terms of mechanical behaviour. The popularity of metals in complaint space applications stems from multiple reasons. One of them is high melting temperature (for titanium and stainless steel and order of magnitude higher that the TPC, PLA and PEEK temperatures presented in Table 3.2. Nonetheless it is important to note that not all mechanisms used in space require such hight range of operations ad therefore non-metalic materials could find use for complaint mechanisms in space. Another advantageous aspect of metals is their low susceptibility to creep, which, as already mentioned, makes them suitable for compliant mechanisms that require a high degree of precision over a large number of cycles, especially in thermal cycling conditions. Nevertheless, in this study, precision is not a major constraint, and the availability of polymers and elastomers for 3D printing (including in space, as discussed in the following paragraphs) outweighs the challenges associated with

their use. Below, a short description of TPC, PLA, and PEEK will be presented, highlighting their advantages and the reasons why they were selected for this work.

Table 3.2: Selected properties of PTC, PLA and PEEK.

Property	Material		
	TPC	PLA	PEEK
Young's modulus E [GPa]	0.029	3	3.72
Yield strength σ_y [MPa]	8	60	100
σ_y/E [Pa/Pa]	0.276	0.017	0.026
Melting temperature [°C]	158	160	343
Glass transition [°C]	-35	65	143
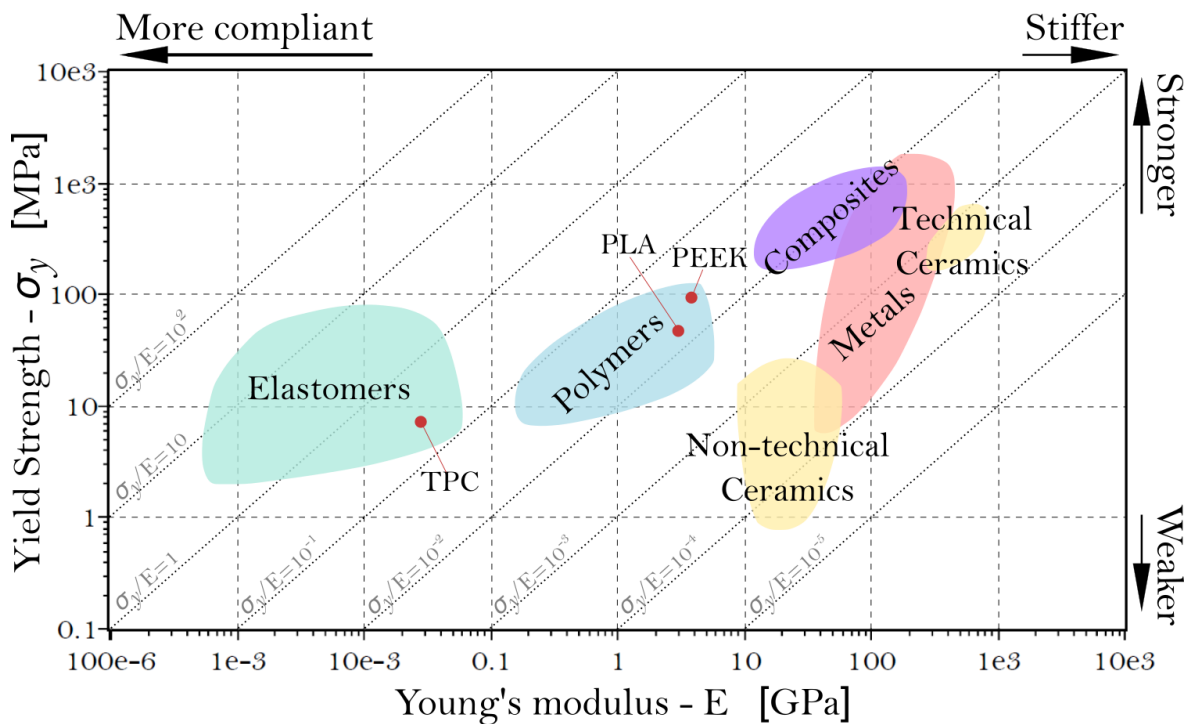
Figure 3.5: Material properties chart with Young's modulus and Yield strength - TPC, PLA and PEEK marked in red. Created in Ansys Granta Selector with additional text added in Inkscape.

TPC, which stands for Thermoplastic Copolyester, is a type of thermoplastic elastomer that is produced through the polycondensation reaction of long-chain ester or ether diols with chain extenders [145]. The length of long-chain diol can be adjusted to achieve a wide range of properties [145]. TPC has several advantages as a material, including good heat resistance, thermal ageing stability, low temper-

ature flexibility and elasticity, as well as good chemical resistance [145]. TPC is available as an FDM 3D printing material. It is quite popular for applications that require large elastic deformations - as visible in Table 3.2 TPC has quite low glass transition temperature which makes it very flexible at room temperature and is a good choice for compliant mechanism prototyping. In this study, TPC was chosen as a fast prototyping analogue of a rubber-like material that operated on the Moon during the Apollo programme; it was fluorosilicone that was used in rock box seals [124].

PLA, or polylactic acid, is a semi-crystalline biodegradable thermoplastic polymer derived from renewable resources such as corn starch or sugar cane [146]. PLA is a versatile material that can be processed using various techniques such as injection moulding, extrusion, and also 3D printing. Additionally, PLA is one of the most popular materials for 3D printing. It has a relatively low melting point, which makes it easy to extrude through the printer's nozzle, and it has the ability to produce high-quality, detailed prints with a quite smooth surface finish. The limitation of PLA usage is usually its strength and durability, particularly for high-stress applications. In this project PLA was chosen for its compatibility with additive manufacturing techniques, in addition, there are ongoing efforts in various research groups to develop composite materials using PLA and lunar regolith particles [147, 148], which adds to the interest of using PLA for in-space manufacturing.

PEEK, or polyether ether ketone, is a high-performance polymer known for its exceptional strength and thermal properties. It has a high strength-to-weight ratio, comparable to stainless steel, and can withstand thermal cycling in vacuum chambers (used for space-qualification tests), radiation, or wear [143, 149]. It is commonly used in the space industry to produce components, as well as in the aerospace industry for out-of-cabin components [143]. PEEK is also known for its abrasion-resistant and radiation-resistant properties, making it suitable for mechanical parts in harsh environments [143]. PEEK can exist in either an amorphous or semi-crystalline phase, with amorphous PEEK having no long-range order in polymer chains and no specific melting temperature. Instead, it has a glass transition temperature at which it transitions from its glassy state to that of rubber. On the contrary, crystalline polymers have a specific melting temperature and their mechanical behaviour remains mostly constant before this temperature is reached [150]. Achieving high-dimensional accuracy is possible with 3D printing in the amorphous phase, but annealing to semi-crystalline phase may be necessary after printing. For PEEK use in space annealing is advisable as the temperature range for most space missions could potentially anneal the material during the mission.

A study by Regis et al. [151] presents the temperature range of PEEK annealing up to 300 °C. Such a temperature can be reached in some space hardware, especially when facing the Sun or being exposed to propulsion environment. Undoubtedly, the annealing process induces changes in the mechanical properties of PEEK, which are highlighted in the test results presented in this study (Chapter 5). PEEK is also compatible with the Additive Manufacturing Facility (AMF) on board the ISS and is being considered for in-space or off-Earth manufacturing by multiple entities [150]. Compared to TPC and PLA, PEEK has a much higher melting temperature (data presented in Figure 3.2), which could potentially make it much more useful for a wider range of space missions, compared to other polymers.

Another material and design-related consideration for the use of compliant mechanisms in space is the response to vibrations. The intense vibrations experienced during launch, generated by the powerful thrust of launch vehicles, can subject the spacecraft and its components and cargo, including compliant mechanisms, to significant mechanical stress. Ensuring that compliant mechanisms can effectively mitigate and absorb these vibrations is crucial to preventing structural damage, maintaining precise functionality, and safeguarding the overall success of the mission. Careful design, material selection, and testing are essential to optimise the damping properties of compliant mechanisms, allowing them to counteract the detrimental effects of launcher vibrations and maintain their intended performance throughout the space mission. There are many ways to design to mitigate the impact of structural vibrations, and in the case of compliant mechanisms, a lock device might need to be used during the launch. Nonetheless, it is also important to examine the characteristics of the material to understand the impact of the selection of the material on the response to vibrations. The work of Ashby [131] presents a range of material properties that can be compared for different groups of materials. In that work, one of the material characteristics presented is the loss coefficient η of groups of materials. The loss coefficient is a parameter that quantifies the damping or energy dissipation characteristics of a material when it undergoes mechanical vibrations or oscillations [152]. In the context of vibrations, damping refers to the ability of a material to dissipate or absorb energy as it vibrates, which reduces the amplitude and duration of the vibration over time. Higher values of the loss coefficient indicate higher damping properties, meaning that the material can absorb and dissipate more energy during vibrations. From the Ashby charts [131], the rough ranges of η are: for metals 0.000015 - 0.15, for polymers 0.015 - 0.3, and for elastomers 0.3 - 3. The higher the loss coefficient, the better the material will perform in energy dissipation. On the basis of this measure and for compliant mechanisms and flexure production, metals seem to be a worse choice than polymers and elas-

tomers from the point of view of launch vibrations. This further justifies that the use of polymers and elastomers for compliant mechanisms in space can be highly favourable.

3.3 MANUFACTURING

Manufacturing is a crucial aspect of the development of compliant mechanisms. It is important to understand the advantages and limitations of the manufacturing methods available to ensure satisfactory results. The list below presents the most popular manufacturing methods for macro-scale compliant mechanisms:

- **Electric Discharge Machining (EDM)**

  EDM is a process that uses a series of electrical sparks to erode the material from the workpiece [153]. EDM is best suited for materials that are electrically conductive. It is quite slow and expensive, but offers an accuracy up to a few microns and a sub-micrometre surface finish. It is also a good choice for delicate features (such as thin flexures), as there is no direct contact between the work piece and a tool.

- **Waterjet cutting**

  This is a versatile cutting process that uses a high-speed stream of water mixed with abrasive particles to cut through a wide variety of materials [154]. It is a quite fast process with accuracy up to tenths of millimetres, but it produces a draft angle (tapper) that might be a problem for thicker elements. Due to this fact, it limits the thickness that can be processed. It is also useful to note that the radius of the jet is usually bigger than 1 mm, and therefore it is hard to produce sharp angles or small openings if they are needed.

- **Laser cutting**

  This method is a thermal cutting method that uses a high-power laser beam to locally melt and separate material, with the help of an assist gas to remove molten material [155]. This process is capable of cutting a wide variety of materials, including metals, ceramics, and composites, without considering their hardness or electrical conductivity. It is a very fast process, providing an accuracy of around tens of microns. The possible radius in the corners can reach tens of micrometres.

- **Milling**

  Milling is a material removal process that uses a rotating cutting tool to re- move material from a workpiece by advancing the tool into it in a certain

direction and angle [156]. It is a versatile machining process that can produce a wide range of complex shapes and features with high precision and accuracy while processing a wide range of materials. It uses high forces and direct contact with the element, so it can be hard to use with delicate thin features. It can also cause surface damage and can change the surface properties as compared to the material properties deeper in the material.

- **Additive manufacturing (AM)**

  AM, with the most popular type: 3D printing, is a process of building three-dimensional objects by adding material layer by layer from a digital design file [157]. The materials used in this process can range from polymers and metals to ceramics and composites. The flexibility of the process allows the creation of complex geometries, including those with internal features and varying wall thicknesses, that are difficult or impossible to achieve using traditional manufacturing methods. More complex shapes may require supports, which lead to the need for post-processing to remove them. The microstucture of the 3D printed sample is often inferior compared to the bulk material, and 3D printed components can have pores or gaps [158].

As space missions extend beyond low Earth orbit, current resupply methods may not adequately account for the likelihood of component failure or the uncertainty of which specific component may fail. It may not be feasible to have spare parts for every piece of equipment taken to the Moon. To address this challenge, an effective solution could involve incorporating repair and fabrication techniques directly into the mission or eventually making them available on the lunar surface. This could enable on-demand capabilities to respond to unforeseen circumstances. Among all the manufacturing methodologies listed above, 3D printing might be the most flexible solution. As mentioned above, this manufacturing method can be used for a wide range of materials (although it uses different technologies to accommodate them). It is also very agile, which makes it a popular choice for fast prototyping and it is user-friendly. In fact, the 3D community of users who have 3D printers at home is constantly growing, while other advanced technologies that can allow the production of complicated shapes are rather reserved for professional workshops. Furthermore, other manufacturing technologies mentioned above involve removing excess material to obtain the final product, which results in the generation of waste material. This waste material would contribute to the overall mass budget of a space mission if the manufacturing is carried out in space. On the contrary, additive manufacturing adds material layer by layer to produce the desired object, resulting in minimal waste generation (although support structures

may be necessary). For all these reasons, 3D printing was selected as the preferred manufacturing methodology in this work. It is also in line with the need to explore the usage of polymers in space, which was discussed in Section 3.2.

It is also worth mentioning that 3D printing has already entered the space industry. Commercial company SpaceX started using 3D printed liquid oxygen valves in 2014 in the engines of the Falcon 9 rocket [150]. Other companies are following the lead, and the number of 3D printed space components is constantly growing. When it comes to 3D printing in space, the experience is quite limited, and as of today, only Fused Deposition Modelling (FDM) has been used so far. It was part of an experiment on the ISS done in Additive Manufacturing Facility (AMF), where Acrylonitrile Butadiene Styrene (ABS) was used to build mechanical property test articles, printer performance capability items and functional tools [159]. In January 2024 ESA delivered a metal 3D printer to ISS [160]. This device uses wire-based laser metal deposition and is expected to be operational in the upcoming months. The current literature makes a strong case for using 3D printing as part of an in-space manufacturing initiative [161]. Ishfaq et al. [162] provide an example of a human spaceflight incident that was life-threatening and could potentially have been solved easier and faster if the crew had access to a 3D printer. In their paper, they describe an incident that occurred during Apollo 13, when the Command Module encountered a failure while on its way to the Moon. The problem that the crew had to solve (after a hardware failure) was that the lithium hydroxide canisters for the command module did not fit the sockets of the lunar module. On the ground, personnel found a way to build an adapter to solve this problem with the resources available to astronauts. In 2013, the engineering staff of Made In Space, Inc. designed a component to solve the same problem and manufactured the adapter using a 3D printer [162]. In the future, access to tools that can help react quickly in the event of damage might be crucial, as humanity will hopefully travel further away from Earth.

The aforementioned FDM technology uses a thermoplastic filament as the printing material. In FDM, the filament is heated to its melting point and then extruded through a nozzle in a controlled manner to build up the desired shape layer by layer [163]. FDM is a widely used 3D printing technique due to its low cost, simplicity, versatility, and, as already mentioned, it is the only technology that has been used for in-space manufacturing so far. These advantages are the reasons why FDM technology was selected to be used in the line of this project as the main manufacturing methodology. Although the compliant mechanisms designed in the line of this work could also be manufactured using different methods, 3D printing offers enormous flexibility when it comes to topologies and shapes that it can produce. It

is a method that can enable novel design technologies like topology optimisation, and incorporating these novel technologies to make compliant mechanisms even easier to design and manufacture is one of the aims of this work. Furthermore, 3D printing can be used with a wide variety of thermoplastics, some of which will be discussed in the next section.

CHAPTER 4

INITIAL DESIGN AND TESTING: PLA AND TPC GRIPPERS

In this chapter, various designs of compliant grippers will be presented. Although some designs were less efficient than others, they are still included here to demonstrate the impact of material and design methodology selection on the final product and its performance. Figure 4.1 shows the concept of primary kinematics that was the basis for the designs presented here. It is clear that the primary motion is the closing action and further sections will show that it is still possible to open the gripper beyond the default position.
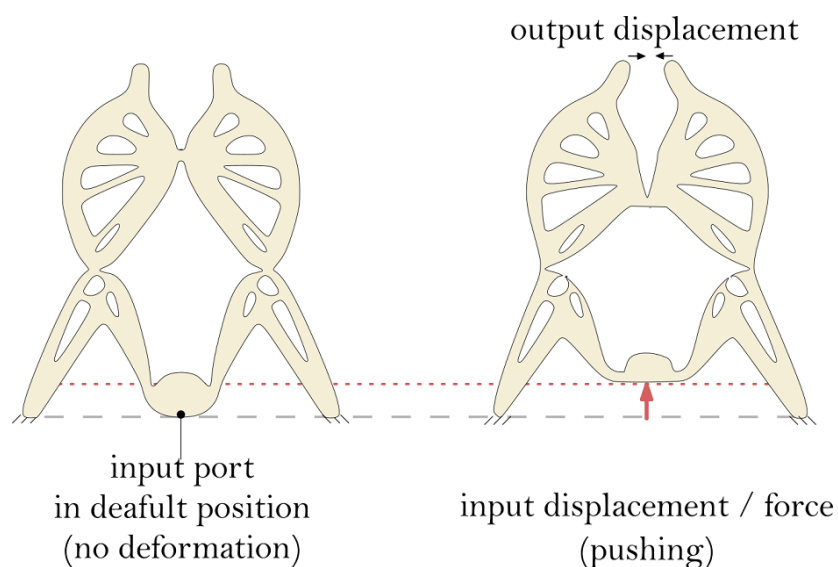
Figure 4.1: Functionality of complaint gripper: on the left before loading, on the right after loading the jaws are closed.

The 3D printed grippers presented in this section were synthesised using two different design methodologies: topology optimisation and instant centre approach,

which is an analytical design method. Example results demonstrating the usage of these two methods are illustrated in Figure 4.2, which also shows how the design domain is divided into two halves to simplify and accelerate the design process and focuses on only one half. Both design methods presented were discussed in the literature review: topology optimisation in Section 2.5.2 and instant centre approach in Section 2.5.1. In this chapter, their application to the compliant gripper problem will be further discussed.
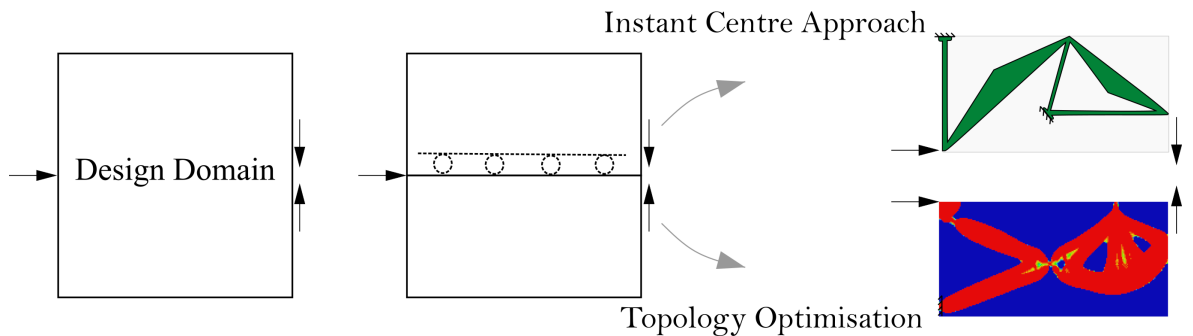
Figure 4.2: Representation of two different design approaches undertaken in this work: Instant Centre Approach and Topology Optimisation.

4.1 ANALYTICAL DESIGN METHODOLOGY FOR COMPLIANT GRIPPERS

In this section, an analytical design method will be demonstrated. It is the instant centre approach that was used to produce compliant grippers discussed in this chapter.
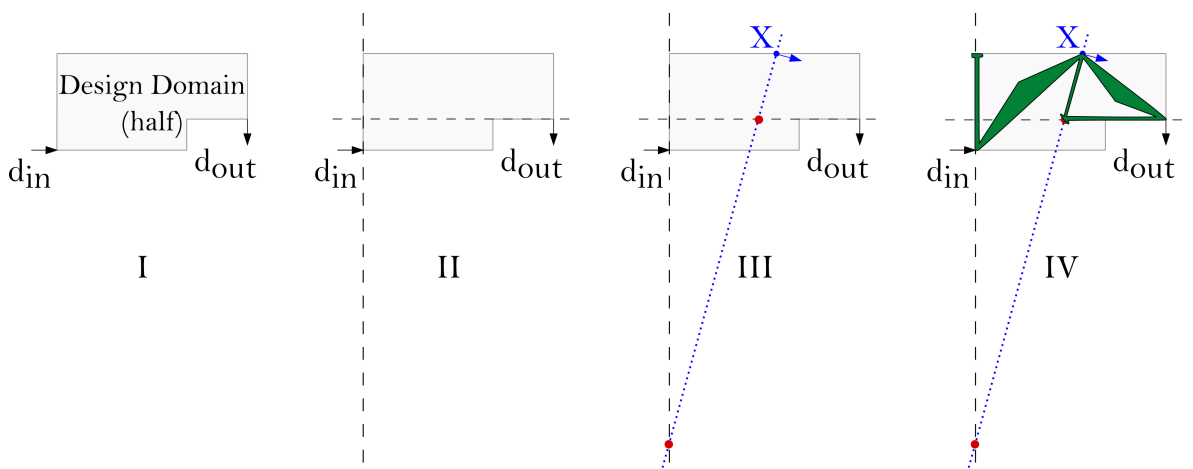
Figure 4.3: Design steps of the instant centre approach for a compliant gripper design.

As the instant centre approach can be employed for various materials without the need of including the material parameters in the design steps, a single design was synthesised and manufactured with two materials: PLA and TPC. Both grippers will be presented in this chapter. The design steps are presented in Figure 4.3, and the final gripper topology is also outlined in Figure 4.4.
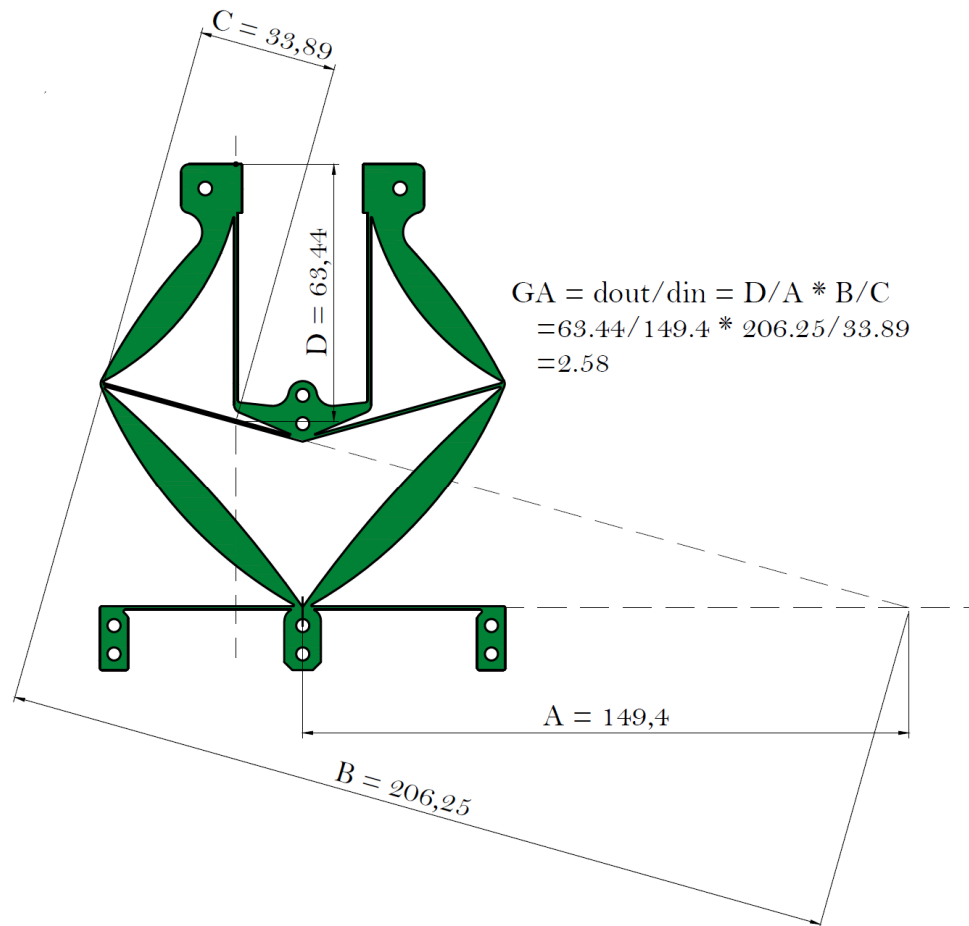
Figure 4.4: PLA compliant gripper model; green - final design, black - measurements and calculations needed to determine expected Geometric Advantage (units: mm).

The initial design step, shown in Figure 4.3, involves defining the design domain, including the input and output nodes with their intended motion directions. In the second step, dashed lines are added perpendicular to the expected input and output displacements. Then a new point is selected, with an arrow indicating its direction of movement, marked in blue in the Figure 4.3. The selection of this point is not bound by any rigid guidelines, but here the intention is to select a point near the outer perimeter of the design domain to maximise the length of flexures that will be created later. This selected point necessitates a dotted line perpendicular to the direction of movement (blue dotted line), which intersects the previous dashed lines to create two additional points (marked in red). These points serve as the

centres of rotation of the design's building blocks. Finally, the geometry is filled with design elements, as seen in green in the final step, where the triangles indicate stiff elements and the long, thin green elements correspond to flexures.

As shown in Figure 4.3, this method requires the addition of an extra fixed point to make the flexure attachment in the middle of the design stationary (fixed). This additional attachment will not be present in the topology optimised grippers. To achieve a full design, various gripper elements need to be modelled on top of this topology, namely jaws, fixture elements (with holes for bolts), and the input element. The design that includes all the parts mentioned is visible in Figure 4.4.

A significant benefit of this design method is that the geometry is quite simple, allowing the geometric advantage (GA) to be analytically determined. GA is the ratio of output displacement to input displacement and can be determined using the distances of the moving point and the rotation points, as discussed in Section 2.5.1. This is presented in Figure 4.4 for the analytically designed gripper. 3D printed prototypes of this gripper can be found in Figure 4.5.
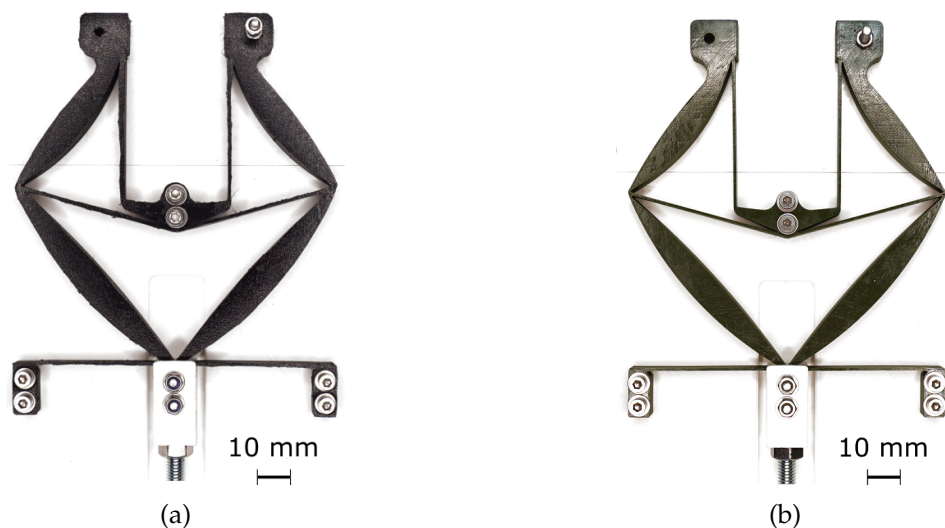
Figure 4.5: Analytically designed compliant grippers, 3D printed: (a) with TPC, (b) with PLA.

4.2 TOPOLOGY OPTIMISATION METHODOLOGY FOR COMPLIANT GRIPPERS

The purpose of this project was to find a way to use commercial software to develop compliant mechanisms using topology optimisation. Usually, commercial software topology optimisation is designed to support mainly the optimisation of static structures by maximising the stiffness or minimising displacements. However, in 2022 Koppen [119] presented a methodology to design compliant mecha-

nisms by defining two loading cases, one of them to maximise stiffness in the direction opposite to desired movement (defining degree of constraint), and another one defining maximum stiffness (or compliance) for a loading case with desirable deflection behaviour (degree of freedom). The load cases are defined using prescribed displacements rather than forces, which is the reason why compliance and stiffness are equivalent, as opposed to force-driven designs where compliance is the inverse of stiffness. This method was described in more detail in 2.5.2. Although the mentioned paper by Koppen [119] focuses on the design of compliant hinges with small strains, this method can be adapted to design compliant mechanisms such as grippers, force inverters, etc. The design presented in this work utilised this methodology in the commercial software HyperWorks.

In this section, grippers obtained by using topology optimisation will be presented. The design domain (half of the gripper for symmetry) is presented in Figure 4.6. The prescribed unit displacements for input and output are visible along with their values and directions.

(a) Load case 1 (b) Load case 2
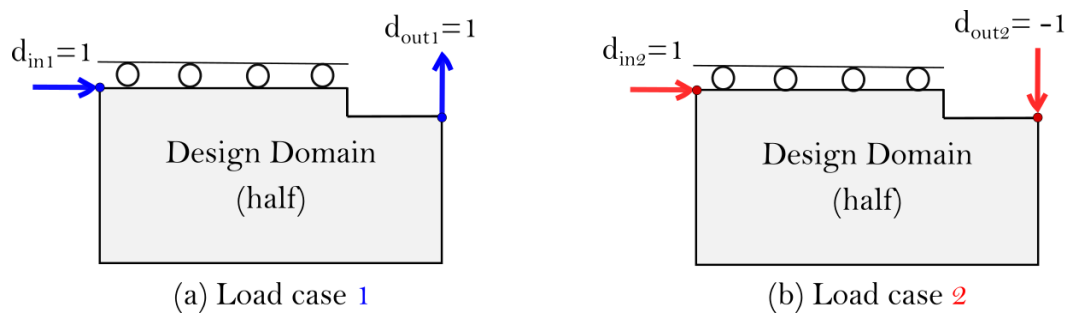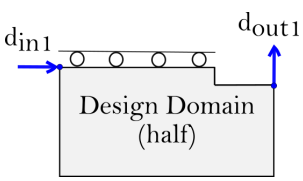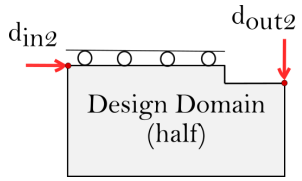
Figure 4.6: Load cases and the design domain of compliant gripper for topology optimisation. This figure was also presented in [14].

The first gripper discussed here was designed using the material characteristics of Thermoplastic Co-Polyesters (TPC). In Table 4.1, the design parameters for both load cases can be found. The expected volume fraction was chosen to be 40% of the volume of the design domain. The input force is placed at the top left corner of the design domain, while the anticipated output point is expected to be located at the right edge of the domain, as clearly depicted in the figures within the Table 4.1. For boundary conditions, the bottom left corner of the design domain remains fixed, and the top edge has certain degrees of freedom restricted to simulate half of the design domain. Consequently, the complete design will encompass a mirrored version of the topology obtained, providing a complete gripper topology.

The parameters used in the topology optimisation process, as detailed in Table 4.1, played a crucial role in guiding the evolutionary progression of the design. In the specific example at hand, the design process starts with a material density equivalent to 0.4 of TPC material, aligned with the predetermined volume con-

Table 4.1: Topology optimisation design parameters for TPC gripper.

	Load case	
	I	II
	d_{in1} … d_{out1} Design Domain (half)	d_{in2} … d_{out2} Design Domain (half)
Input (d_{in}) [mm]	+ 1	+ 1
Output (d_{out}) [mm]	+ 1	- 1
Objective	-	maximise compliance
Constraints	compliance $\leq$ 0.1 Nmm	-
	volume fraction $\leq$ 0.4	
Max. iteration no.	100	
TPC Young's modulus [MPa]	29	
TPC Poisson's ratio	0.48	

straint of 40%. This density will also be referred to as pseudo-density in the further discussions to highlight the fact that it does not have a physical representation outside of the CAD model.

The design evolution is depicted in Figure 4.7, which encapsulates the design transformation of a 50-iteration topology optimisation simulation.

Figure 4.7: Topology optimisation, TPC compliant gripper evolution of density presented with colour map; *i* - iteration number.

Although the maximum iteration limit for this simulation was initially set at 100, the software's convergence criterion was met after only 50 iterations, leading

to the termination of the simulation. The convergence criterion in HyperWorks, by default, relies on assessing the relative change in the objective function. If the relative change falls below 0.5% between two successive design iterations, the optimisation process is stopped.

During this iterative process, specific elements within the design domain experience a significant reduction in density, transitioning to a blue hue. At the same time, other elements shift towards red, signifying a density of 1. The final iteration results in a topology that incorporates intermediate densities, with values below 0.75 being filtered out to refine the design.

Intermediate densities (or as mentioned pseudo-densities) deserve a short discussion to explain why it is not attempted to provide their physical representation in the final design. The software employed uses the SIMP method, which stands for Solid Isotropic Material with Penalisation. This method was already introduced in Section 2.5.2. In this approach, a pseudo-density variable is employed as a design parameter. The pseudo-density value can assume any value greater than zero but not exceeding one. The value of one is equivalent to the physical density of the material used in the design and elements with pseudo-density of one also have stiffness of that design material. The voids are represented by low but non-zero pseudo-density (as discussed in Section 2.5.2) and a low stiffness. The method employs power penalisation to transform elements into one of the desired states, either void (approaching zero pseudo-density) or solid (approaching full pseudo-density, which is one). The stiffness of each element within the design domain is a product of the penalised pseudo-density and the stiffness of the design material. Additional information on the methodology can be found in the following references [14, 107, 108, 117].

In the context of manufacturing, pseudo-densities lack a direct physical representation. In other words, elements with a pseudo-density below one should have mechanical properties that scale down with the value of pseudo-density, as already discussed in Section 2.5.2. This means that the areas with lower pseudo-densities should be represented by material with lower density but also Young's modulus (and stiffness) that follows the, already discussed, Equation 2.7 (also presented in Section 2.5.2. However, in reality, when 3D printing with lower infill or using porous material, this requirement is not met because stiffness and Young's modulus do not change with the (real) density the same way that the Young's modulus changes with pseudo-density in SIMP model.

During the final iteration of the topology optimisation presented in Figure 4.7, intermediate pseudo-densities are present. Because it is infeasible to accurately manufacture intermediate densities, a binary approach has been adopted.

Pseudo-densities below 0.75 have been filtered out and substituted with voids, while pseudo-densities equal to or greater than 0.75 have been replaced with full-density TPC. The selection of the threshold value is typically at the discretion of the designer to strike a balance between ensuring that all parts of the design are interconnected (as setting the threshold too high may lead to disconnected components) and preserving the compliance of the flexures (as setting the threshold too low may add excess material to the flexures, increasing their stiffness).

To enhance the overall functionality of the gripper presented, additional components were introduced, which included fixed points and gripper claws. This refined design is visually represented in Figure 4.8a. Finally, the tangible manifestation of this design, in the form of a 3D printed prototype, is presented in Figure 4.8b, which illustrates the culmination of the optimisation process.

(a) Final design of TPC optimised compliant gripper.

(b) Optimised compliant gripper 3D printed with TPC [14].
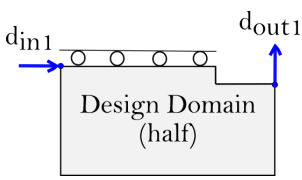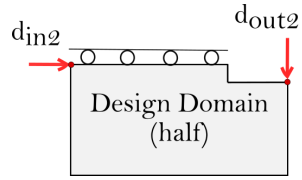
Figure 4.8: TPC optimised compliant gripper.

Using the same methodology, a gripper constructed from Polylactic Acid (PLA) was subjected to the topology optimisation process.

Table 4.2 comprehensively presents the boundary conditions, the objective of the optimisation, and the constraints that were employed throughout this process. To provide a visualisation of the development of the design, a sequence of intermediate topologies has been documented and is shown in Figure 4.9. These depictions provide valuable insight into the progressive evolution of the design as it underwent the topology optimisation procedure.

Upon observing the final iteration portrayed in Figure 4.9, it becomes evident that certain intermediate densities (pseudo-densities) persist within the design. To ensure a seamless material connection between the input, output, and fixed corner, it was necessary to consider a minimum pseudo-density threshold lower than that of the TPC-optimised example. The resulting design, depicted in Figure 4.11a, was

Table 4.2: Topology optimisation design parameters for PLA gripper.

	Load case	
	I	II
Input (d_{in}) [mm]	+ 1	+ 1
Output (d_{out}) [mm]	+ 1	- 1
Objective	-	maximise compliance
Constraints	compliance $\leq$ 0.1 Nmm	-
	volume fraction $\leq$ 0.4	
Max. iteration no.	100	
PLA Young's modulus [MPa]	3000	
PLA Poisson's ratio	0.33	

Element Density

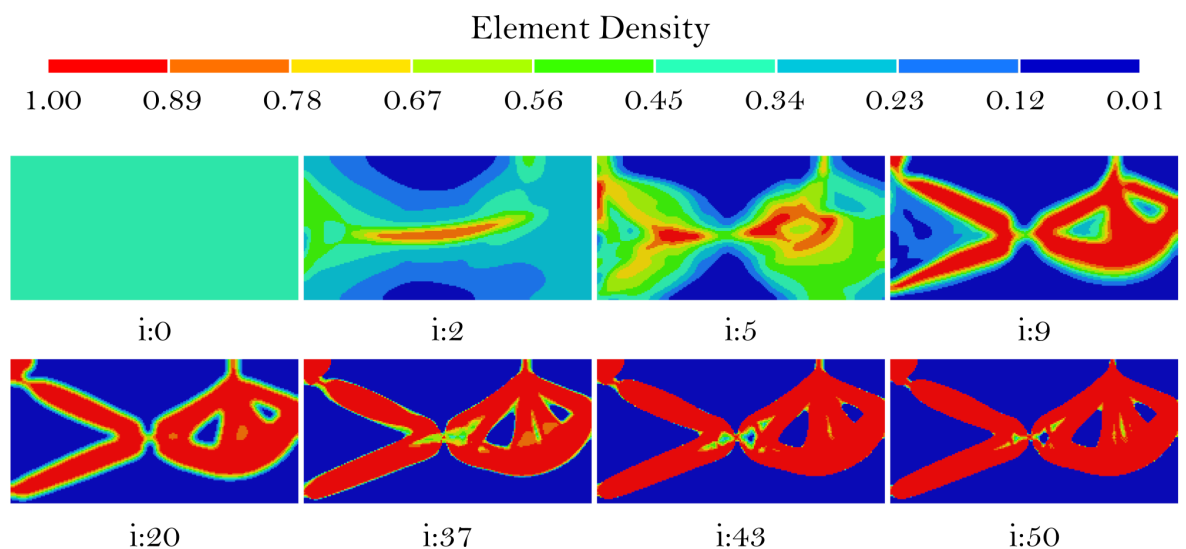| 1.00 | 0.89 | 0.78 | 0.67 | 0.56 | 0.45 | 0.34 | 0.23 | 0.12 | 0.01 |
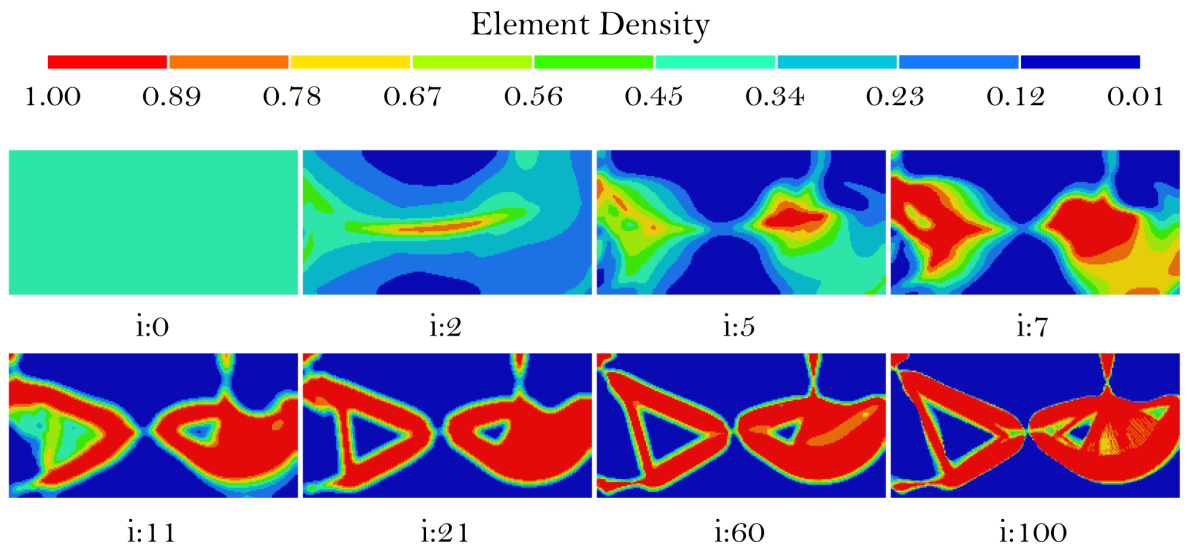
Figure 4.9: Topology optimisation, PLA compliant gripper evolution of density presented with colour map; *i* - iteration number.

obtained by retaining elements with densities equal to or greater than 0.35.

As compared to the TPC example presented before the densities threshold is significantly lower (0.35 as compared to 0.75). The threshold was selected to ensure suitable design. Figure 4.10a showcases the areas of the obtained topology that pose a challenge. As visible these areas (marked with white dashed circles) have lower densities (pseudo-densities). Figure 4.10b shows what can happen when the

threshold is set to high: the gripper is not characterised by continuous material and therefore it would not be able to provide the expected kinematic function. As such a suitably low threshold needs to be found to ensure material continuity. In this case, the resulting number is, as already discussed, 0.35.
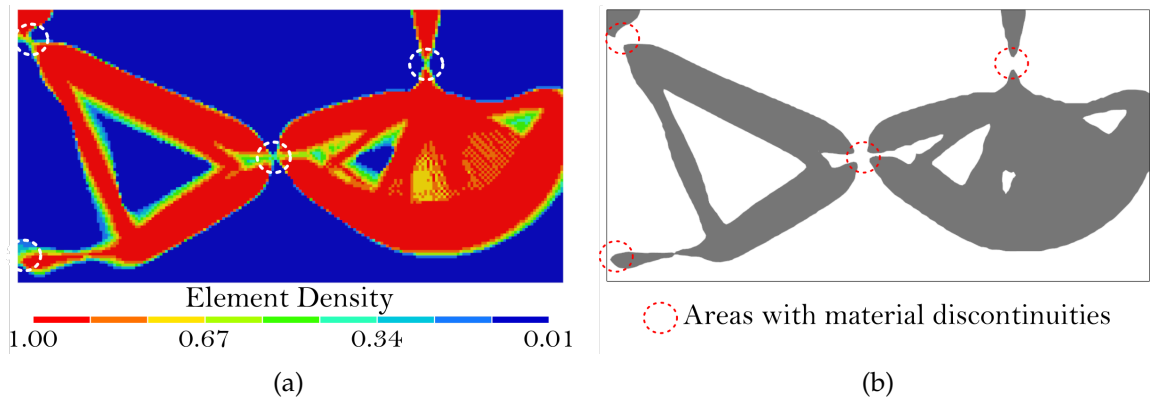
Figure 4.10: Density threshold selection for topology optimised PLA design; a) density map with problematic low density areas marked by white dashed circles; b) example topology achieved by setting the density threshold too high (at 0.75) - with discontinuities marked by red dashed circles.

(a) Final design of optimised PLA compliant gripper.

(b) Optimised compliant gripper 3D printed with PLA.
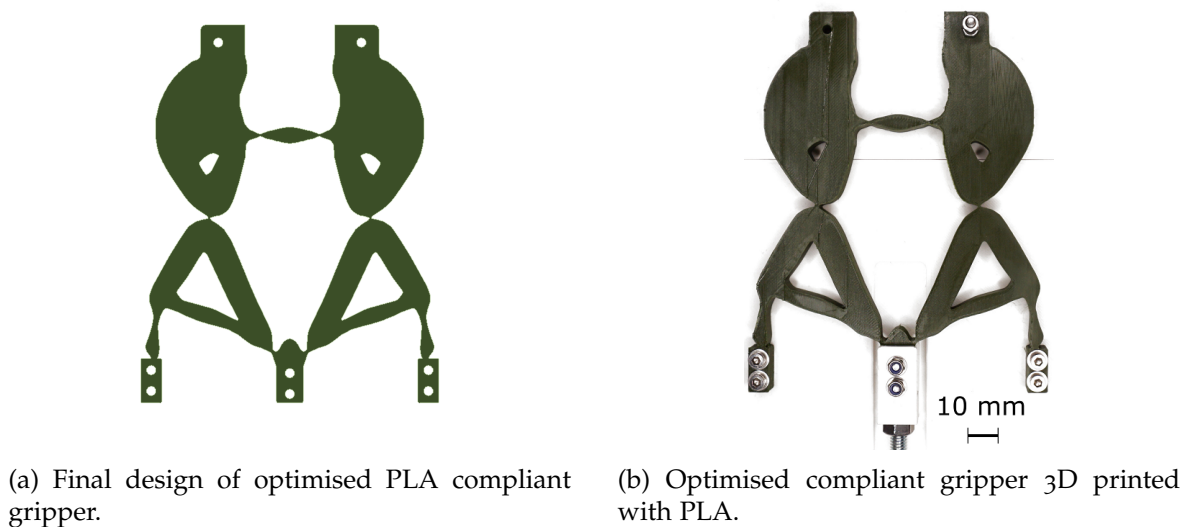
Figure 4.11: PLA compliant gripper.

Adjustment of the pseudo-density threshold implies that the PLA-fabricated gripper is expected to possess greater rigidity compared to its TPC counterpart, which managed to retain only elements with densities exceeding 0.75. The 3D printed representation of the PLA gripper is shown in Figure 4.11b, providing a tangible representation of the optimised design in PLA material.

4.3 TESTING: METHODOLOGY

All grippers discussed in Sections 4.1 and 4.2 were tested to determine their Geometric Advantage (GA), Mechanical Advantage (MA) and relationship between forces and displacements of the system. Three tests, presented in Figure 4.12, have been conducted. The details of the output measurements and the inputs supplied are provided in Table 4.3.
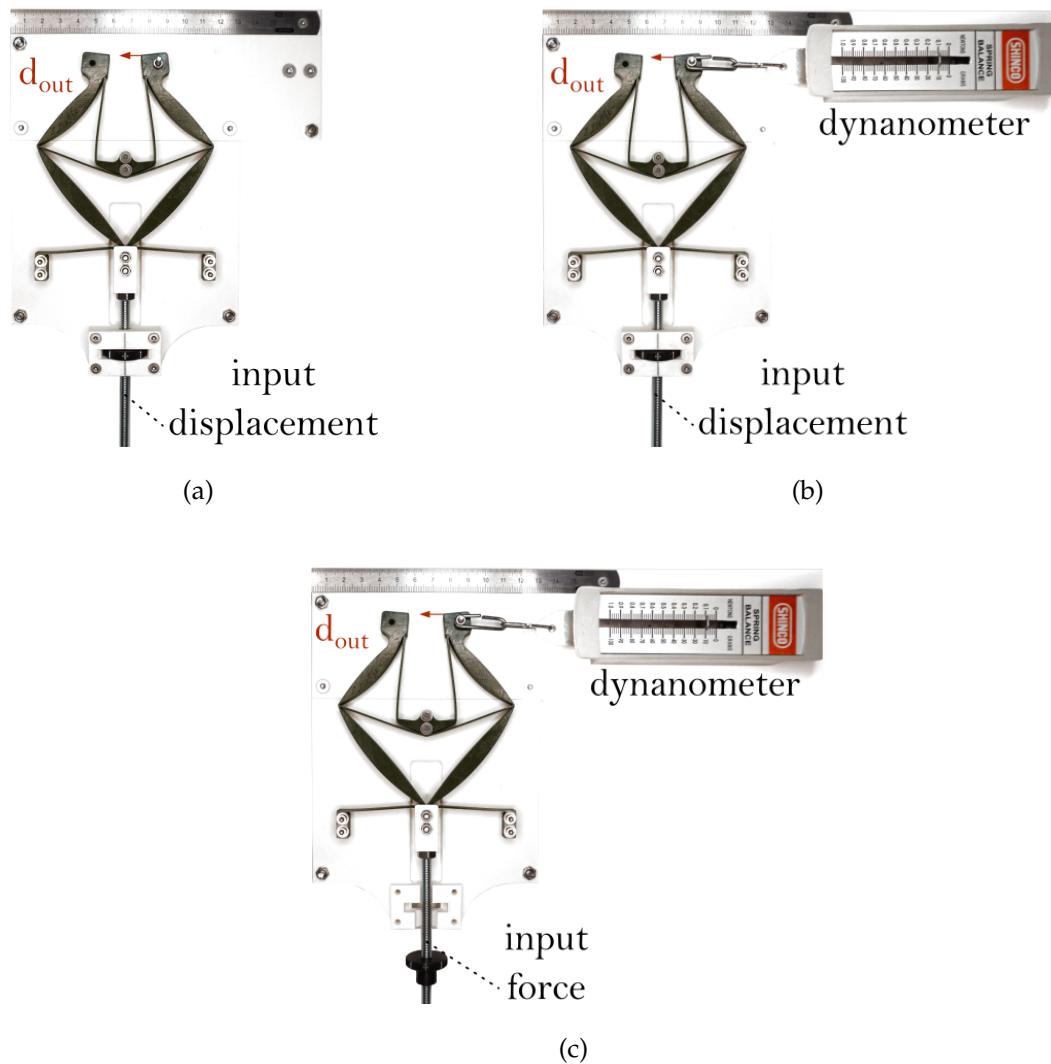
Figure 4.12: Test rig in all tests configurations; red arrow shows the point on the gripper and the direction of output displacement measurements; (a) Test 1, (b) Test 2, (c) Test 3.

The objectives outlined in this chapter revolved around the prototyping process and the acquisition of valuable information for the subsequent series of prototypes. Consequently, certain grippers were subjected to more rigorous tests compared to others. Specifically, in certain scenarios, some grippers were subjected to three repetitions of selected tests, while others were tested only once. This discrepancy arose

Table 4.3: Input actuators and output measurements of the tests.

	Test 1	Test 2	Test 3
Input	linear displacement screw-nut mechanism	linear displacement screw-nut mechanism	force supplied through force gauge
Output	displacement measurement	displacement measurement, force measurement (dynamometer)	displacement measurement, force measurement (dynamometer)

from the identification of evident issues with certain designs, leading to the decision to conduct brief tests on unsuccessful grippers and more tests on successful grippers in order to enhance efficiency in moving to the next cycle of prototyping. The summary of test repetitions (number of runs) for all grippers and test types is outlined in Table 4.4. Notably, italicized text highlights the issues that prompted the decision not to subject two of the grippers to multiple tests. These issues are thoroughly examined in subsequent sections.

Table 4.4: Number of test repetitions for all grippers and tests presented in this chapter. Text in *italic* indicates the issues identified with two of the grippers.

	Test 1	Test 2	Test 3
Analytical design: TPC	no. of runs: 1 *underconstraint behaviour*	no. of runs: 1 *underconstraint behaviour*	no. of runs: 1 *underconstraint behaviour*
Analytical design: PLA	no. of runs: 3	no. of runs: 3	no. of runs: 3
Topology optimisation: TPC	no. of runs: 3	no. of runs: 3	no. of runs: 3
Topology optimisation: PLA	no. of runs: 1 *narrow motion range*	no. of runs: 1 *narrow motion range*	no. of runs: 1 *narrow motion range*

The output data for each test consist of equipment readings and pictures. The displacement values are determined by post-processing the pictures using ImageJ software based on the scale from the ruler attached to the test rig. The position of the output was individually determined on each picture and displacements compared to the first picture were calculated. The equipment used in the tests includes a digital force gauge (maximum force: 250N, resolution: 0.1N) for the input force measurements and a dynamometer (maximum force: 1 N, resolution given

by the dynamometer scale: 0.02 N - improvement in resolution explained below, spring stiffness: $\frac{1}{60}\frac{N}{mm}$) for output force measurements. The resolution of the dynamometer was digitally improved using the following technique: 1 N corresponds to 60mm of reading indicator displacement, based on the spring stiffness that has linear behaviour. Any displacement of the spring (determined from the pictures) corresponds to a force that is calculated on the basis of the force-displacement linear relationship, based on the data on the pictures. This allows to read values that are between two lines on the scale of dynamometer. The input displacement is supplied by the screw-nut mechanisms that provides a resolution of 0.125 mm. It is important to note that such a mechanism would not be desirable in the Lunar dust environment, but since the drive of the gripper is not part of this project, it has been selected to ensure easy assembly and the possibility of stopping at any position during the tests. Also, the assumption that the displacement-based drive could be used was based on the design of an Apollo geological tool, tongs, that has a handle connected to the end effector through a stainless steel rope attached to a spring loaded mechanism. The movement of the end effector was determined by the position of the handle pulled by the astronaut, as already discussed in the Chapter 3.

4.4 ANALYTICAL DESIGN: TPC GRIPPER

In this section, the test results of the analytically designed and 3D printed TPC gripper will be discussed. Before the gripper was tested, the 3D model was subjected to non-linear FEM analysis presented in Figure 4.13. It was done on a 2D shell model, as visible in Figure 4.13a. The size of the mesh was set between 0.25 mm and 1.5 mm, with a finer mesh located around thin flexures.

Figure 4.13b shows the simulation performed for 5.25 mm (pushing) of input displacement which resulted in full gripper closure. Maximum stress (its location is marked in the figure with the arrow) reached 0.643 MPa. Figure 4.13c presented a displacement of 2 mm applied in opposite direction (pulling). This load case results in a maximum stress of 0.165 MPa and a gripper opening beyond its default position. It is evident that the stress in both load cases is below the yield strength of the TPC (which is 8 MPa, as indicated in Section 3.2). The maximum stress observed in the analysis of this gripper constitutes 8% of the TPC yield strength.

After FEM analysis, tests were performed on the 3D printed gripper. This section summarises the data collected in three tests described in Section 4.3. All the tests discussed in this section were performed on a single gripper prototype; the gripper was already presented in Figure 4.5. It was previously mentioned that certain grippers were not tested as extensively as others due to their limited perfor-
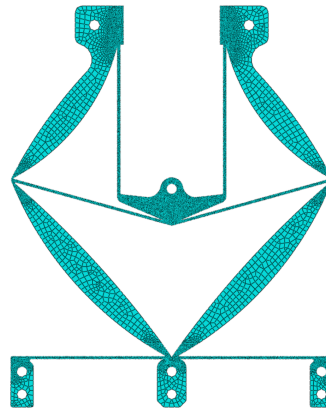
(a) Mesh in the FEM model.
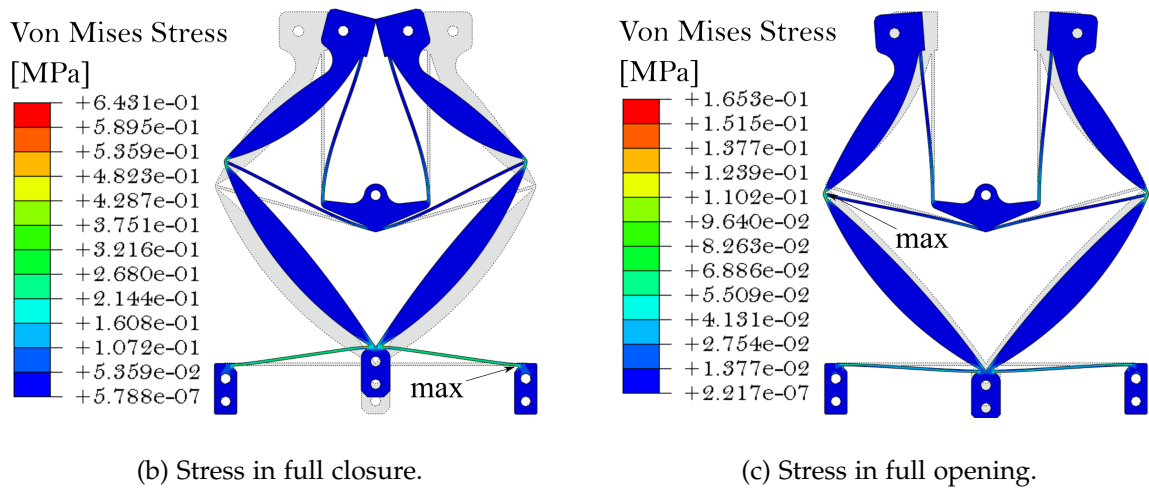
(b) Stress in full closure.

(c) Stress in full opening.

Figure 4.13: Nonlinear FEM analysis of analytically designed TPC gripper.

mance. Designs that were not deemed promising were not given extensive testing, allowing more time to be devoted to the more promising samples. As such, the gripper discussed here was subject to single run for each type of test. This is why standard deviations are not presented.

The first test collected data on the input and output displacements and their relationship. For this test, hysteresis is visible in Figure 4.14a. The slope indicates a linear relationship, with linear regression, where geometric advantage: GA = 2.66, which is slightly higher than the GA calculated at the design stage. It is also higher than GA of the same geometry that was produced with PLA (further discussed in Section 4.5). Figure 4.14b shows the evolution of the GA with changing input displacement. For small displacements in the negative input direction, the GA is negative. This means that the TPC gripper must be pulled back to its original position at the input before testing. This behaviour indicates that the precision positioning of the TPC gripper is limited.

(a) Input-output displacements relationship.

(b) Geometric Advantage (GA) changing with input displacement.
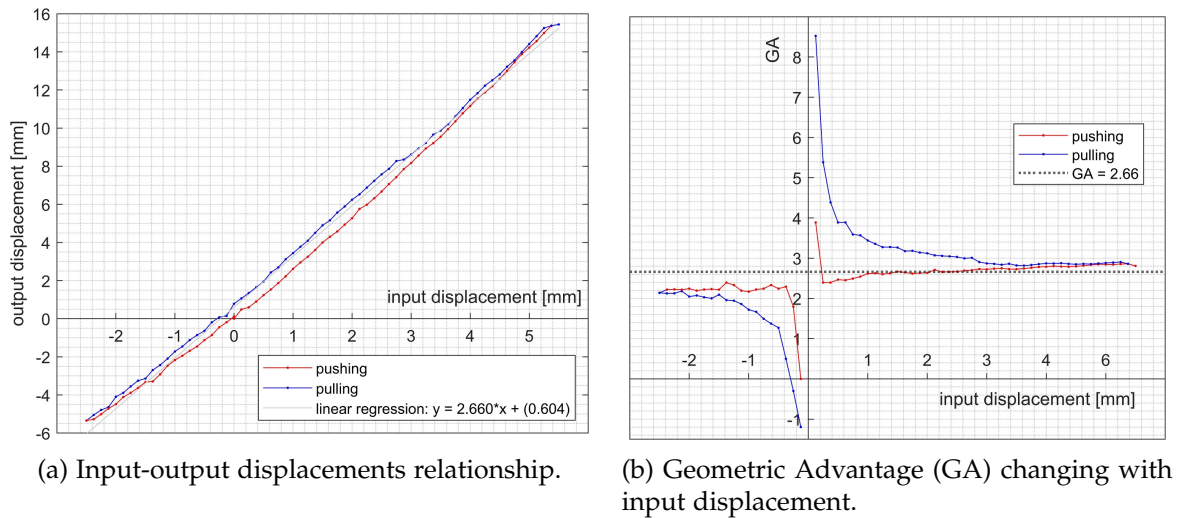
Figure 4.14: Test 1 data of TPC analytically designed gripper - displacements.

(a) Analytically designed TPC gripper deformation: top - default position to closed position; bottom - opening beyond default position.

(b) Path of the right gripper jaw.
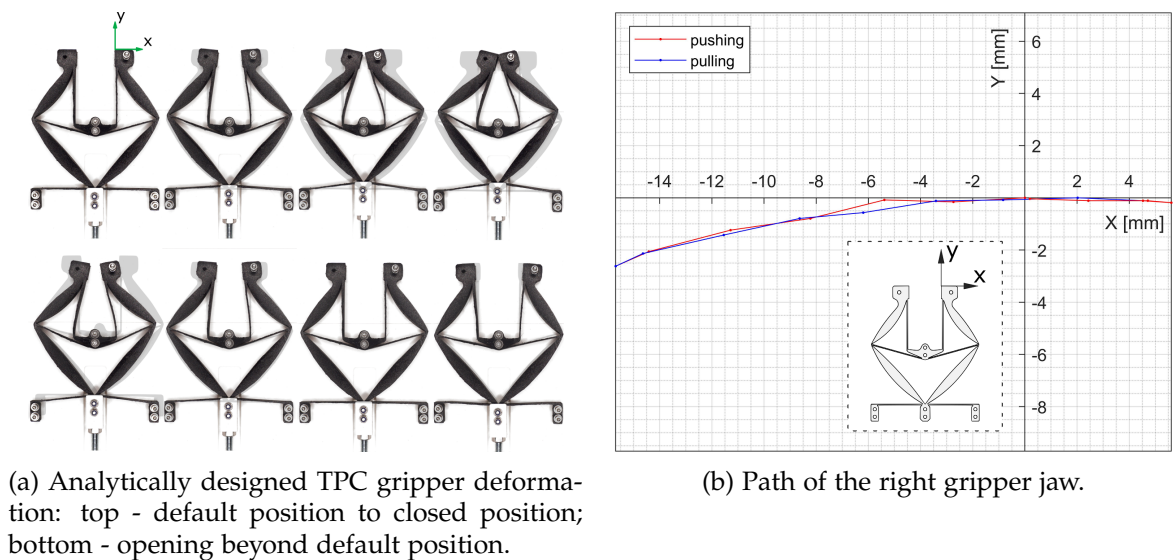
Figure 4.15: Test 1 data of analytically designed TPC gripper - motion; coordinate system (arrows) marked on the gripper - starting point for output displacement measurements.

The different stages of gripper deformation are presented in Figure 4.15a with the grey shade of the unreformed gripper (unloaded) in the background. Figure 4.15b displays the motion path of the output port located on the top right, marked with the green coordinate system on the first unreformed gripper in Figure 4.15a. The graph shows that the path of the output point is mostly in the horizontal direction, as assumed in the initial design discussion.

The tests revealed that the flexures had a low level of stiffness, which was insufficient to provide axial stiffness. This led to an underconstrained behaviour. When the input was fixed, it was possible to move the jaws with minimal effort. This is demonstrated in Figure 4.16, which shows the jaws being closed with tweezers

while the input is held in a default position (visible on the right) compared to the unloaded position (on the left). This is the only gripper discussed in this chapter that has this issue. It is important to note that the behaviour is not caused by the geometric underconstraint, but rather by the lack of suitable axial stiffness of the flexures.
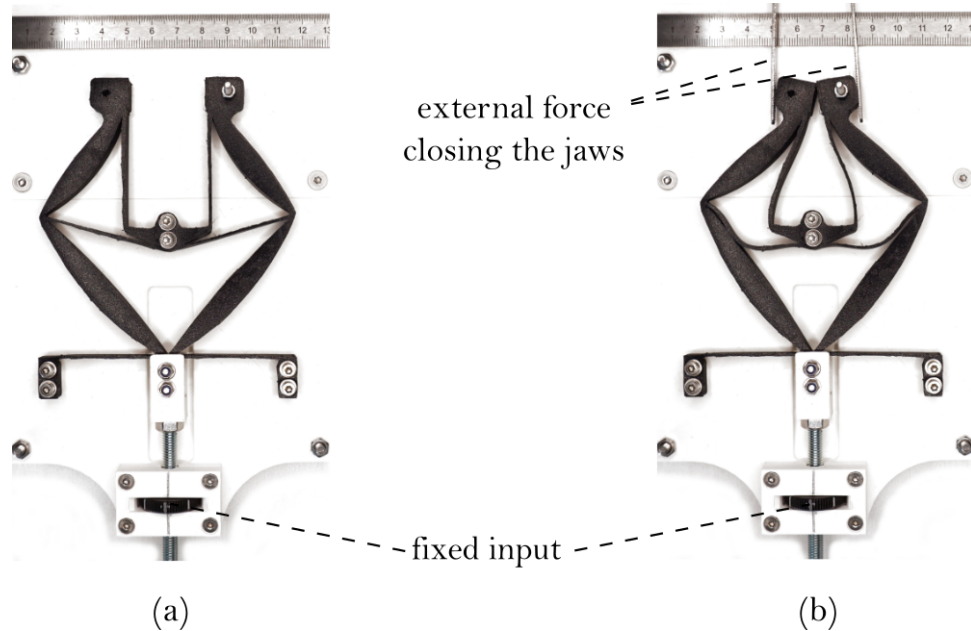
Figure 4.16: The presentation of unconstrained behaviour of the TPC analytically designed gripper; (a) default positions with fixed input, (b) external force applied at the jaws with fixed input.
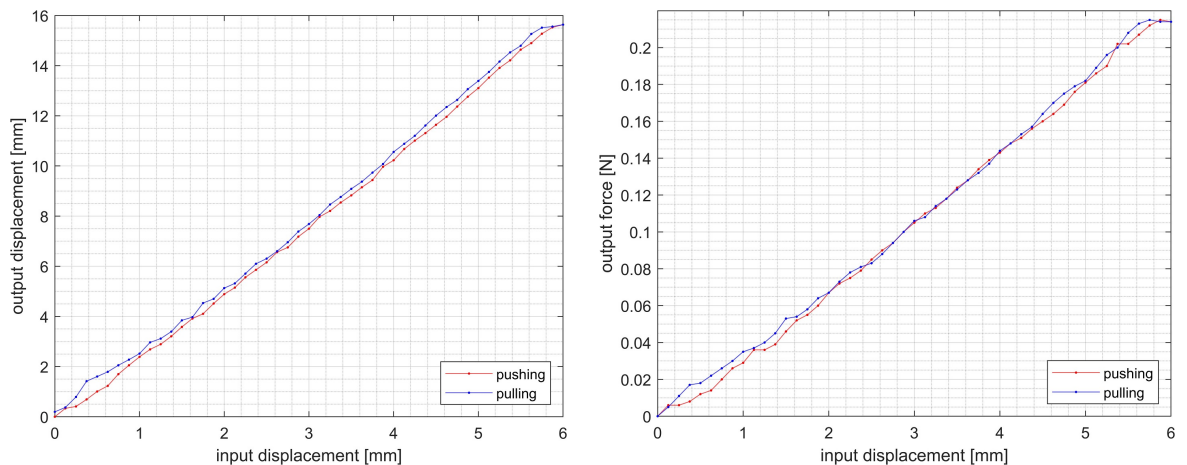
(a) Experimental data of TPC analytically designed gripper, displacements relationship with dynamometer attached.

(b) Experimental data of TPC analytically designed gripper, input displacement - output force relationship.

Figure 4.17: Test 2 data of TPC analytically designed gripper - displacements and force.

The data from test number 2 is presented in Figure 4.17. The hysteresis is also evident here, and is more noticeable for small displacements. The relationship

between the input and output parameters is very close to linear. The dynamometer attached to the output has its own stiffness as already mentioned in Section 4.3. In this case, its stiffness is high enough (compared to the stiffness of the gripper) to affect the behaviour of the gripper during the test. In test 1 (without dynamometer), the gripper required 5.5 mm of input displacement to achieve complete closure. For test 2, it required 6 mm of input displacement for full closure. This additional 0.5 mm of input displacement is needed to overcome the external added resistance (stiffness) at the output.
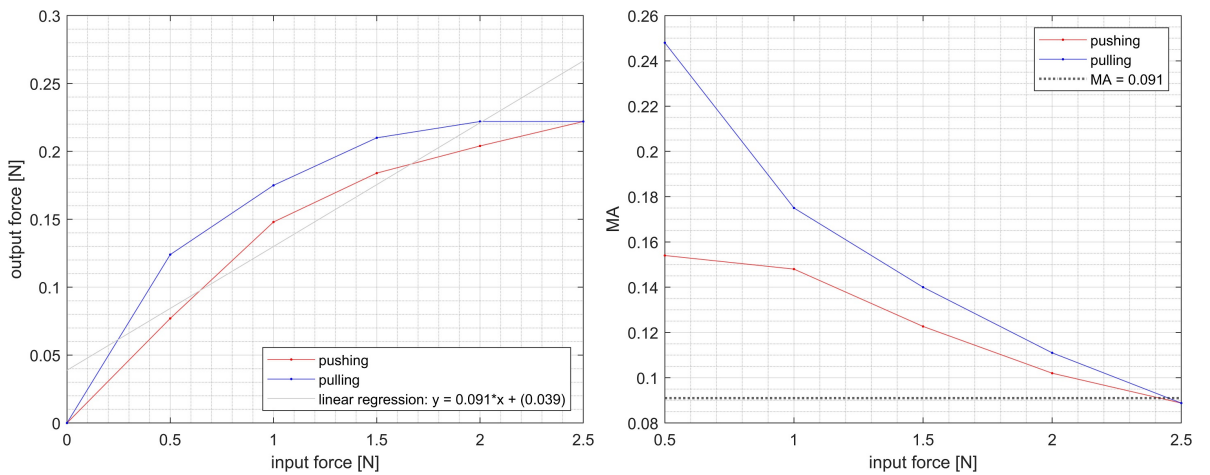
(a) Experimental data of TPC analytically designed gripper, measured forces relationship.

(b) Mechanical Advantage (MA) changing with input displacement.

Figure 4.18: Test 3 data of TPC analytically designed gripper - Mechanical Advantage.
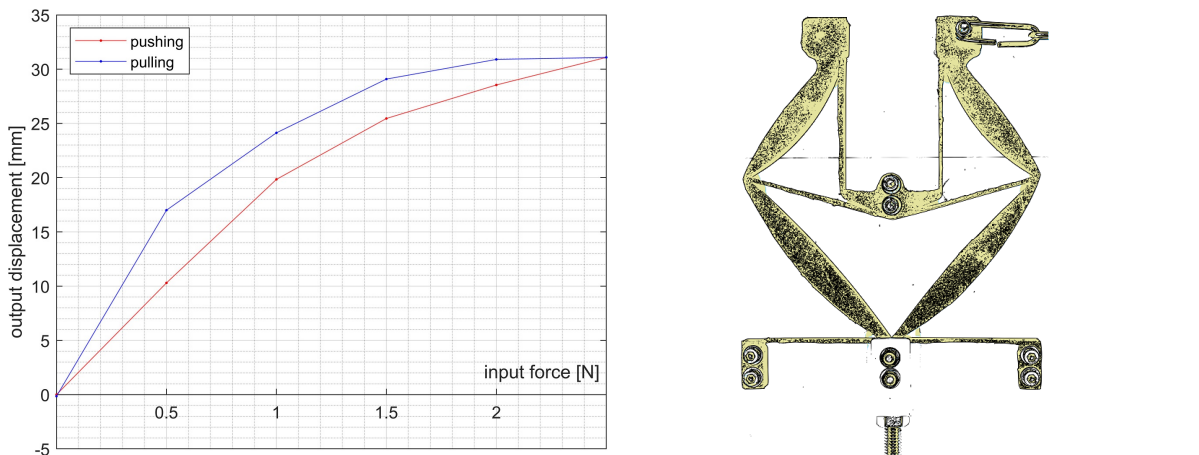
(a) Experimental data of TPC analytically designed gripper, input force - output displacement.

(b) Stack of pictures before and after test; before - yellow and after - blue (invisible as gripper returned to original shape).

Figure 4.19: Test 3 data of TPC analytically designed gripper - displacement and deformation.

The results of test 3 are shown in Figures 4.18 and 4.19. This gripper requires

2.5N to fully close its jaws. Compared to the examples in the following sections (which include the same gripper topology but made with different materials), significantly less force was needed here. Because the input force resolution was set to 0.5 N (for all tests in this chapter), the number of measurement points is limited, as visible in Figure 4.18. The MA determined as the linear regression of the input-output relationship (from Figure 4.18a) is 0.091. The force-displacement relationship in Figure 4.19a shows hysteresis. However, the gripper flexes almost exactly to its original shape. The displacement remaining after the test is negative, it is -0.15 mm. Before the test, the dynamometer was calibrated to be in its nominal unloaded state. However, the remaining negative deformation might suggest that the dynamometer was actually pulling slightly on the output. After the dynamometer was removed, the original shape of the gripper was restored; this means that there was no plastic deformation. The stiffness of any output force measuring devices should be carefully considered in future tests, and any plastic deformation assessment must be done without any measurement devices attached to the output.

4.5 ANALYTICAL DESIGN: PLA GRIPPER

This section focuses on the test results obtained from the analytically designed and 3D printed gripper using PLA materia. Before performing the gripper tests, a FEM analysis was performed on the model, as depicted in Figure 4.20. The two-dimensional mesh model, illustrated in Figure 4.20a, featured a mesh size ranging from 0.25 mm to 1.5 mm, with finer mesh elements concentrated around the thin flexures.

Figure 4.20b shows the simulation conducted to evaluate the gripper response under an input displacement of 5.2 mm, resulting in complete gripper closure. The corresponding maximum stress is marked with an arrow and is equal to 58.69 MPa. Figure 4.20c shows the displacement of 2 mm applied in the opposite direction, representing an opening motion. This load case yields a maximum stress value of 11.94 MPa. As the PLA yield strength is 60 MPa, the maximum stress recorded in the simulation (for the closing motion) constitutes approximately 98% of that value. The gripper was originally designed for TPC for which the maximum stress was much lower. It is important to note at this point that since the exact yield strength of the material was not known (and was selected based on data from the literature as already discussed in Section 3.2), it was assumed that the maximum stress can actually exceed the elastic limit and cause plastic deformations. However, it was considered useful to test the same topology with two different materials (PLA and TPC) regardless of high stress levels and possible plastic deformations.

(a) Mesh in the FEM model.

(b) Stress in full closure.

(c) Stress in full opening.
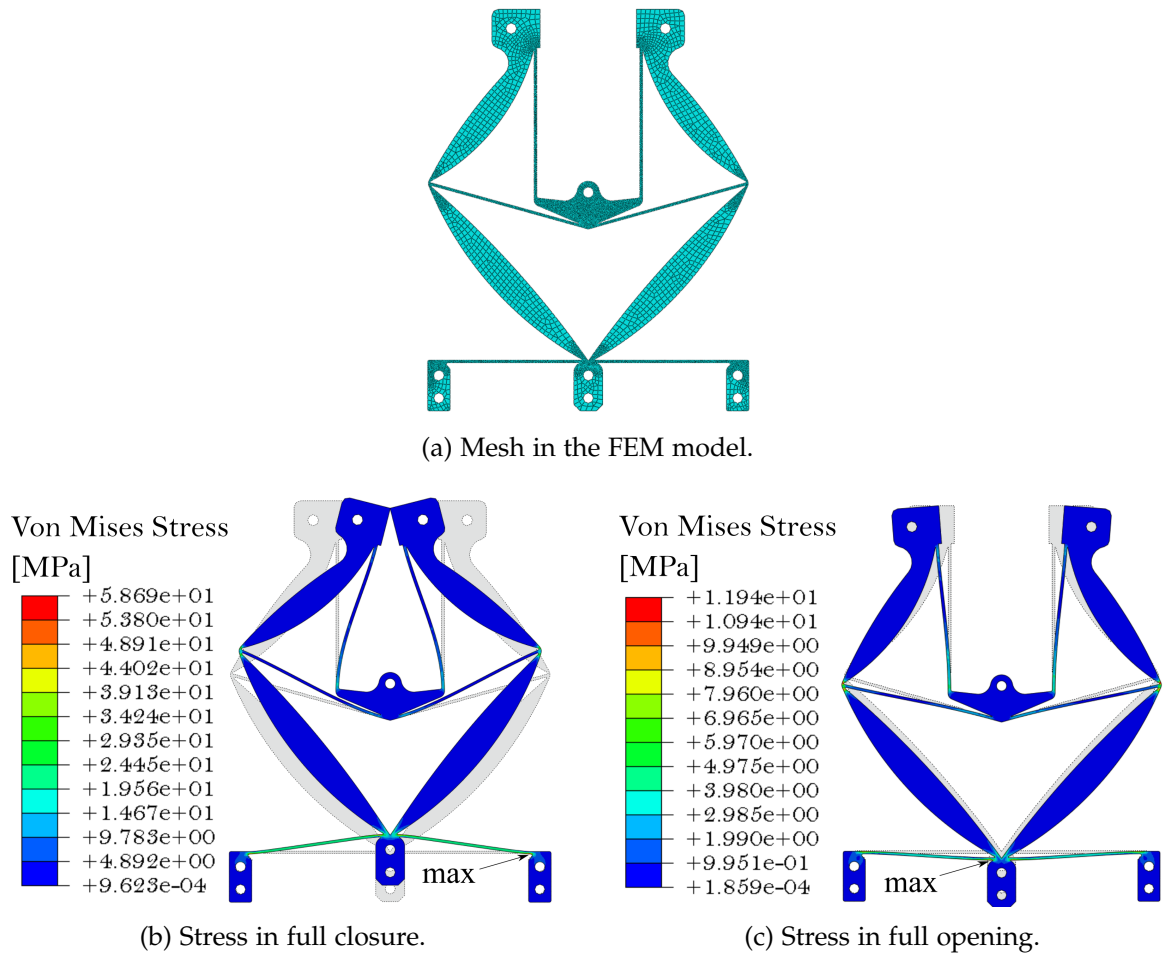
Figure 4.20: Nonlinear FEM analysis of analytically designed PLA gripper.

The data presented here was collected in three tests described in Section 4.3. All the tests discussed in this section were performed on a single gripper prototype designed using analytical methods and 3D printed with PLA, the gripper was already presented in Figure 4.5. The input displacement - output displacement test was repeated three times, while the other tests were performed once. For the data resulting from repeated tests, the maximum standard deviations are presented in the caption of the respective figures.

The first test collected measurements of the input and output displacements and their relationship. The results are presented in Figure 4.21. The data for pushing on the input (which results in the jaws coming closer together and closing the gripper) is marked in red, while the opposite movement - pulling or moving back to the gripper original position - is marked in blue. Around 1 mm of input displacement hysteresis is visible. The change in behaviour for small displacements depending on the direction of movement has been observed in next tests done on the same gripper, and it was later determined that it could be caused by the slip of the input displacement mechanism. However, the rest of the slope indicates a linear

relationship, as expected. The slope of the linear regression is an indicator of Geometric Advantages (GA), which in this case is the ratio of output displacement in the desired direction to input displacement. The linear regression gives GA = 2.524 which is comparable to the GA calculated in the analytical method for this gripper design. The theoretical value of GA is 2.58 - calculations provided in Figure 4.4. Figure 4.21b presents the GA evolution during test 1. In this case, the GA is calculated separately for every measurement point as the input displacement in the horizontal direction divided by the output displacement. The data shows that GA is not constant and changes with the gripper position.
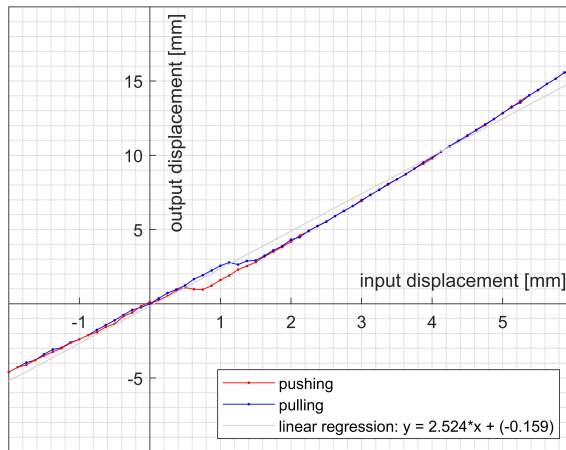
(a) Input-output displacement relationship. Max. standard deviation 0.622 mm.
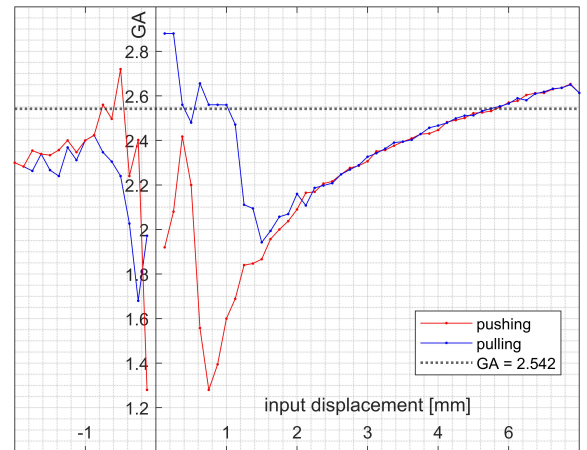
(b) Geometric Advantage changing with input displacements. Max. standard deviation 0.277 mm.

Figure 4.21: Test 1 data of PLA analytically designed gripper - displacements.
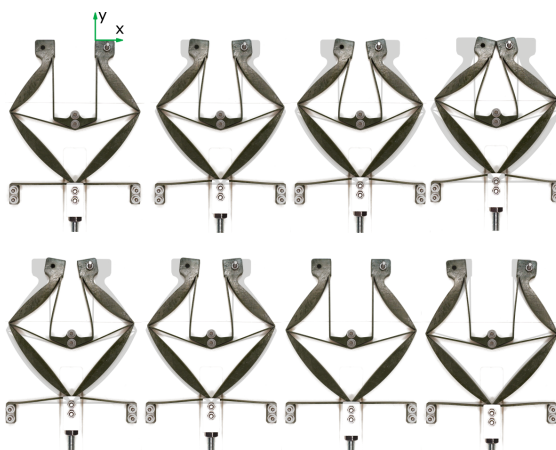
(a) Analytically designed PLA gripper deformation: top - default position to closed position; bottom - opening beyond default position.
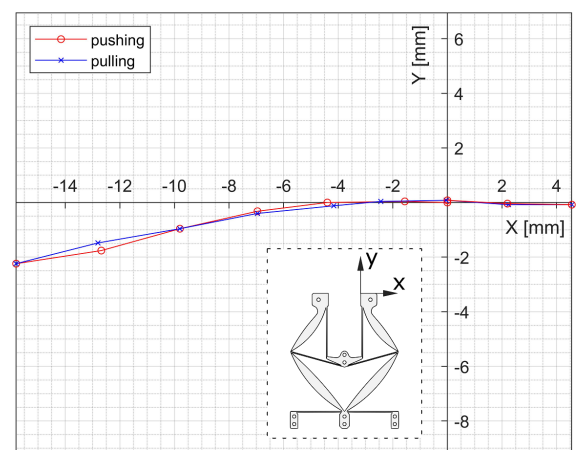
(b) Path of the right gripper jaw. Max standard deviation X: 0.622 mm, max standard deviation Y: 0.394 mm.

Figure 4.22: Test 1 data of analytically designed PLA gripper - motion; coordinate system (arrows) marked on the gripper - starting point for output displacement measurements.

Figure 4.22a depicts the various stages of gripper deformation, with the undeformed gripper (unloaded) in the background shaded in grey. Figure 4.22b illustrates the motion path of the output port, located at the top right, which is indicated by the green coordinate system on the first undeformed gripper shown in Figure 4.22a. The output port is also the centre point for the measurements; this is why the gripper closure produces negative values along the x-axis. Figure 4.22b presents the path of the output point, as visible the dominant direction is the horizontal one, as assumed in the design stage. The paths for pushing and releasing to the original position are closely matched.

The underconstrained behaviour, which was observed in the tests of the analytically designed TPC gripper (Section 4.4), was not observed for the PLA gripper of the same topology presented here. It is evident that for this given geometry of the flexures PLA had enough axial stiffness to support their function.
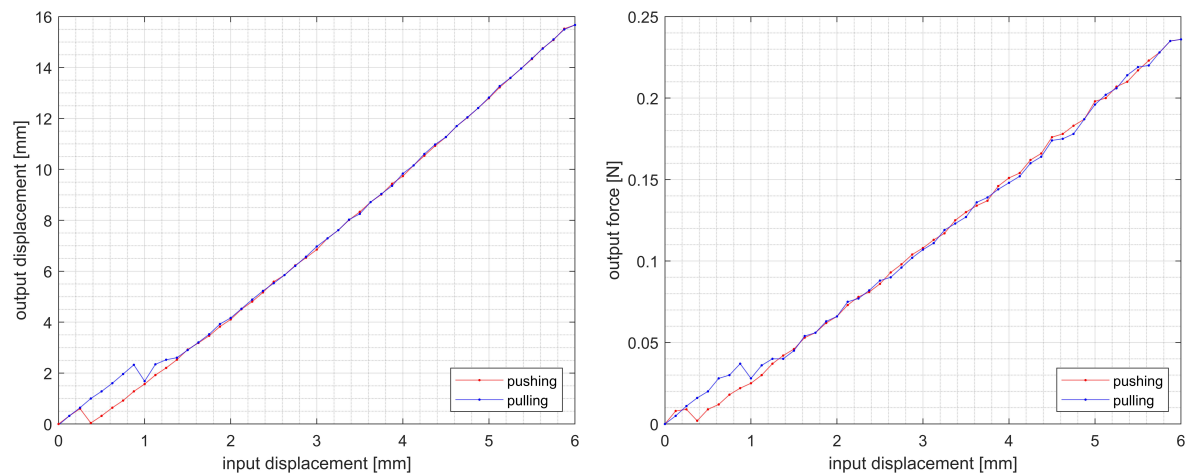
(a) Experimental data of PLA gripper, displacements relationship with dynamometer attached.

(b) Experimental data of PLA gripper, input displacement - output force relationship.

Figure 4.23: Test 2 Data of PLA gripper - displacements and force.

The data from test number 2 is presented in Figure 4.23. The maximum output force measured in this test is 0.236 N. Hysteresis around 1 mm of input is visible, but in the rest of the measurement range, the relationship between input and output is almost linear. Two peaks of force and displacement at the output have been recorded during the push and pull phases. In future tests, it was assessed that they are caused by the slip of the input displacement mechanism.

Data from test 3 is presented in Figures 4.24 and 4.25. In this test, the input is supplied through the force gauge. The red colour corresponds to the portion of motion caused by pushing, and the blue colour represents retracting (or reducing the force). Figure 4.24a is a plot of the relationship between the input force and the output force. The grey line represents the linear regression of the measurements. The slope represents the relationship between them, which is also the Mechanical

(a) Experimental data of PLA gripper, measured forces relationship.

(b) Mechanical Advantage (MA) changing with input displacement.
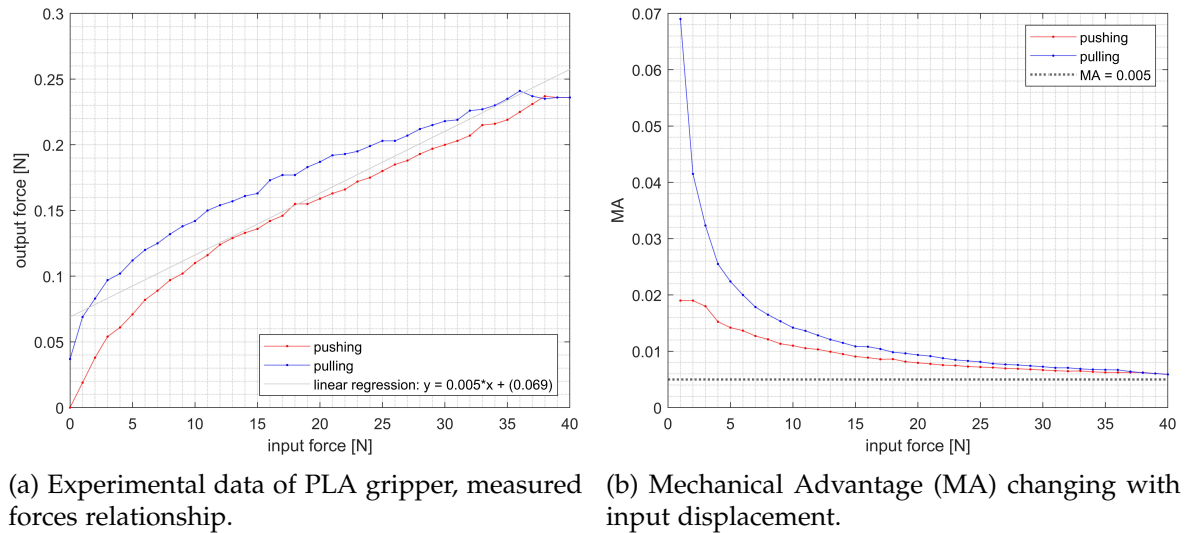
Figure 4.24: Test 3 data of PLA gripper - Mechanical Advantage.

Advantage (MA), from the graph MA = 0.005. Figure 4.24b shows the MA changing with the input force. This data shows MA calculated separately for each gripper position as output force divided by input force. It is visible that the actual MA for all measurement points is higher than the one suggested by linear regression. Similarly to GA the MA changes with the position of the gripper.

(a) Experimental data of PLA gripper, input force - output displacement.

(b) Difference between the shape of gripper before (yellow) and after (blue) the test.
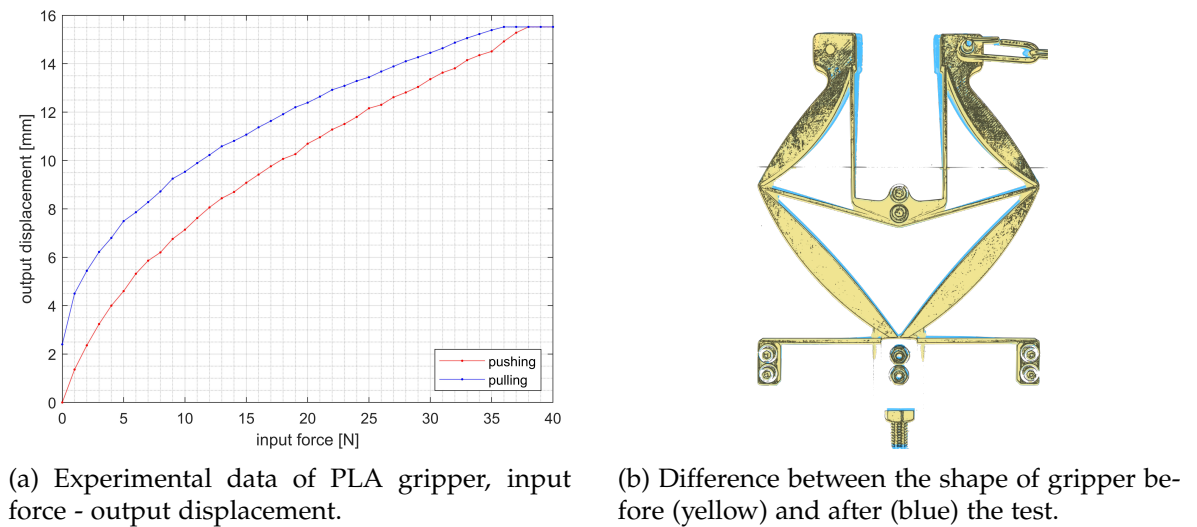
Figure 4.25: Test 3 data of PLA gripper - displacement and deformation.

Another depiction of the data from test 3 is visible in Figure 4.25. It is the input force - output displacement relationship. It shows the hysteresis of the system that is also visible in Figure 4.24a. Figure 4.25a also shows that the gripper does not return to its original position after the input force is fully removed. This is visible as the remaining displacement with input force of 0 in the blue (pulling) part of the data in Figure 4.25a. Figure 4.25b is a stack of the first and last pictures of this test. The yellow gripper represents the system before measurements (input force

equal to 0) and the blue represents the gripper after the force has been removed at the end of the test (input force equal to 0 again). This clearly shows the remaining deformation (1.8 mm). This deformation was assumed to be plastic, i.e. permanent. Plastic deformations should be avoided in compliant mechanisms, similar to the gripper presented here, as they have a negative impact on the repeatability of the movement. As already demonstrated with the FEM analysis at the beginning of this section, the gripper was loaded at 98% of the theoretical PLA yield strength and therefore plastic deformation can be associated with high stress levels.

4.6 TOPOLOGY OPTIMISATION: TPC GRIPPER

This section presents the FEM analysis and tests performed on topology optimised TPC gripper. FEM analysis is shown in Figure 4.26. The 2D mesh, illustrated in Figure 4.20a, featured a mesh size ranging from 0.25 mm to 1.5 mm, as in previous models. The finer elements are concentrated around compliant hinges. Figure 4.26b presents the simulation with an input displacement of 8.75 mm, which results in the closure of the gripper. The maximum stress is marked in the figure and measured at 4.058 MPa. Figure 4.26c presents the simulation with a displacement of 2 mm applied in the opposite direction, representing an opening motion. Here, the maximum stress value of 0.788 MPa is measured. In both load cases, stress levels remain below the TPC yield strength (8 MPa). In summary, the analysis demonstrate that the maximum stress observed in this study constitutes around 51% of the TPC yield strength, which is a satisfactory result at this stage of the study.

The next paragraphs summarise the data collected in three tests performed on the gripper prototype designed using topology optimisation in commercial software HyperWorks. The prototype was 3D printed with TPC, the gripper is visible in the picture 4.8b. The input displacement - output displacement test was iterated three times, whereas the remaining tests were conducted once. Regarding the data derived from repeated tests, the captions of the respective figures show the maximum standard deviations.

The measurements of test 1 are presented in Figure 4.27a. Again, hysteresis is visible for small displacements - around 1mm of input displacement. From linear regression, GA = 1.450, while Figure 4.27b shows the evolution of GA with changing input displacement, where GA is calculated for each step separately. This comparison shows again that the GA is not constant, and it changes with the position of the gripper.

Figure 4.28a presents the deformation stages of the TPC gripper with a grey shade representing the undeformed gripper in the background. Figure 4.28b shows the motion path of the output port located on the right, the same location as for the
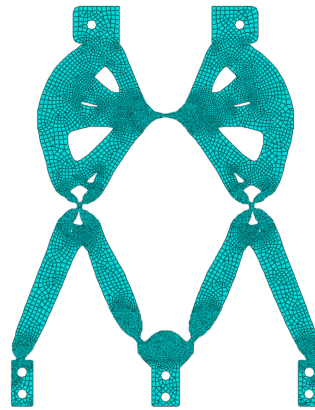
(a) Mesh in the FEM model.
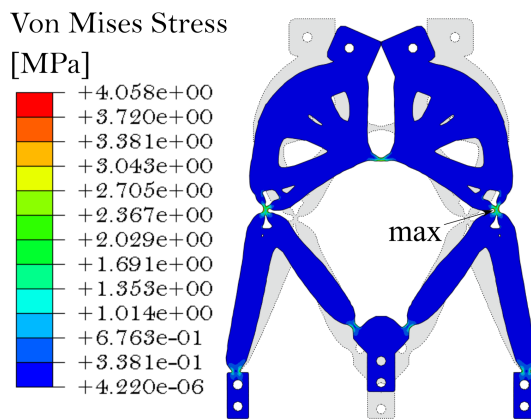
(b) Stress in full closure.
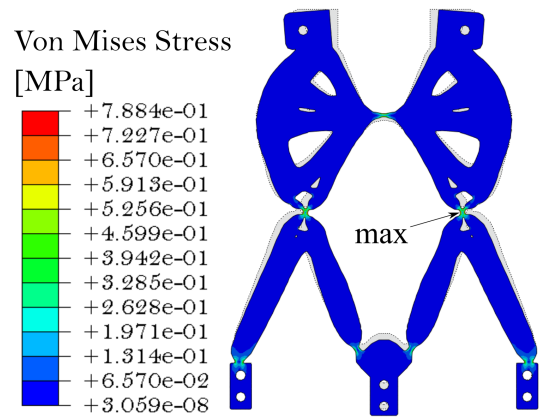
(c) Stress in full opening.

Figure 4.26: Nonlinear FEM analysis of topology optimised TPC gripper.
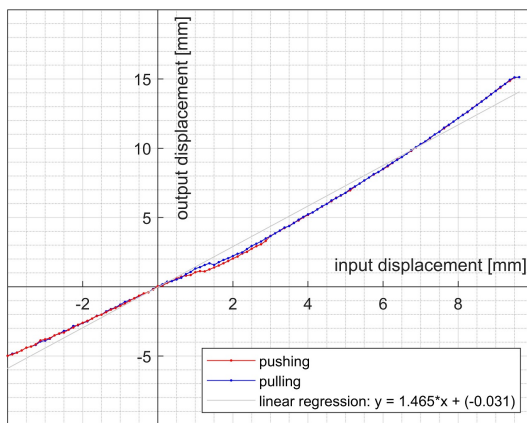
(a) Input-output displacement relationship. Max. standard deviation 0.725 mm.
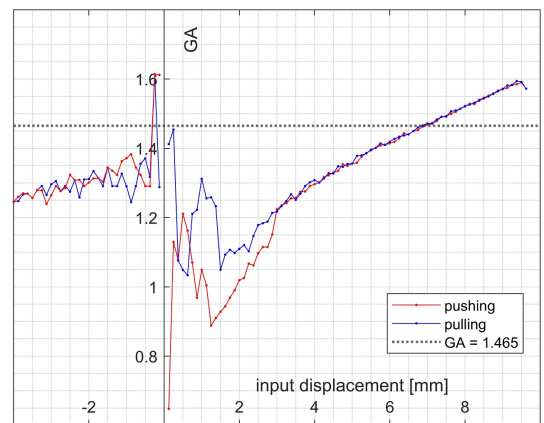
(b) Geometric Advantage changing with input displacements. Max. standard deviation 0.343 mm.

Figure 4.27: Test 1 data of TPC topology optimised gripper - displacements.

previous tests, the coordinate system marked in green in Figure 4.28a. As visible, there is a significant vertical motion of the output port. The range of y-motion is

(a) Topology optimised TPC gripper deformation: top - default position to closed position; bottom - opening beyond default position.

(b) Path of the right gripper jaw. Max standard deviation X: 0.725 mm, max standard deviation Y: 0.484 mm.

Figure 4.28: Test 1 data of topology optimised TPC gripper - motion; coordinate system (arrows) marked on the gripper - starting point for output displacement measurements.

equal 25% of motion in the x-direction. The expected horizontal movement is still dominant, although compared to analytically designed grippers the motion in the y-direction is more than double.

(a) Experimental data of TPC gripper, test 2, displacements relationship with dynamometer attached.

(b) Experimental data of TPC gripper, input displacement - output force relationship.
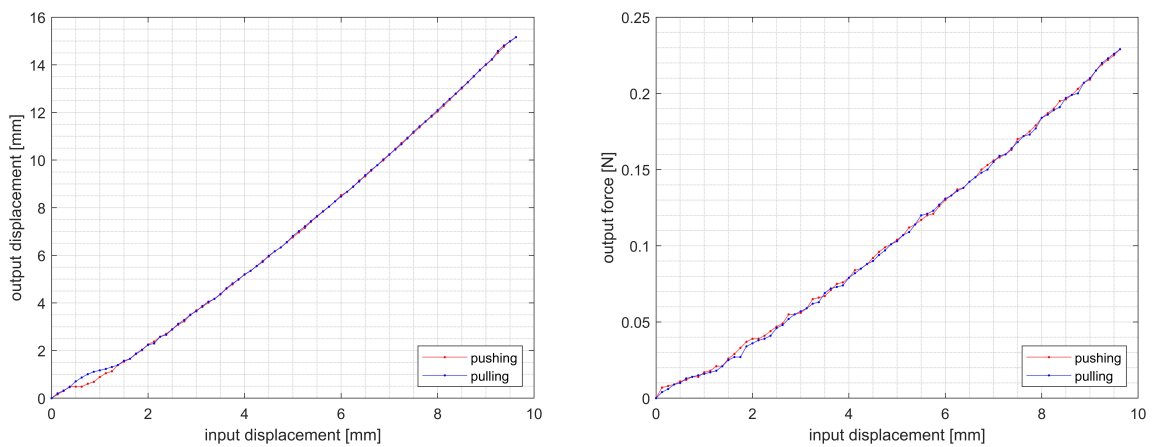
Figure 4.29: Test 2 data of TPC gripper - displacements and force.

The data from test 2 is presented in Figure 4.29. Here hysteresis around 0.5 - 1mm of the input is visible, but in the data presenting pushing and pulling motion fits almost the same linear path. The hysteresis is not visible in Figure 4.29b, which presents the relationship between the displacement of the input and the force of the output. The input displacement in test 2 matches the maximum input displacement in test 1 suggesting that the impact of additional stiffness from the dynamometer

is negligible.
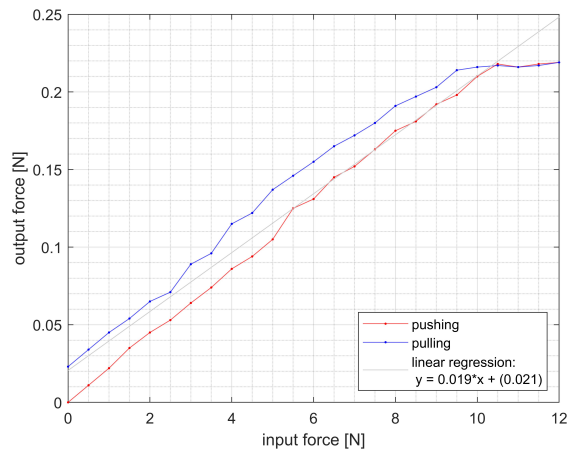
(a) Experimental data of TPC gripper, measured forces relationship.
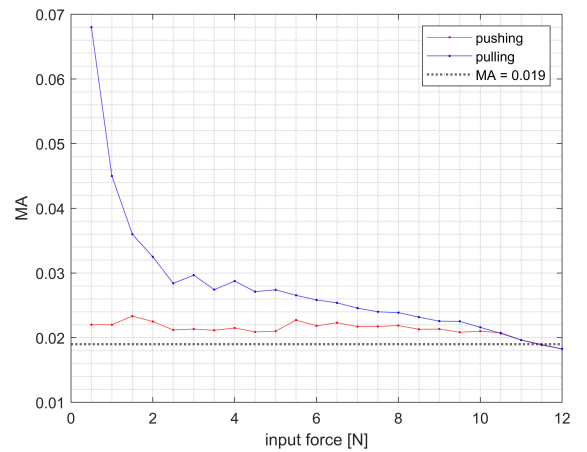
(b) Mechanical Advantage (MA) changing with input displacement.

Figure 4.30: Test 3 data of TPC gripper - Mechanical Advantage.

Test 3 is presented in Figure 4.30. Grey line a represents linear regression, MA = 0.019. Figure 4.30b shows the MA changing with the input force. As observed with grippers discussed above, this data also shows that the actual MA differs depending on the position (deformation) of the gripper.
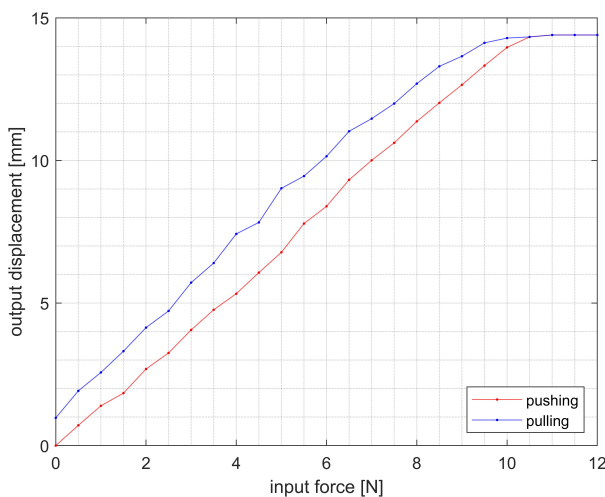
(a) Experimental data of TPC gripper, input force - output displacement.
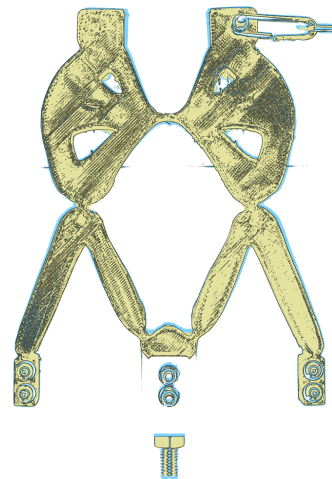
(b) Difference between the shape of gripper before (yellow) and after (blue) the test.

Figure 4.31: Test 3 data of TPC gripper - displacement and deformation.

Figure 4.31a shows the hysteresis of the system, which is also visible in Figure 4.30a. As presented in Figure 4.31a also shows that the gripper did not flex back to its original position after the input force was fully removed; it is visible as the remaining displacement with the input force of 0 (blue data set). Figure 4.31b is a stack of first and last pictures of this test. As with the previous gripper, this

one also shows remaining deformation - it is 0.6 mm. This deformation appears to be plastic, although the stress was expected to stay below the yield strength. It is possible that the 3D printed hinges exhibit stress concentration beyond what the analysis could foresee, as FEM analysis for 3D printed specimens (even with 100% infill) are not straightforward to model. It is also worth reminding that the yield strength values used in this work were based on the literature while the real values can change slightly even with the 3D printing parameters. Nevertheless, as demonstrated in displacement-driven tests, displacement control does not appear to be effected by the small plastic deformations in the gripper.

4.7 TOPOLOGY OPTIMISATION: PLA GRIPPER

The FEM analysis of the last gripper of this chapter - topology optimised PLA gripper - is presented in this section. The results of the analysis are shown in Figure 4.32.
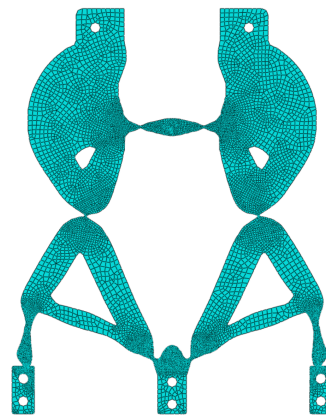
(a) Mesh in the FEM model.
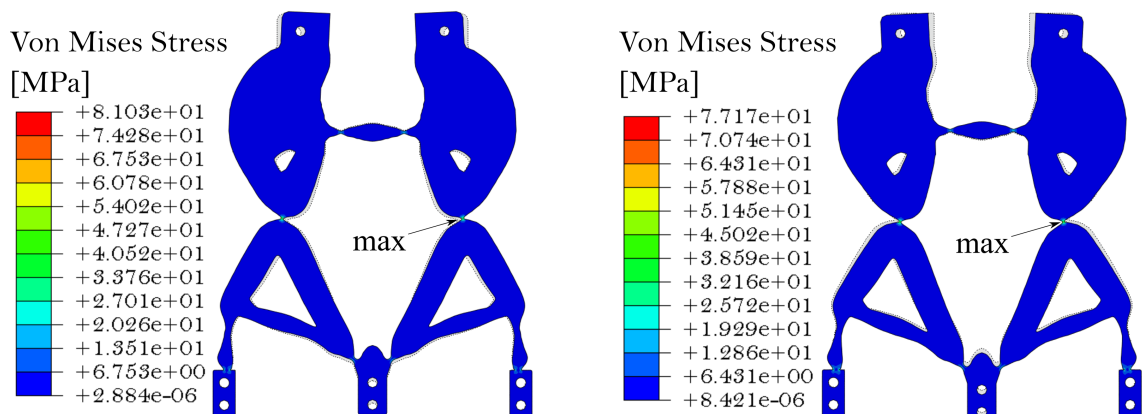
(b) Stress in full closure.

(c) Stress in full opening.

Figure 4.32: Nonlinear FEM analysis of topology optimised PLA gripper.

The 2D mesh visible in Figure 4.32a, had a size ranging from 0.25 mm to 1.5 mm.

The finer finite elements are concentrated around compliant hinges. Figure 4.32b presents the stress distribution while the gripper is subject to an input displacement of 1.125 mm. As opposed to previous designs, this is a small input displacement that does not result in gripper closure, and the maximum stress of 81 MPa already exceeds the yield strength of PLA. Because of this, no analysis was performed for higher input displacements; this will also be reflected in the tests. Figure 4.32c presents the simulation with a displacement of 1.125 mm applied in the opposite direction, representing an opening motion. Here, the maximum stress value of 77 MPa, also exceeding the yield strength. It is evident that this gripper is much stiffer than the previous prototypes, and it is not particularly compliant - at least not in the wide range of deformation that is expected in line with this work. This gripper required 20 N of input force to achieve only 1 mm of horizontal output displacement - for comparison analytically designed PLA gripper required 40 N to achieve full gripper closure - 15 mm of horizontal displacement. Data collected in the lower displacement range will still be presented and discussed.

As discussed in Section 4.2, designing this gripper emphasises some of the challenges of using topology optimisation for compliant mechanisms. No dedicated post-processing of the design was employed, and therefore the threshold of densities left in the design domain was lower than for topology optimised TPC gripper. Due to that, the PLA gripper was expected to be stiffer compared to the TPC optimised gripper. As discussed above, FEM analysis confirmed that suspicion. As such, the tests cover the input displacement from -1.125 to 1.125 mm. As this is not a satisfactory displacement range for the application discussed in this work, the gripper was tested only once to demonstrate its limited capabilities.

(a) Experimental data of PLA topology optimised gripper, displacements relationship.

(b) Geometric Advantage (GA) changing with input displacements.
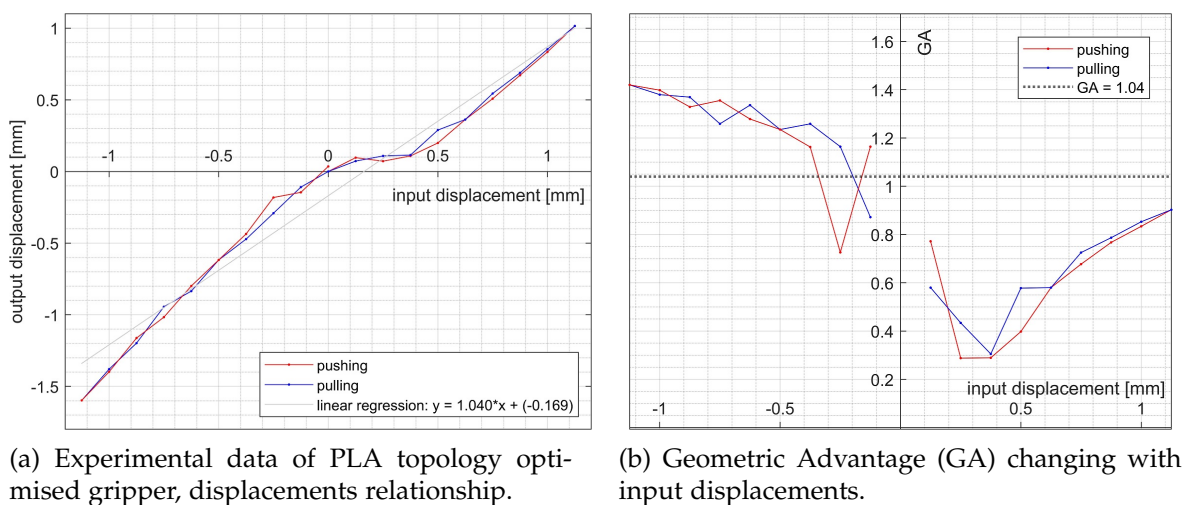
Figure 4.33: Test 1 data of PLA topology optimised gripper - displacements.

The measurements of test 1 are presented in Figure 4.33. Similarly to other tests presented, pushing is marked in red, and pulling in blue. The linear regression

results in GA = 1.04, but Figure 4.33b shows that GA is dependent on the gripper state. This comparison shows again that the GA is not constant and changes with the position of the gripper. Similarly to the other designs, the GA is not constant throughout the range of motion that has been evaluated.
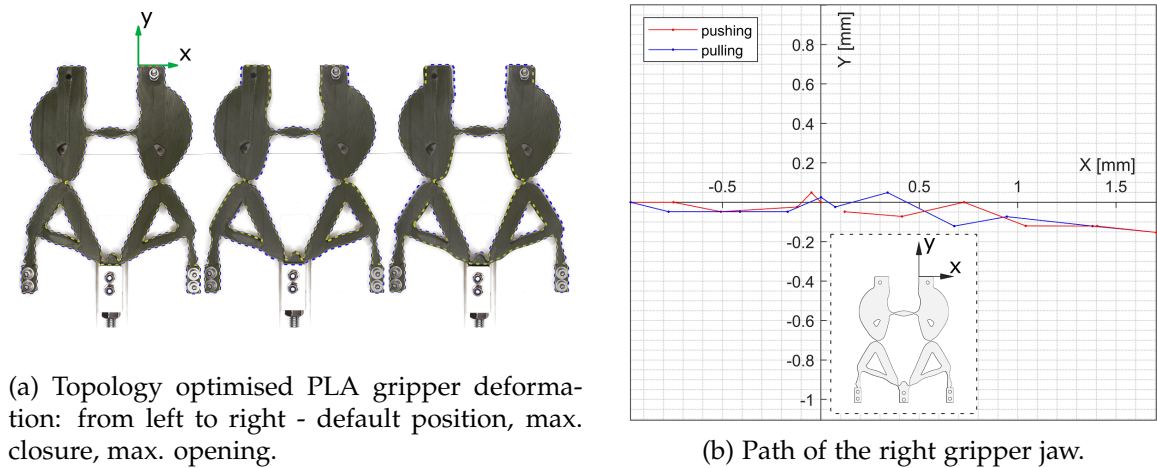
(a) Topology optimised PLA gripper deformation: from left to right - default position, max. closure, max. opening.
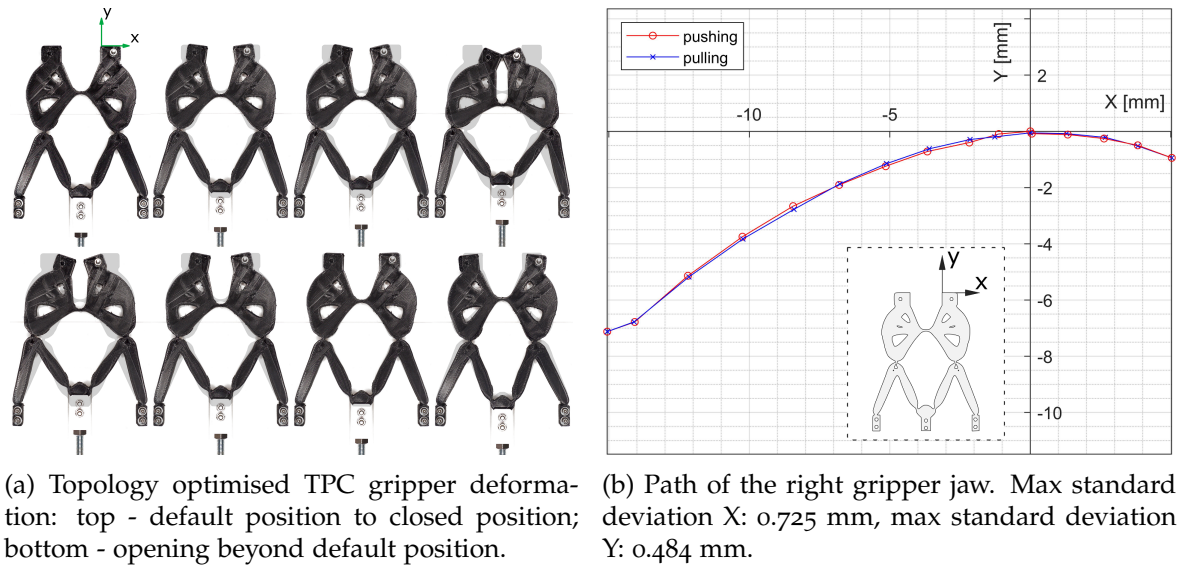
(b) Path of the right gripper jaw.

Figure 4.34: Test 1 data of topology optimised PLA gripper - motion; coordinate system (arrows) marked on the gripper - starting point for output displacement measurements.

Figure 4.34a presents the deformation stages of the gripper. Because the motion range is significantly smaller, only three positions are shown: starting position (0), maximum closed, and maximum opened. The outline of the undeformed gripper is presented as a grey shade with a dashed outline in the background. It is evident that the displacements are small; they are in the range of up to 1.6 mm. Figure 4.34b shows the path of motion of the output port. The precision of position measurement is limited as compared to the relatively small output displacement range. As expected, vertical movement remains predominant, consistent with other gripper designs.

The data from test 2 is presented in Figure 4.35. The data is insufficient to judge the hysteresis of the system. This is because the movement range is very limited compared to the size of the test rig. This poses a challenge to the measurement system presented here, which has limited precision with such a small range of movement. Moreover, since the resolution of the input displacement was the same for all grippers, the number of measurement points on the graph is limited due to the narrow measurement range. In Figure 4.35b an initial peak of the output force is visible. It is similar to the behaviour of the analytically designed PLA gripper (see Figure 4.23b).

Test 3 is presented in Figure 4.36. Data shows significant oscillation in measurments but it is important to point out that the range of the output force is very narrow (0-0.025), because of this any measurment errors have significant impact on the results, and as discussed before, the default resolution of dynamometer is
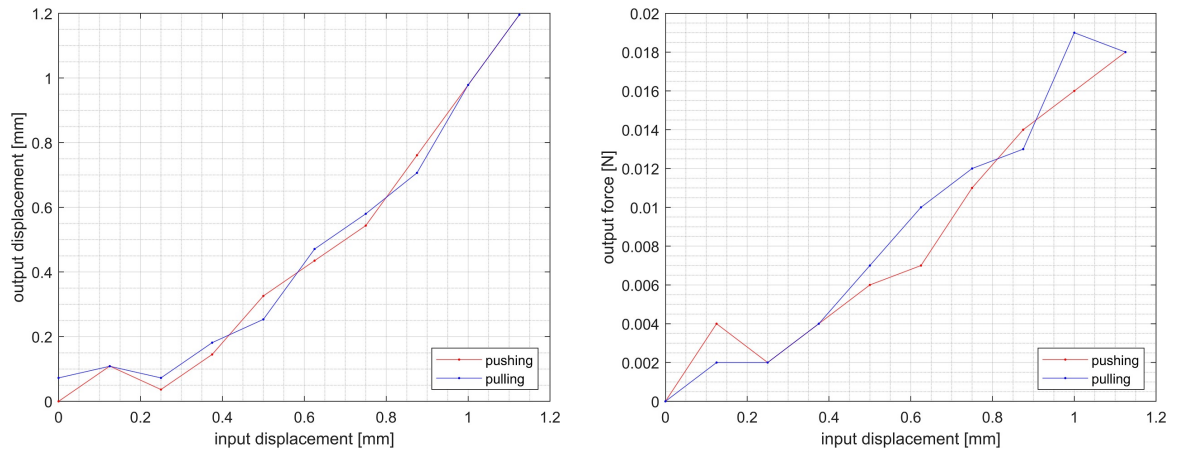
(a) Experimental data of PLA topology optimised gripper, test 2, displacements relationship with dynamometer attached.

(b) Experimental data of PLA topology optimised gripper, input displacement - output force relationship.

Figure 4.35: Test 2 data of PLA topology optimised gripper - displacements and force.
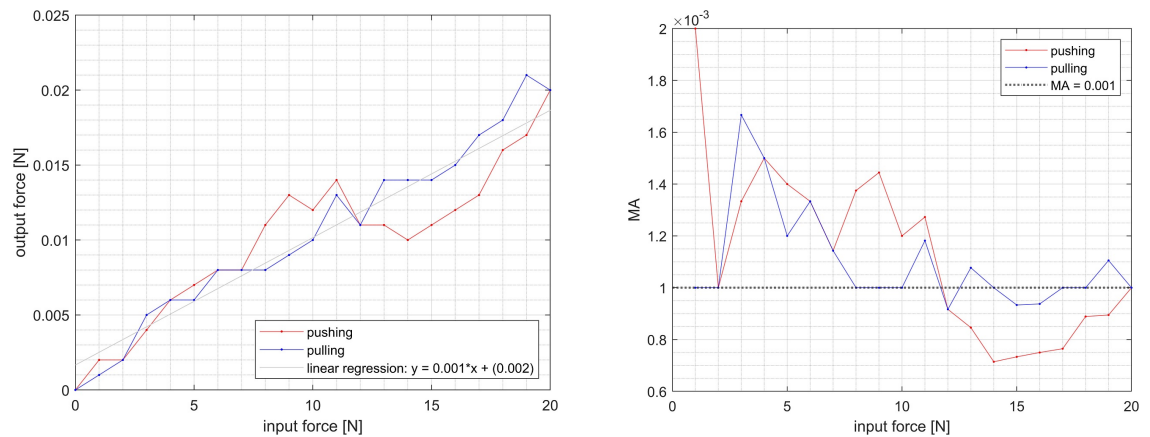
(a) Experimental data of PLA topology optimised gripper, measured forces relationship.

(b) Mechanical Advantage (MA) changing with input displacement.

Figure 4.36: Test 3 data of PLA topology optimised gripper - Mechanical Advantage.

0.1 N. Figure 4.36a is a plot of the output force versus the input force. From the graph (linear regression) MA = 0.001. This is the lowest value of all designs presented in this chapter. The gripper presented here is characterised by relatively high stiffness, and therefore, even though the input force was comparable to the other designs, it results in a lower output force and lower output displacement. The output force was small enough to challenge the limits (resolution) of the measuring system; therefore, the fluctuations visible on the graph could be caused by the limited precision. Figure 4.36b shows the variation of MA with input force. As observed with the other grippers discussed in this work, the MA changes over the measurement range.

Figure 4.37a shows the relationship between the input force and the output displacement. As visible, after the test, the gripper does not flex back to its original
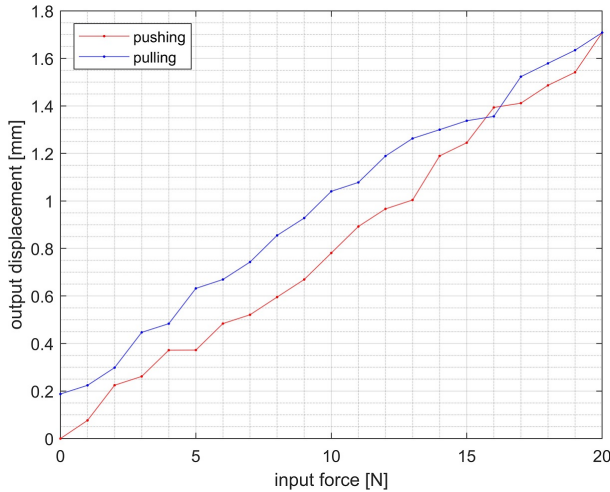
(a) Experimental data of PLA topology optimised gripper, input force - output displacement.
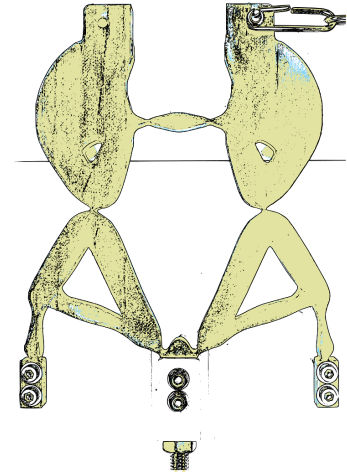
(b) Stack of pictures before and after test; before - yellow and after - blue (barely visible as gripper returned to almost original shape).

Figure 4.37: Test 3 data of PLA topology optimised gripper - displacement and deformation.

position after the input force is fully removed, visible as the remaining displacement with the input force of 0. The remaining displacement is equal to 0.19 mm. As demonstrated with FEM, plastic deformation of the gripper was expected in the range of motion presented here. Figure 4.37b is a stack of the first and last images of this test. The remaining deformation is barely visible because of the small size of the deformation. However, plastic deformation occurred even though the overall motion range was an order of magnitude smaller than for all other grippers presented in this chapter.

4.8 DISCUSSION

This chapter explored the use of two different design methodologies: the instant centre approach, which is an analytical design method, and topology optimisation. It also focused on two different materials: PLA and TPC that were used to achieve compliant gripper designs with the characteristics discussed in the Chapter 3. Four grippers were manufactured and tested: analytically designed TPC and PLA grippers and topologically optimised TPC and PLA grippers. The summary of all test results are presented in Table 4.5 and discussed in the next paragraphs. The material used and topology differences presented in this chapter helped guide the choices for the next gripper prototypes, which will be presented in the next Chapter 5.

In this section, some differences in grippers' performance will be outlined. Worst performance was measured for the gripper designed using topology op-

Table 4.5: Summary of tests done on all gripper prototypes with selected relevant parameters; GA - Geometric Adventage; MA - Mechanical Adventage; $d_{in_{max}}$ - maximum output displacement; y/x - ratio of vertical and horizontal movement of the output; $F_{out_{max}}$ - maximum output force; $F_{in_{max}}$ - maximum input force; * maximum displacement of topology optimised PLA gripper is much lower than for remaining grippers due to the fact that the motion range was lowered to avoid material failure.

	Test 1	Test 2	Test 3
Analytical design: TPC	$GA = 2.660$ $d_{in_{max}} = 5.5mm$ $y/x = 12.3\%$ *underconstraint* *behaviour*	$F_{out_{max}} = 0.215N$ *underconstraint* *behaviour*	$MA = 0.091$ $F_{out_{max}} = 0.222N$ $F_{in_{max}} = 2.5N$ *underconstraint* *behaviour*
Analytical design: PLA	$GA = 2.524$ $d_{in_{max}} = 6mm$ $y/x = 11.4\%$	$F_{out_{max}} = 0.236N$	$MA = 0.005$ $F_{out_{max}} = 0.237N$ $F_{in_{max}} = 40N$
Topology optimisation: TPC	$GA = 1.465$ $d_{in_{max}} = 9.625mm$ $y/x = 25.5\%$	$F_{out_{max}} = 0.229N$	$MA = 0.019$ $F_{out_{max}} = 0.219N$ $F_{in_{max}} = 12N$
Topology optimisation: PLA	$GA = 1.040$ $d^*_{in_{max}} = 1.125mm$ $y/x = 7.6\%$ *narrow motion* *range*	$F_{out_{max}} = 0.019N$ *narrow motion* *range*	$MA = 0.021$ $F_{out_{max}} = 0.021N$ $F_{in_{max}} = 20N$ *narrow motion* *range*

timisation and produced with PLA. The selected design method in combination with the stiffer material presented some challenges with the removal of intermediate pseudo-densities, as already mentioned in Section 4.2. The finite elements that had intermediate pseudo-densities had to be left as part of the design to ensure a continuous connection between the input and output of the gripper. Those intermediate elements were preserved in the final topology with maximum density (fully occupied by the material), adding too much stiffness to the gripper. Because of this, the range of movement was very limited, and therefore full data could not be obtained without breaking the gripper during the test. As such, for the PLA topology optimised gripper it is impossible to compare its maximum input displacement or maximum force with the other grippers. This gripper never achieved full jaw closure. It is worth mentioning that to achieve a small range of motion for this gripper, a force of 20 N was needed, which is relatively high compared to the maximum forces required in the other grippers. For comparison, PLA analyti-

cally designed gripper needed 40 N, TPC analytically designed gripper 2.5 N and topology optimised TPC 12 N. Overall, compared to the other designs, the topology optimised PLA gripper did not achieve the desired function, the jaws could not be fully closed, and even a small deflection required a great amount of force while providing a very small MA - only 0.001; and GA of 1.04. Furthermore, the gripper experienced plastic deformation which is visible as a displacement of 0.19 mm measured in the gripper jaw after the last test. This is an expected outcome of the stress that surpasses the yield strength. In the future, designs like this should be post-processed to improve some of the flexibility in compliant hinges\flexures.

The TPC topology optimised gripper performed considerably better than the PLA design which was already discussed. From the GA perspective, it is the third-best gripper of the four grippers presented in this chapter. It is important to recall that due to the design assumptions taken, the topology optimised grippers were supposed to have lower GA than the analytically designed ones. The measured GA value was 1.465 and the MA 0.019. The vertical to horizontal jaw displacement ratio was 0.25, which is more than double compared to analytically designed grippers. The maximum input displacement needed to close the gripper is 9.625 mm, which is the highest of all grippers in the current chapter. As such, this efficacy of the gripper in terms of transfer of the input displacement into the output displacement was not satisfactory, which means that a significant portion of the energy was needed for the flexible deformation of the material. In the last Test 3 (input force - output displacement), the maximum measured force was 12 N and after the gripper unloaded a plastic deformation of 0.6 mm was observed. This is another proof that further re-design of the topology optimised models shall be considered to minimise stress and avoid unwanted plastic deformations. As polymers are prone to stress relaxation and creep (which was discussed in Chapter 3) and can be affected by fatigue, the maximum stress endured shall stay much below the yield strength. Some of the designs presented in this chapter had their maximum stress quite close to the yield strength, and plastic deformations occurred as discussed.

The analytically designed PLA gripper achieved a GA value close to the one calculated at the design level - 2.58 - the measured value stood at 2.524. The MA reached 0.005. This particular gripper required a force input of 40 N or a input displacement of 6 mm to fully close its jaws. This is considerably higher when compared with the two TPC designs - the analytically designed TPC gripper and the topology-optimised TPC gripper. This discrepancy underscores a significant disparity in the force requirements. The analytical design boasts the most favourable vertical-to-horizontal displacement ratio among all grippers that achieved the desired jaw force. This implies a dominant motion along the desirable x direction.

Nonetheless, it is crucial to highlight a notable drawback within the analytically designed PLA gripper: a residual displacement of 1.8 mm per jaw, which constitutes 12% of the range of motion. Detailed in Section 4.5, the gripper's capacity to revert to its initial shape in displacement-driven tests was evident. However, the force-driven tests revealed the plastic deformation mentioned. This outcome is hardly surprising, given that the maximum stress reached 98% of the material's yield strength (which was assumed based on the data in the literature as discussed in Section 3.2, inevitably leading to some level of plastic deformation in the stress-cycled compliant mechanism.

The analytically designed TPC gripper emerged as the least rigid among the quartet of designs detailed in this chapter. In Section 4.4, it is demonstrated that the lack of axial stiffness in flexures caused the gripper to behave as if it were not sufficiently constrained. This inherent lack of stiffness had ripple effects on the output load measurements, particularly due to the vast mismatch in stiffness between the gripper and the dynamometer's spring. This manifested itself as a 0.19 mm residual output deformation, which deviated in the opposite direction compared to the remaining grippers. However, unlike the plastic deformation observed in other designs, this deformation in the TPC gripper was elastic (reversible) and appeared in the opposite direction to expected. After the dynamometer was removed from the test rig, the gripper regained its original shape. The GA of the analytically designed TPC gripper topped the charts at 2.66, representing the highest amongst all the grippers showcased. Associated with this achievement was an MA of 0.91, while the maximum force required for jaw closure remained modest at 2.5 N. Interestingly, the input displacement mandated for the gripper closure measured 5.5 mm, undercutting the analytically designed PLA gripper by 0.5 mm, despite both sharing an identical geometry.

This chapter investigated two design methodologies and two materials for compliant gripper development, with four prototypes tested. Material and topology differences that were discussed in this chapter were taken into account when deciding on the prototype for the following chapter. Performance differences between grippers were observed, and the topology-optimised PLA gripper exhibited the poorest performance due to design and material challenges, leading to restricted movement and excessive stiffness. The TPC topology-optimised gripper outperformed the PLA counterpart despite energy transfer inefficiency. The analytically designed PLA gripper achieved a GA close to the design value and exhibited plastic deformation, while the TPC variant showed inadequate axial stiffness of the flexures. This section provides information on gripper design, performance, and material behaviour. The results of the tests presented here suggest some initial

conclusions about the design and testing activities of complaint grippers:

- Input force without the control of the input displacements can lead to an inaccuracy of positioning which was visible for all grippers in the tests driven by input force. In future evaluation, displacement-driven tests shall be prioritised.

- It seems that materials with a higher Young's modulus pose more challenges for topology optimisation than materials with more structural flexibility (here, TPC). To solve this, either the simulations need to be more effective at removing intermediate densities (pseudo-densities without an actual physical representation, as discussed in Section 4.2), or additional re-design steps need to be applied to reduce the stiffness of some designs.

- The force measurement equipment (dynamometer) of the output (jaws) of a gripper has an impact on the results, and the stiffness of the device used should be anticipated or tests adjusted.

- Some combinations of design methods and material selection are more successful in generating reliable results. In this study, a combination of stiffer material (PLA) with analytical design and more flexible material (TPC) combined with topology optimisation performed much better than stiff-material topology optimisation and flexible-material analytical design. This conclusion, together with material properties depicted in Figure 3.5, can suggest that the topology optimisation of PEEK gripper can be rather challenging as it was in the case of PLA gripper. The next section validates this conclusion and for the PEEK model additional re-design step was added to mitigate the impact of high stiffness of the material (this is discussed in detail in Section 5.3).

- In the future, it could also be considered to compare the experimental data with the FEA. This will have limited accuracy, as the grippers are 3D printed and their internal material structure is not easy to model. However, FEA has proved to be a useful tool for anticipating input displacement, as well as for evaluating stress.

- The precision of the linear displacement input could be improved by using other designs of screw-nut mechanisms, and it could potentially remove some of the peaks of displacements visible for small deformations in all grippers. This change was a priority for the tests presented in the next chapter.

The points considered above were an important input to the next round of tests done on new gripper prototypes introduced in Chapter 5.

CHAPTER 5

REVISED DESIGN METHODOLOGY AND TESTING: PLA AND PEEK GRIPPERS

In this chapter, improved versions of compliant grippers will be presented. Compared to the previous Chapter 4, significant upgrades have been achieved in both the testing methodology as well as in the design process. All these enhancements will be presented in the following Sections 5.1 and 5.2. Two types of grippers will be presented: one made of PLA (Section 5.3) and another type made of PEEK (Section 5.4). Furthermore, two PEEK grippers were manufactured, one of them was subject to thermal post-processing, which will be discussed in the corresponding section. The reasons for such an approach and the test results will be explained in more detail in this chapter. It is important to note that Z-PEEK - PEEK from the commercial company Zortrax that was used in this work - is space-grade material evaluated by the European Space Agency [164]. The collaboration with Zortrax and Astronika - a company specialising in space mechanisms - contributed to the content of this chapter and the publication titled "Design, manufacturing, and testing of 3d printed compliant mechanisms for lunar equipment" [165] which was presented at the European Space Mechanisms and Tribology Symposium.

5.1 TOPOLOGY OPTIMISATION WITH ANALYTICAL ENHANCEMENT

In this section an updated design methodology will be discussed. The initial design step utilised is the Koppen method [119] also presented in Chapter 4. On top of the constraints presented in the previous chapter (volume and compliance constraints), an additional stress constraint was added to improve the results. In the context of compliant mechanisms, the stress constraint refers to the limitation

imposed on the maximum stress levels experienced by the mechanism under simulated loads (and displacements). Excessive stress can lead to material failure, permanent deformation, or reduced lifespan of the mechanism. Therefore, it is crucial to ensure that stress levels in compliant mechanisms remain within acceptable limits of yield strength to avoid plastic deformation. Moreover, from the optimisation point of view, stress constraint can help to avoid forming topologies with so-called point flexures (areas with very localised compliance). An example of the impact of stress constraint on point flexure formation is visible in Figure 5.1.
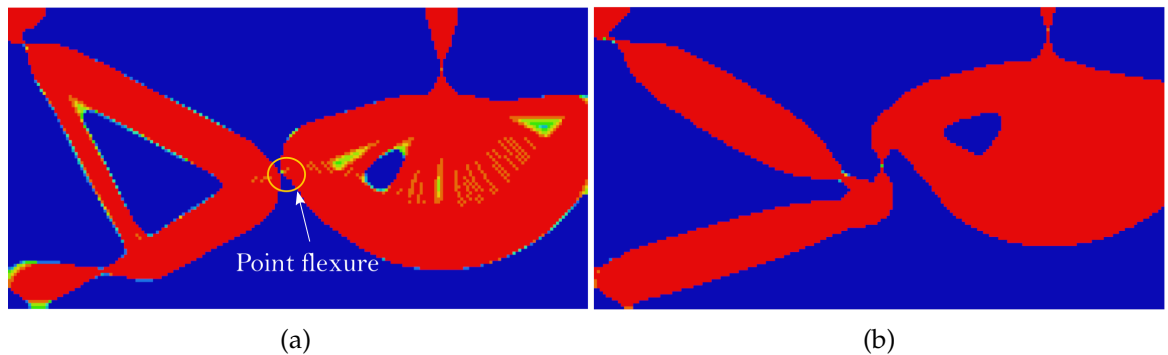
Figure 5.1: Example of topology optimisation (a) without stress constrained - with visible point flexure, (b) with stress constraint.

The examples in Chapter 4 demonstrated the challenges associated with using topology optimisation for stiffer materials and large displacements. This problem is also discussed in the literature written on the basis of the work published in IOP Conference Series: Materials Science and Engineering [14]. To avoid excessive stress and plastic deformation in a large displacement range, an additional design step was needed to adjust the stiffness of the flexures.

Section 2.5 discussed various methods used to influence stiffness, in short: geometry, topology, or material change. For the grippers presented in this chapter, the adjustment was achieved by controlling the geometry, specifically the thickness of the flexures while ensuring the minimum possible wall thickness for manufacturing purposes. Additionally, elongation of the flexures was applied. Figure 5.2 illustrates an example of such an alteration, where a single flexure is shown. In the first drawing (a), the flexure is depicted, while in (b), the nonlinear FEA results reveal high levels of stress, which are undesirable. To minimise stress, adjustments are made to the width and length of the flexure, as demonstrated in Figure (c). As a result, the updated FEA shows a reduction in stress while maintaining displacement identical to that shown in Figure (b).

It is important to note that reducing the thickness of the flexures can effectively minimise stress while maintaining the desired displacement. However, it may not be feasible to produce extremely thin flexures using 3D printing technology. There-

(a) Flexure example design.

(b) Nonlinear FEM analysis of flexure from (a); von Mises stress (no scale, visualisation of stress levels).

(c) Improved flexure designed - red, original design from (a) - grey.

(d) Nonlinear FEM analysis of flexure from (c); von Mises stress (no scale, visualisation of stress levels).
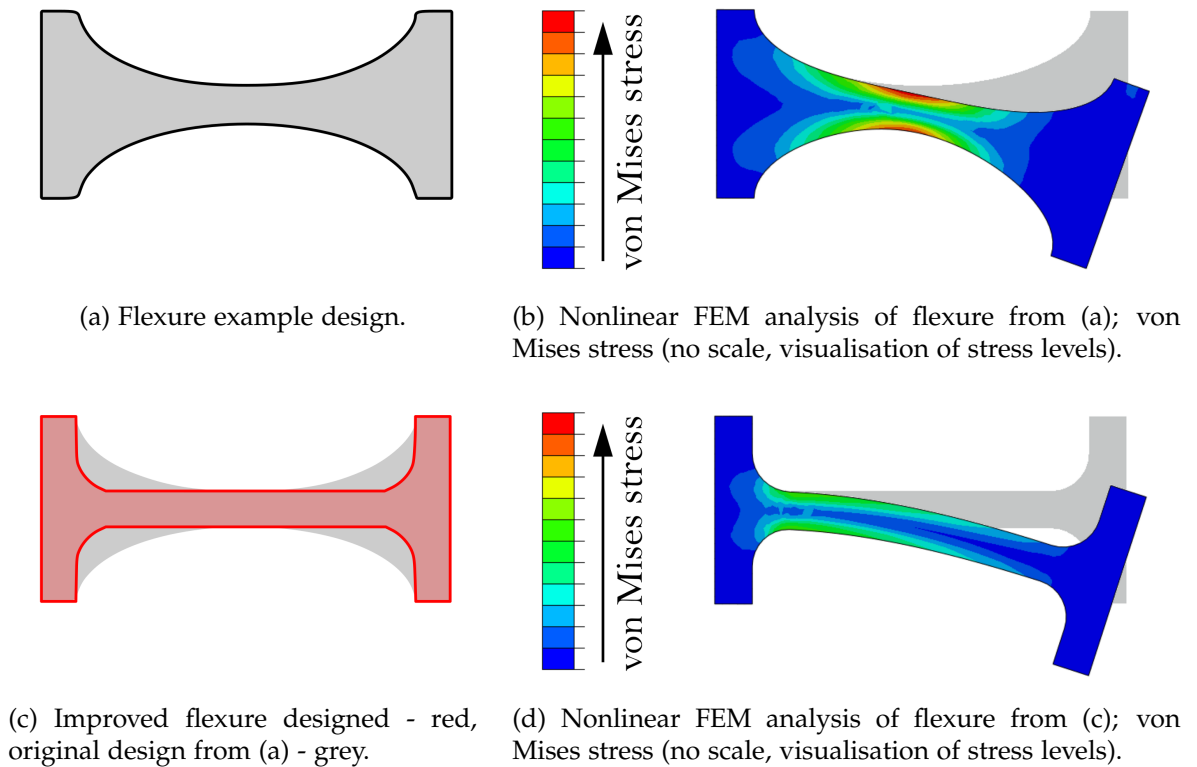
Figure 5.2: Design steps undertaken to improve flexure design; visualisation of re-design analytical step aiming at minimising stress while keeping the same desired displacement.

fore, it is crucial to consider the minimum wall thickness parameter specific to the printer and nozzle that are used. This value represents the absolute minimum for designing flexures. In this project, it was determined that flexures with a thickness of 0.8 mm can be manufactured using the available equipment. Therefore, this value is established as the minimum thickness for the flexures in this particular context.

5.2   TESTING: METHODOLOGY IMPROVEMENTS

The objective of the test campaign presented in this chapter, similar to the one presented in Chapter 4, was to determine the Geometric Advantage (GA), Mechanical Advantage (MA) and relationship between forces and displacements of the gripper system. Three different sets of tests were conducted, and each test was repeated three times. The test detials are provided below:

- Test 'a'

  providing information about the relationship between displacements and about GA:

  – input - linear displacement achieved by miniature optical linear bench with micrometre screw,

  – output - displacement measurement (Digital Image Correlation - DIC).

- Test 'b'
  examining the relationship between input force and output displacement:

    – input - force supplied through force gauge,

    – output - displacement measurement (Digital Image Correlation - DIC).

- Test 'c'
  providing information about the relationship between forces and about MA:

    – input - force supplied through force gauge,

    – output - force measurement (dynamometer).

The equipment and measured parameters of the tests listed above are also depicted in Figure 5.3 and will be discussed further. It is important to note that Test 'b' has been modified compared to the previous test campaign in Chapter 4. In the previous version, a linear input displacement was used and both force and displacement measurements were taken at the output. However, as discussed in Chapter 4, the force measurement at the output interferes with the precise positioning of the output, so the test was not continued in that form. Instead, the test mentioned above as 'b' was conducted to gather information about the hysteresis of the system.

To facilitate the use of the Digital Image Correlation tool, which will be discussed later, the measurement of the output point was taken on the left jaw of the gripper, whereas in the previous test campaign (Chapter 4), it was done on the right jaw. Furthermore, tests 'a' and 'b' were also repeated while using the lunar regolith simulant EAC-1A [166] for the PEEK gripper, which is made of space-grade material. On the other hand, the PLA gripper was subjected to all tests without the presence of the lunar regolith. Another parameter refined in the new set of tests is the improved resolution of the input displacement, in the data presented here it is 0.1 mm.

Figure 5.3 provides an overview of the equipment and measurements used in all tests discussed in this chapter. For measuring the input force, a digital force gauge with a maximum force of 250 N and a resolution of 0.1 N was employed. The output force was measured using a dynamometer with a maximum force of 1 N, a resolution of 0.02 N, and a spring stiffness of $\frac{1}{60} \frac{N}{mm}$.To enhance the resolution of the dynamometer, a photo-processing technique was applied for displacement measurements. Specifically, a reading indicator displacement of 60 mm corresponded to 1 N. Taking into account any intermediate displacement of the spring, the corresponding force was calculated based on the linear relationship between force
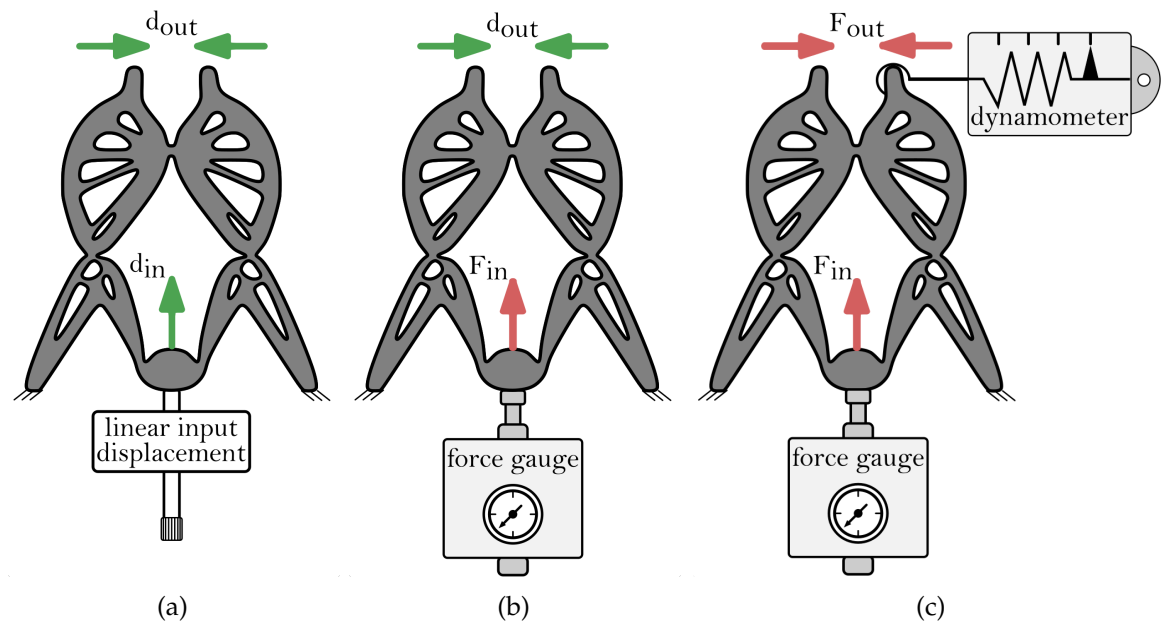
Figure 5.3: Sketches of three types of tests described above. Green arrows represent measured displacements, red arrows represent measured forces.

and displacement. The input displacement was applied in 0.1 mm intervals, as already mentioned, while the input intervals of force were set to 0.5 N. The input displacement mechanism, which was previously provided by the screw nut mechanism (Chapter 4), was also updated to a precision linear table equipped with a micrometre screw; this update is presented in Figure 5.4.
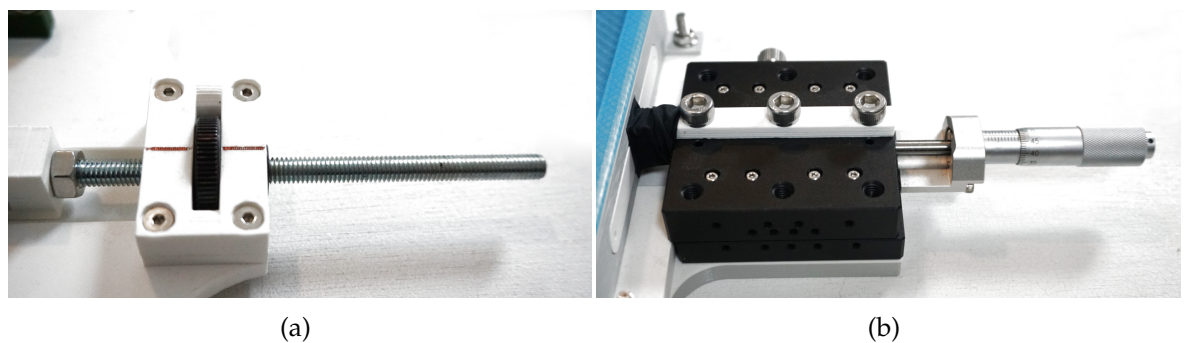
Figure 5.4: Input displacement mechanism a) old version with M6 screw-nut mechanism, b) new version with linear table equipped with micrometer screw.

Figure 5.5 illustrates the additional components integrated into the test rig to facilitate image calibration during data post-processing. To enable Digital Image Correlation using the open-source MatLab code Ncorr [167], the grippers were painted with a black and white speckle pattern. Additionally, a static calibration patch, featuring the same speckle pattern, was installed to eliminate any displacement between images - having a fixed landmark was a safety feature to be able

to remove any shift between pictures during post-processing. A ruler was also attached to the test rig for calibration of the displacement values. The blue coordinate system in Figure 5.5 denotes the output point for which the putput displacement measurements presented in the subsequent sections were taken.
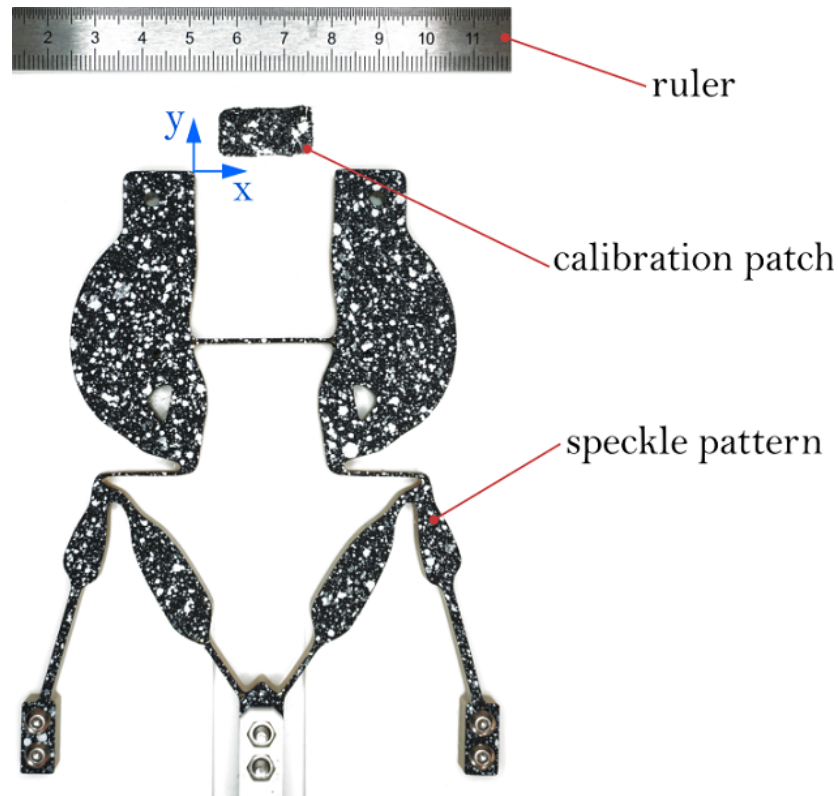
Figure 5.5: Calibration items embedded into test rig.

Each test produced output data in the form of equipment readings and photographs that captured the displacements of the speckles (in the speckle pattern visible on the surface of the gripper). ImageJ, an image processing and calibration software, was used for post-processing of the photographs in order to convert them into 8-bit format (to reduce the data size), remove any unwanted shift, and crop pictures to size needed in the next step. The displacement values were then determined by post-processing pictures (and the deformation of the speckle pattern) in the DIC tool - Ncorr [167].

Digital Image Correlation (DIC) is a non-contact full-field optical technique that enables the measurement of surface deformation and strain of solid objects under various loading conditions [168, 169]. DIC compares images of the object of interest captured before and after deformation. To ensure reliable and accurate matching of information between images, it is necessary to select subsets of the object's surface that contain sufficient intensity variations, allowing unique and accurate identification in the deformed image [169]. This requires the use of a speckle pattern on the

object's surface that deforms along with the specimen during testing and is subsequently used as a carrier of surface deformation information during DIC analysis. Speckle patterns can be natural, such as those found in the texture of the object's surface, or artificial patterns created by spraying white and / or black paint on the surface [168, 169]. The images are then analysed to determine the displacement of each point on the object's surface, and, subsequently, the strain field can be calculated. DIC has wide applications in mechanical, civil, and aerospace engineering, material science, biology, and many other fields where precise measurements of surface deformation and strain are essential.

DIC has several advantages over traditional strain measurement techniques. It provides detailed information about the displacement and strain distribution across the entire surface of the object. Moreover, it is non-intrusive, meaning it does not require direct contact with the object under test, minimising the risk of altering the behaviour of the specimen. It is a versatile technique that is applicable to a wide range of sample sizes. The resolution of DIC analysis can be adjusted to accommodate various length scales by selecting an appropriate pixel size. For example, in some applications, a single pixel may correspond to a distance of 1 cm, while in other cases it may correspond to a distance of 1 μm [170]. With advances in digital imaging technology, such as high-speed cameras and improved image analysis algorithms, DIC has become a powerful tool for researchers and engineers to better understand the behaviour of materials under various loading conditions.

In this particular study, the DIC technique served as a valuable tool to precisely track the movement of the gripper's output point throughout its deformation. Additionally, it was utilised to generate a comprehensive colour map that visually represents the overall deformation of the gripper, effectively presenting the system's response to input forces and displacements.

The decision was made to adopt an open source solution compatible with MatLab, specifically Ncorr [167]. Ncorr proves to be an efficient tool specialised in 2D DIC, offering an intuitive Graphical User Interface (GUI) that can facilitate large strain analysis. In particular, this tool excels at accommodating data sets with substantial deformations by automatically updating the region of interest (ROI). To illustrate, Figure 5.6 depicts the Ncorr GUI, where the 'High-Strain Analysis' option must be selected to achieve optimal results for this project. Given the significant magnitudes of deformations and displacements observed in the tests conducted for this study, Ncorr's ability to handle large strains rendered it an invaluable asset. Consequently, the large strain option for all analyses was selected in the GUI for all examples presented in this work.

The literature also assesses the Ncorr methodology by comparing it with com-
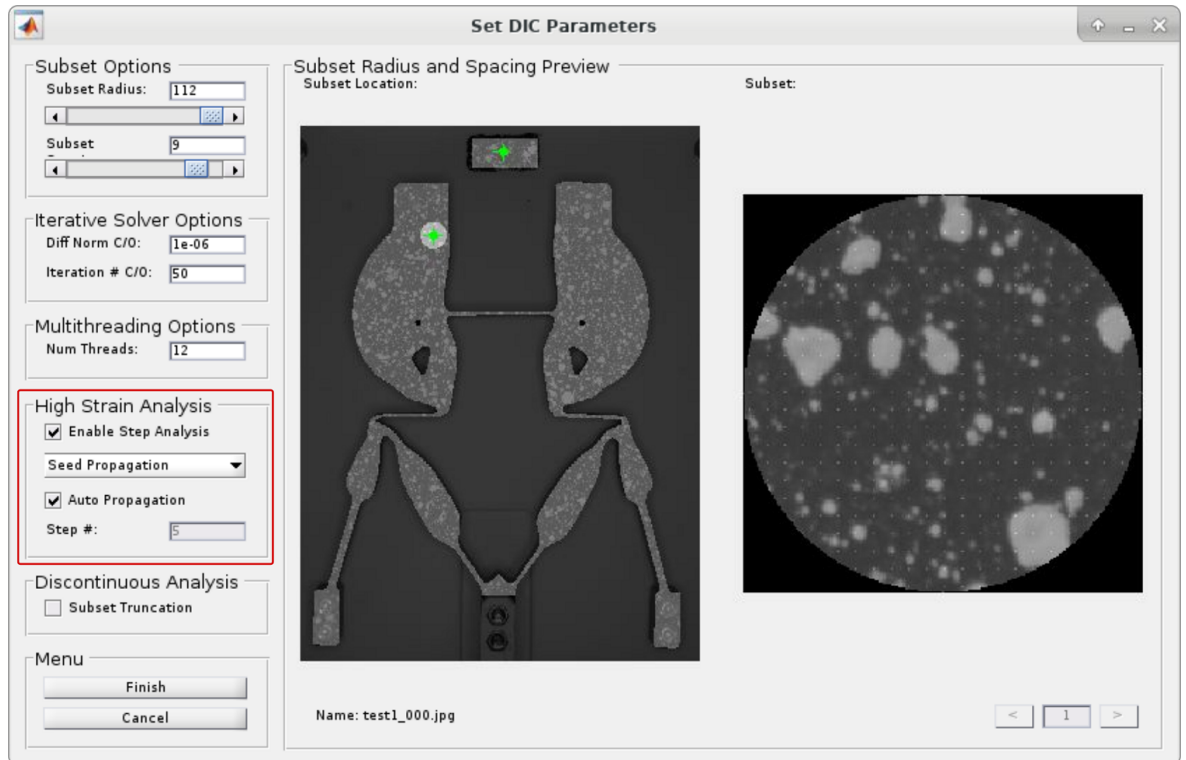
Figure 5.6: Ncorr GUI, setting DIC parameters, including high strain analysis (marked in red), for compliant gripper.

mercial software, and the results indicate that it is a very capable tool [171]. To use Ncorr in this work, the samples needed measured surfaces to be adequately prepared. Grippers presented in this chapter were painted with black matt paint and then a white speckle pattern was applied by low pressure spraying. The result is a stochastic speckle pattern that will be visible on all grippers presented in next sections. The test rig also includes a stainless steel ruler that was used to calibrate the displacement values from the pictures, which is one of the steps of the analysis in Ncorr. The basic data visualisation functionality of Ncorr presents displacements and strains as a colour map in the ROI. Nevertheless, all the data is stored in matrices available through the MatLab user interface. As such it is possible to access displacements of any given point in ROI which is how the data for output point of the gripper was collected. In addition, horizontal displacements were scaled to their absolute values to better visualise the deformation of a gripper (which is symmetric) - this is also presented in Figure 5.7. The following sections will present data acquired during the tests that used the tools and methodology discussed here.
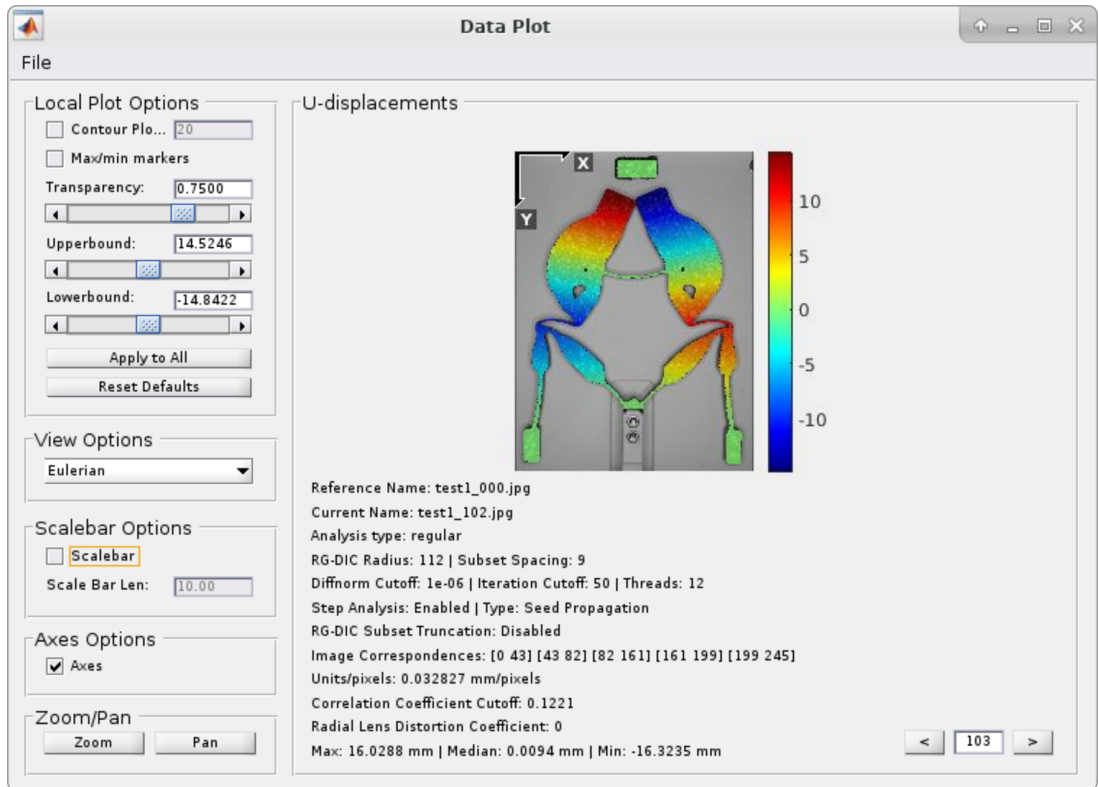
(a)
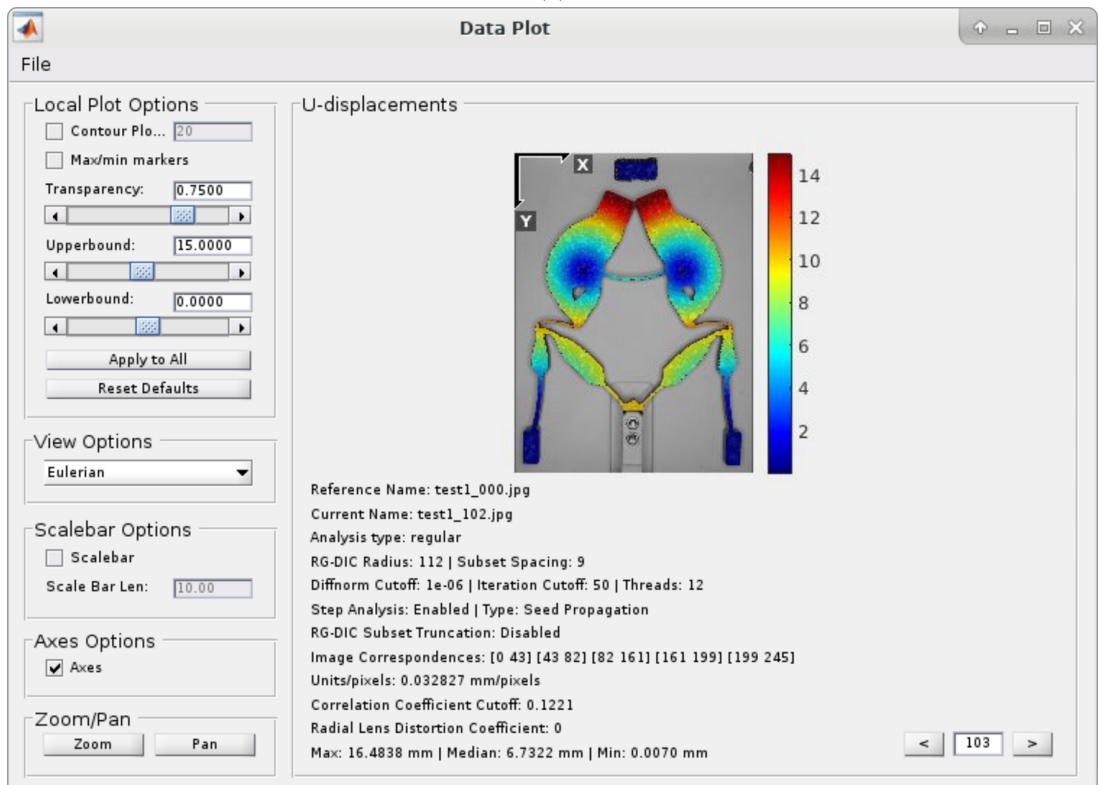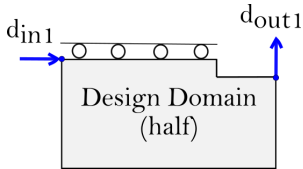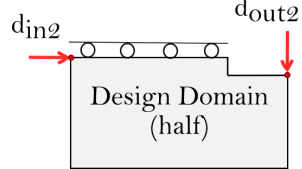
(b)

Figure 5.7: Adjustment of the horizontal displacements scale in Ncorr: (a) original data processed by Ncorr, (b) data after applying absolute value function to avoid displaying negative values of the displacements - showing displacement magnitude (without the direction).

5.3 TOPOLOGY OPTIMISED ENHANCED PLA GRIPPER

The topology optimisation using two loading cases was already described in a Chapters 2 and 4. Adjustments made to the topology optimisation process and additional analytical steps were also discussed in Section 5.1 of this chapter. A summary of the design parameters for the PLA gripper discussed here is presented in Table 5.1.

Table 5.1: Topology optimisation design parameters for PLA gripper.

	Load case	
	I	II
Input (d_{in}) [mm]	+ 1	+ 1
Output (d_{out}) [mm]	+ 1	- 1
Objective	-	maximise compliance
Constraints	compliance $\leq$ 0.1 Nmm	-
	volume fraction $\leq$ 0.4	
	stress constraint $\leq$ 60 MPa	
Max. iteration no.	500	
PLA Young's modulus [MPa]	3000	
PLA Poisson's ratio	0.33	

The selection of the stress constraint value was determined by a process of trial and error. Multiple iterations were conducted to explore various parameter values and assess their effect on the topology, which is presented in Figure 5.8. As visible changes in the stress constraint have an impact on the geometry of compliant hinges. 60 MPa, which is a value resulting in longer flexures, was chosen to allow for large displacements and to minimise stress in the next design steps.

The intermediate topologies achieved during the optimisation process can be seen in Figure 5.10, showcasing the progression of the design as it underwent 445 iterations. To achieve the final design, a post-processing step was used, in which finite elements with densities (or pseudo-densities as defined in Section 4.2) below
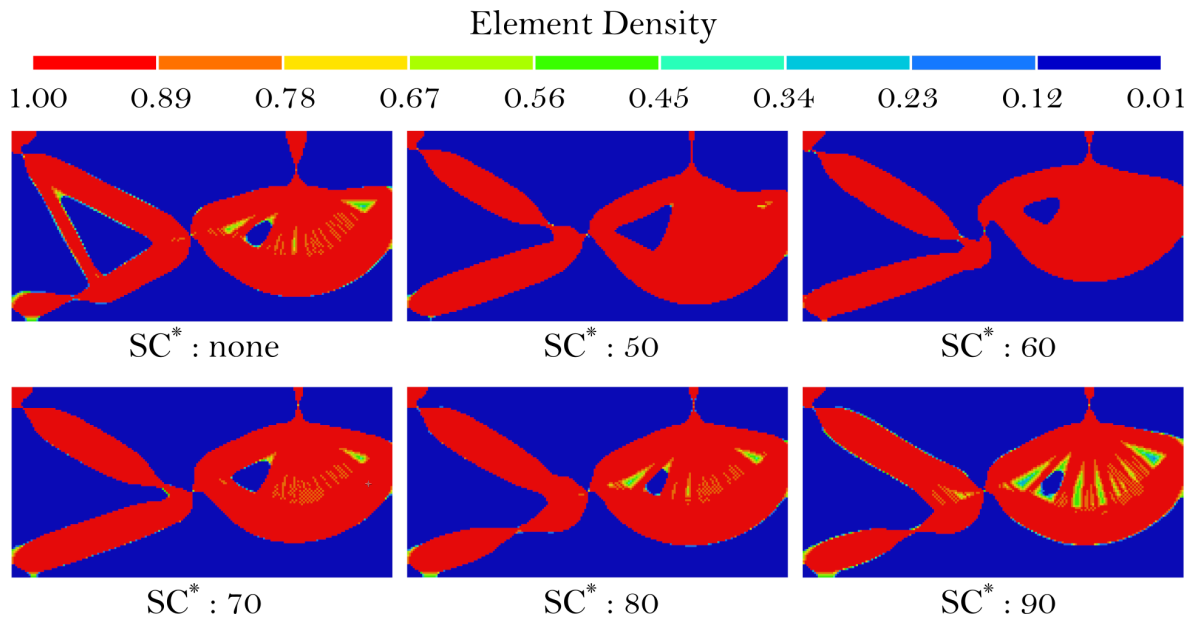
Figure 5.8: Different stress constraint levels and their impact on final topology of PLA gripper; *SC - stress constraint (values in MPa).

0.3 were removed from the design domain. As discussed in the previous chapter, the design needs to be transferred into binary state to allow for 3D printing. This is due to the fact that printing with lower infills (which could reduce the density) does not scale the mechanical parameters of the material accordingly. As with the previous examples of topology optimisation presented in Chapter 4 the selection of exact threshold for the densities removal was based on the avoidance of material discontinuities as depicted in Figure 5.9.
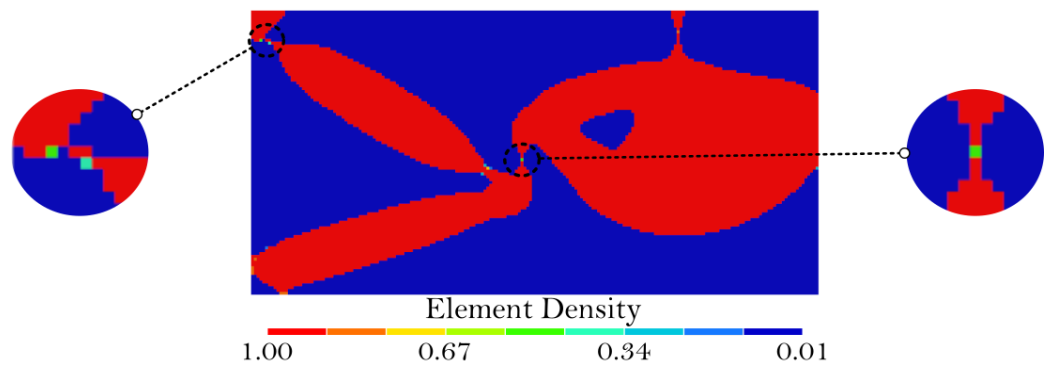
Figure 5.9: Density threshold selection for topology optimised PLA gripper - problematic low density areas marked by dashed circles and enlarged.

Building upon the optimised topology, the subsequent design step involved mirroring the final topology to achieve a fully symmetric gripper design. Furthermore, to augment the gripper's capabilities, specific features such as jaws and mounting holes were added to the model. These additions serve to enhance gripping functionality and provide convenient attachment points, resulting in a comprehensive

and functional design, as presented in Figure 5.11a.
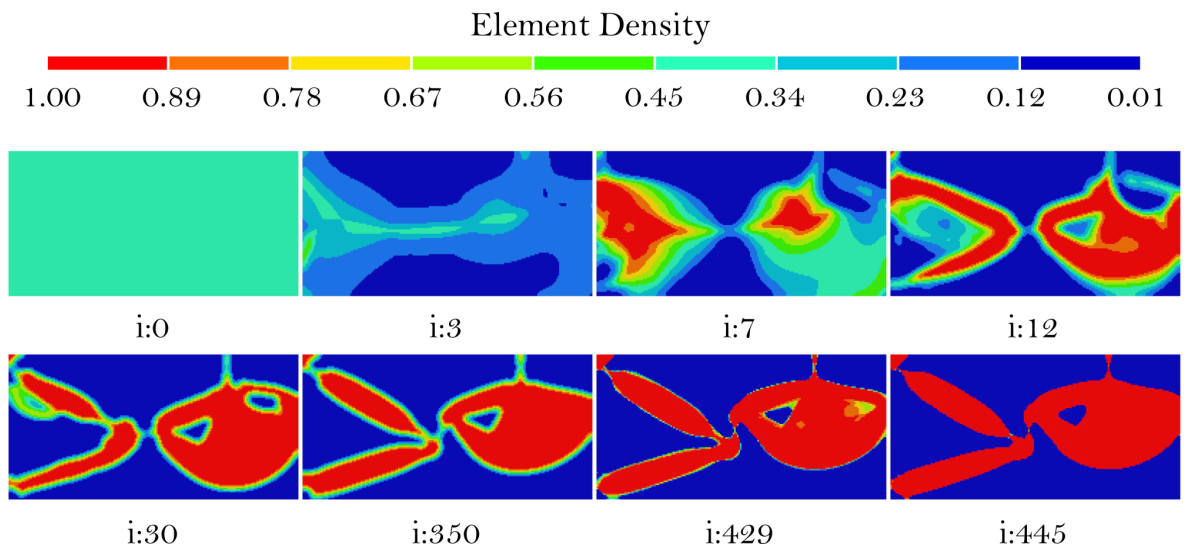
Figure 5.10: Topology optimisation of PLA compliant gripper: evolution of density colour map; *i* - iteration number.

The desired kinematic behaviour of the gripper should allow for full closure of the jaws. As such, the nonlinear FEA conducted looked at the stress distribution of a model with input displacement large enough to achieve the maximum output displacement corresponding to the closure of the gripper, which is illustrated in Figure 5.11b. The exact value of the input displacement in the model is 8.4 mm. During the analysis, it was observed that the stress exceeded the assumed Yield strength of PLA - 60 MPa. All stress values exceeding that number were marked in red in Figure 5.11b and the maximum value reached 255.8 MPa.

To address the issue of high stress concentration, an analytical re-design step was employed, in which the length of the flexures was extended while maintaining a minimum flexure thickness. This simple modification allowed a decrease in stress while preserving the same displacement of the output. This improved the overall performance and reliability of the gripper. The resulting re-designed gripper is marked in red in Figure 5.11c, showcasing the extended length of the flexures.

Subsequently, another round of FEA was performed using the updated model. The results are shown in Figure 5.11d. The updated analysis revealed a maximum stress value of 54 MPa, representing a significant stress reduction compared to the levels achieved in the previous design iteration (see Figure 5.11b). The input displacement needed to achieve gripper closure was also reduced to 8.2 mm. The mesh used in the model is presented in Figure 5.11b. As visible, the size of the mesh was reduced in the flexure areas that were expected to experience the highest strains, while the stiffer areas of the design had a coarser mesh (0.25 and 1.25 mm respectively). Figure 5.11b shows the FEA of a load case where the input
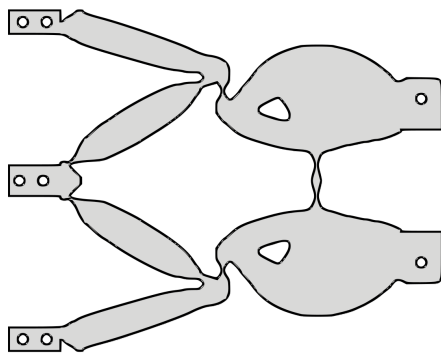
(a) Gripper designed based on the optimised topology.
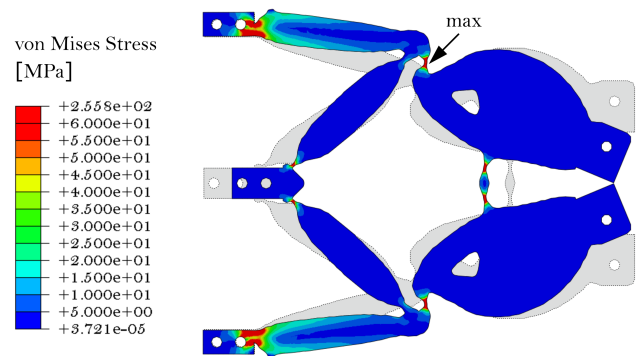
(b) Nonlinear FEM analysis of gripper from (a); von Mises stress.
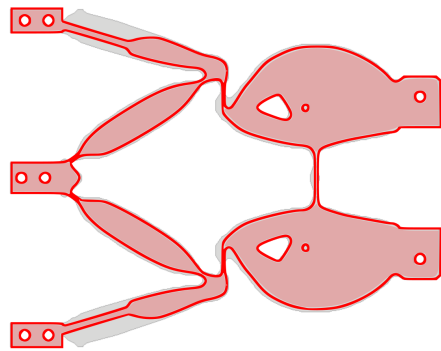
(c) Improved gripper designed - red, original design from (a) - grey.
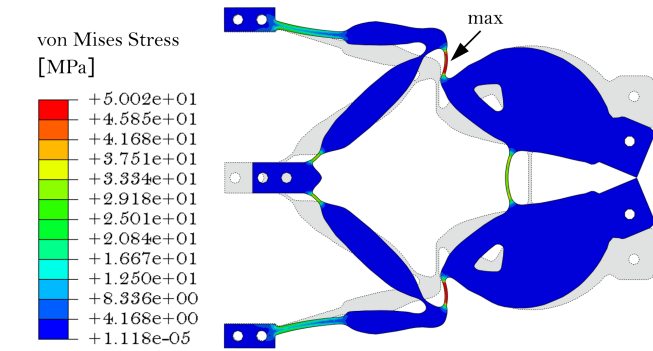
(d) Nonlinear FEM analysis of gripper from (c); von Mises stress.
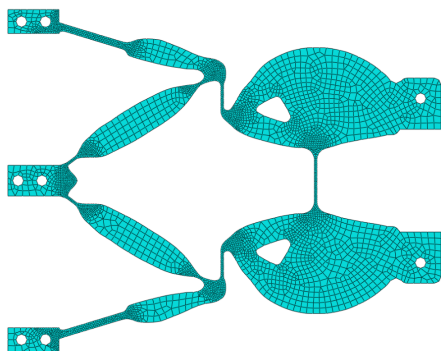
(e) Mesh used in the analysis (size range: 0.25 - 1.5 mm).
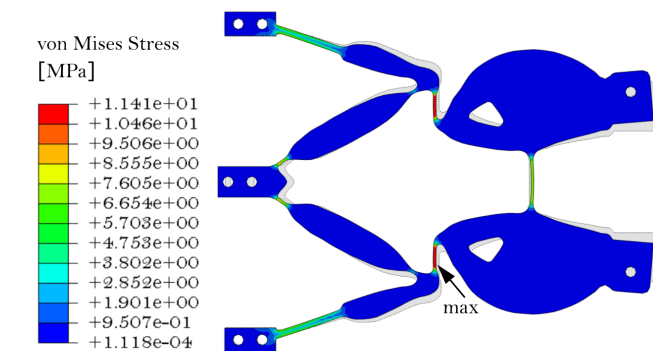
(f) Nonlinear FEM analysis of gripper from (c); von Mises stress; gripper opening.

Figure 5.11: Various design steps undertaken to produce compliant PLA gripper.

displacement works in the direction to open the gripper beyond its default position. In this case, 2 mm of input dicplacement was applied in the opposite direction compared to the analysis presented in Figure 5.11b. In this case, the maximum

stress reached around 11 MPa and was localised in the same flexure region.

By integrating the advantages from both the topology optimisation and analytical re-design processes, a comprehensive solution was achieved. The topology optimisation stage facilitated the identification of an optimised general topology (and flexures distribution), while the analytical re-design phase fine-tuned flexures' deformation-stress performance. The iterative combination of these steps ultimately led to the development of a gripper design that exhibits superior structural integrity while fully deformed, as confirmed by the reduced stress levels observed in the final FEA results.

In the following paragraphs, the data acquired from the tests described in Section 5.2 are presented. All tests were carried out on the same PLA compliant gripper, manufactured according to the design presented in this section.

In order to facilitate the subsequent Digital Image Correlation (DIC) analysis, the gripper was subjected to a specific surface preparation process. As previously mentioned, this involved the application of black paint to the gripper's surface, followed by the spraying of a white speckle pattern. This meticulous procedure ensured optimal contrast and visual tracking of the gripper's deformation throughout the testing process.

The resulting gripper deformation, along with the corresponding speckle pattern, is visually represented in Figure 5.12. The DIC technique, which combines visual tracking and deformation measurement, allowed for a precise understanding of the gripper's performance, which will be further discussed in this section.
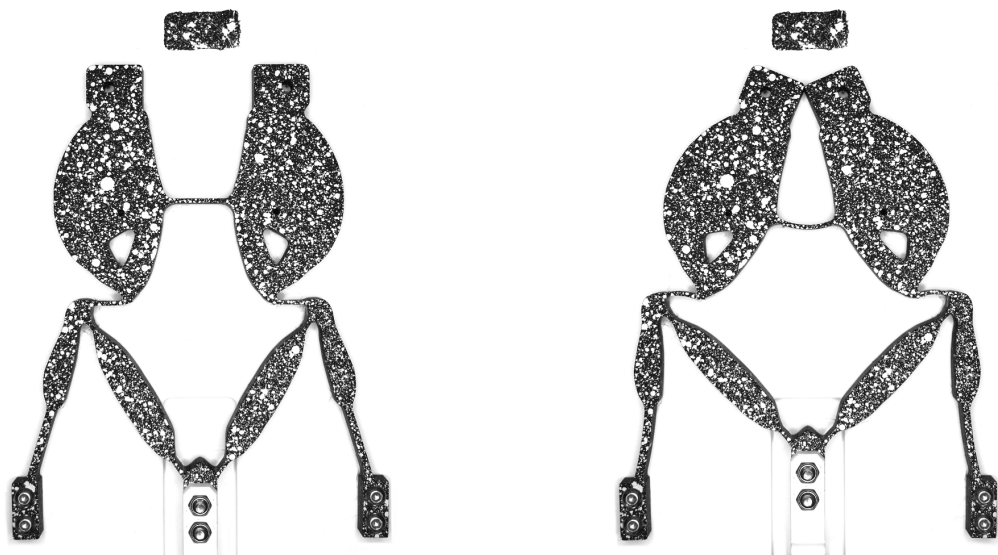
(a) Unreformed gripper mounted in the test rig, speckle pattern visible.

(b) Fully deformed gripper mounted in the test rig, speckle pattern visible.

Figure 5.12: Unreformed and fully deformed enhanced PLA gripper during test 'a'.

The fully deformed gripper configuration, achieved through a linear input displacement of 8.8 mm, is illustrated in Figure 5.12b. During the design process, nonlinear FEM analysis was used to predict the input displacement required for complete gripper closure, which was estimated to be 8.2 mm. It is evident that a longer stroke was necessary in the test to fully close the physical gripper. This disparity between the FEM model and the test data can be attributed to the fact that the FEM analysis assumed a homogeneous material, whereas 3D printed materials can contain pores, even with the printing settings of 100% infill. This fact and other inherent imperfections in the printed material can influence its mechanical behaviour, leading to variations between the predicted and actual performance of the gripper. At the same time, it is important to note that due to the lack of mechanical properties data provided by the PLA filament supplier, some mechanical characteristics were initially estimated based on the literature as explained in Chapter 3 Section 3.2. However, this disparity between FEM and tests is not problematic for further discussion.

(a) Input-output displacement relationship. Max. standard deviation 0.066 mm.

(b) Path of the left gripper jaw. Max standard deviation X: 0.066 mm, max standard deviation Y: 0.061 mm.
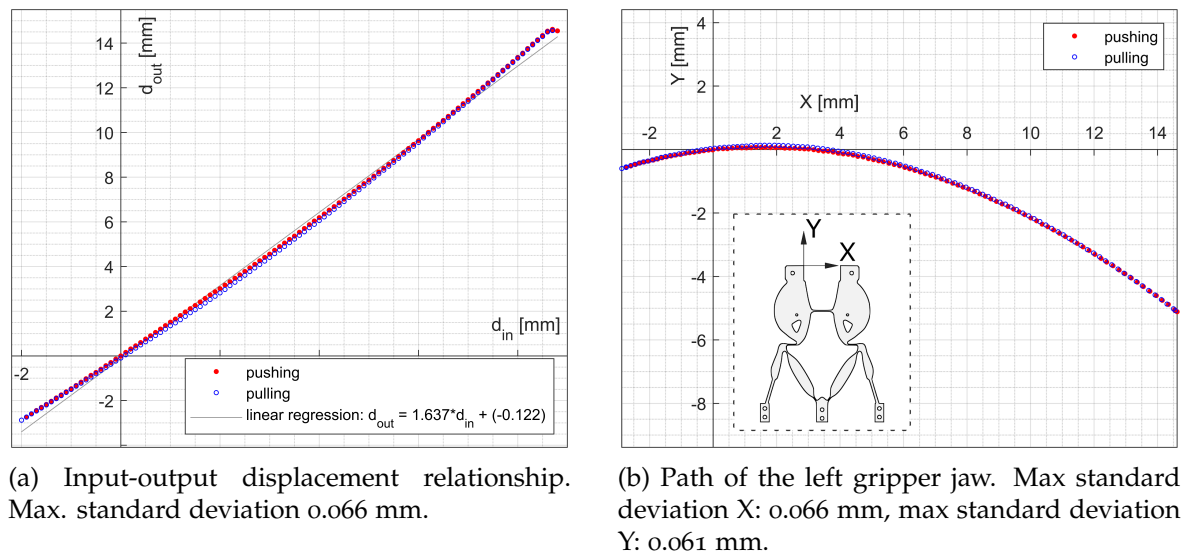
Figure 5.13: Improved PLA gripper - test 'a' data: displacements and motion.

Figure 5.13a shows the correlation between the linear input displacement (d_{in}) and the corresponding desired output displacement in the horizontal direction (d_{out}). The data set that encompasses both gripper closing (illustrated in red) and opening (in blue) was obtained by exerting displacement on the input for closure and releasing the input to enable the gripper to use stored strain energy for elastic deformation release. The evaluation of the Geometric Advantages (GA) parameter, which represents the ratio of the output displacement in the desired direction to the input displacement, was accomplished through linear regression analysis. The resulting GA value of 1.637, as specified in the legend of Figure 5.13a, serves as

an indicator of the gripper's ability to translate input displacement into desired output displacement.

Figure 5.13b complements the analysis by illustrating the precise trajectory of the tip of the left jaw, which serves as a point of interest. Consistent with the previous figure, the red data set corresponds to the gripper closing, while the blue data set corresponds to the gripper opening. In particular, both data sets exhibit remarkable similarity and negligible standard deviations. Although the figures do not depict these small standard deviations due to their magnitude, the respective maximum values are mentioned in the figure captions.

It should be noted that the vertical displacement range of 5.25 mm constitutes approximately 30% of the horizontal (intended) displacement range, which spans 17.5 mm. Despite the significant contribution of the vertical direction to the overall displacement, the intended direction remains dominant, signifying the gripper's performance in achieving the desired displacement.

(a) Horizontal displacement magnitude [mm].   (b) Total displacement magnitude [mm].
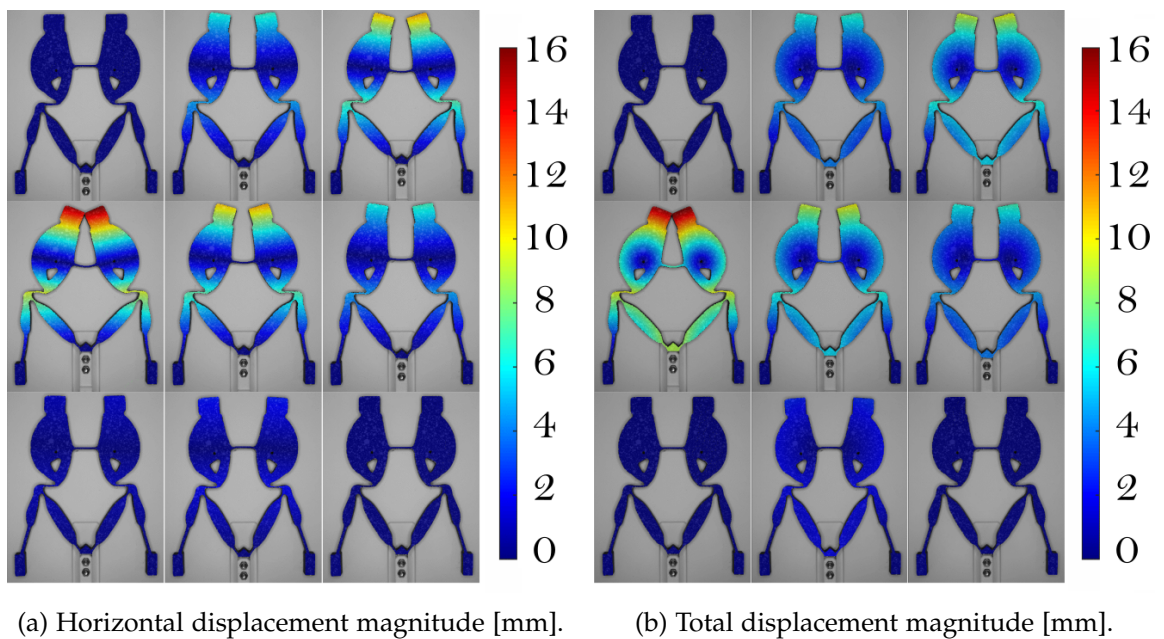
Figure 5.14: Test 'a' Digital Image Correlation data of PLA improved gripper.

Figure 5.14 presents a visual representation of the data collected during DIC analysis. This figure demonstrates the overall deformation of the gripper by presenting the displacements of individual points located on its surface. To provide further insight, Figure 5.14a specifically focuses on the desired output direction, namely horizontal displacement. On the other hand, Figure 5.14b illustrates the magnitude of the total displacement, encompassing both horizontal and vertical components. In both figures, the bottom rows depict a slight opening of the gripper beyond its default position, while the top two rows portray the gripper in closed and semi-closed configurations. These visual representations serve to elu-

cidate the elastic and kinematic behaviour of the gripper throughout the tests. By highlighting the displacements of individual points on the gripper's surface, the figures provide valuable insights into the extent and distribution of deformation across different configurations.

Figure 5.15a presents a comprehensive representation of the Geometric Advantage (GA) as it evolves with varying input displacements. Unlike in Figure 5.13a, where GA was calculated using linear regression for the entire data set, here it is calculated individually for each measurement point. This calculation involves dividing the input displacement in the horizontal direction by the corresponding output displacement. The graphed data reveal that the GA is not a constant value but rather varies depending on the position of the gripper. Furthermore, for comparative analysis, the GA value of 1.637 obtained from Figure 5.13a is included, along with the GA value of 1 indirectly indicated during the topology optimisation phase of the gripper design. This value arises from the fact that the prescribed input and output displacements were equal to 1, resulting in a ratio of 1.

(a) Test 'a' Geometric Advantage (GA). Max. GA standard deviation: 0.440.

(b) Test 'b' input force - output displacement relationship. Max standard deviation of d_{out}: 0.261.
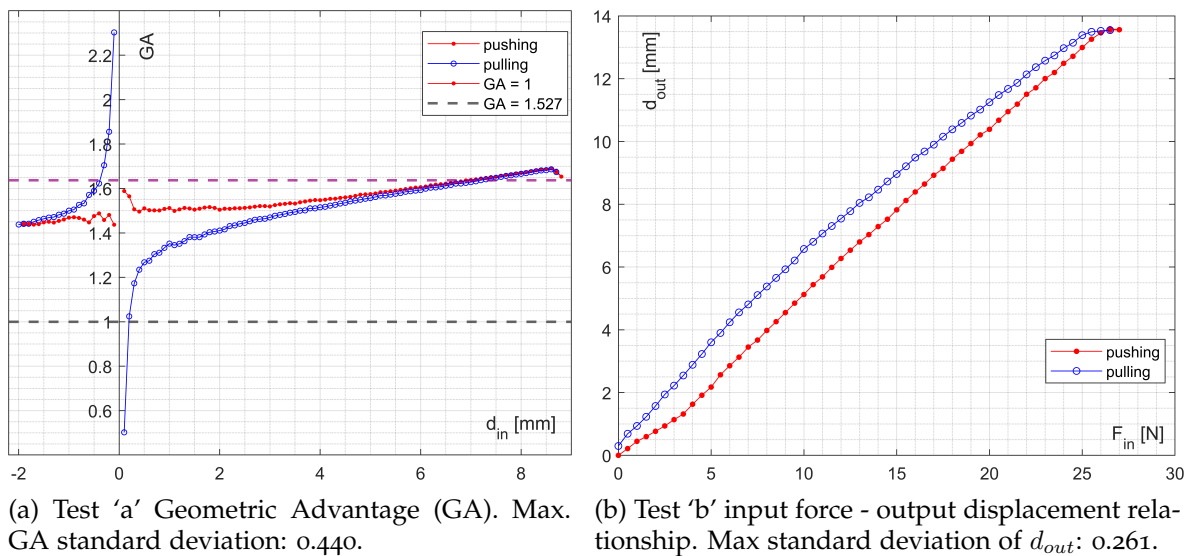
Figure 5.15: PLA improved gripper - test 'a' and 'b' data.

In Figure 5.15b, the relationship between the input force, measured by the force gauge, and the horizontal output displacement during Test 'b' is depicted. This visualisation depicts the gripper's hysteresis, which is an anticipated phenomenon given the magnitudes of deformation involved. Additionally, a small deformation is observable after the test - it is visible that the 'pulling' curve does not come back to point 0 at the end of the test. A deformation of 0.13 mm persists. This is a fairly small deformation that constitutes around 0.8% of the motion range for the gripper jaw. Furthermore, the gripper recovers its original shape when mounted back into the displacement-driven test set-up, meaning that the relationship between the

input and output positions is intact. This is another instance where displacement-driven control provides more precision in terms of positioning accuracy.

Data collected from Test 'c', where the input force was applied using a force gauge, is presented in Figure 5.16. The figures employ the same colour scheme as before, with red and blue denoting the motion associated with pushing and retracting, respectively, as with previous examples. The relationship between the input force and the corresponding output force is depicted in Figure 5.16a, which again reveals the presence of hysteresis. Additionally, the grey line in the figure represents the linear regression analysis. The slope of this regression line signifies the mechanical advantage (MA), which represents the ratio of the output force to the input force. Analysis of the graph indicates an MA value of 0.008.

(a) Input force - output force relationship. Max standard deviation of F_{out}: 0.007.

(b) Input force - MA relationship. Max standard deviation of MA: 0.011.
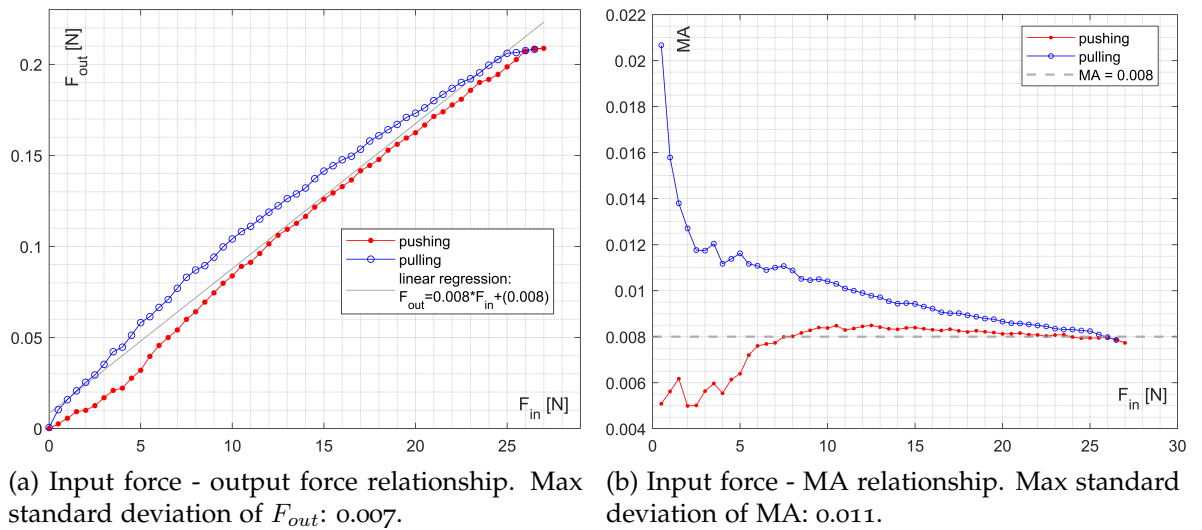
Figure 5.16: PLA improved gripper - test 'c' data.
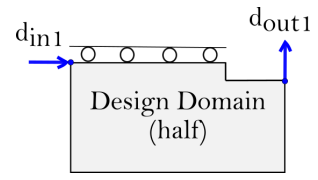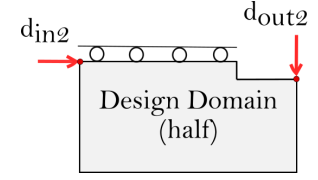
Figure 5.16b focuses on the MA values calculated individually for each gripper position by dividing the output force by the corresponding input force. MA values exhibit variations across different deformation positions of the gripper and are subject to changes depending on the direction of the gripper's deformation.

5.4   TOPOLOGY OPTIMISED ENHANCED PEEK GRIPPERS

The same topology optimisation approach used in the case of Section 5.3 was also applied to the PEEK grippers. The parameters of the model and the topology optimisation process for the PEEK grippers discussed in this section are presented in Table 5.2.

The selection of the stress constraint followed a systematic process that involved iterative exploration and evaluation of various parameter values. This trial-and-error methodology, consistent with the previous PLA gripper example, aimed to

Table 5.2: Topology optimisation design parameters for PEEK gripper.

	Load case	
	I	II
Input (d_{in}) [mm]	+ 1	+ 1
Output (d_{out}) [mm]	+ 1	- 1
Objective	-	maximise compliance
Constraints	compliance ≤ 0.1 Nmm	-
	volume fraction ≤ 0.4	
	stress constraint ≤ 70 MPa	
Max. iteration no.	500	
PEEK Young's modulus [MPa]	3720	
PEEK Poisson's ratio	0.38	
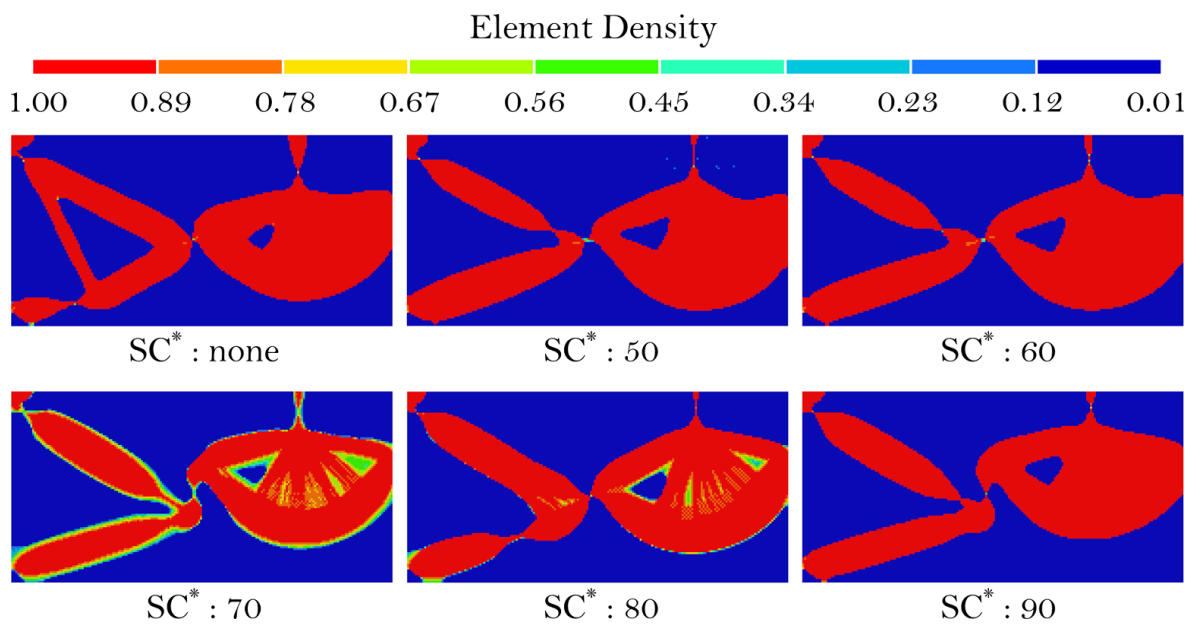
Figure 5.17: Different stress constraint levels and their impact on final topology of PEEK gripper; *SC - stress constraint (values in MPa).

determine the optimal stress constraint that would yield favourable results. The outcomes of this iterative process are depicted in Figure 5.17, which highlights the relationship between the stress constraint and the resulting topology.

To achieve the desired topology, a stress constraint value of 70 MPa was chosen. This particular level was found to promote longer slender flexures, facilitating significant displacements while simultaneously minimising stress levels.

Figure 5.18 presents the selected iterations achieved in the optimisation process. The design converged in the 449th iteration, which was the final stage of topology optimisation. This topology is the foundation for the subsequent design discussed in the following paragraphs.
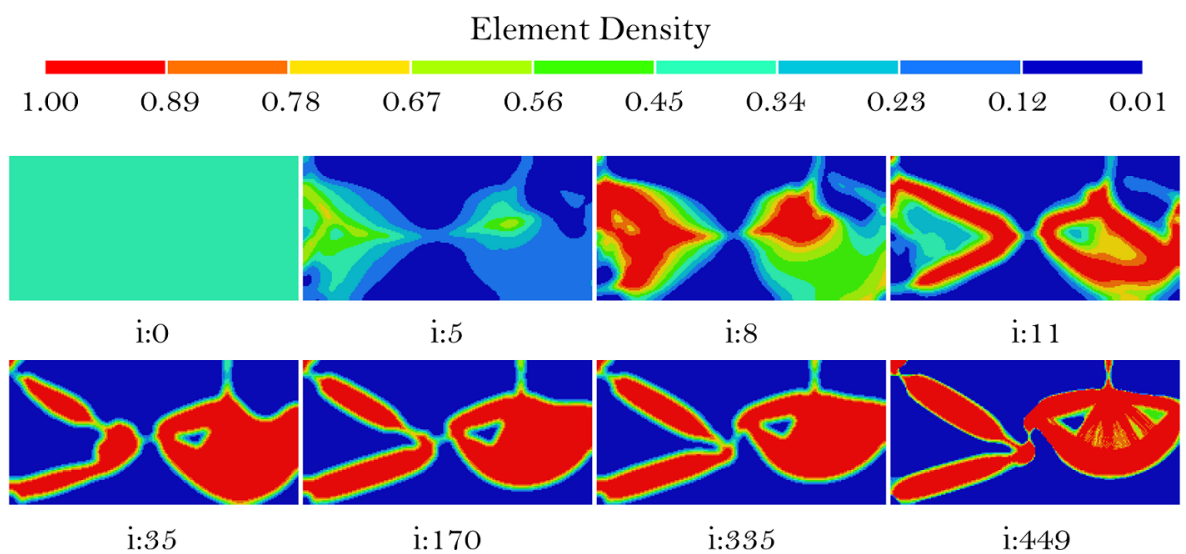
Figure 5.18: Topology optimisation of PEEK compliant gripper: evolution of density colour map; *i* - iteration number.

The last iteration in Figure 5.18 presents half of the design domain. Pseudodensities below 0.3 were removed exactly as for the PLA topology optimised gripper presented in the previous section. The problematic areas driving the threshold value are presented in Figure 5.19. To synthesise the entire gripper, another half of the mirrored frame was added along with the jaws of the gripper, elements to fix it and a mount for input. All these elements are visible in Figure 5.20a. This design is based solely on the result of topology optimisation. Figure 5.20b presents the FEA of the gripper in Figure 5.20a. As for the previous PLA gripper, here analysis was also carried out with the gripper fixed in the left corners (top and bottom), and the input was applied to the element in the middle-left. The input displacement was equal to 8.5 mm, corresponding to full jaw closure. The yield strength of Z-PEEK used here is around 100 MPa, and as such values above that level are coloured red. The maximum stress in this simulation reached 258.5 MPa. Therefore, it is evident that this gripper would be damaged during closing as it massively exceeds

the yield strength of PEEK. As planned, an additional design step was taken to update the topology. This step aimed to reduce stress in areas that undergo the most significant bending, namely flexures. As visible in Figure 5.20c, the existing (grey) topology was adjusted to create a new (red) design with elongated flexures with a minimum thickness of 0.8 mm. The previous design (Figure 5.20a) featured very localised flexures with thicknesses of 0.1 mm, which would be challenging to manufacture using 3D printing. The updated design was also evaluated in FEA, as shown in Figure 5.20d. The maximum stress achieved in full gripper closure is 54 MPa, which is a significant reduction compared to the result in Figure 5.20b. It is also clear that the stress distribution here is more uniform, which can potentially promote better fatigue performance. In the case of the updated design, the input displacement needed to close the gripper in the analysis increased from 8.5 mm (5.20b) to 9.5 mm. Figure 5.20e presents the mesh of the FEA model (0.25 - 1.25 mm). The last picture (Figure 5.20f) depicts the stress distribution while the gripper is open beyond its default position (with 2 mm of input displacement). As visible, the maximum stress is again located in the flexure close to the attachment point and is around 13 MPa.
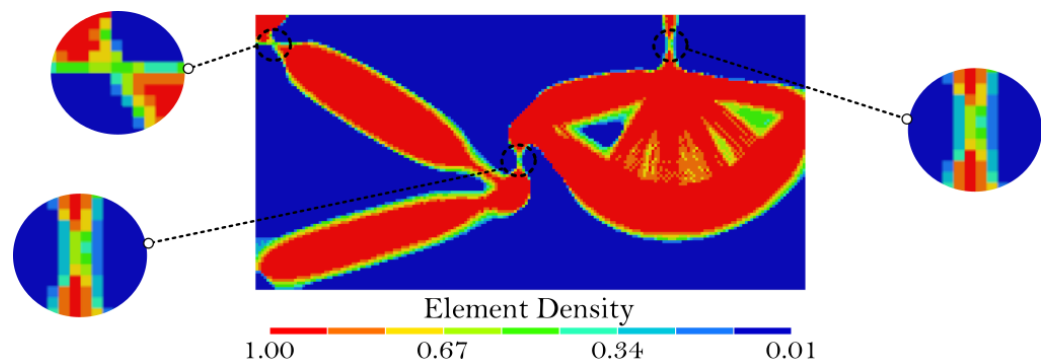
Figure 5.19: Density threshold selection for topology optimised PEEK gripper - problematic low density areas marked by dashed circles and enlarged.

Two grippers were 3D printed using PEEK: specifically, Z-PEEK from the commercial company Zortrax. To enhance the proportion of the crystalline phase within the specimen, annealing was performed on one of the grippers. The utilisation of crystalline (or semi-crystalline) PEEK offers increased stiffness in comparison to that of amorphous PEEK. However, increased stiffness can present challenges when designing compliant mechanisms, especially for topology optimisation, as demonstrated in Chapter 4 and publication of results from this work [83]. Despite this, the decision to employ it in this study was motivated by the thermal cycling to which hardware is usually exposed in space and lunar environments that usually have extreme temperature amplitudes [133, 172, 173]. Such conditions can facilitate the transformation of PEEK into a state with a larger share of the crys-
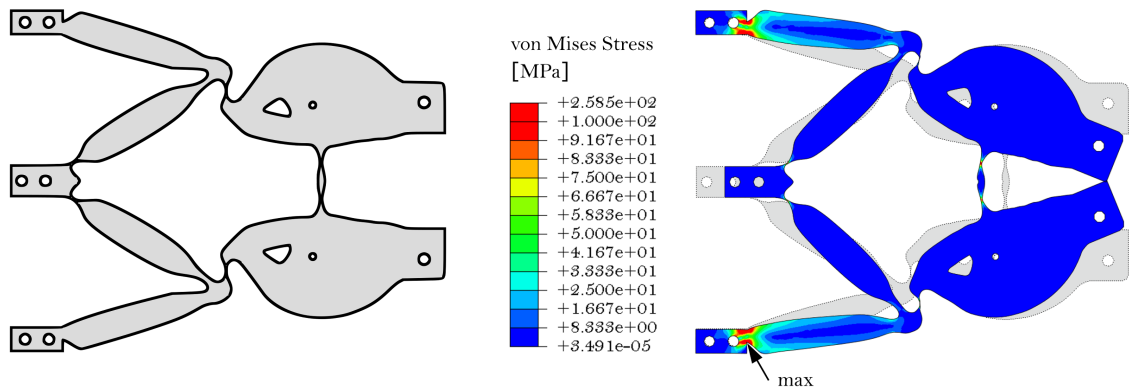
(a) Gripper designed based on the optimised topology.

(b) Nonlinear FEM analysis of gripper from (a); von Mises stress.
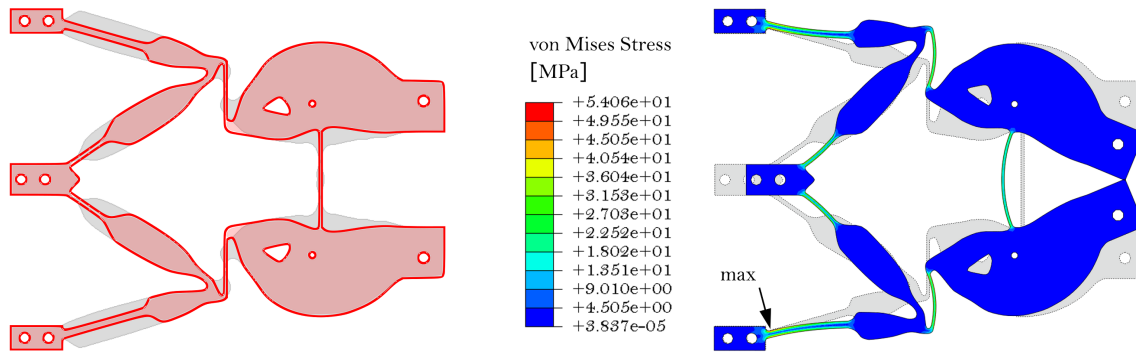
(c) Improved gripper designed - red, original design from (a) - grey.

(d) Nonlinear FEM analysis of gripper from (c); von Mises stress; gripper closing.
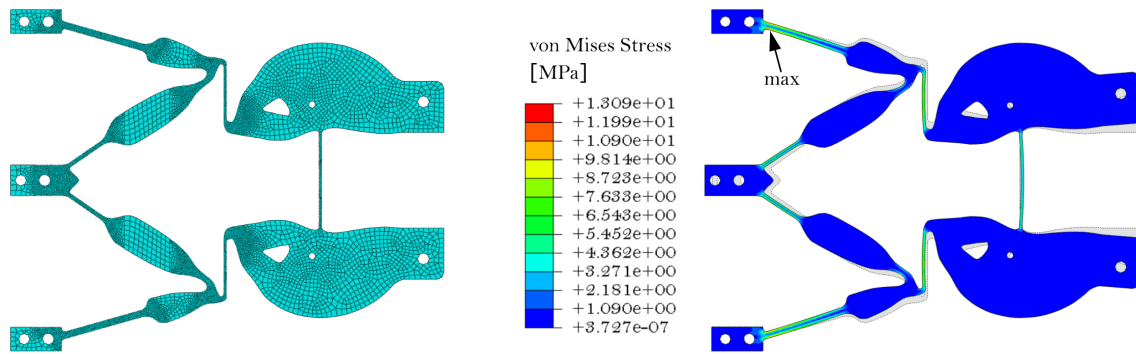
(e) Mesh used in the analysis (size range: 0.25 - 1.5 mm).

(f) Nonlinear FEM analysis of gripper from (c); von Mises stress; gripper opening.

Figure 5.20: Various design steps undertaken to produce compliant PEEK gripper.

talline structure. Consequently, the performance evaluation focused on unannealed (amorphous) and annealed (semi-crystalline) PEEK material.

5.4.1 Unannealed gripper

Figure 5.21 illustrates the gripper fabricated using 3D printing. A minor deviation from the dimensions specified in the 3D model was observed, particularly a reduction in the distance between the gripper jaws from 30 mm to 28.6 mm, as depicted in the mentioned figure. This discrepancy may have arisen due to thermal stresses experienced during the additive manufacturing process or during transport. However, despite this deviation, the functional capability of the gripper remained intact, allowing further testing. Figure 5.21b visually presents the distinction in appearance between amorphous and semi-crystalline PEEK. The gripper appears to be semi-transparent which is typically the characteristic of an amorphous structure.

(a) Gripper with the dimension deviation noted.

(b) Close up showing the semi-transparency of the PEEK, indicative of amorphous structure.
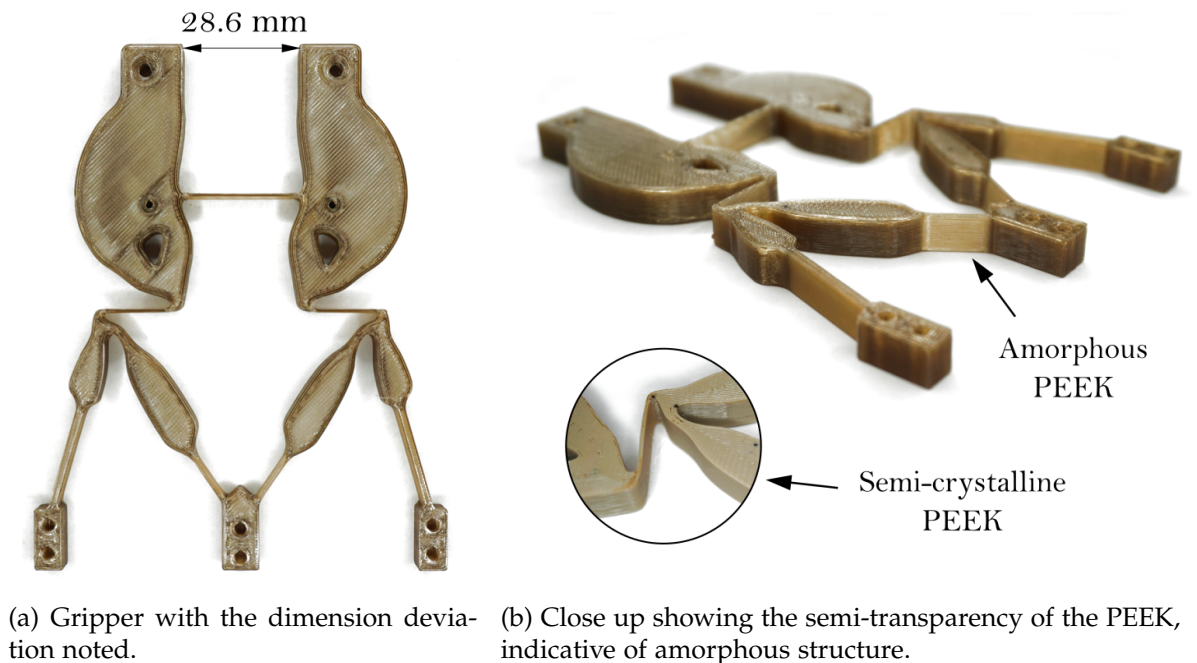
Figure 5.21: 3D printed amorphous PEEK gripper.

The gripper showcased here underwent a testing campaign that paralleled the approach used for the PLA gripper, as outlined in Section 5.3. Furthermore, to comprehensively evaluate the performance of the PEEK grippers for lunar application, an additional testing phase was conducted within the regolith simulant chamber, which will be elaborated upon in this section. To facilitate the analysis of displacements and deformations, a speckle pattern was applied to the gripper surface using a combination of black matte paint and white low pressure spray. This technique enabled capturing the relevant data for subsequent analysis. Figure 5.22 displays the speckle pattern on the unannealed PEEK gripper. The fully deformed configuration of the closed gripper (visible in Figure 5.22b) was achieved using a linear input displacement of 9.6 mm.

(a) Unreformed gripper mounted in the test rig, speckle pattern visible.

(b) Fully deformed gripper mounted in the test rig, speckle pattern visible.
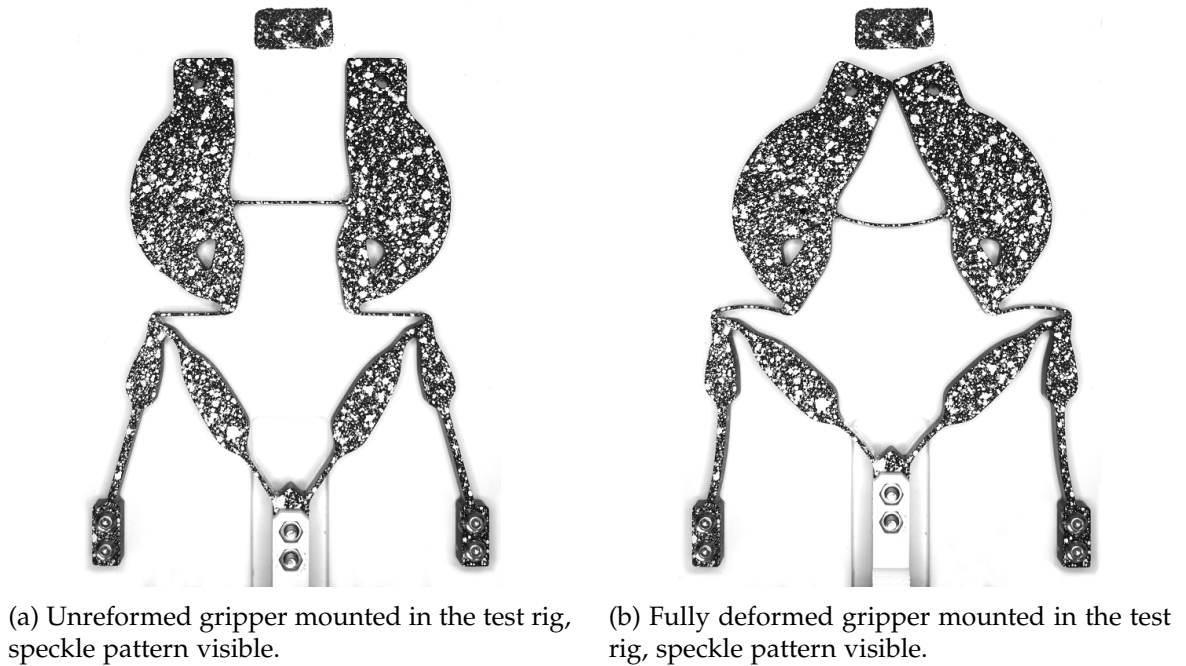
Figure 5.22: Unreformed and fully deformed PEEK unannealed gripper during test 'a'.

The nonlinear FEM analysis performed as part of the design process predicted that a 9.5 mm input displacement would be required for complete closure of the gripper. However, a longer stroke (9.6 mm) is necessary to achieve full closure in this 3D printed specimen. This disparity between the FEM model and the experimental data is negligible but can be attributed to the assumptions made in the FEM analysis, which considered the material as a homogeneous bulk substance. In contrast, as already mentioned, 3D printed materials can contain internal voids or pores resulting in variations in the actual mechanical behaviour compared to the idealised model. However, the input displacement increase for this specific gripper is very small.

Figure 5.23a illustrates the correlation between the linear input displacement (d_{in}) and the corresponding output displacement in the horizontal direction (d_{out}). Data collected during the gripper's closing phase (indicated in red) and opening phase (indicated in blue) are presented. The interpretation of the red and blue data sets is the same as for the PLA gripper presented in Section 5.3. The slope of the linear regression analysis in Figure 5.23a represents the Geometric Advantage. In this particular case, the linear regression analysis indicates a GA value of 1.527, as indicated in the figure's legend.

In Figure 5.23b, the precise motion path of the tip of the left jaw, which serves as an output point, is depicted. The output point is also marked in the figure, shown on the model of the gripper as the coordinate system centre. Similarly to the previous measurements, the red data set corresponds to gripper closing, while
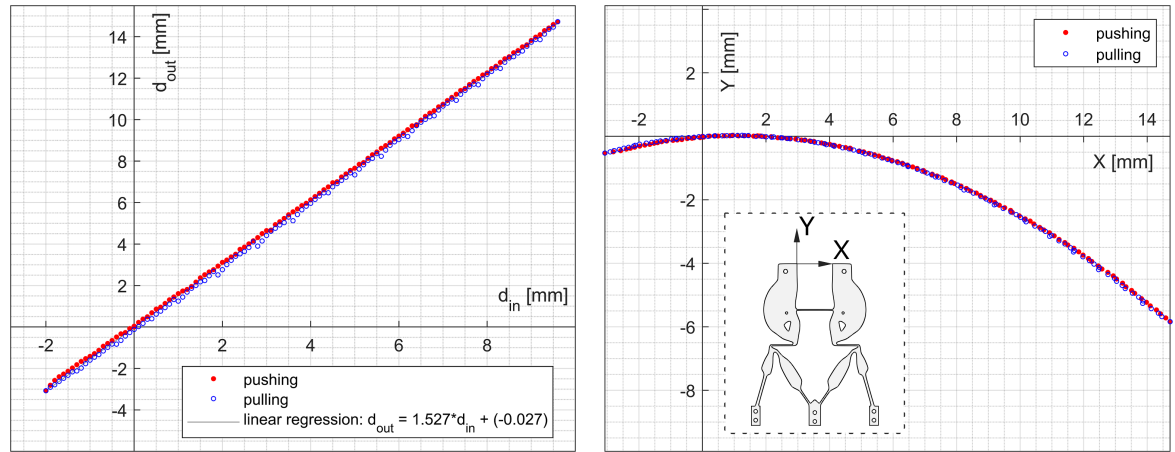
(a) Input-output displacement relationship. Max. standard deviation 0.198 mm.

(b) Path of the left gripper jaw. Max standard deviation X: 0.198 mm, max standard deviation Y: 0.072 mm.

Figure 5.23: Test 'a' data for unannealed PEEK gripper: displacements and motion.

the blue data set corresponds to gripper opening. Both data sets exhibit minimal differences, with small standard deviations that are not illustrated in the figures due to their size. However, the values of the standard deviations are provided in the captions of each figure. In particular, the vertical displacement range of 5.87 mm accounts for approximately 33% of the horizontal (intended) displacement range of 17.8 mm. Although vertical displacement makes a significant contribution, it is evident that the intended horizontal direction maintains dominance in terms of overall displacement.
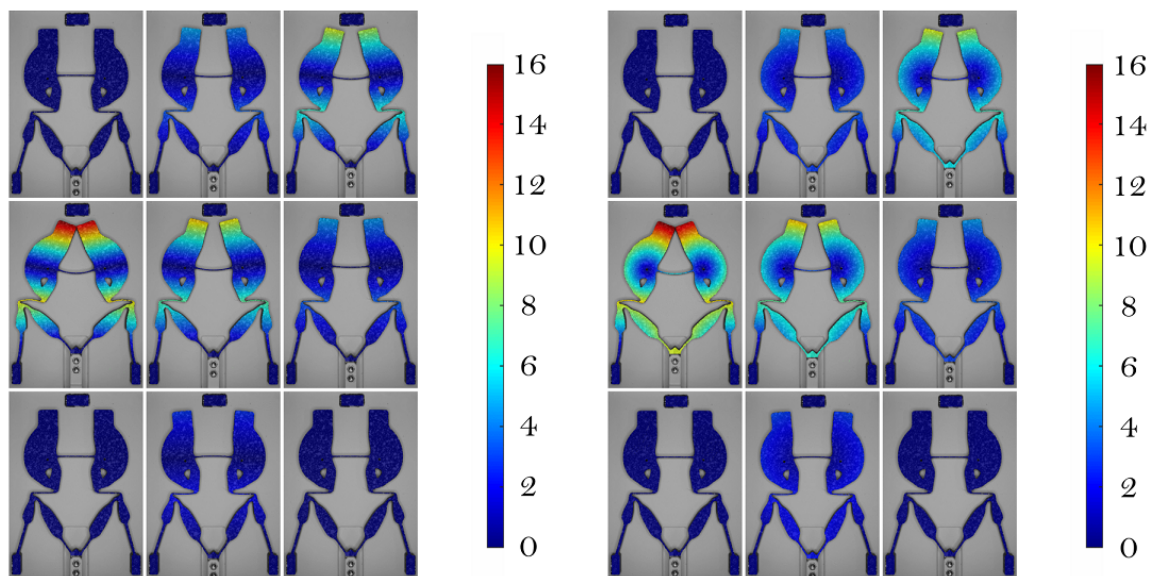
(a) Horizontal displacement magnitude [mm].

(b) Total displacement magnitude [mm].

Figure 5.24: Test 'a' Digital Image Correlation data for unannealed PEEK gripper.

Figure 5.24 illustrates the visualisation of the data obtained from the DIC analysis, specifically focusing on selected deformation stages. This depiction provides insight into the overall deformation of the gripper by showing the displacements of individual points on its surface. Figure 5.24a shows the values related to the desired output direction, which is the horizontal displacement. Furthermore, Figure 5.24b presents the magnitude of the total displacement, which includes both horizontal and vertical directions. In both subfigures, the bottom rows represent slight opening of the gripper beyond its default position, while the two top rows depict the gripper in closed or semi-closed configurations. These variations in the gripper's positioning allow for a comprehensive analysis of its behaviour under different states of loading.

(a) Test 'a' Geometric Advantage (GA). Max. GA standard deviation: 0.536.

(b) Test 'b' input force - output displacement relationship. Max standard deviation of d_{out}: 0.21.
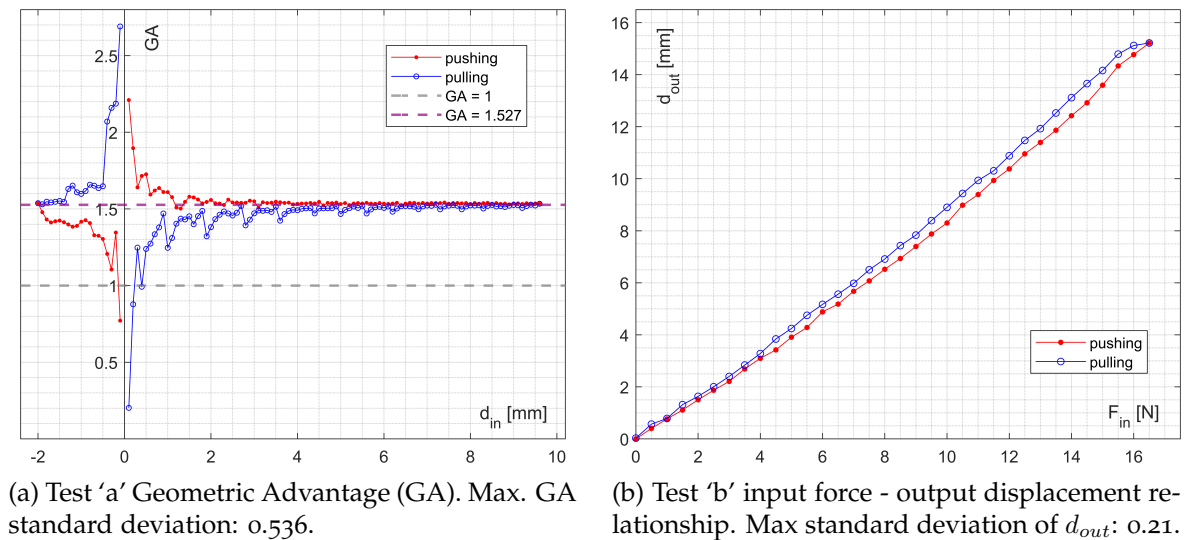
Figure 5.25: Test 'a' and 'b' data for unannealed PEEK gripper.

Figure 5.25a presents the dynamic evolution of Geometric Advantages in response to changing input displacement. Unlike Figure 5.23a, where GA was determined through linear regression analysis of the entire data set, here it is calculated individually for each measurement point. The graphed data illuminate the non-constant nature of GA, which exhibits variation depending on the position of the gripper. For comparison purposes, the GA value of 1.527 obtained from Figure 5.23a is included in this graph, along with the GA value of 1 indirectly indicated during the topology optimisation phase of the gripper design.

Next, Figure 5.25b presents the relationship between the input force, measured by the force gauge, and the horizontal output displacement during Test 'b'. The depicted graph reveals the presence of hysteresis in the gripper's behaviour, which, as already mentioned while presenting PLA gripper, is an expected characteristic given the magnitude of deformations involved.

(a) Input force - output force relationship. Max standard deviation of F_{out}: 0.004.

(b) Input force - Mechanical Advantage relationship. Max standard deviation of MA: 0.003.
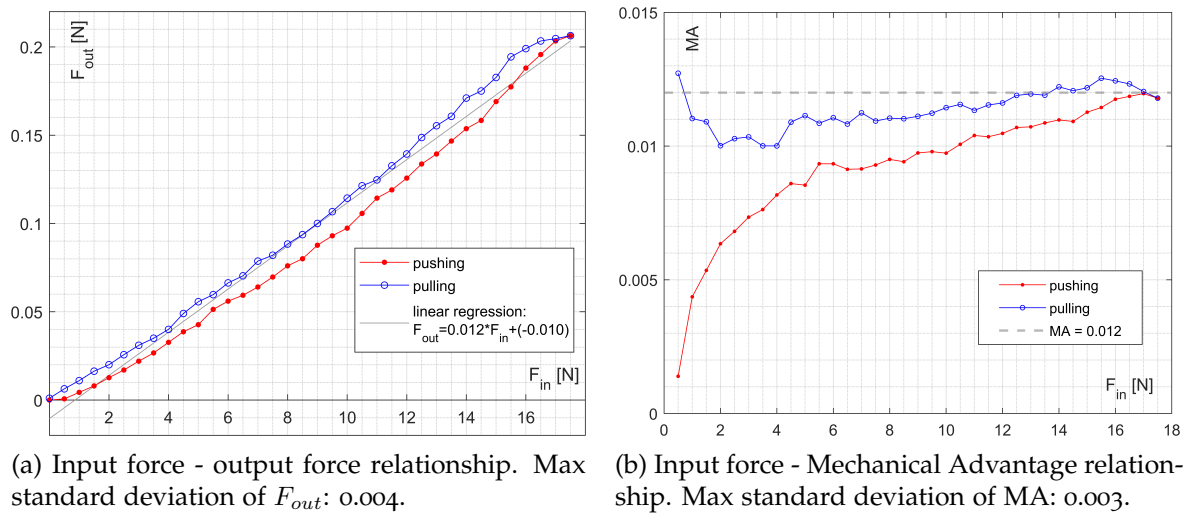
Figure 5.26: Test 'c' data of unannealed PEEK gripper.

Figure 5.26 presents the data collected during test 'c', where the input was provided through the force gauge. The figures are colour-coded, with red indicating the motion resulting from pushing, and blue representing the motion during retraction, like in the case of previous tests. In Figure 5.26a, the relationship between the input force and the output force is shown, revealing the presence of hysteresis. The grey line in the figure represents the linear regression analysis of the measurements, and the slope of this line represents the Mechanical Advantage (MA) between the input and output forces. The graph indicates an MA value of 0.012. Furthermore, Figure 5.26b demonstrates the variation in MA in relation to the input force. The data shown in this figure demonstrate the calculation of MA for each gripper position individually. As visible in the same figure, MA varies across different deformation positions of the gripper and is influenced by the direction of the gripper's deformation.

In order to further investigate gripper performance, Tests 'a' and 'b' were conducted in a dusty environment using a chamber filled with lunar regolith simulant EAC-1A [166], obtained from the European Space Agency. The chamber had a volume of 324 cm³. It was filled with regolith to submerge the gripper to at least half of its with which required around 62 cm³ of the regolith simulant. The experimental setup closely resembled the one used in the previously presented tests, with the primary difference being the inclusion of a regolith-filled chamber during gripper deformation. While the gripper maintained contact with the regolith, the top surface remained uncovered to ensure visibility of the speckle pattern used for DIC analysis. After each test the regolith simulant was gently raked to start each test with smooth particle distribution. The main area of contact between the gripper and the regolith simulant was present below the gripper and over the chamber

base. Figure 5.27 offers a visual representation of the various stages of deformation observed throughout the experiment, providing valuable information on the gripper's behaviour within the regolith-filled environment.
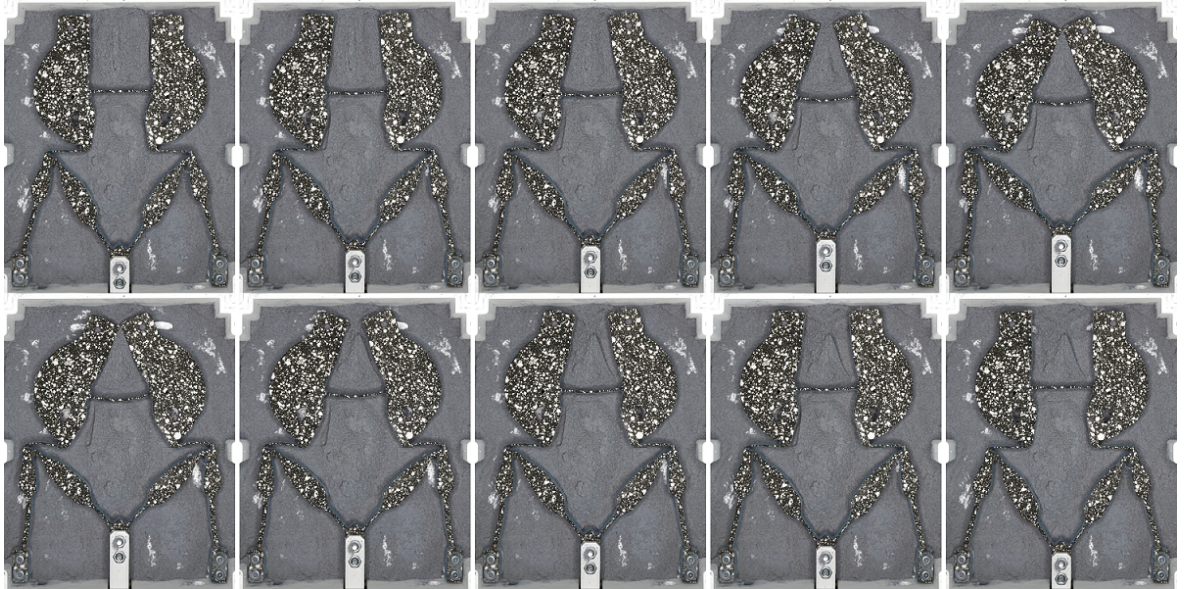
Figure 5.27: Various deformation stages of the unannealed PEEK gripper tested in the dust chamber: top raw from default position to closed; bottom raw from closed position to default.

Figures 5.28 and 5.29 provide a comprehensive depiction of the data collected during Tests 'a' and 'b', which mirror the experiments conducted without the presence of regolith. In Figure 5.28a, the relationship between input displacement and output displacement in the horizontal direction is showcased, with data from the no-regolith test displayed in green for comparison purposes. Notably, a remarkable resemblance between the regolith and no-regolith data is evident. Furthermore, a linear regression analysis was conducted to determine the GA, yielding a value of 1.554.

Moreover, Figure 5.28b offers a detailed visualisation of the precise path followed by the gripper jaws. The green data represent the motion path observed in the absence of regolith, enabling a direct comparison between the two scenarios.

Figure 5.29a showcases the variations in the GA as a function of the displacement of the input. In particular, the changing behaviour of the GA is observed to be consistent in both the presence and absence of regolith. The GA values obtained by linear regression for the tests conducted with and without regolith are represented by the green and purple dashed lines, respectively. The disparity between these values is negligible, indicating minimal impact from the presence of regolith.

Furthermore, Figure 5.29b illustrates the relationship between input force and output displacement within the regolith chamber. For comparative analysis, the
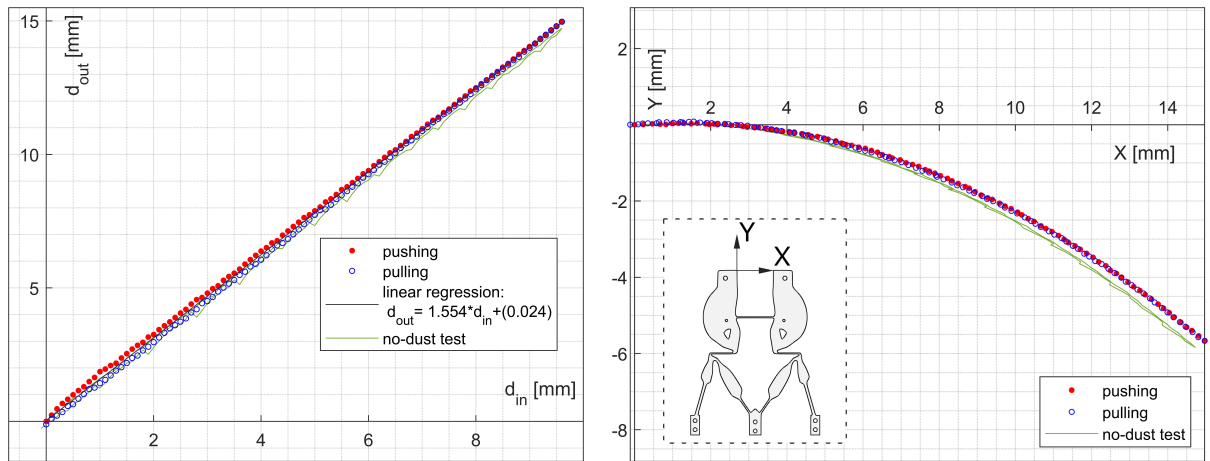
(a) Input-output displacement relationship tested in regolith chamber. Max. standard deviation 0.355 mm.

(b) Path of the left gripper jaw in the regolith chamber. Max standard deviation X: 0.355 mm, max standard deviation Y: 0.092 mm.

Figure 5.28: Unannealed PEEK gripper - Test 'a' in regolith chamber: displacements and motion.
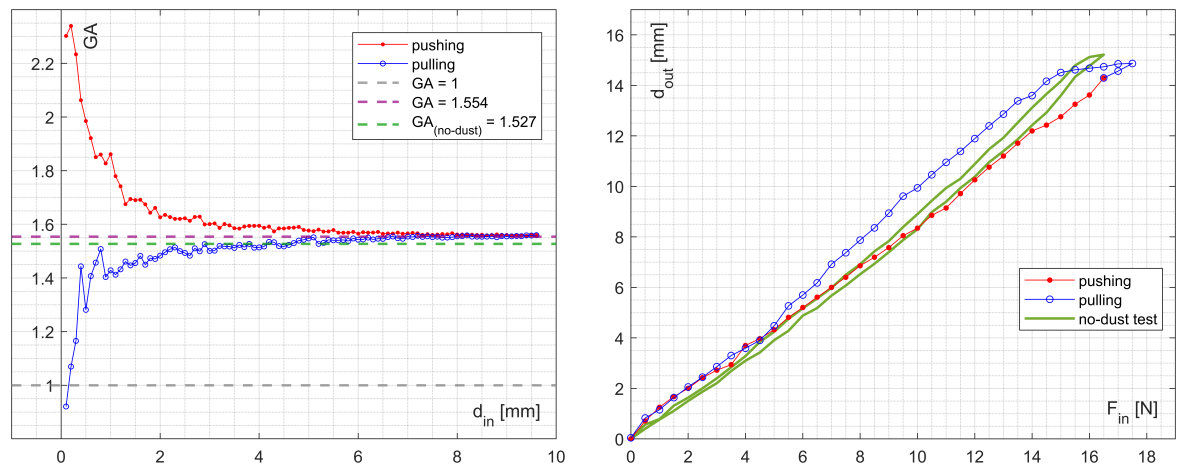
(a) Test 'a' in regolith chamber: Geometric Advantage (GA). Max. GA standard deviation: 0.817.

(b) Test 'b' in regolith chamber: input force - output displacement relationship. Max standard deviation of d_{out}: 0.664.

Figure 5.29: Unannealed PEEK gripper - Test 'a' and 'b' data in regolith chamber.

data from the test conducted without regolith are also depicted in green. It becomes apparent that achieving full closure of the gripper required a greater force (specifically an additional 1 N) in the presence of regolith. This discrepancy arises due to the additional friction generated between the gripper, regolith particles, and the chamber bottom, resulting in increased resistance to movement. It is important to note that this is not a friction in the gripper system, as it is a tribology-free compliant mechanism. In the case of rigid body gripper, the increase in friction could be caused by the regolith increasing the friction between the gripper elements. The compliant gripper is a monolithic design where inter-element gaps were elim-

inated. Nevertheless, it is inside of the chamber and the particles between the chamber and the gripper can still add friction component to the test. However, as demonstrated, the impact was minor.

5.4.2 ANNEALED GRIPPER

The 3D printed PEEK annealed gripper is depicted in Figure 5.30. A minor discrepancy was observed in the dimensions of the printed model, specifically in the distance between the gripper jaws, which was reduced from the intended 30 mm to 27.9 mm, as illustrated in the figure. This discrepancy appeared to be asymmetric, with more noticeable deformation occurring on the right side of the gripper in the same figure. The cause of this deformation could be attributed to thermal stress during thermal post-processing or plastic deformation that occurred during transportation. Despite this asymmetry, the functional capacity of the gripper remained intact and tests were still carried out.

(a) Gripper with the dimension deviations noted.

(b) Close up of the voids and gaps in gripper structure.
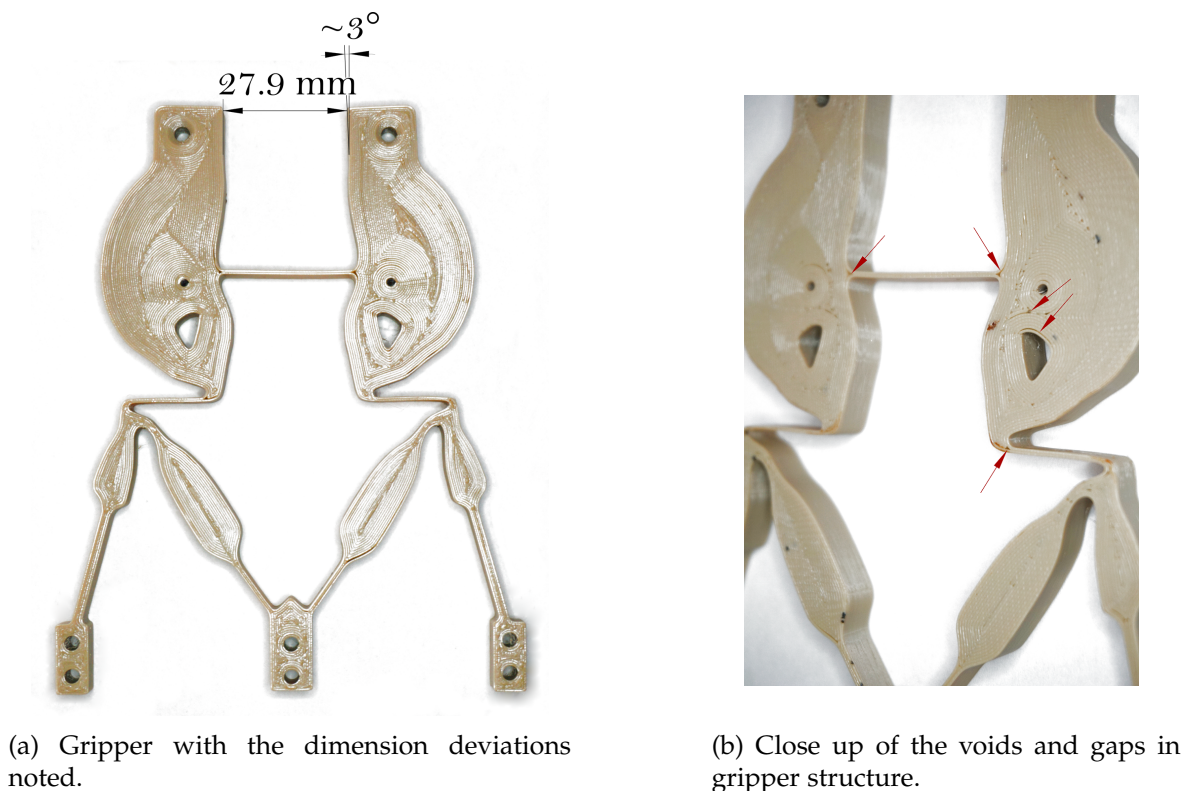
Figure 5.30: 3D printed and annealed PEEK gripper.

The gripper discussed here underwent an annealing process to achieve a semi-crystalline structure. Annealing is a carefully and precisely controlled heat treatment method which is used to induce molecular reorganisation of the material and can reduce internal stresses. This process involves subjecting the material (here PEEK) to temperatures above its glass transition temperature, allowing the amor-

phous regions of PEEK to become more ordered and crystalline in structure. The transition from the amorphous to crystalline (or semi-crystalline) phase results in increased stiffness and strenght of the material, and enhances dimensional stability of the specimen.

In the case of the PEEK gripper in this section, a specific annealing procedure was implemented. The amorphous Z-PEEK (PEEK from Zortrax) print was placed in a sand-filled steel container to ensure superior thermal control and prevent model deformation. The use of quartz sand with a grain gradation of 0.2-0.8 mm reduces thermal inertia, providing mechanical stabilisation and minimising the risk of distortion during annealing. The annealing process was carried out in a laboratory dryer according to a precise programme. It involved three hours at 100°C, followed by a gradual increase in temperature of 0.5 degrees per minute over three hours to reach 200°C. The gripper temperature was then maintained at 200°C for five hours before natural cooling to room temperature. As visible in Figure 5.30 the resulting gripper does not resemble the semi-transparent amorphous model from Section 5.4.1. This gripper is more opaque, which indicates a transition into semi-crystalline structure.

Furthermore, it is important to mention that Figure 5.30b highlights the presence of small voids between the filament passes in the gripper structure. Such imperfections are commonly observed in 3D printed components and can occasionally impact the kinematic behaviour of compliant mechanisms. It is crucial to assess whether specimens with these imperfections can still fulfil their intended function.

Here, a summary of the data acquired from tests described previously is presented. The testing campaign was identical to the one presented in Section 5.4.1, including the regolith testing phase. All tests were conducted on a single annealed PEEK compliant gripper. To facilitate Digital Image Correlation (DIC) analysis, as with previous prototypes, the gripper underwent black paint application, followed by white speckle pattern spraying. The deformation of the gripper (and the speckle pattern) can be found in Figure 5.31.

Figure 5.31b displays the gripper in a fully deformed configuration, obtained through a linear input displacement of 10.2 mm. Nonlinear FEM analysis conducted during the design process predicted that the input displacement necessary for gripper closure would be 9.5 mm. As demonstrated, a longer stroke is required to fully close the actual gripper. Again, as with the previous grippers, this discrepancy between the FEM model and the test data may be attributed to the fact that the FEM analysis assumed bulk material. As already discussed, that is not a fully accurate representation of 3D printed material, but this specific specimen
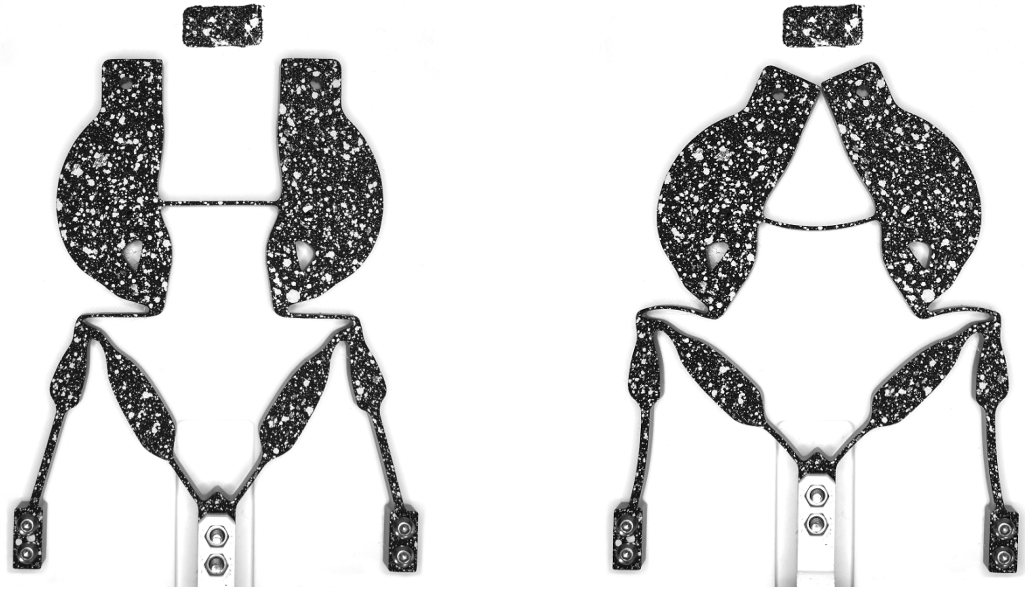
(a) Unreformed gripper mounted in the test rig, speckle pattern visible.

(b) Fully deformed gripper mounted in the test rig, speckle pattern visible.

Figure 5.31: Undeformed and fully deformed PEEK annealed gripper during test 'a'

also underwent an annealing process that produced semi-crystalline structure and therefore increase of the stiffness was expected.

Figure 5.32a demonstrates the relationship between the linear input displacement (d_{in}) and the desired output, specifically the output in the horizontal direction (d_{out}). The data was collected during both gripper closing (red) - which was achieved by pushing on the input - and opening (blue) - achieved by gradually releasing the input and allowing the gripper to use stored strain energy to release the deformation. The slope of the linear regression reveals a GA value of 1.451, as indicated in the legend of Figure 5.32a. Figure 5.32b depicts the exact motion path of the left jaw tip, which is considered an output point, which is also marked as a coordinate system on a gripper drawing at the bottom of the figure. Similarly to the previous figure, the red data set represents gripper closing, while the blue data set represents gripper opening. Both data sets are almost identical, with small standard deviations that are not depicted in the figures because of their size, their values are indicated in the captions of each figure. It is worth noting that the vertical displacement range of 6.95 mm represents 39% of the horizontal (i.e., intended) displacement range of 17.7 mm. The share of the intended direction of displacement is still dominant.

Figure 5.33 is a graphical representation of the data collected during DIC analysis. It shows the deformation of the whole gripper by depicting the displacements of individual points on the gripper surface. Figure 5.33a presents the value of the

(a) Input-output displacement relationship. Max. standard deviation 0.14 mm.

(b) Path of the left gripper jaw. Max standard deviation X: 0.143 mm, max standard deviation Y: 0.127 mm.
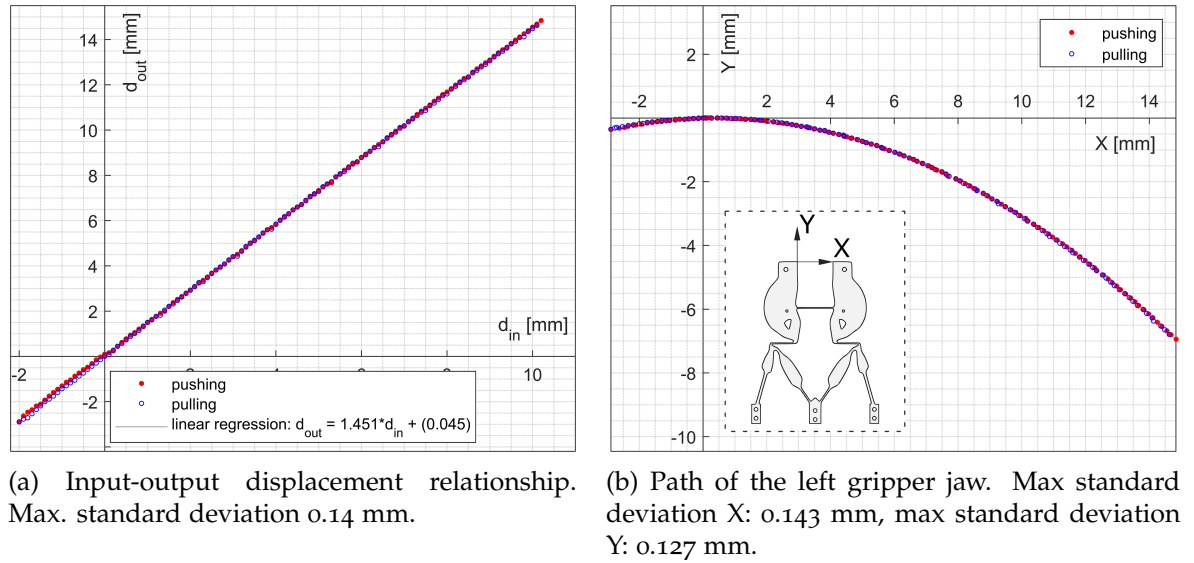
Figure 5.32: Test 'a' data for annealed PEEK gripper: displacements and motion.

(a) Horizontal displacement magnitude [mm].

(b) Total displacement magnitude [mm].
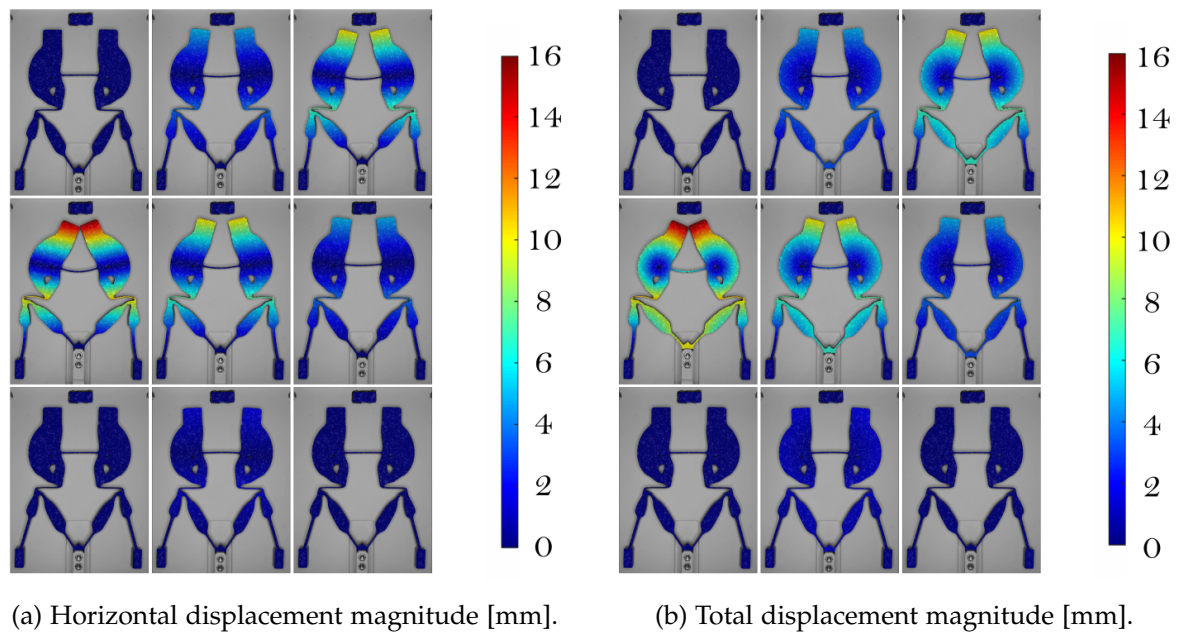
Figure 5.33: Test 'a' Digital Image Correlation data for annealed PEEK gripper.

desired output direction - horizontal, and Figure 5.33b presents the magnitude of the total displacement (both combined directions). The bottom rows in each of those figures present a slight opening of the gripper beyond its default position, while the two top rows present a gripper in closed or semi-closed configurations.

Figure 5.34a displays the evolution of the GA with changing input displacement. In this case, the GA is calculated individually for each measurement point (as opposed to Figure 5.32a where it was calculated for the entire data set using linear regression) by dividing the input displacement in the horizontal direction by the output displacement. The graphed data reveal that the GA is not constant and

(a) Test 'a' Geometric Advantage (GA). Max. GA standard deviation: 1.288.

(b) Test 'b' input force - output displacement relationship. Max standard deviation of d_{out}: 0.204.
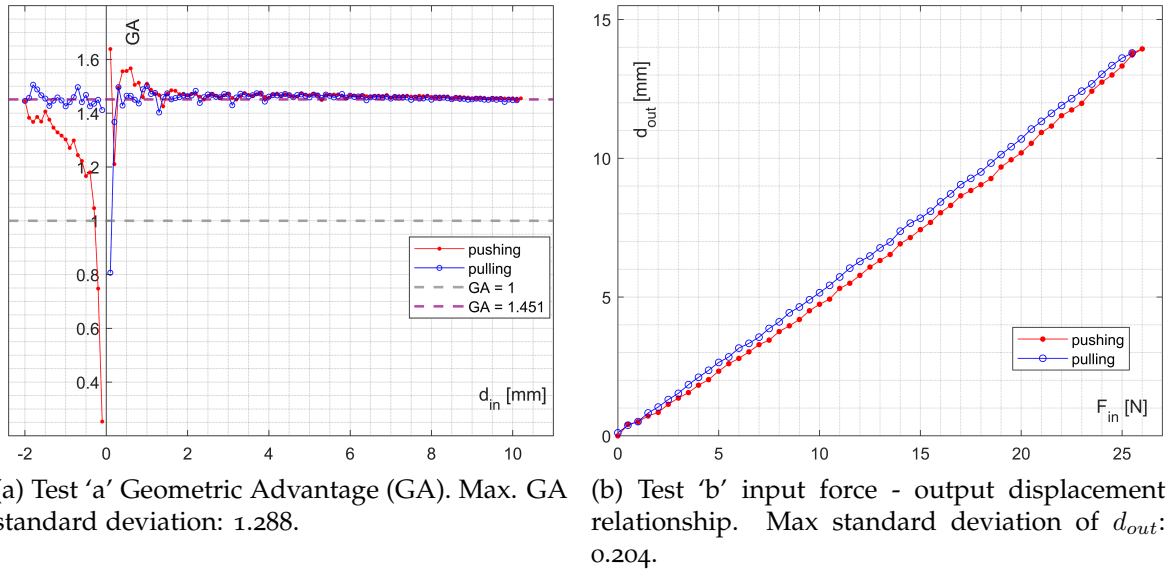
Figure 5.34: Test 'a' and 'b' data for annealed PEEK gripper.

varies with the gripper's position. The GA value of 1.451 derived from Figure 5.32a is also included in this graph for comparison, along with the GA value of 1 which was indirectly indicated during the topology optimisation phase of the gripper design (because the prescribed input and output displacements were equal to 1 and therefore their ratio is equal to 1). Figure 5.34b illustrates the relationship between the input force supplied by the force gauge and the horizontal output displacement during Test 'b'. It reveals the gripper's hysteresis, which, as in previous examples, is to be expected with deformations of substantial magnitude.

(a) Input force - output force relationship. Max standard deviation of F_{out}: 0.015.

(b) Input force - Mechanical Advantage relationship. Max standard deviation of MA: 0.019.
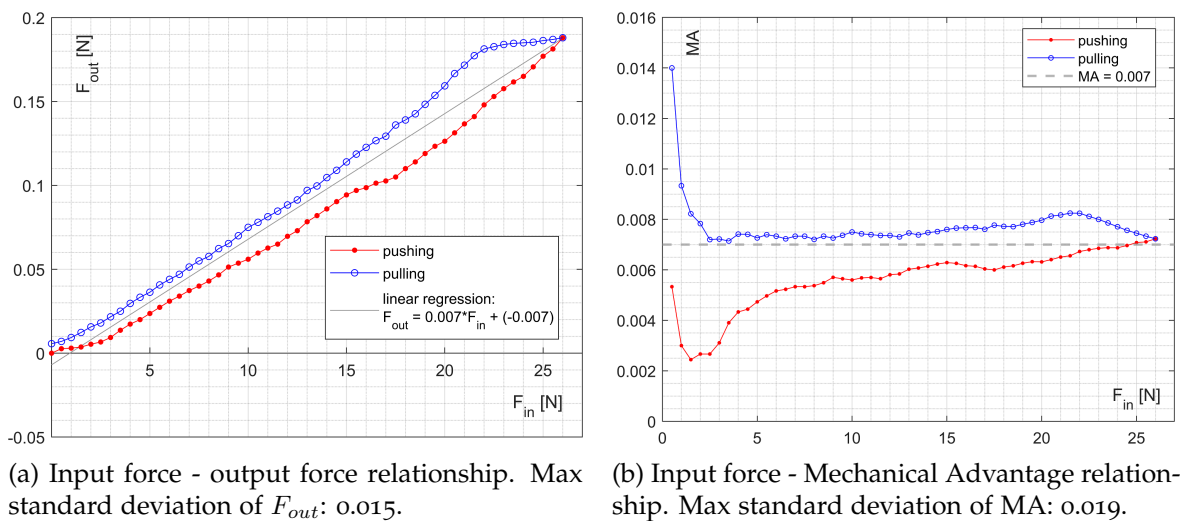
Figure 5.35: Test 'c' data of annealed PEEK gripper.

Figure 5.35 depicts the data acquired during Test 'c', where the input was supplied through the force gauge and the output force was measured with a dynamometer. The red and blue colours in the figures correspond to the portion

of motion caused by pushing and retracting, respectively. Figure 5.35a shows the relationship between the input force and the output force, which shows a noticeable hysteresis. The grey line in the figure represents the linear regression of the measurements, with the slope indicating the Mechanical Advantage (MA). From the graph, it is evident that MA=0.007. Figure 5.35b demonstrates the variation in MA with input force. This graph represents MA calculated individually for each gripper position as the output force divided by the input force. Similarly to previous examples, the MA differs for different gripper deformation positions and varies depending on the direction of gripper deformation.
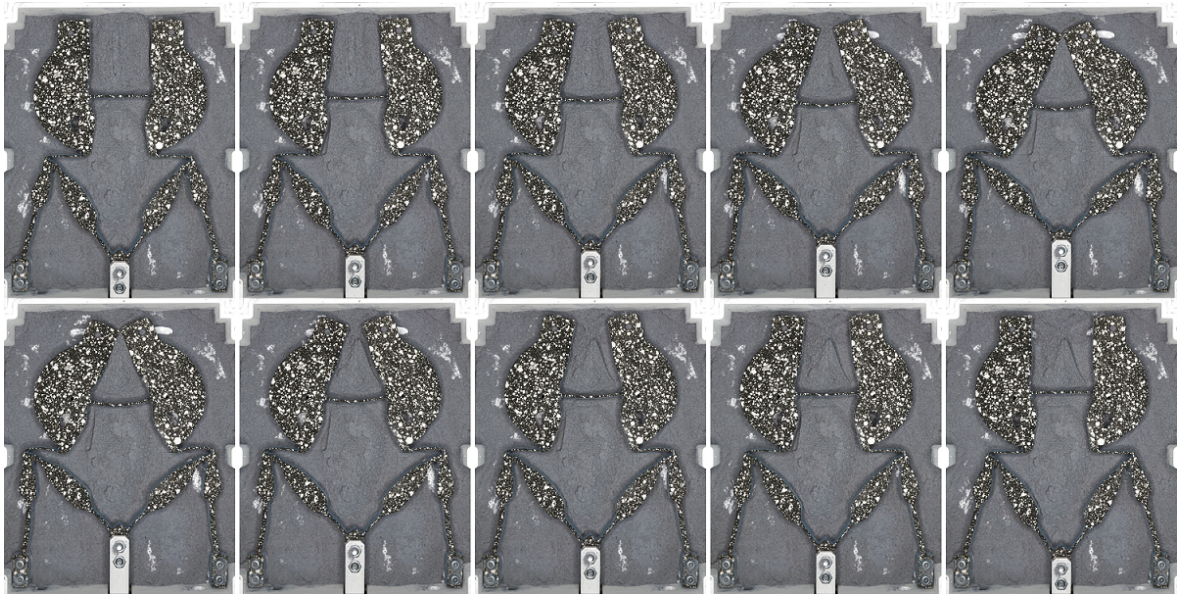
Figure 5.36: Various displacement stages of the annealed PEEK gripper tested in the dust chamber.

Tests 'a' and 'b' were also repeated in a chamber filled with the lunar simulant EAC-1A, as was already done for the unaannealded PEEK gripper. The test rig was nearly identical to the one used in previous tests done for the annealed gripper, with the exception that the gripper was deformed within a regolith-filled chamber. The gripper was in contact with the regolith, but the upper surface was kept uncovered to maintain a visible speckle pattern for Digital Image Correlation (DIC). Figure 5.36 shows various stages of deformation visible during testing.

Figures 5.37 and 5.38 illustrate the data obtained from Tests 'a' and 'b' that are analogous to the tests conducted without regolith. Figure 5.37a depicts the relationship between the input displacement and the output horizontal displacement, where the data of the test without regolith are also shown in green for comparison. The close alignment between the regolith and no-regolith data is noticeable. Furthermore, linear regression analysis was used to determine the GA, resulting in a value of 1.425. Figure 5.37b illustrates the precise path of the gripper jaws, with
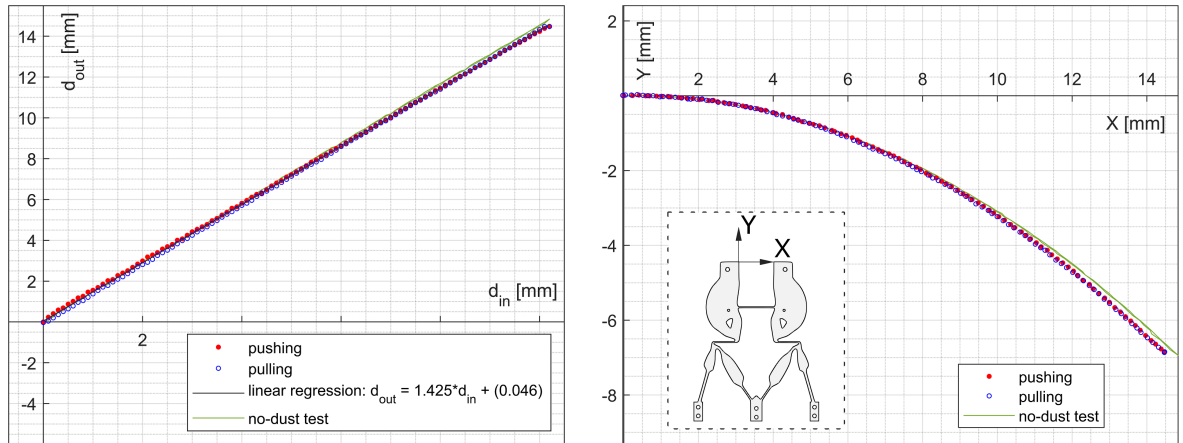
(a) Input-output displacement relationship tested in regolith chamber. Max. standard deviation 0.514 mm.

(b) Path of the left gripper jaw in the regolith chamber. Max standard deviation X: 0.514 mm, max standard deviation Y: 0.111 mm.

Figure 5.37: Annealed PEEK gripper - Test 'a' in regolith chamber: displacements and motion.

the green data representing the path of motion in the absence of regolith.
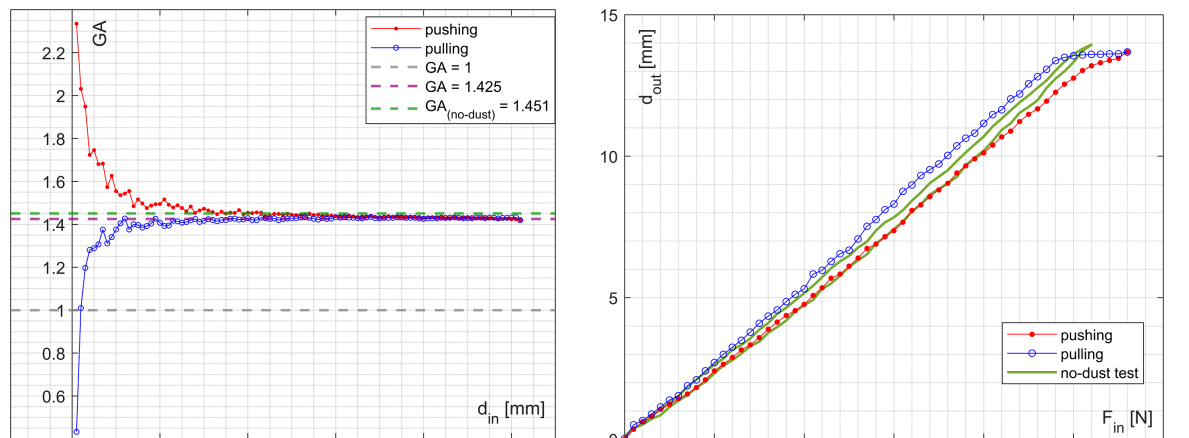
(a) Test 'a' in regolith chamber: Geometric Advantage (GA). Max. GA standard deviation: 0.673.

(b) Test 'b' in regolith chamber: input force - output displacement relationship. Max standard deviation of d_{out}: 0.376.

Figure 5.38: Annealed PEEK gripper - Test 'a' and 'b' data in regolith chamber.

Figure 5.38a displays the changes in GA as a function of input displacement. It can be observed that the GA exhibits a similar changing behaviour in the presence and absence of regolith. The GA values determined from linear regression for both tests, with and without regolith, are indicated by the green and purple dashed lines, respectively. The difference between these values is negligible. Figure 5.38b shows the relationship between the input force and the output displacement in the regolith chamber. The data from the test conducted without regolith is also represented in green for comparison purposes. It is evident that to achieve full closure of the

gripper a greater force (specifically, 2 N more) was required in the regolith test due to the additional friction generated between the gripper, the regolith particles and the chamber. This behaviour is in line with observations of behaviour of the unannealed PEEK gripper.

5.5 DISCUSSION

This chapter presented a topology optimisation-based design methodology, enhanced with an analytical re-design step aimed at minimising the stiffness of flexures. The topology optimisation approach used was originally developed for applications involving small strains. However, the addition of an analytical step allows for better stress distribution, resulting in improved performance in applications with large deformations. This combined design methodology was used to create three grippers using PLA and PEEK materials. The topology optimisation process took into account their specific material properties. Furthermore, two separate PEEK grippers were fabricated, and one of them underwent a thermal post-processing step known as annealing. The annealing process increased the stiffness of the PEEK gripper, as demonstrated by the data presented in this chapter.

Compared to the previous Chapter 4, significant improvements were made to the testing methodology. The most notable enhancement was the adoption of the Digital Image Correlation tool, specifically Ncorr. This tool streamlined the measurements of the displacements on the image data collected during the tests and provided a comprehensive understanding of the deformation of the entire gripper models.

Furthermore, Subsections 5.3 and 5.4 detailed the steps taken to synthesise gripper designs, including the selection of stress constraints and the impact of analytical redesign on maximum stress and the final shape of the flexures. Section 5.3 also presented data from tests conducted on the PLA enhanced gripper. This gripper achieved the highest Geometric Advantage (GA) among all grippers discussed in this chapter, with a value of 1.637. It also required the smallest maximum input displacement for gripper closure, measuring 8.8 mm. Furthermore, the vertical displacement, which is undesired, was equal to 30% of the horizontal (desired) output displacement. The performance of the different grippers tested in this study exhibited variations depending on the material used. Although the PLA gripper displayed the highest GA, this indicates better performance compared to the other grippers discussed in this chapter. However, it required the highest maximum force (27 N) to close the gripper among all grippers tested. The maximum output force for this gripper was 0.208 N, which was also higher than for the other grippers. It can be concluded that this gripper was the stiffest of the three presented, as

it required the most force to close fully. Although it had the lowest Mechanical Advantage, the final output force for this gripper was the highest.

The PLA gripper underwent slight plastic deformation (0.13 mm) even though the maximum stress level from FEM was around 83% of the yield strength. Assessing the safe maximum stress margin will differ for various materials (taking into account, for example, their ductility), and this example demonstrated that the maximum stress concentration corresponding to 83% of the yield strength could be too high for the use of PLA without plastic deformation. It is also worth noting that the yield strength for compression and tension generally differs for most materials [174] which can lead to plastic deformation even though the stress was below the yield strength indicated in the properties of the material. The last thing worth mentioning is that PLA has a semi-crystalline structure [175–177] and, as such, plastic deformation starts as slip (or micro-slip) which occurs when materials undergo motion of dislocations in the crystalline structure [132, 178–180]. As the literature shows, this is an important mechanism that is ramping up slowly while more and more dislocations become immobilised. In fact, it is difficult to determine the exact yield strength from the stress-strain curve of some materials, and sometimes the 0.002 strain offset method is used to approximate it [132]. This short discussion of the yield strength highlights the fact that the exact value of yield strength for all flexures (which undergo tension, compression, or both) may not be known, and it is good practise to keep the maximum stress possibly far below the yield strength. For the 3d printed PLA gripper discussed here, future re-design steps could potentially improve its performance by further optimising the flexures. However, even with the plastic deformation problem discussed, the output displacement path was still the most favourable for the PLA gripper - with the desired direction contribution being the highest.

PEEK grippers also need to be discussed in detail. Differences between the performance of the unannealed and annealed PEEK grippers were observed an will be highligheted here. The unannealed gripper had a higher GA value (1.527) compared to the annealed gripper (1.451). The unannealed gripper required 9.6 mm of input displacement, while the annealed gripper required 10.2 mm. In terms of output displacement performance, the vertical displacement of the unannealed gripper was at a value equal to 33% of the desired horizontal displacement. For the annealed gripper, this value was 39% (which is less desirable). The input displacement levels in the regolith simulant tests remained the same, and the difference in GA between the tests conducted with and without regolith was negligible. However, a more pronounced difference between the two grippers was observed in the tests that examined the force required to close the gripper. The unannealed grip-

per required 16.5 N, while the annealed gripper required 26 N. This significant difference indicates a substantial increase in stiffness achieved through thermal post-processing and an increase in the crystallinity of the material. Similar tests carried out in the lunar regolith simulant chamber showed an additional increase in the force required to close the grippers (1 N for the unannealed gripper and 2 N for the annealed gripper). This increase can be attributed to the additional friction introduced to the system by the interaction of grain particles between the gripper and the chamber. However, as demonstrated by the input-output displacement test, the path of the output displacement and the input displacement levels remained unchanged. This implies that regolith intrusion affects force-controlled but not displacement-controlled input. The Mechanical Advantage measured for the unannealed and annealed grippers were 0.012 and 0.07, respectively.

The results of the tests presented in this chapter demonstrate the validity of the design methodology and indicate that similar compliant mechanism performance can be achieved using both PLA and PEEK in the amorphous and semicrystalline state. This observation is valuable considering that the price of PLA is currently much lower than that of PEEK. Consequently, prototyping with PLA is more cost-effective and can potentially be used to work towards PEEK designs that could be applicable in space.

In summary, this chapter presents a merger of different design methodologies: topology optimisation and analytical design. The study demonstrates its applicability to materials with varying levels of stiffness. The tests verified the kinematic behaviour of all grippers, confirming their ability to close the jaws as expected. Furthermore, valuable insights regarding the control of compliant mechanisms in a regolith environment were obtained. The displacement-driven control remains unaffected by the presence of dust, while the force-driven control is impacted by regolith, causing additional friction between the mechanism and external elements that requires an increase in input force. As a result, displacement control is more forgiving of regolith intrusions and can be a better solution for compliant mechanisms in dusty surface environments. Another observation was on the maximum stress in the flexures. It is hard to provide an indefinite recommendation for the maximum stress of PLA, but it is clear 83% that the yield strength does not leave enough margin and can result in some plastic deformation. However, the example presented here also shows that minimal plastic deformation can be negligible for the performance of compliant grippers in the force-driven scenario.

CHAPTER 6

CONCLUSIONS

The core focus of this thesis revolves around the challenges caused by lunar dust within the domain of hardware development and operations for lunar surface missions. The topic deserves special attention as a result of the ongoing efforts of prominent space agencies, such as NASA, ESA, CSA, and CNSA, which are actively developing mission plans for lunar exploration, including sending crews to the surface of the Moon. Furthermore, even though considerable time has passed since Apollo missions, the invaluable knowledge gained from the experiences of Apollo astronauts regarding lunar dust effects remains highly relevant and merits thorough investigation, as elaborated in Chapter 1. Consequently, this research initiative focused on a comprehensive examination of these insights, their implications, and efforts to tackle the challenges that are not yet fully addressed.

Complex lunar dust problems affect a wide range of activities related to exploring the Moon. These problems, as discussed in this work, cover a wide range of lunar exploration activities and include the adhesion of lunar dust to equipment, the penetration of backlashes, and the jamming of mechanisms. It is important to note that the origin of this research can be traced back to past efforts of the European Space Agency (ESA), where a project on geological lunar sampling tools was carried out in 2017-2020. The main goal of the work done in ESA was to develop new design solutions for EVA tools. The project presented here continued the topic by searching for solutions that could prevent the harmful effects of lunar dust on the hardware.

The literature review in Chapter 2 introduced a multitude of challenges faced by Apollo missions due to lunar dust, including increased friction, seal failures, dust accumulation, and contamination, among others. The problem statement, as elaborated within this thesis, is focused specifically on the issue of lunar dust-induced

clogging of rigid-body mechanisms within lunar surface equipment. This problem originates in the presence of fine dust particles characterised by sharp, abrasive edges that inflict damage on hardware components. The distinctive properties of lunar dust, which encompass its inherent hardness and electrostatic attributes, render it profoundly disruptive to hardware operations. And the work presented here focused on solving the mechanisms deterioration and jamming problem.

This research effort was dedicated to bridging the technological gap associated with addressing the environmental impact of lunar dust on hardware. The proposed implicit dust mitigation strategy aligns with the concept of layered engineering defence strategies devised to combat lunar dust challenges. In particular, this work introduced the innovative use of compliant mechanisms as a design approach to mitigate dust-induced damage to lunar equipment. As discussed and demonstrated in this work, compliant mechanisms are naturally dust resilient. Their addition to dust mitigation methods expanded the range of viable dust mitigation solutions.

6.1   PROJECT OUTCOMES

In the context of developing compliant mechanisms for space missions (and possibly one day manufacturing them in space), 3D printing plays an important role as a manufacturing methodology that can ensure minimal material waste and the possibility of developing complex compliant topologies. Additive manufacturing can also aid and streamline the iterative design process, as shown in this work. The project presented here demonstrated the applicability of FDM 3d printing with polymers as a suitable manufacturing method for the compliant gripper. 3D printing not only enabled rapid prototyping and testing of various designs but also allowed the exploration of different materials. The TPC, which is characterised by high flexibility, was an excellent material for the first ideas synthesis and testing. PLA, known for its affordability and ease of printing, also proved to be a valuable option, while PEEK, with its superior mechanical properties, showcased potential for more demanding applications while also being a promising (and already proven) candidate for use in space. This manufacturing approach not only enabled rapid iteration of designs, but also provided samples with satisfactory mechanical characteristics. Furthermore, this project demonstrated that thermal post-treatment of components produced by additive manufacturing can help to fine-tune material properties. Although it is important to note that the quality control in FDM 3D printing might pose a challenge, and in the case of compliant mechanisms even small disturbances can have an impact on the final kinematic behaviour. However, even though the stiffness of mechanisms presented in this work differ slightly from

the FEM models, the results presented in this work are reproducible for each gripper, and as such this project demonstrates that it is possible to create 3D printed compliant systems with reliable and repeatable behaviour.

A diverse range of gripper designs was created using different methodologies and various materials. Notable findings included the challenges encountered with topology optimisation of materials with higher stiffness, where the presence of intermediate density in the final design severely increased the stiffness of the topology (while produced with full stiffness) and restricted the range of movement and overall performance. At the same time, analytically designed grippers made of more flexible materials (namely, TPC) lacked the stiffness to provide degrees of constraint of the slender flexures. Some challenges were also encountered while using PLA in a stress range close to its yield strength. The outcome was the appearance of plastic deformations. It is not in the scope of this work to judge what should be the safe maximum stress compared to the yield strength of the material, but it is justifiable to claim that minimisation of maximum stress in compliant mechanisms can help to improve the precision and avoid permanent deformations. This approach helped to develop a methodology that improved the performance of the designs presented in Chapter 5.

The work on 3D printing of mechanisms in the scope of this project resulted in collaboration with two commercial companies: Astronika working in the field of space mechanisms and Zortrax who specialises in additive manufacturing and worked with ESA on a qualification of Z-PEEK for space use. As such, Z-PEEK (PEEK from Zortrax) was the main candidate for the final designs due to its compatibility with the space environment. PEEK has relatively high Young's modulus and, because of that, methodology to improve topology optimisation outcomes for stiffer materials, was developed during this project. The final approach combined topology optimisation with an analytical re-design step that aimed at the reduction of stress in the flexures. This approach resulted in grippers made of PEEK capable of accommodating larger deformations while maintaining structural integrity and avoiding plastic deformations. The analytical re-design step focused on optimisation of flexure geometries by refining their thickness for given displacements region. Furthermore, the accuracy of displacement measurements during testing was enhanced by the introduction of Digital Image Correlation, specifically Ncorr, which provides a comprehensive understanding of gripper deformation in its entirety.

In conclusion, the iterative nature of the design process presented here is showcased in the journey from prototyping to improved gripper designs. The challenges faced and the lessons learnt in the prototyping phase laid the foundation for the

significant improvement presented in Chapter 5. The innovative combination of design methodologies, careful selection of materials with consideration of their implications on final design, and advanced testing techniques led to compliant grippers that are better suited for applications involving substantial deformations and dusty lunar conditions. These improvements are not only relevant for space applications but also hold promise for a wider range of applications where compliant mechanisms are viable candidates that can offer multiple advantages over rigid body mechanisms.

6.2 CONTRIBUTIONS TO THE FIELD

Several key achievements and impacts in the field of this work can be highlighted. They are listed below:

- **Dust mitigation**

  The research work presented here was the first instance in which compliant mechanisms were proposed as a dust mitigation strategy. The idea was advertised to the dust mitigation and space hardware community in the proceedings of two biggest space mechanisms conferences in the world: European Space Mechanisms And Tribology Symposium and Aeruspace Mechanisms Symposium (papers listed in the bibliography [37, 55]. Since the establishment of this concept, it has also appeared in publications of other researchers (with appropriate citations of the work presented here); examples are also provided in the bibliography [181–183]. The work on lunar dust mitigation is especially relevant today, when the biggest space agencies in the world are planning and already designing new equipment that will fly to the Moon.

- **Regolith Environment**

  This research highlighted the rigid-body problems in contact with lunar dust. Furthermore, insights gained from testing of compliant mechanisms in a regolith simulant environment shed light on what should be considered in the planning of such tests in the future. The findings emphasised that displacement-driven control remains resilient to regolith intrusions, making it a more suitable choice for compliant mechanisms in such environments. As demonstrated, force-driven control might be disturbed by friction not between the mechanism elements but in between mechanism system and the force rig.

- **Design Methodology**

  A shift toward a hybrid design methodology that harnessed topology optimisation and analytical redesign offered improvement of the kinematic char-

acteristics and stress-strain performance, as observed in a journey from the prototyping Chapter (4) to the improved gripper Chapter (5). This innovative approach enhanced the grippers' performance in applications involving substantial deformations, a crucial improvement for compliant applications. This was also presented in the publication in Acta Astronautica [14] and during the European Space Mechanisms And Tribology Symposium (with publication in proceedings [165]. The methodology used in this work can be replicated for different projects, and the designs presented here are also easy to scale up or down if needed. Althought the application discussed in this work focused on the space industry, the possibilities for use of presented methodology and advantages of complaint mechanisms in different industries are very wide. Examples include biomedical industry with compliant agile endoscopic surgical tools, agriculture with compliant adaptable grippers for fruit and vegetable handling (to avoid damage possible by grippers with high stiffness), environments requiring extreme cleanliness like food or medicine production (as complaint mechanisms can be produced without inter-element gaps that can be source of contaminants) and precision instruments in optical systems.

- **Material Selection**

  Material choices were carefully considered due to the challenges of topology optimisation discussed in this work. The analytical design methodology also proved to be challenging with materials that are characterised by low Young's modulus. In this work, a set of useful insights into combinations of material selection and design methodology is presented. Furthermore, the improved gripper designs presented in Chapter 5 demonstrated the feasibility of using cost-effective PLA as a suitable prototyping material to prepare the design and the test methodology for the more expensive (but space-qualified) PEEK. This demonstration expands the range of material options and offers more accessible solutions for rapid prototyping. In-depth material considerations were also presented at a joint conference on Materials in the Space Environment ISMSE-15/ICPMSE-13, and peer-reviewed findings were published in the conference proceedings [83].

- **Testing Methodology**

  The precision and reliability of displacement measurements during gripper testing was significantly improved with the introduction of Digital Image Correlation, Ncorr, enabling a more accurate assessment of gripper performance. In the research community, DIC is most prevalent in the assessment of small deformations, and this work demonstrated its use with large defor-

mations and high strains. This methodology was also demonstrated in one of the publications already mentioned in one of the previous points [165].

- **Performance Characterisation**

  The improved gripper designs showcased remarkable progress in terms of Geometric Advantage (GA), input displacement requirements, and displacement-controlled input. In particular, the PLA-enhanced gripper exhibited the highest GA, while the annealed PEEK gripper demonstrated increased stiffness through thermal post-processing, opening up possibilities for improved performance. These considerations were also outlined in one of the publications produced in line with this work [165] which contributed to the field of compliant mechanisms in space.

6.3 FUTURE WORK RECOMMENDATIONS

This work involved several technologies and research areas that can be further explored in future projects. The list below highlights the most promising research avenues and provides a short summary of what could be the focus of the next projects.

- **Additive manufacturing with composite materials with lunar dust**

  The application of 3D printing in space missions aligns with the growing trend of in-situ resource utilisation (ISRU). By using local resources and 3D printing, astronauts could manufacture tools and spare parts on celestial bodies such as the Moon or Mars. This approach reduces the dependence on Earth for resupply missions and enhances the sustainability of the lunar presence. One of the possible continuations of this project is to assess the applicability of ISRU in the production of geological tools on the Moon. This could be realised by using composite polymers that contain lunar regolith dust in them. As already mentioned in this work, preliminary research on the topic of the production of polymeric FDM filaments with lunar dust simulant EAC-1A inclusions is already ongoing in ESA in the SpaceShip EAC team. The next interesting step would be to conduct an assessment to examine whether such a filament can be used for compliant mechanism production. Furthermore, exploring the potential of composite materials that incorporate lunar dust not only presents opportunities for lunar resource utilisation, but also raises questions about the durability, thermal stability, and mechanical properties of such materials in the extreme lunar environment. Investigating these aspects would contribute to a comprehensive understanding of the suitability of regolith-based composites for use in long-duration missions.

- **Novel and active materials**

  Investigation of bulk metallic glasses with their high elasticity and large elastic strain limits as well as smart materials, known for their unique properties such as superelasticity, could be beneficial in the design of compliant mechanisms for lunar dust mitigation. Research can focus on understanding how these materials can enhance the design and utilisation of compliant mechanisms. This project could also assess the feasibility of integrating these materials into existing designs or developing new mechanisms that harness their exceptional mechanical characteristics for improved dust mitigation performance. Moreover, delving deeper into the research of metallic glasses and smart materials opens doors to exploring novel applications beyond lunar dust mitigation. Smart material can also be used as actuators that can react to the changes of the environment (temperature, radiation, etc.). This could be a starting point for building compliant mechanisms with incorporated actuation that could also reduce the mass, volume, and assembly efforts.

- **Multimaterial approach**

  There is room to investigate the feasibility of 3D printing compliant mechanisms using multiple materials or applying metallic layers to polymeric structures. The metalisation of PEEK was preliminaryly evaluated in the project of Astronika and Zortrax, which supported the fabrication of the PEEK prototypes presented in this work. Here, the metalised parts were not evaluated, but further research could explore how different combinations of polymers and metals can enhance mechanical properties, wear resistance, and overall performance of mechanisms, especially in the lunar environment. The topology optimisation of multimaterial design domain is also an interesting topic that could potentially provide tools to build flexible but strong flexures. A future project could focus on finding multimaterial approach capable of representing the pseudo-densities (and reduced Young's modulus) present in SIMP topology optimisation. Additionally, exploring the possibilities of a multimaterial approach in a compliant mechanism design introduces exciting prospects for adaptable and multifunctional mechanisms. Investigating the interactions between various materials and their synergistic effects on performance can lead to innovations not only in lunar applications but also in terrestrial robotics, where versatile and durable mechanisms are highly sought after.

- **Launch vibrations response analysis**

  The work presented in this thesis did not focus on assessing the impact of

the launch vibration on the flexures. A modal analysis and vibration testing could check the behaviour of the mechanisms in dynamic environemnts. For most space equipment, Hold Down and Release Mechanisms (HDRM) are used to ensure that moving parts are safely stowed during launch. Unfortunately, long slender flexures are susceptible to launch vibration problems even if the output of the mechanism is secured by HDRM. More work looking into the assessment of flexures' behaviour in vibration environments and potential optimisation (including damping) would be beneficial. Understanding the response to launch vibrations is crucial to ensuring that more complex mechanisms can be safely launched to the Moon. Furthermore, exploring the effects of launch vibrations on compliant mechanisms extends beyond lunar missions. It has broad implications for the design and safety of spacecraft and payloads in various contexts, including satellite launches and planetary exploration missions. A comprehensive analysis of the vibration response can guide the development of more robust and reliable space systems.

- **Topology optimisation of complex mechanisms**

  The gripper presented in this work has a single input and a single output. More complex mechanisms with multiple inputs and/or outputs would require additional considerations in topology optimisation. It would be interesting to find out what more complex space mechanisms could benefit from being compliant and assess the use of topology optimisation for those mechanisms. The methods presented here in different applications could be very interesting and expanded in terms of complexity. Moreover, as space missions become increasingly ambitious, the need for complex and adaptable mechanisms is growing. Exploring the topology optimisation of intricate space mechanisms opens up new avenues for designing mission-specific, highly efficient systems that can fulfil a variety of tasks.

- **Integrated sensors and actuators**

  The next area for improvement in compliant mechanisms is to integrate actuation and sensing into their topologies. This could be aided by the use of strain gauges, smart materials, etc. It could also enable the use of compliant mechanisms in closed-loop control. Such a project could explore how these designs enable precise and adaptive control, making them suitable for missions that require real-time adjustments and responses. Furthermore, the integration of sensors and actuators within compliant mechanisms holds great promise for the evolution of robotic systems in space. Beyond lunar dust mitigation, this technology can find applications in autonomous planetary exploration,

where robots equipped with compliant mechanisms and advanced sensing capabilities can adapt to unforeseen terrain and perform intricate scientific tasks, while maintaining high precision and efficiency.

- **Integration with other dust mitigation technologies**

  The review of the literature in this work outlined other dust mitigation technologies. Future projects could examine the use of combinations of different passive or active methods to be added to compliant mechanisms. As demonstrated here, the function of the compliant mechanisms is not affected by the dust environment. Nevertheless, it is possible that some applications require that the mechanisms be completely clean (and not only operational). In such a situation, additional protection would be needed, and compliant mechanisms should then be integrated synergistically with other technologies. This should also include the assessment of the combined effectiveness. Moreover, exploring the integration of compliant mechanisms with a spectrum of dust mitigation technologies underscores their versatility and adaptability. This approach is not limited to lunar applications alone but can be extrapolated to planetary exploration, where hybrid solutions that combine the strengths of multiple technologies can optimise the overall mission success rate by ensuring equipment cleanliness, longevity, and achievement of mission objectives.

- **Long term durability studies**

  Studies examining the potential life (maximum number of cycles) of polymer-based compliant mechanisms could help to propose their future use in a wider space exploration context. Conducting long-term durability studies by exposing compliant mechanisms to vacuum conditions and thermal gradients while subjecting them to repeatable stress and elastic deformations would assess their potential lifespan. This research could provide information on the resilience and reliability of compliant mechanisms for long-duration missions. Additionally, a more comprehensive understanding of the long-term durability and failure modes of compliant mechanisms can have far-reaching implications for space missions that extend well beyond lunar exploration. Investigating the behaviour of these mechanisms over extended periods in space-like conditions contributes to the development of highly reliable and enduring technologies with the predictable fatigue life.

BIBLIOGRAPHY

[1] J. R. Gaier, "The Effects of Lunar Dust on EVA Systems During the Apollo Missions," *Nasa/Tm-2005-213610/Rev1*, no. March, 2007.

[2] D. Budzyń, H. Stevenin, M. Maurer, F. Sauro, and L. Bessone, "Prototyping of Lunar surface geological sampling tools for Moon spacewalk simulations by ESA," *Proceedings of the International Astronautical Congress, IAC*, vol. 2018-Octob, no. October, pp. 1–5, 2018.

[3] E. N. Slyuta, "Physical and mechanical properties of the lunar soil (a review)," *Solar System Research*, vol. 48, no. 5, pp. 350–353, 2014.

[4] S. Wagner, "Asteroid, lunar and planetary regolith management a layered engineering defense," tech. rep., NASA, 2014.

[5] J. S. Levine, D. Winterhalter, and R. L. Kerschmann, *The Impact of Lunar Dust on Human Exploration*. Cambridge Scholars Publishing, 2021.

[6] D. Rickman and K. W. Street, "Some expected mechanical characteristics of lunar dust: A geological view," *AIP Conference Proceedings*, vol. 969, no. January 2008, pp. 949–955, 2008.

[7] J. E. Colwell, S. Batiste, M. Horányi, S. Robertson, and S. Sture, "Lunar surface: Dust dynamics and regolith mechanics," *Reviews of Geophysics*, vol. 45, no. 2, pp. 1–26, 2007.

[8] J. R. Gaier, "Regolith activation on the lunar surface and its ground test simulation," *SAE Technical Papers*, no. April, 2009.

[9] J. E. Colwell, S. R. Robertson, M. Horányi, X. Wang, A. Poppe, and P. Wheeler, "Lunar dust levitation," *Journal of Aerospace Engineering*, vol. 22, no. 1, pp. 2–9, 2009.

[10] L. L. Howell, S. P. Magleby, and B. M. Olsen, *Handbook of Compliant Mechanisms*. No. 2013, Wiley Online Library, 2013.

[11] Richard W. Orloff; David M. Harland, *Apollo: The Definitive Sourcebook*, vol. 4. Springe, 2006.

[12] International Agency Working Group, "Dust mitigation gap assessment report," 2016.

[13] I. Crawford, "The scientific legacy of apollo," *Astronomy & Geophysics*, vol. 53, no. 6, pp. 6–24, 2012.

[14] D. Budzyń, H. Zare-Behtash, A. Cowley, and A. Cammarano, "Implicit lunar dust mitigation technology: Compliant mechanisms," *Acta Astronautica*, vol. 203, no. 203, pp. 146–156, 2023.

[15] T. W. Group, "Global exploration roadmap critical technology neends," in *International Space Exploration Coordination Group*, 2019.

[16] G. H. HEIKEN, D. T. VANIMAN, and B. M. FRENCH, "Lunar Sourcebook," *Cambridge University Press*, p. 778, 1991.

[17] T. J. Stubbs, J. S. Halekas, W. M. Farrell, and R. R. Vondrak, "Lunar surface charging: A global perspective using lunar prospector data," *ESA - Workshop on Dust in Planetary Systems*, pp. 181–184, 2007.

[18] T. L. Jackson, W. M. Farrell, and M. I. Zimmerman, "Rover wheel charging on the lunar surface," *Advances in Space Research*, 2015.

[19] Z. Sternovsky, S. Robertson, A. Sickafoose, J. Colwell, and M. Horányi, "Contact charging of lunar and Martian dust simulants," *Journal of Geophysical Research E: Planets*, vol. 107, no. 11, pp. 15–1, 2002.

[20] S. Berkebile and J. R. Gaier, "Adhesion in a vacuum environment and its implications for dust mitigation techniques on airless bodies," *42nd International Conference on Environmental Systems 2012, ICES 2012*, no. September 2012, 2012.

[21] R. P. Feynman, R. B. Leighton, and M. Sands, *The Feynman Lectures on Physics, Vol. I: The New Millennium Edition: Mainly Mechanics, Radiation, and Heat*, vol. I. Hachette UK, 2015.

[22] O. Walton, "Adhesion of lunar dust (nasa/cr-2007-214685)," *NASA Report, Cleveland*, pp. 1–45, 2007.

[23] V. Harrigan, K. Carter, and M. R. Shaeri, "Electrostatic cleaning system integrated with thunderon brush for lunar dust mitigation," *International Journal of Aerospace and Mechanical Engineering*, vol. 15, no. 8, pp. 347–350, 2021.

[24] Z. Liu, A. Mahmud, K. Sjolund, C. Lum, P. Panda, C. Paris, G. Rizzo, E. Smith, H. Zhang, and L. Zhang, "Hybrid dust mitigation brush utilizing eds and uv technologies," tech. rep., Georgia Institute of Technology, 2021.

[25] H. Kawamoto, "Electrostatic transport and manipulation of lunar soil and dust," in *AIP Conference Proceedings*, vol. 969, pp. 203–212, American Institute of Physics, 2008.

[26] C. I. Calle, J. McFall, C. Buhler, S. Snyder, E. Arens, A. Chen, M. Ritz, J. Clements, C. Fortier, and S. Trigwell, "Dust particle removal by electrostatic and dielectrophoretic forces with applications to nasa exploration missions," in *Proc. ESA Annual Meeting on Electrostatics*, vol. 2008, ESA Minneapolis, MN, 2008.

[27] C. Calle, E. Arens, J. McFall, C. Buhler, S. Snyder, J. Geiger, R. Hafley, K. Taminger, and C. Mercer, "Reduced gravity flight demonstration of the dust shield technology for optical systems," in *2009 IEEE Aerospace conference*, pp. 1–10, IEEE, 2009.

[28] H. Kawamoto, M. Uchiyama, B. Cooper, and D. McKay, "Mitigation of lunar dust on solar panels and optical elements utilizing electrostatic traveling-wave," *Journal of Electrostatics*, vol. 69, no. 4, pp. 370–379, 2011.

[29] B. Guo, W. Javed, C. Pett, C.-Y. Wu, and J. R. Scheffe, "Electrodynamic dust shield performance under simulated operating conditions for solar energy applications," *Solar Energy Materials and Solar Cells*, vol. 185, pp. 80–85, 2018.

[30] H. Kawamoto, "Electrostatic cleaning device for removing lunar dust adhered to spacesuits," *Journal of Aerospace Engineering*, vol. 25, no. 3, pp. 470–473, 2012.

[31] M. Adachi, *Dynamics of electromagnetic particles and its application for mitigation and utilization technologies of regolith on moon, mars, and asteroids*. PhD thesis, Waseda University, 2017.

[32] H. Kawamoto, "Handheld cleaning tool for lunar dust adhered to spacesuits using magnetic and electrodynamic forces," *Journal of Aerospace Engineering*, vol. 34, no. 4, 2021.

[33] S. Masuda, K. Fujibayashi, K. Ishida, and H. Inaba, "Confinement and transportation of charged aerosol clouds via electric curtain," *Electrical Engineering in Japan*, vol. 92, no. 1, pp. 43–52, 1972.

[34] M. Adachi, H. Moroka, H. Kawamoto, S. Wakabayashi, and T. Hoshino, "Particle-size sorting system of lunar regolith using electrostatic traveling wave," *Journal of Electrostatics*, vol. 89, pp. 69–76, 2017.

[35] H. Kawamoto and N. Hara, "Electrostatic cleaning system for removing lunar dust adhering to space suits," *Journal of Aerospace Engineering*, vol. 24, no. 4, pp. 442–444, 2011.

[36] K. K. Manyapu, *Spacesuit Integrated Carbon Nanotube Dust Mitigation System for Lunar Exploration*. PhD thesis, University of North Dakota, 2017.

[37] D. Budzyń, E. Tuohy, N. Garrivier, T. Schild, A. Cowley, R. Cruise, M. Adachi, H. Zare-Behtash, and A. Cammarano, "Lunar Dust: Its Impact on Hardware and Mitigation Technologies," *46th Aerospace Mechanisms Symposium*, p. 287, 2022.

[38] SKF, "Deep groove ball bearing with seals or shields: 623-2rs1."

[39] G. S. Watson, D. W. Green, L. Schwarzkopf, X. Li, B. W. Cribb, S. Myhra, and J. A. Watson, "A gecko skin micro/nano structure–a low adhesion, superhydrophobic, anti-wetting, self-cleaning, biocompatible, antibacterial surface," *Acta biomaterialia*, vol. 21, pp. 109–122, 2015.

[40] S. M. Kelleher, O. Habimana, J. Lawler, B. O'reilly, S. Daniels, E. Casey, and A. Cowley, "Cicada wing surface topography: an investigation into the bactericidal properties of nanostructural features," *ACS applied materials & interfaces*, vol. 8, no. 24, pp. 14966–14974, 2016.

[41] G. D. Bixler and B. Bhushan, "Rice-and butterfly-wing effect inspired self-cleaning and low drag micro/nanopatterned surfaces in water, oil, and air flow," *Nanoscale*, vol. 6, no. 1, pp. 76–96, 2014.

[42] J. Song, R. Shi, X. Bai, H. Algadi, and D. Sridhar, "An overview of surface with controllable wettability for microfluidic system, intelligent cleaning, water harvesting, and surface protection," *Advanced Composites and Hybrid Materials*, vol. 6, no. 1, p. 22, 2023.

[43] J. Gaier, D. Waters, B. Banks, R. Misconin, and M. Crowder, "Evaluation of surface modification as a lunar dust mitigation strategy for thermal control

surfaces," in *41st International Conference on Environmental Systems*, p. 5183, 2011.

[44] J. A. Dominguez and J. Whitlow, "Upwards migration phenomenon on molten lunar regolith: New challenges and prospects for isru," *Advances in Space Research*, vol. 63, no. 7, pp. 2220–2228, 2019.

[45] M. Adachi and H. Kawamoto, "Electrostatic sampler for large regolith particles on asteroids," *Journal of Aerospace Engineering*, vol. 30, no. 3, p. 04016098, 2017.

[46] M. Adachi, H. Maezono, and H. Kawamoto, "Sampling of regolith on asteroids using electrostatic force," *Journal of Aerospace Engineering*, vol. 29, no. 4, p. 04015081, 2016.

[47] E. S. T. Laboratory, *Space Tribology Handbook*. AEA Technology, 1997.

[48] X. Zhang and B. Zhu, *Topology optimization of compliant mechanisms*. Springer, 2018.

[49] X. Pei, J. Yu, G. Zong, and S. Bi, "An effective pseudo-rigid-body method for beam-based compliant mechanisms," *Precision Engineering*, vol. 34, no. 3, pp. 634–639, 2010.

[50] L. L. Howell, *Compliant Mechanisms*. Wiley, 2001.

[51] R. M. Fowler, L. L. Howell, and S. P. Magleby, "Compliant space mechanisms: A new frontier for compliant mechanisms," *Mechanical Sciences*, vol. 2, no. 2, pp. 205–215, 2011.

[52] L. Zhao, X. Yu, P. Li, and Y. Qiao, "High-precision compliant mechanism for lens XY micro-adjustment," *Review of Scientific Instruments*, vol. 91, no. 3, 2020.

[53] J. Pinskier, B. Shirinzadeh, M. Ghafarian, T. K. Das, A. Al-Jodah, and R. Nowell, "Topology optimization of stiffness constrained flexure-hinges for precision and range maximization," *Mechanism and Machine Theory*, vol. 150, p. 103874, 2020.

[54] L. Liu, S. Bi, Q. Yang, and Y. Wang, "Design and experiment of generalized triple-cross-spring flexure pivots applied to the ultra-precision instruments," *Review of Scientific Instruments*, vol. 85, no. 10, 2014.

[55] D. Budzyń, H. Zare-Behtash, A. Cowley, and A. Cammarano, "Topology optimization of compliant mechanisms as a design method to improve hardware performance in lunar dust," *19th European Space Mechanisms and Tribology Symposium*, no. 1, 2021.

[56] J. A. Gallego and J. Herder, "Synthesis methods in compliant mechanisms: An overview," *Proceedings of the ASME Design Engineering Technical Conference*, vol. 7, no. PARTS A AND B, pp. 193–214, 2009.

[57] M. Kahr, H. Steiner, W. Hortschitz, M. Stifter, A. Kainz, and F. Keplinger, "3D-Printed MEMS Magnetometer Featuring Compliant Mechanism," *Proceedings*, vol. 2, no. 13, p. 784, 2018.

[58] E. G. Merriam, J. E. Jones, and L. L. Howell, "Design of 3d-printed titanium compliant mechanisms," in *The 42nd Aerospace Mechanism Symposium*, 2014.

[59] E. G. Merriam, J. E. Jones, S. P. Magleby, and L. L. Howell, "Monolithic 2 DOF fully compliant space pointing mechanism," *Mechanical Sciences*, vol. 4, no. 2, pp. 381–390, 2013.

[60] H. Saudan, L. Kiener, G. Perruchoud, K. Vaideeswaran, and M. Dadras, "Additively manufactured and topologically optimized compliant mechanisms: technological assessment approach, latest achievements and current work in progress," in *Proceedings of the 17th European Space Mechanisms & Tribology Symposium, Hatfield, United Kingdom*, pp. 20–22, 2017.

[61] L. Kiener, H. Saudan, G. Perruchoud, and J. Kruis, "Compliant mechanisms re-design based on additive manufacturing and topology optimization," in *44th Aerospace Mechanisms Symposium*, p. 239, 2018.

[62] L. Kiener, H. Saudan, F. Cosandier, J. Kruis, G. Perruchoud, V. Pejchal, P. Spanoudakis, and J. Rouvinet, "Innovative concept for additive manufacturing of compliant mechanisms," in *18th European Space Mechanisms and Tribology Symposium. Presented at the ESMATS*, 2019.

[63] P. Spanoudakis, L. Kiener, F. Cosandier, and P. Schwab, "Large angle flexure pivot development and test campaign results," in *19th European Space Mechanisms and Tribology Symposium. Presented at the ESMATS*, 2021.

[64] P. Spanoudakis, L. Kiener, F. Cosandier, P. Schwab, L. Giriens, J. Kruis, D. Grivon, G. Psoni, C. Vrettos, and N. Bencheikh, "Large angle flexure pivot development for future science payloads for space applications," *MATEC Web of Conferences*, vol. 304, no. September, p. 07016, 2019.

[65] Y. Puyol, L. Blecha, M. Humphries, S. Hayoz, and F. Rottmeier, "Innovation in large angle flexible pivot design & material accelerated fatigue screening tests results," in *18th European Space Mechanisms and Tribology Symposium*, 2019.

[66] E. Lamacchia, R. Edeson, and M. E. Humphries, "Design and analysis of a novel flexible compliant joint for space mechanisms," in *17th European Space Mechanisms and Tribology Symposium. Presented at the ESMATS*, 2017.

[67] A. Verhaeghe, G. Perruchoud, P. Schwab, and M. Gumy, "Development challenges of a focus mechanism design for exomars mission submitted to the harsh martian environment and utilizing off-the-shelf equipment," in *17th European Space Mechanisms and Tribology Symposium*, 2017.

[68] A. Verhaeghe, G. Perruchoud, P. Schwab, M. Gumy, and J. Rouvinet, "Lessons learnt during the development of a compliant focus mechanism for the exomars rover mission," in *18th European Space Mechanisms and Tribology Symposium*, 2019.

[69] J. Vinals, F. Valls, J. Lozano, F. Faure, T. Blais, and H. Langenbach, "Mtg scan mechanism predevelopment: design\& performance," in *14th European Space Mechanisms and Tribology Symposium*, 2011.

[70] I. Arregui, I. Eguidazu, A. González, G. Lobato, J. Peña, and J. R. de Gopegui, "Flip mirror device for sentinel-3 slstr," *16th European Space Mechanisms and Tribology Symposium*, 2015.

[71] S. Henein, P. Spanoudakis, P. Schwab, I. Kjelberg, L. Giriens, Y. Welte, L. Dassa, R. Greger, and U. Langer, "Design and development of the point-ahead angle mechanism for the laser interferometer space antenna (lisa)," in *13th European Space Mechanisms and Tribology Symposium*, 2009.

[72] S. Henein, P. Spanoudakis, P. Schwab, L. Giriens, L. Lisowski, E. Onillon, and L. I. Myklebust, "Mechanical slit mask mechanism for the james webb space telescope spectrometer," in *Optical, Infrared, and Millimeter Space Telescopes*, vol. 5487, pp. 765–776, SPIE, 2004.

[73] E. Urgoiti, A. Ramirez, and P. Coste, "Gaia m2m positioning mechanism," in *14th European Space Mechanisms and Tribology Symposium*, vol. 47, 2005.

[74] C. Compostizo, R. López, and L. Rivera, "Gaia m2m pointing mechanism qualification," in *14th European Space Mechanisms and Tribology Symposium*, 2011.

[75] T. Sarafin and W. Larson, *Spacecraft Structures and Mechanisms: From Concept to Launch*. Space Technology Library, Springer Netherlands, 1995.

[76] Z. Chu, Y. Lei, and D. Li, "Dynamics and robust adaptive control of a deployable boom for a space probe," *Acta Astronautica*, vol. 97, no. 1, pp. 138–150, 2014.

[77] Z. Y. Chu, J. Hu, S. B. Yan, and M. Zhou, "Experiment on the retraction/deployment of an active-passive composited driving deployable boom for space probes," *Mechanism and Machine Theory*, vol. 92, pp. 436–446, 2015.

[78] M. Tokarz, J. Grygorczuk, H. Gut, D. Nolbert, S. Jarzynka, P. Brunne, and G. Rodrigues, "Coilable tapes for deployable antennas and booms in space applications," *Proceedings of the 3rd International Conference: Advanced Lightweight Structures and Reflector Antennas*, 10 2018.

[79] W. Smith, J. Nuth, D. Wegel, J. Church, and P. Barfknecht, "Boom retraction mechanism as part of sample acquisition system from remote and hazardous extra-terrestrial sites," in *European Space Mechanisms and Tribology Symposium*, no. GSFC-E-DAA-TN69939, 2019.

[80] H. Arora, R. Dangarwala, S. Mukherjee, and B. Singh Munjal, "Investigation of tape flexures for space borne deployable structures," *International Journal of Space Structures*, vol. 37, no. 1, pp. 37–48, 2022.

[81] H. Ye, Y. Zhang, Q. Yang, Y. Xiao, R. V. Grandhi, and C. C. Fischer, "Optimal design of a three tape-spring hinge deployable space structure using an experimentally validated physics-based model," *Structural and Multidisciplinary Optimization*, vol. 56, no. 5, pp. 973–989, 2017.

[82] O. Testoni, T. Lumpe, J. L. Huang, M. Wagner, S. Bodkhe, Z. Zhakypov, R. Spolenak, J. Paik, P. Ermanni, L. Muñoz, and K. Shea, "A 4D printed active compliant hinge for potential space applications using shape memory alloys and polymers," *Smart Materials and Structures*, vol. 30, no. 8, 2021.

[83] D. Budzyn, H. Zare-Behtash, A. Cowley, and A. Cammarano, "Compliant mechanisms for dust mitigation in lunar hardware development: technology and material considerations," in *IOP Conference Series: Materials Science and Engineering*, vol. 1287, p. 012001, IOP Publishing, 2023.

[84] K. K. De Groh, B. A. Banks, C. E. McCarthy, R. N. Rucker, L. M. Roberts, and L. A. Berger, "MISSE 2 PEACE polymers atomic oxygen erosion experiment

on the international space station," *High Performance Polymers*, vol. 20, no. 4-5, pp. 388–409, 2008.

[85] I. Gouzman, E. Grossman, R. Verker, N. Atar, A. Bolker, and N. Eliaz, "Advances in Polyimide-Based Materials for Space Applications," *Advanced Materials*, vol. 31, no. 18, pp. 1–15, 2019.

[86] J. Hopkins and M. L. Culpepper, "Synthesis of multi-degree of freedom, parallel flexure system concepts via Freedom and Constraint Topology (FACT) - Part I: Principles," *Precision Engineering*, vol. 34, no. 2, pp. 259–270, 2010.

[87] C. J. Kim, "A Building Block Approach to the Conceptual Synthesis of Compliant Mechanisms Utilizing," *Journal of Mechanical Design*, vol. 130, no. February, pp. 1–11, 2008.

[88] N. Wang, X. Liang, and X. Zhang, "Pseudo-rigid-body model for corrugated cantilever beam used in compliant mechanisms," *Chinese Journal of Mechanical Engineering (English Edition)*, vol. 27, no. 1, pp. 122–129, 2014.

[89] J. B. Hopkins and M. L. Culpepper, "Synthesis of multi-degree of freedom, parallel flexure system concepts via freedom and constraint topology (FACT). Part II: Practice," *Precision Engineering*, vol. 34, no. 2, pp. 271–278, 2010.

[90] J. B. Hopkins and M. L. Culpepper, "Synthesis of multi-degree of freedom, parallel flexure system concepts via Freedom and Constraint Topology (FACT) - Part I: Principles," *Precision Engineering*, vol. 34, no. 2, pp. 259–270, 2010.

[91] J. B. Hopkins and M. L. Culpepper, "Synthesis of precision serial flexure systems using freedom and constraint topologies (FACT)," *Precision Engineering*, vol. 35, no. 4, pp. 638–649, 2011.

[92] J. Hopkins, "Freedom and constraint topologies (fact) library of freedom and constraint spaces used to design parallel flexure systems.." `https://commons.wikimedia.org/wiki/File:Freedom_and_constraint_topologies_(FACT)_library_of_freedom_and_constraint_spaces_used_to_design_parallel_flexure_systems.jpg`, 2010. [Online; accessed 20-February-2023].

[93] J. B. Hopkins, "A visualization approach for analyzing and synthesizing serial flexure elements," *Journal of Mechanisms and Robotics*, vol. 7, no. 3, pp. 1–12, 2015.

[94] J. B. Hopkins, "Synthesizing parallel flexures that mimic the kinematics of serial flexures using freedom and constraint topologies," *Journal of Mechanisms and Robotics*, vol. 5, no. 4, pp. 1–9, 2013.

[95] R. M. Panas, F. Sun, L. Bekker, and J. B. Hopkins, "Combining cross-pivot flexures to generate improved kinematically equivalent flexure systems," *Precision Engineering*, vol. 72, no. December 2020, pp. 237–249, 2021.

[96] C. J. Kim, S. Kota, and Y.-M. Moon, "An Instant Center Approach Toward the Conceptual Design of Compliant Mechanisms," *Journal of Mechanical Design*, vol. 128, pp. 542–550, 07 2005.

[97] A. S. Mata, A. B. Torras, J. A. C. Carrillo, F. E. Juanco, A. J. G. Fernández, F. N. Martínez, and A. O. Fernández, *Fundamentals of machine theory and mechanisms*, vol. 40. Springer, 2016.

[98] M. P. Querin OM, Victoria M, Alonso C, Loyola RA, *Topology design methods for structural optimization*. Butterworth-Heinemann, 2017.

[99] G. K. Ananthasuresh, "Topology Synthesis of Compliant Mechanisms for Nonlinear Force-Deflection and Curved Path," *Journal of Mechanical Design*, vol. 123, no. March, pp. 33–42, 2001.

[100] A. Saxena and G. K. Ananthasuresh, "On an optimal property of compliant topologies," *Structural and Multidisciplinary Optimization*, pp. 36–49, 2000.

[101] B. Zhu, X. Zhang, H. Zhang, J. Liang, H. Zang, H. Li, and R. Wang, "Design of compliant mechanisms using continuum topology optimization : A review," *Mechanism and Machine Theory*, vol. 143, 2020.

[102] N. Aulig and M. Olhofer, "Evolutionary computation for topology optimization of mechanical structures: An overview of representations," *2016 IEEE Congress on Evolutionary Computation, CEC 2016*, no. July 2016, pp. 1948–1955, 2016.

[103] J. D. Deaton and R. V. Grandhi, "A survey of structural and multidisciplinary continuum topology optimization: Post 2000," *Structural and Multidisciplinary Optimization*, vol. 49, no. 1, pp. 1–38, 2014.

[104] A. Saxena, "A material-mask overlay strategy for continuum topology optimization of compliant mechanisms using honeycomb discretization," *Journal of Mechanical Design, Transactions of the ASME*, vol. 130, no. 8, pp. 0823041–0823049, 2008.

[105] W. Zhang, J. Yuan, J. Zhang, and X. Guo, "A new topology optimization approach based on Moving Morphable Components (MMC) and the ersatz material model," *Structural and Multidisciplinary Optimization*, pp. 1243–1260, 2016.

[106] V. J. Challis, "A discrete level-set topology optimization code written in Matlab," *Structural and Multidisciplinary Optimization*, vol. 41, no. 3, pp. 453–464, 2010.

[107] M. P. Bendsoe and O. Sigmund, *Topology optimization: theory, methods, and applications.* Springer Science & Business Media, 2003.

[108] E. Andreassen, A. Clausen, M. Schevenels, B. S. Lazarov, and O. Sigmund, "Efficient topology optimization in MATLAB using 88 lines of code," *Structural and Multidisciplinary Optimization*, vol. 43, no. 1, pp. 1–16, 2011.

[109] G. I. Rozvany, "A critical review of established methods of structural topology optimization," *Structural and Multidisciplinary Optimization*, vol. 37, no. 3, pp. 217–237, 2009.

[110] X. Huang and Y. M. Xie, "A further review of ESO type methods for topology optimization," *Structural and Multidisciplinary Optimization*, vol. 41, no. 5, pp. 671–683, 2010.

[111] S. Nishiwaki, M. I. Frecker, S. Min, and N. Kikuchi, "Topology optimization of compliant mechanisms using the homogenization method," *International Journal for Numerical Methods in Engineering*, vol. 42, no. 3, pp. 535–559, 1998.

[112] J. Remacle, J. Lambrechts, and B. Seny, "Blossom-Quad: A non-uniform quadrilateral mesh generator using a minimum-cost perfect-matching algorithm," *International*, vol. 2, no. February, pp. 1102–1119, 2012.

[113] R. Ansola, E. Veguería, C. Alonso, and O. M. Querin, "Topology optimization of 3D compliant actuators by a sequential element rejection and admission method," *IOP Conference Series: Materials Science and Engineering*, vol. 108, no. 1, 2016.

[114] L. Cao, A. Dolovich, and W. Zhang, "On understanding of design problem formulation for compliant mechanisms through topology optimization," *Mechanical Sciences*, vol. 4, no. 2, pp. 357–369, 2013.

[115] C. B. W. Pedersen, T. Buhl, and O. Sigmund, "Topology synthesis of large-displacement compliant mechanisms," *International Journal for numerical methods in engineering*, no. May 2000, pp. 2683–2705, 2001.

[116] S. Rahmatalla and C. C. Swan, "Sparse monolithic compliant mechanisms using continuum structural topology optimization," *International Journal for Numerical Methods in Engineering*, no. August 2004, pp. 1579–1605, 2005.

[117] O. Sigmund, "A 99 line topology optimization code written in matlab," *Structural and Multidisciplinary Optimization*, vol. 21, no. 2, pp. 120–127, 2001.

[118] F. Baumann, H. Bugdayci, J. Grunert, F. Keller, and D. Roller, "Influence of slicing tools on quality of 3d printed parts," *Computer-Aided Design and Applications*, vol. 13, no. 1, pp. 14–31, 2016.

[119] F. Koppen, Stijn and Langelaar, Matthijs and van Keulen, "A simple and versatile topology optimization formulation for flexure design," *Mechanism and Machine Theory*, vol. 172, pp. 1–14, 2022.

[120] Altair, "Altair OptiStruct 2022 User Guide," tech. rep., 2022.

[121] W. F. Hosford, *Mechanical behavior of materials*, vol. 9780521846. 2005.

[122] A. Klarbring and N. Strömberg, "Topology optimization of hyperelastic bodies including non-zero prescribed displacements," *Structural and Multidisciplinary Optimization*, vol. 47, no. 1, pp. 37–48, 2013.

[123] F. Niu, S. Xu, and G. Cheng, "A general formulation of structural topology optimization for maximizing structural stiffness," *Structural and Multidisciplinary Optimization*, vol. 43, no. 4, pp. 561–572, 2011.

[124] J. H. Allton, "Catalog of Apollo Lunar Surface Geological Sampling Tools and Containers," *NASA*, 1989.

[125] D. Budzyń, H. Stevenin, M. Maurer, F. Sauro, and L. Bessone, "Prototyping of Lunar surface geological sampling tools for Moon spacewalk simulations by ESA," *Proceedings of the International Astronautical Congress, IAC*, vol. 2018-Octob, no. October, pp. 1–5, 2018.

[126] Wikimedia Commons, "File:apollo 12 lunar hand tong (as12-47-6932).jpg." [Online; accessed 28-July-2022].

[127] Wikimedia Commons, "File: Apollo 12 lunar hand tong." [Online; accessed 28-February-2023].

[128] C. Bryan, W. Strasburger, and H. Kalkowsky, "Lunar module structures handout," tech. rep., NASA, 1969.

[129] W. D. Callister Jr and D. G. Rethwisch, *Callister's materials science and engineering*. John Wiley & Sons, 2020.

[130] J. Peng and G. J. Snyder, "A figure of merit for flexibility," *Science*, vol. 366, no. 6466, pp. 690–691, 2019.

[131] M. F. Ashby, *Materials selection in mechanical design*. Burlington, MA: Butterworth-Heinemann, 4th ed., 2011.

[132] W. D. Callister, D. G. Rethwisch, *et al.*, *Materials science and engineering: an introduction*, vol. 7. John wiley & sons New York, 2007.

[133] J. A. Dever, S. K. Miller, E. A. Sechkar, and T. N. Wittberg, "Space environment exposure of polymer films on the materials international space station experiment: Results from MISSE 1 and MISSE 2," *High Performance Polymers*, vol. 20, no. 4-5, pp. 371–387, 2008.

[134] N. S. Prasad and W. H. Kinnard, "MISSE 6: testing materials in space," *Nanophotonics and Macrophotonics for Space Environments II*, vol. 7095, no. August 2008, p. 70950D, 2008.

[135] N. Naveed, "Investigate the effects of process parameters on material properties and microstructural changes of 3D-printed specimens using fused deposition modelling (FDM)," *Materials Technology*, vol. 36, no. 5, pp. 317–330, 2021.

[136] P. Scallan, "Comparative Study of the Sensitivity of PLA, ABS, PEEK, and PETG's Mechanical Properties to FDM Printing Process Parameters," *Process Planning*, pp. 219–250, 2003.

[137] A. Rodríguez-Panes, J. Claver, and A. M. Camacho, "The influence of manufacturing parameters on the mechanical behaviour of pla and abs pieces manufactured by fdm: A comparative analysis," *Materials*, vol. 11, no. 8, p. 1333, 2018.

[138] J. A. Travieso-Rodriguez, R. Jerez-Mesa, J. Llumà, O. Traver-Ramos, G. Gomez-Gras, and J. J. Roa Rovira, "Mechanical properties of 3d-printing polylactic acid parts subjected to bending stress and fatigue testing," *Materials*, vol. 12, no. 23, p. 3859, 2019.

[139] X. Wang, L. Zhao, J. Y. H. Fuh, and H. P. Lee, "Effect of porosity on mechanical properties of 3D printed polymers: Experiments and micromechanical modeling based on X-ray computed tomography analysis," *Polymers*, vol. 11, no. 7, 2019.

[140] P. P. by Josef Prusa, "Prusament pla data sheet." [Online; accessed 21-December-2023].

[141] P. P. by Josef Prusa, "How to improve your 3d prints with annealing." [Online; accessed 21-March-2024].

[142] Arnitel, "Arnitel® id 2045 data sheet." [Online; accessed 10-January-2022].

[143] Zortrax, "Z-peek data sheet." [Online; accessed 10-January-2023].

[144] Y. X. Xu and J. Y. Juang, "Measurement of nonlinear poisson's ratio of thermoplastic polyurethanes under cyclic softening using 2d digital image correlation," *Polymers*, vol. 13, no. 9, 2021.

[145] V. R. Sastri, *Plastics in medical devices: properties, requirements, and applications*. William Andrew, 2021.

[146] A. Jiménez, M. Peltzer, and R. Ruseckaite, *Poly (lactic acid) science and technology: processing, properties, additives and applications*. No. 12, Royal Society of Chemistry, 2014.

[147] H. Li, W. Zhao, X. Wu, H. Tang, Q. Li, J. Tan, and G. Wang, "3D printing and solvent dissolution recycling of polylactide-lunar regolith composites by material extrusion approach," *Polymers*, vol. 12, no. 8, 2020.

[148] "Spaceship eac: 3d printing with lunar dust." [Online; accessed 12-March-2022].

[149] D. P. Mariam Al Ali AlMaadeed and M. A. Carignano, *Polymer Science and Innovative Applications*. Elsevier, 2020.

[150] S. W. Paek, S. Balasubramanian, and D. Stupples, "Composites Additive Manufacturing for Space Applications: A Review," *Materials*, vol. 15, no. 13, 2022.

[151] M. Regis, A. Bellare, T. Pascolini, and P. Bracco, "Characterization of thermally annealed peek and cfr-peek composites: Structure-properties relationships," *polymer Degradation and Stability*, vol. 136, pp. 121–130, 2017.

[152] S. Rao, *Mechanical Vibrations*. Pearson Education, Incorporated, 2017.

[153] G. F. Schrader and A. K. Elshennawy, *Manufacturing processes and materials*. Society of Manufacturing Engineers, 2000.

[154] R. Sharma, S. Maurya, and R. Saini, "A review paper on current research and development in abrasive waterjet machining," *Mathematical Statistician and Engineering Applications*, vol. 71, no. 4, pp. 4160–4169, 2022.

[155] E. Akinlabi, R. Mahamood, and S. Akinlabi, *Advanced Manufacturing Techniques Using Laser Material Processing*. Advances in Civil and Industrial Engineering (2326-6139), IGI Global, 2016.

[156] A. Y. C. Nee, *Handbook of manufacturing engineering and technology*. Springer Publishing Company, Incorporated, 2014.

[157] N. Guo and M. C. Leu, "Additive manufacturing: technology, applications and research needs," *Frontiers of mechanical engineering*, vol. 8, pp. 215–243, 2013.

[158] Y. L. Yap, W. Toh, R. Koneru, K. Lin, K. M. Yeoh, C. M. Lim, J. S. Lee, N. A. Plemping, R. Lin, T. Y. Ng, *et al.*, "A non-destructive experimental-cum-numerical methodology for the characterization of 3d-printed materials—polycarbonate-acrylonitrile butadiene styrene (pc-abs)," *Mechanics of Materials*, vol. 132, pp. 121–133, 2019.

[159] E. Sacco and S. K. Moon, "Additive manufacturing for space: status and promises," *International Journal of Advanced Manufacturing Technology*, vol. 105, no. 10, pp. 4123–4146, 2019.

[160] ESA, "Esa launches first metal 3d printer to iss.." `https://www.esa.int/Science_Exploration/Human_and_Robotic_Exploration/ESA_launches_first_metal_3D_printer_to_ISSg`, 2024. [Online; accessed 28-February-2024].

[161] M. Hoffmann and A. Elwany, "In-Space Additive Manufacturing: A Review," *Journal of Manufacturing Science and Engineering*, vol. 145, no. 2, 2023.

[162] K. Ishfaq, M. Asad, M. A. Mahmood, M. Abdullah, and C. Pruncu, "Opportunities and challenges in additive manufacturing used in space sector: a comprehensive review," *Rapid Prototyping Journal*, vol. 28, no. 10, pp. 2027–2042, 2022.

[163] V. Mishra, S. Negi, S. Kar, A. K. Sharma, Y. N. K. Rajbahadur, and A. Kumar, "Recent advances in fused deposition modeling based additive manufacturing of thermoplastic composite structures: A review," *Journal of Thermoplastic Composite Materials*, p. 08927057221102857, 2022.

[164] "Zortrax z-peek filament certified by european space agency." [Online; accessed 18-April-2023].

[165] D. Budzyń, A. Cowley, M. Ossowski, M. Siemaszko, H. Zare-Behtash, and A. Cammarano, "Design, manufacturing, and testing of 3d printed compliant mechanisms for lunar equipment," *20th European Space Mechanisms and Tribology Symposium*, 2023.

[166] V. S. Engelschiøn, S. Eriksson, A. Cowley, M. Fateri, A. Meurisse, U. Kueppers, and M. Sperl, "Eac-1a: A novel large-volume lunar regolith simulant," *Scientific reports*, vol. 10, no. 1, pp. 1–9, 2020.

[167] J. Blaber, B. Adair, and A. Antoniou, "Ncorr: open-source 2d digital image correlation matlab software," *Experimental Mechanics*, vol. 55, no. 6, pp. 1105–1122, 2015.

[168] N. McCormick and J. Lord, "Digital image correlation," *Materials Today*, vol. 13, no. 12, pp. 52–54, 2010.

[169] B. Pan, "Recent progress in digital image correlation," *Experimental mechanics*, vol. 51, pp. 1223–1235, 2011.

[170] P. K. Rastogi and E. Hack, *Optical methods for solid mechanics: a full-field approach*. John Wiley & Sons, 2013.

[171] R. Harilal *et al.*, "Adaptation of open source 2d dic software ncorr for solid mechanics applications," *9th International Symposium on Advanced Science and Technology in Experimental Mechanics*, 2014.

[172] S. K. Miller and J. A. Dever, "Materials international space station experiment 5 polymer film thermal control experiment," *Journal of Spacecraft and Rockets*, vol. 48, no. 2, pp. 240–245, 2011.

[173] J.-P. Williams, B. Greenhagen, D. Paige, N. Schorghofer, E. Sefton-Nash, P. Hayne, P. Lucey, M. Siegler, and K. M. Aye, "Seasonal polar temperatures on the moon," *Journal of Geophysical Research: Planets*, vol. 124, no. 10, pp. 2505–2521, 2019.

[174] A. Bertram, *Elasticity and Plasticity of Large Deformations: Including Gradient Materials*. Springer Nature, 2021.

[175] S. C. Ligon, R. Liska, J. Stampfl, M. Gurr, and R. Mülhaupt, "Polymers for 3d printing and customized additive manufacturing," *Chemical reviews*, vol. 117, no. 15, pp. 10212–10290, 2017.

[176] D. Vaes and P. Van Puyvelde, "Semi-crystalline feedstock for filament-based 3d printing of polymers," *Progress in Polymer Science*, vol. 118, p. 101411, 2021.

[177] T. van Hooy, V. Srinivas, D. Auhl, and J. Harings, "Molecular structure and design of thermoplastic polymers for 3d printing." `https://www.zuyd.nl/binaries/content/assets/zuyd/onderzoek/interviews--artikelen/material-sciences_research-paper_3d-fab-print.pdf`. [Online; accessed 10-September-2023].

[178] S. Vidoli and G. Sciarra, "A model for crystal plasticity based on micro-slip descriptors," *Continuum Mechanics and Thermodynamics*, vol. 14, pp. 425–435, 2002.

[179] D. R. Owen, "Deformations and stresses with and without microslip," 1992.

[180] K. W. Siu and A. H. W. Ngan, "Relation between yield stress and peierls stress," *physica status solidi (b)*, vol. 256, no. 8, p. 1900107, 2019.

[181] D. Ignjatović Stupar, V. Ogrizović, J. Rošer, V. Poslončec-Petrić, and G. Vižintin, "Conceptual navigation and positioning solution for the upcoming lunar mining and settlement missions based on the earth's mining experiences: Lunar regional navigation transceiver system," *Minerals*, vol. 13, no. 3, p. 371, 2023.

[182] G. Barkó, G. Kalácska, R. Keresztes, L. Zsidai, H. Shegawu, and Á. Kalácska, "Abrasion evaluation of moon and mars simulants on rotating shaft/sealing materials: Simulants and structural materials review and selection," *Lubricants*, vol. 11, no. 8, p. 334, 2023.

[183] P. Zanon, M. Dunn, and G. Brooks, "Current lunar dust mitigation techniques and future directions," *Acta Astronautica*, 2023.